

MATER. TEHNOL.	LETNIK VOLUME	48	ŠTEV. NO.	4	STR. P.	451-606	LJUBLJANA SLOVENIJA	JULY-AUG. 2014
-------------------	------------------	----	--------------	---	------------	---------	------------------------	-------------------

VSEBINA – CONTENTS

IZVIRNI ZNANSTVENI ČLANKI – ORIGINAL SCIENTIFIC ARTICLES

Application of a neural network for estimating the crack formation and propagation in sol-gel CeO₂ coatings during processing at temperature

Uporaba nevronske mreže za ugotavljanje nastanka in širjenja razpoke v sol-gel premazu CeO₂ med postopkom ogrevanja
A. Savran, M. Alci, S. Yıldırım, R. Yiğit, E. Çelik 453

Optimization of the mechanical and tribological properties of extruded AMCs: extension of the algorithm searching area via multi-strategies

Optimizacija mehanskih in triboloških lastnosti ekstrudiranih AMC: razširitev algoritma iskalnega področja z uporabo več strategij
M. O. Shabani, A. A. Tofigh, M. R. Rahimpour, M. Razavi, A. Mazahery, F. Heydari 459

Tribo-corrosion properties of a NiTi dental wire

Tribokorozijske lastnosti dentalne žice NiTi
P. Močnik, T. Kosec 467

Effect of a nano-ceramic mold coating on the fluidity length of thin-wall castings in Al4-1 alloy gravity sand casting

Vpliv nanokeramičnega premaza peščene forme na tekočnost v tankostenskih ulitkih iz zlitine Al4-1 pri gravitacijskem ulivanju
M. Borouni, B. Niroumand, M. H. Fathi 473

Influence of the thermo-mechanical treatment on the exfoliation and pitting corrosion of an AA5083-type alloy

Vpliv termo-mehanske obdelave zlitine AA5083 na luščenje in jamičasto korozijo
A. Halap, M. Popović, T. Radetić, V. Vaščić, E. Romhanji 479

Structural and electrical studies of fullerene (C₆₀) dispersed polymer electrolytes

Študij strukturnih in električnih lastnosti polimernega elektrolita z dispergiranim fulerenom (C₆₀)
A. Saxena, P. Kumar Singh, B. Bhattacharya 485

Effect of tunneling defects on the joint strength efficiency obtained with FSW

Vpliv tunelskih napak na učinkovitost trdnosti spoja, izdelanega z drsno mešalnim varjenjem
S. Balos, L. Sidjanin 491

The influence of lamination and conductive printing inks on smart-card operability

Vpliv laminacije in prevodnih tiskarskih barv na delovanje pametnih kartic
M. Đokić, V. Radonić, V. Mladenović, A. Pleteršek, U. Kavčič, A. Hladnik, V. Crnojević-Bengin, T. Muck 497

Characterization of the substrates from two cultural-heritage sites and a preparation of model substrates

Karakterizacija gradbenih materialov iz dveh objektov kulturne dediščine in priprava modelnih materialov
S. Kramar, V. Ducman, S. Vucetic, E. Velkavrh, M. Radeka, J. Ranogajec 505

Long-term durability properties of pozzolanic cement mortars

Dolgoročna obstojnost pučolanske cementne malte
L. Završnik, J. Strupi Šuput, S. Kramar 509

Estimation of the effective boron-diffusion coefficient in the Fe₂B layers grown on gray cast iron

Določanje efektivnega koeficienta difuzije bora pri rasti plasti Fe₂B na sivem litem železu
B. Bouarour, M. Keddou, O. Allaoui 515

Optimization of the secondary cooling in a continuous casting process with different slab cross-sections

Optimizacija sekundarnega hlajenja pri kontinuirnem ulivanju slabov z različnimi prerezi
T. Mauder, J. Stetina 521

Unsteady model-based predictive control of continuous steel casting by means of a very fast dynamic solidification model on a GPU

Predvidevanje kontrole kontinuirnega litja na podlagi neravnotežnega modela z zelo hitrim dinamičnim modelom strjevanja na GPU
L. Klimes, J. Stetina 525

DSC/TG of Al-based alloyed powders for P/M applications

DSC/TG prahov na osnovi Al primernih za P/M uporabo
B. Šuštaršič, J. Medved, S. Glodež, M. Šori, A. Korošec 531

Microstructure characteristics of the model spring steel 51CrV4 Značilnosti mikrostrukture modelnega vzmetnega jekla 51CrV4 M. Torkar, F. Tehovnik, B. Arh, M. Jenko, B. Šarler, Ž. Rajčič	537
---	-----

Effect of creep strain on creep rate in the temperature range 550–640 °C Vpliv deformacije na hitrost lezenja pri temperaturah od 550 °C do 640 °C B. Žužek, F. Vodopivec, M. Jenko, B. Podgornik	545
--	-----

STROKOVNI ČLANKI – PROFESSIONAL ARTICLES

Identification of the initial failure and damage of substituents of a unidirectional fiber-reinforced composite using a micromodel Uporaba mikromodela za ugotavljanje začetnih napak in poškodb sestavin kompozita, enosmerno ojačanega z vlakni H. Srbová, T. Kroupa, R. Zemčík	549
--	-----

Transformation-induced plasticity in steel for hot stamping Vpliv pretvorbe na plastičnost jekla za vroče štancanje B. Mašek, C. Štädler, H. Jirková, P. Feuser, M. Selig	555
--	-----

Influence of temperature and binder content on the properties of a sintered product based on red mud Vpliv temperature in količine veziva na lastnosti proizvoda iz sintranega rdečega blata M. Krgović, I. Bošković, R. Zejak, M. Knežević	559
--	-----

Influence of the precipitation temperature on the thrust force and torque in drilling an Al 2219-SiC_p composite Vpliv temperature izločevalnega žarjenja na potisno silo in navor pri vrtnanju kompozita Al 2219-SiC R. Ganesh, K. Chandrasekaran	563
---	-----

Optimization of the recycling processes for magnesium from a highly contaminated waste Optimiranje postopka recikliranja magnezija iz močno kontaminiranih odpadkov V. Manojlović, Ž. Kamberović, M. Sokić, Z. Gulišija, V. Matković	571
---	-----

Machinability of a Ti-6Al-4V alloy with cryogenically treated cemented carbide tools Obdelovalnost zlitine Ti-6Al-4V s kriogensko obdelanimi orodji iz karbidne trdine A. Mavi, I. Korkut	577
--	-----

A cost-effective approach to the rapid fabrication of functional metal prototypes Stroškovno učinkovit način za hitro izdelavo funkcionalnih kovinskih prototipov C. C. Kuo	581
--	-----

Thermomechanical treatment of Ti-Nb-V-B micro-alloyed steel forgings Termomehanska obdelava odkovkov iz mikrolegiranega jekla Ti-Nb-V-B M. Opiela	587
--	-----

Progressive failure analysis of composite sandwich beam in case of quasistatic loading Napredna analiza poškodb sestavljenega kompozitnega nosilca pri kvazistatičnem obremenjevanju T. Mandys, T. Kroupa, V. Laš	593
--	-----

Influence of heat treatment on the microstructure and mechanical properties of aluminium bronze Vpliv toplotne obdelave na mikrostrukturo in mehanske lastnosti aluminijevega brona P. Sláma, J. Dlouhý, M. Kövér	599
--	-----

DOGODKI – EVENTS

Šolski Center Škofja Loka se je predstavil tudi predsedniku RS Borutu Pahorju	605
---	-----

APPLICATION OF A NEURAL NETWORK FOR ESTIMATING THE CRACK FORMATION AND PROPAGATION IN SOL-GEL CeO₂ COATINGS DURING PROCESSING AT TEMPERATURE

UPORABA NEVRONSKE MREŽE ZA UGOTAVLJANJE NASTANKA IN ŠIRJENJA RAZPOKE V SOL-GEL PREMAZU CeO₂ MED POSTOPKOM OGREVANJA

Aydogan Savran¹, Musa Alcı¹, Serdar Yıldırım^{2,3}, Recep Yiğit^{3,4,5}, Erdal Çelik^{2,3,5}

¹Ege University, Dept. of Electrical and Electronics Engineering, 35100 Bornova, Izmir, Turkey

²Dokuz Eylul University, Dept. of Metallurgical and Materials Engineering, 35160 Buca, Izmir, Turkey

³Dokuz Eylul University, Center for Production and Applications of Electronic Materials (EMUM), 35160 Buca, Izmir, Turkey

⁴Dokuz Eylul University, Izmir Vocational School, Department of Technical Programs, 35150 Buca, Izmir, Turkey

⁵Dokuz Eylul University, Dept. of Nanoscience and Nanoengineering, 35160 Buca, Izmir, Turkey
recep.yigit@deu.edu.tr

Prejem rokopisa – received: 2012-09-21; sprejem za objavo – accepted for publication: 2013-10-28

In this study the application of a neural network to estimate the crack propagation and crack size in CeO₂ coatings on a Ni substrate during processing at temperature was evaluated as a function of the Ce content in solutions with increasing processing temperatures from 24 °C and 700 °C. In this respect, CeO₂ coatings were prepared on Ni tapes from solutions derived from Ce-based precursors using a sol-gel method for YBCO-coated conductors. The crack size of the coating was determined using an in-situ Hot-Stage ESEM depending on the temperature at a certain time in vacuum conditions. It was determined that the crack size of the coating increased with the increasing processing temperature. Measuring the crack sizes of the coatings using Hot-Stage ESEM is an expensive and time-consuming process. In order to eliminate these kinds of problems a neural-network approach was used to estimate the crack sizes of the coatings at different temperatures. The neural network was constructed directly from the experimental results. It was concluded that the estimation of the crack propagation of CeO₂ coatings on a Ni tape substrate are reasonable for the processing temperatures.

Keywords: CeO₂, sol-gel, neural network, crack

V tej študiji je bila ocenjena uporaba nevronske mreže za določanje širjenja razpoke in velikosti razpoke v premazu iz CeO₂ na podlagi iz Ni med ogrevanjem kot funkcija vsebnosti Ce v raztopini med ogrevanjem od 24 °C do 700 °C. Za ta namen je bil pripravljen premaz iz CeO₂ na traku iz Ni iz predhodne raztopine Ce z uporabo sol-gel metode za premaz na prevodniku YBCO. Velikost razpoke v premazu je bila določena v vročem z in-situ ESEM v odvisnosti od temperature po določenem času v vakuumu. Ugotovljeno je bilo, da velikost razpoke v premazu narašča z naraščanjem temperature procesa. Merjenje velikosti razpoke v vročem z uporabo ESEM je drag in časovno zamuden postopek. Za odpravo teh težav je bila za določanje velikosti razpoke v premazu pri različnih temperaturah uporabljena nevronska mreža. Ta je bila postavljena na podlagi eksperimentalnih rezultatov. Ugotovljeno je bilo, da je mogoče določanje širjenja razpoke v premazu CeO₂ na traku iz Ni pri različnih temperaturah procesa.

Ključne besede: CeO₂, sol-gel, nevronska mreža, razpoka

1 INTRODUCTION

Neural networks (NNs) possess massive parallelism, a powerful mapping capacity, and a learning property.¹ They are capable of making decisions based on incomplete, noisy and disordered information. In addition, they can provide reasonable outputs for inputs not encountered during training. Because of these properties they have gained the attention of scientist from many different areas. There are a huge number of papers in the area of control, identification and estimation.²⁻⁵ Most of the industrial productive processes exhibit a certain degree of nonlinearity. By means of their nonlinear mapping and learning properties, neural networks have been employed in the identification of unknown nonlinear systems.

The development of the new, high-temperature superconductors has resulted in many applications in the fields

of magnetic, electronic and microwave technologies. Ceramic superconductors have been deposited as thin films using various methods, e.g., electron-beam co-evaporation, chemical vapor deposition, ion-beam sputtering, pulsed-laser deposition and the sol-gel technique on many buffered substrates.⁶ CeO₂ is one of the buffer layers frequently used for surface-coated YBCO superconductors on textured nickel substrates.⁷ The sol-gel process offers a new possibility for the synthesis of oxide layers by applying liquid precursors to substrates by dipping, spinning or spraying methods.⁸ The major factors affecting the CeO₂ sol-gel coatings are the nature of the coating and the substrate, and the reaction parameters at the temperature of YBCO formation.⁹ The nature of the coatings are influenced by sol-gel parameters such as types of precursor, solvent and chelating agents, viscosity, Ce content, dilution, chelation, complexation, withdrawal rate, coating thickness and annealing conditions.

In particular, the cracks of buffer layers are the main problem in sol-gel processing.¹⁰

In our initial attempts¹¹ we determined the crack-propagation rate and the crack size of CeO₂ buffer layers on Ni tapes for YBCO-coated conductors using an in-situ, hot-stage, environmental scanning electron microscope (ESEM). In the present investigation, in order to determine the crack size of the CeO₂ sol-gel coatings by avoiding time-consuming and expensive experimental works, we propose to use a multilayer feed-forward NN to estimate the crack size at the processing temperatures.

2 NEURAL NETWORKS

Neural Networks (NNs) are massively parallel, distributed, adaptive, nonlinear information processing tools. They consist of simple nonlinear processing elements (PEs), referred to as neurons. Each neuron receives connections from other PEs and/or itself. The block diagram of a neuron is shown in **Figure 1**.

The neuron collects the values from all of its input connections, performs a predefined mathematical operation, and produces a single output value computed as:

$$y_j = f\left(\sum_{i=1}^n w_{ji}u_i + b_j\right) \quad (1)$$

where u_i is the input value, w_{ji} is the connection weight between the i^{th} input and the j^{th} neuron, and f is the activation function. The sum of the weighted inputs and the bias forms the input to an activation function f . The neurons may use any differentiable activation function f to generate their output. The sigmoid function is the one of the most common activation functions, as follows:

$$f(x) = \frac{1}{1 + e^{-x}} \quad (2)$$

The interconnectivity defines the topology of the NN. An important class of NNs is the multilayer feed-forward neural network, as shown in **Figure 2**. They consist of simple nonlinear processing elements (PEs) and weighted connections in a layered structure. The input signal propagates through the network in a forward direction from one layer to the next. The neurons are connected with weighted connections represented by the arrows in **Figure 2**.

The training of the NN is performed by adjusting the connection weights. It is performed by iteratively adjusting the weights (w) of the connections and biases (b) in the network in order to minimize a predefined cost function. A popular cost function is the sum of the squared error between the actual output and the desired output value for each unit in the output layer:

$$E = \frac{1}{2} \sum_k (t_k - y_k)^2 \quad (3)$$

where t_k is the desired or target response on the k^{th} unit and y_k is the produced network output on the same unit.

In order to perform training, a training set, including the input and desired response vectors, is prepared. The training is performed in two phases referred to as the forward and backward phases. In the forward phase, the input patterns from the training set are applied to the input layer. These inputs are multiplied by the associated weights, passed through the activation functions and transferred to the next layer. They propagate through the network, layer by layer. Finally, the actual response of the network is produced at the output layer. The errors between the desired and the network outputs are found. In the backward phase, the error signal propagates backwards through the network and the gradients are computed. These are then used to determine the weight changes in the net according to used learning rule. A more common learning algorithm is the back-propagation algorithm, which is introduced in¹².

The standard back-propagation implements the steepest-descent method (also called the gradient-descent method). At each step of the steepest-descent method the weights are adjusted in the direction in which the error function decreases most rapidly. This direction is determined by the gradient of the error surface at the current point in the weight space. The weights are updated in a negative direction to the gradient with a certain rate, as given by:

$$\begin{aligned} w_{ji}^{\text{new}} &= w_{ji}^{\text{old}} - \eta \frac{\partial E}{\partial w_{ji}} \\ w_{lj}^{\text{new}} &= w_{lj}^{\text{old}} - \eta \frac{\partial E}{\partial w_{lj}} \\ w_{kl}^{\text{new}} &= w_{kl}^{\text{old}} - \eta \frac{\partial E}{\partial w_{kl}} \end{aligned} \quad (4)$$

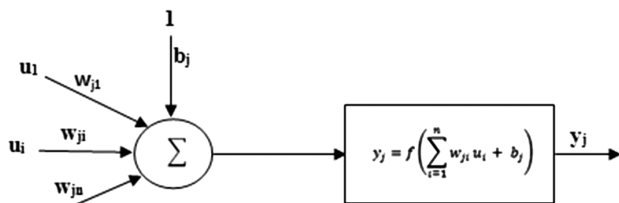


Figure 1: Artificial neuron model

Slika 1: Model umetne nevronske mreže

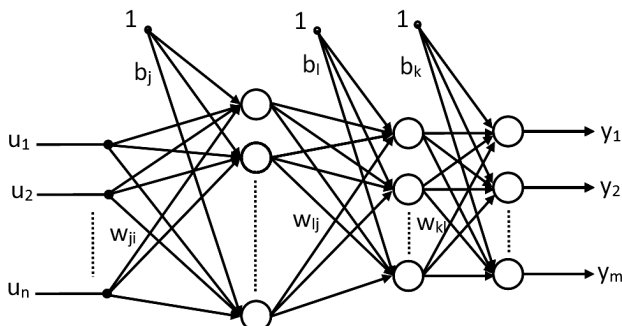


Figure 2: Multilayer feed-forward neural network

Slika 2: Večplastno napajanje nevronske mreže

in which η is the learning rate that determines the step size through the gradient direction. Similarly, the biases are updated as follows:

$$\begin{aligned} b_j^{\text{new}} &= b_j^{\text{old}} - \eta \frac{\partial E}{\partial b_j} \\ b_l^{\text{new}} &= b_l^{\text{old}} - \eta \frac{\partial E}{\partial b_l} \\ b_k^{\text{new}} &= b_k^{\text{old}} - \eta \frac{\partial E}{\partial b_k} \end{aligned} \quad (5)$$

More details regarding the NN training can be found elsewhere.¹³

3 EXPERIMENTAL AND NUMERICAL PROCEDURES

Ce-based solutions were prepared from cerium nitrate precursors ($\text{Ce}(\text{NO}_3)_3 \cdot 6\text{H}_2\text{O}$). The powder precursors were first dissolved in glacial acetic acid, which is used as a chelating agent. Eleven different amounts of Ce precursor, including (0.0499, 0.1990, 0.3490, 0.7500, 1.4900, 2.9900, 4.2500, 4.9900, 5.9900, 7.0080, 43.4000) g, which are called as concentration indexes, were used to estimate the effects on the crack formation and propagation of the coatings in the solutions as a processing parameter. The obtained solutions were subsequently diluted with isopropanol. All the solutions were stirred at room temperature for 60–120 min in order to yield transparent solutions. The thickness of the CeO_2 thin films measured by ESEM varied between 0.4 μm and 7 μm , depending on the Ce concentration in the solution. More details regarding the preparations of Ni tape and CeO_2 thin films were given in^{11,14,15}.

In order to investigate the surface morphology, the crack formation and the propagation of CeO_2 films, in-situ hot stage ESEM was used. For this procedure, Ni tape substrates were separately dipped into the eleven different Ce-based solutions at room temperature in air. Ce-based gel coatings were obtained from this process. These gel coatings were then placed in the hot-stage ESEM. The gel coatings were examined in the temperature range 24 °C to 700 °C for 5 min in vacuum conditions. After placing the Ce-based gel coatings contain-

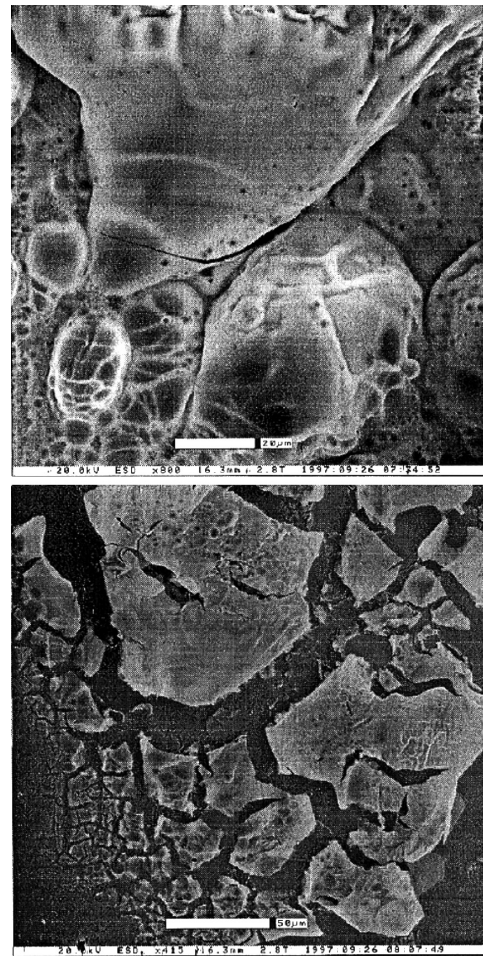


Figure 4: ESEM microstructures of Ce-based gel and CeO_2 coatings on Ni tape at: a) 25 °C and b) 600 °C¹¹

Slika 4: ESEM-posnetka koloida na osnovi premaza Ce in CeO_2 na traku iz Ni pri: a) 25 °C in b) 600 °C¹¹

ing a bubble structure in the ESEM, they were dried and heat treated from room temperature to 700 °C. The crack length and the size of the coatings were measured in the ESEM at several temperatures, i.e., (25, 100, 200, 300, 500, 600 and 700) °C, for a period of 5 min under vacuum conditions. However, here we utilized the temperatures 400 °C and 700 °C. A computer program of an in-situ hot-stage ESEM was used to measure the crack

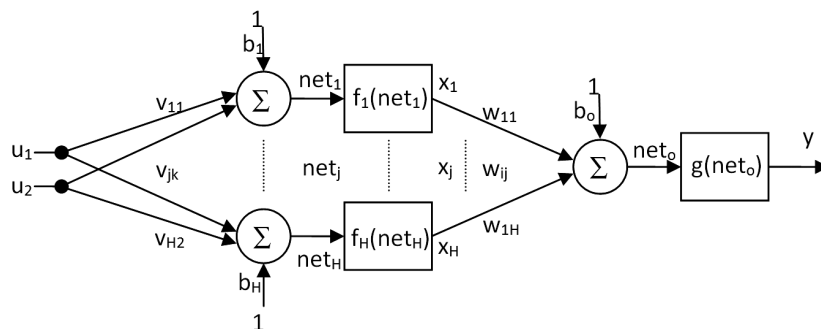


Figure 3: The used NN structure

Slika 3: Uporabljena NN-struktura

size of the coating as a function of concentration index (Ce content in the solutions) and processing temperature. In as much as the coating is a gel-like structure at 25–100 °C, and amorphous at 100–350 °C, the CeO₂ coating was formed on Ni tape at 420 °C and densified at 700 °C. For these reasons, the crack size of the CeO₂ coatings was also measured at 400 °C and 700 °C in detail. When measuring the crack sizes of the gel and oxide coatings, ESEM micrographs were taken with the scale bar 20 µm.

The NN used in this study is shown in **Figure 3**. Where v and w represent the weights, and b represents the biases. The NN has two inputs (u_1, u_2) and 1 output (y). There are six neurons in the hidden layer. $f(\cdot)$ and $g(\cdot)$ are the hidden-layer and the output-layer activation functions, respectively. The sigmoid-type activation functions are used by both layers. All the programs for the NN were developed under Matlab. The inputs of the NN represent the amount of material and the processing temperature at which the experiment was performed. The output of the NN represents the crack sizes of the coatings. The training data set contains 66 elements, includ-

Table 1: NN estimated and experimental crack sizes for 400 °C

Tabela 1: Določen NN in eksperimentalna velikost razpok pri 400 °C

Concentration index	NN inputs		NN output	
	Amount of precursor material (g)	Temperature (°C)	NN estimated crack size (µm)	Experimental crack size (µm)
1	0.0499	400	1.6309	2.4133
2	0.1990	400	1.6980	2.4345
3	0.3490	400	1.9820	2.5000
4	0.7500	400	10.2419	9.7605
5	1.4900	400	14.5338	15.0000
6	2.9900	400	14.8854	15.6250
7	4.2500	400	15.2480	17.6410
8	4.9900	400	15.6821	15.7140
9	5.9900	400	18.7295	25.0500
10	7.0080	400	9.6382	16.8900
11	43.4000	400	33.5412	30.5000

Table 2: NN estimated and experimental crack sizes for 700 °C

Tabela 2: Določen NN in eksperimentalna velikost razpok pri 700 °C

Concentration index	NN inputs		NN output	
	Amount of precursor material (g)	Temperature (°C)	NN estimated crack size (µm)	Experimental crack size (µm)
1	0.0499	700	2.2660	2.6886
2	0.1990	700	2.8976	2.6547
3	0.3490	700	5.4302	3.0000
4	0.7500	700	17.2949	13.8090
5	1.4900	700	18.5257	15.6000
6	2.9900	700	22.9032	17.5000
7	4.2500	700	55.6694	26.4710
8	4.9900	700	71.0257	44.4700
9	5.9900	700	75.8715	71.4200
10	7.0080	700	110.6222	73.9000
11	43.4000	700	142.2619	140.0000

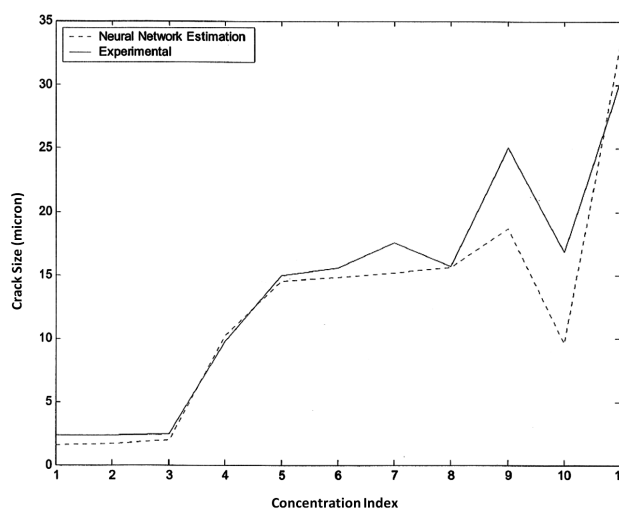


Figure 5: The NN estimation and experimental results for CeO₂ coatings on Ni tape at 400 °C. In this figure, the x and y axes indicate the crack size of the coating and the concentration index, respectively.

Slika 5: Določanje NN in rezultati preizkusov za premaz CeO₂ na traku iz Ni pri 400 °C. Na sliki x - in y -os pomenita velikost razpoke in indeks pogostosti.

ing the data for temperatures (25, 100, 200, 300, 500 and 600) °C. We left the data for temperatures 400 °C and 700 °C as the testing data sets. Both test sets contain 11 elements. A batch-training procedure was applied to train the NN using the Steepest Descent (SD) method and then the crack size of the CeO₂ buffer layer was estimated for 400 °C and 700 °C. The details of test data sets and the NN estimation results are shown in **Tables 1** and **2**.

4 RESULTS AND DISCUSSION

In-situ, hot-stage ESEM, depending on the temperature, the crack formation and propagation of the coatings were evaluated as a function of the Ce content in the solutions. **Figure 4** shows ESEM microstructures of the Ce-based gel and CeO₂ coatings on Ni tape at 25 °C and 600 °C, respectively.¹¹ The ESEM observations revealed that the crack surface of the Ce-based films changed slightly with increasing temperatures, from 25 °C to 500 °C, when compared with the other thin films. After CeO₂ formation at about 420 °C, microcracks were observed on the surface. It is interesting to note here that the bubbles and micro-bubbles were produced on the surface once the precursor material increased in this solution. The bubbles showed characteristic properties that caused the cracks to start on the surfaces of the gel films of the nitrate-salt-based precursors. Note that there are many factors influencing the bubbling problem, such as types of precursors, solvent and chelating agent, viscosity, dilution, Ce content in solution and so on. It was found that the size and propagation rate of the cracks increased with the increasing Ce content. It is clear from the ESEM observations that the measured values of the

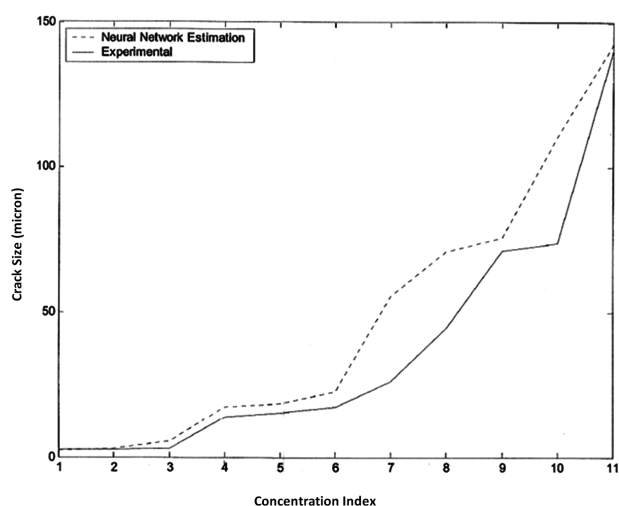


Figure 6: The NN estimation and experimental results for CeO₂ coatings on Ni tape at 700 °C. In this figure, the *x* and *y* axes indicate the crack size of the coating and the concentration index, respectively.

Slika 6: Določanje NN in rezultati preizkusov za premaz CeO₂ na traku iz Ni pri 700 °C. Na sliki *x*- in *y*-os pomenita velikost razpoke in indeks pogostosti.

crack-propagation rate altered slightly at (300, 400 and 500) °C, whereas at 600 °C they changed considerably.

Figure 5 shows the NN estimation and the experimental results for CeO₂ on Ni tape at 400 °C. In this figure, the *x* and *y* axes indicate the crack size of the coating and the concentration index, respectively. The concentration index corresponds to eleven type solutions, including several Ce(NO₃)₃ · 6H₂O contents. As mentioned just previously, the Ce(NO₃)₃ · 6H₂O precursors were dissolved using a solvent and a chelating agent. The eleven solutions were prepared by changing the amount of precursors and thus eleven type coatings were obtained using the hot-stage ESEM. As a result of this, the crack sizes were measured at 400 °C in the ESEM and the concentration index was taken as numerical values, such as from 1 to 11. Actually, the concentration indexes are not real values indicating the amount of precursor. It is clear from **Figure 5** that the estimated crack size of the coating is close to the experimental results for 400 °C. Similarly, the NN estimation and the experimental results of the crack size for 700 °C are presented in **Figure 6**. It is worth noting that the predicted result approaches the mean values when the standard deviation associated with the measurements is small. Now that the goal is to fabricate low-cost, high-quality products in a short time in a modern industry, the optimization of the processing temperature can be estimated using the NN technique. The key feature of this research is that the NN approach is useful for the prediction of the cracks size and the crack-propagation rate during the heat treatment of the sol-gel coatings. This study can be extended by using other buffer layers, depending on the sol-gel parameters. This technique is quite likely to be a key area for the development of all sol-gel films in the future, prior to the coating processes.

5 CONCLUSIONS

In summary, the NN-based approach was developed to estimate the crack sizes of a CeO₂ coating on a Ni tape for YBCO-coated conductors, depending on processing temperatures such as 400 °C and 700 °C using a hot-stage ESEM. A multilayer feed-forward NN was trained to estimate the crack size of the coating during processing at temperature in the range 24–700 °C. The experimental measurements of the crack size on the coating on the Ni tape substrate are a very expensive and a time-consuming process. The approach proposed in the present study provides simplicity and is cost-effective for preparing the new solutions and subsequent processing in the sol-gel technique.

Acknowledgements

The authors would like to thank Dr. Y. S. Hascicek and R. E. Goddard for their assistance in obtaining the ESEM micrographs at the National High Magnetic Field Laboratory of Florida State University in Tallahassee, Florida USA.

6 REFERENCES

- K. Hornik, M. Stinchcombe, H. White, *Neural Networks*, 2 (1989), 359–366
- K. J. Hunt, D. Sbarbaro, R. Zbikowski, P. J. Gawthrop, *Automatica*, 28 (1992), 1083–1112
- M. Agarwal, *IEEE Control Systems Magazine*, 17 (1997), 75–93
- K. S. Narendra, K. Parthasarathy, *IEEE Transactions on Neural Networks*, 1 (1990), 4–27
- A. G. Parlos, S. K. Menon, A. F. Atiya, *IEEE Transactions on Neural Networks*, 12 (2001), 1411–1432
- I. H. Mutlu, E. Celik, M. K. Ramazanoglu, Y. Akin, Y. S. Hascicek, *IEEE Transactions on Applied Superconductivity*, 10 (2000), 1154–1157
- E. Celik, I. H. Mutlu, Y. S. Hascicek, *IEEE Transactions on Applied Superconductivity*, 10 (2000), 1162–1166
- E. Celik, H. Okuyucu, I. H. Mutlu, M. Tomsic, J. Schwartz, Y. S. Hascicek, *IEEE Transactions on Applied Superconductivity*, 11 (2001), 3162–3165
- H. Okuyucu, E. Celik, M. K. Ramazanoglu, Y. Akin, I. H. Mutlu, W. Sigmund, J. E. Crow, Y. S. Hascicek, *IEEE Transactions on Applied Superconductivity*, 11 (2001), 2889–2892
- X. D. Wu, S. R. Foltyn, P. Arendt, J. Townsend, I. H. Campbell, P. Tiwari, Q. X. Jia, J. O. Willis, M. P. Maley, J. Y. Coulter, D. E. Peterson, *IEEE Transactions on Applied Superconductivity*, 5 (1995), 2001–2006
- E. Celik, Y. S. Hascicek, *Materials Science & Engineering B*, 94 (2002), 176–180
- P. J. Werbos, *Beyond Regression, New Tools for Prediction and Analysis in the Behavioral Sciences*, PhD. Dissertation, Harvard University, Boston, USA, 1974
- M. S. Al-Haik, H. Garmestani, A. Savran, *International Journal of Plasticity*, 20 (2004), 1875–1907
- E. Celik, J. Schwartz, E. Avci, H. J. Schneider-Muntau, Y. S. Hascicek, *IEEE Transactions on Applied Superconductivity*, 9 (1999), 2264–2268
- E. Celik, H. I. Mutlu, E. Avci, Y. S. Hascicek, *Advances in Cryogenic Engineering (Materials)*, 46 (1999), 895–900

OPTIMIZATION OF THE MECHANICAL AND TRIBOLOGICAL PROPERTIES OF EXTRUDED AMCs: EXTENSION OF THE ALGORITHM SEARCHING AREA VIA MULTI-STRATEGIES

OPTIMIZACIJA MEHANSKIH IN TRIBOLOŠKIH LASTNOSTI EKSTRUDIRANIH AMC: RAZŠIRITEV ALGORITMA ISKALNEGA PODROČJA Z UPORABO VEČ STRATEGIJ

Mohsen Ostad Shabani, Ali Asghar Tofigh, Mohammad Reza Rahimpour, Mansour Razavi, Ali Mazahery, Fatemeh Heydari

Materials and Energy Research Center (MERC), Tehran, Iran
aliasghartofigh60@gmail.com

Prejem rokopisa – received: 2013-01-14; sprejem za objavo – accepted for publication: 2013-10-24

The present article focuses on the development of a comprehensive method for the optimization of the mechanical and tribological properties of metal-matrix composites using multi-strategy ensemble particle-swarm optimization. An aluminum-alloy matrix reinforced with coated B₄C particles was used for the present study. The cohesion of the reinforcing ceramic particles represents a very important factor, which is mostly poor at temperatures near the melting point of aluminum and leads to the inferior mechanical and tribological properties of the developed aluminum matrix composites with a non-uniform distribution of the reinforcement. The main reason for coating the particles is to improve the bonding between the reinforcement and the molten alloy and thus to eliminate any interfacial reactions. The great enhancement in the strength values of the composites in this study can be ascribed to the effective load-bearing capacity of the disintegrated B₄C particles, which are adherently bonded to the matrix alloy. Homogeneity and a reduction in the particle size of the B₄C during the extrusion process is evidenced in the microstructural studies.

Keywords: tribological properties, particle, extrusion process

Članek je osredinjen na razvoj celovite metode za optimizacijo mehanskih in triboloških lastnosti kompozitov s kovinsko osnovo z uporabo optimizacije več strategij združevanja gruč delcev. Za študij je bila uporabljena Al-zlitina, ojačana z obloženimi delci B₄C. Kohezija oplasčenih keramičnih delcev za utrjevanje je pomembna: navadno je slaba pri temperaturah blizu tališča aluminija in povzroča slabše mehanske in tribološke lastnosti razvitega kompozita na osnovi Al z neenakomerno razporeditvijo delcev za ojačanje. Glavni namen oplasčenja delcev je izboljšanje povezave med delcem za ojačanje in staljeno zlitino ter odprava reakcij na površini stika. Veliko povečanje trdnosti kompozita v tej študiji se lahko pripiše učinkoviti nosilnosti razpadlih delcev B₄C, ki so adherentno vezani na osnovno zlitino. Študije mikrostrukture so pokazale homogenost in zmanjšanje delcev B₄C med iztiskovanjem.

Ključne besede: tribološke lastnosti, delec, postopek iztiskovanja

1 INTRODUCTION

The particle-swarm algorithm tries to simulate the social behavior of a population of agents or particles, in an attempt to optimally explore a given problem space.¹ At a time instant (an iteration in the optimization context), each particle is associated with a stochastic velocity vector, which indicates where the particle is moving to²⁻⁵. The velocity vector for a given particle at a given time is a linear stochastic combination of the velocity in the previous time instant, of the direction to the particle's best position, and of the direction to the best swarm positions (for all particles).⁶ The particle-swarm algorithm is a stochastic algorithm in the sense that it relies on parameters drawn from random variables, and thus different runs for the same starting swarm may produce different outputs.⁷ Some of its advantages are that it is simple to implement and easy to parallelize.^{8,9} It depends, however, on a few of parameters that influence the rate of convergence in the vicinity of the global optimum.¹⁰ Overall,

it does not require many user-defined parameters, which is important for practitioners that are not familiar with optimization.¹¹⁻¹³ Some numerical evidence seems to show that a particle swarm can outperform genetic algorithms on difficult problem classes, i.e., for unconstrained global optimization problems. Moreover, it fits nicely into the pattern search framework.^{14,15}

During the past decade, novel computational methods have been introduced in some fields of engineering sciences, including the solidification and deformation of metal-matrix composites in materials science.¹⁶⁻¹⁸ Aluminum metal-matrix composites (AMCs) are gaining importance as the most sought-after candidate materials in the space and automotive industries owing to their excellent properties, such as superior wear resistance, low density and high specific stiffness.¹⁹⁻³² Several reports have been published addressing the problems associated with their developments, mechanical behavior, microstructure and the distribution of particulates.³³⁻⁴¹ Presently, particulate-reinforced composites are being

produced by several different methods: powder metallurgy, liquid metallurgy, diffusion bonding techniques, infiltration, squeeze casting, compocasting and spray deposition techniques.^{42–48} The most simplified approach to develop near-net -shaped aluminum-based composites is by the liquid metallurgy route as it is economical and can result in mass production.^{18–20} Generally, these composites consist of a metal matrix, which is melted during casting, and ceramic reinforcement, which is added to the molten matrix material by a mechanical stirrer. However, some challenges need to be addressed in the development of AMCs to intensify their uses in different engineering fields, including inferior bond and interfacial reaction product. These problems do have a direct deteriorating effect on the mechanical and tribological properties of the composites, making them unsuitable for industrial components.³ These challenges have been addressed to by the use of coated reinforcement and the addition of reactive metals like magnesium by several researchers. In addition, instead of conventional stir-casting techniques, semi-solid agitation processes can be employed. The benefits include reduced solidification shrinkage, a lower tendency for hot tearing, suppression of segregation, settling or agglomeration and faster process cycles. These advantages are accompanied by a lack of superheat (lower operating temperatures) as well as a lower latent heat, which results in a longer die life together with a reduced chemical attack of the reinforcement by alloy, also a globular, non-dendritic structure of the solid phase, which then explains the thixotropic behavior of the material.^{18–20} Furthermore, these compocast-coated composites can be subjected to secondary processing such as extrusion and forging to improve upon the mechanical properties in particular strength coupled with practical ductility.^{39–43} The purpose of this study is first to investigate the effects of extrusion and reinforcing coated particles on the microstructures and mechanical properties of AA6061 aluminum alloy matrix composites produced by compocasting. Another objective is to solve the global problems using Multi-strategy ensemble particle-swarm optimization, which helps to increase the possibility of industrial application.

2 EXPERIMENTAL PROCEDURE

In this study, composites were produced by the compocasting process using the mechanical mixing of the AA6061 aluminum matrix, i.e., B_4C particles. The AA6061 aluminum alloy was produced from the mass fraction $w = 99.9\%$ pure aluminum that had been melted and then a pure silicon master alloy in mass fractions of Al–75% Cr, Al–50% Cu, and pure magnesium were added in order. Boron carbide (B_4C) in powder form is used as the reinforcement, having a particle range size of 1–60 μm . We attempted to coat the B_4C powders with TiB_2 , which helps the incorporation of the particles and reduces interfacial reactions. Titanium tetraisopropoxide was selected as a sol-gel precursor and diluted with ethanol. The boron carbide powders were first dispersed

in the ethanol using a stirrer and then titanium tetraisopropoxide and distilled water were added to the stirred suspension. The processing was conducted at room temperature at a solution pH of 7. The solution was then aged for 105 min at room temperature, with constant, gentle stirring. When titanium tetraisopropoxide is used as the precursor, TiO_2 can be produced by hydrolysis and heat treatment. Since titanium oxide does not support good wettability, it is converted to TiB_2 . **Figure 1** presents the X-ray diffraction (XRD) analysis of the coated powders.

The composites were developed using the stir-cast method. The process involved melting the alloy in a graphite crucible using an electrical resistance furnace. The stirrer was positioned just below the surface of the slurry. The furnace is controlled using a J-type thermocouple located inside the gas chamber. The temperature of the alloy was raised to about 680 °C and stirred at (400, 500, 600, 700) r/min using an impeller fabricated from graphite and driven by a variable ac motor. The stirring times were noted at (5, 10 and 15) min after the addition of B_4C during the process. Both TiB_2 coated and uncoated boron carbide was varied in proportions of volume fractions (2.5, 5, 7.5, 10, 12.5, 15) %. The temperature of the furnace was gradually lowered until the melt reached a temperature in the liquid-solid state (corresponding to a 0.2 solid fraction) while the stirring was continued. The coated particles were added uniformly at a rate of 50 g/min over a time period of approximately 3 min. The casting was obtained by pouring the composite slurry into a steel die placed below the furnace. A continuous purge of nitrogen gas is used inside and outside the crucible to minimize the oxidation of the molten aluminum. The cast matrix alloy and the developed Al6061– B_4C composites (both uncoated and TiB_2 coated) were machined to 70 mm diameter and 200 mm length. The machined billets were then subjected to hot extrusion using a 200 t hydraulic extrusion press. The extrusion billets were heated in a muffle furnace for 2 h. An extrusion ratio of 1 : 10 with a constant ram velocity (extrusion speed) of 2 mm/s was implemented. The extruded Al6061 alloy and Al6061– B_4C composites (both

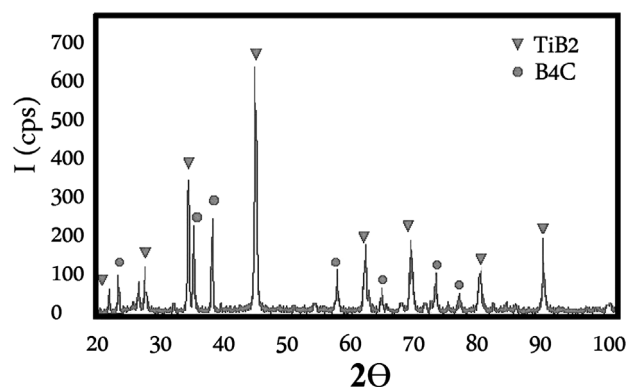


Figure 1: X-ray diffraction (XRD) analysis of the coated powders
Slika 1: Rentgenska difrakcijska analiza oplaščenega prahu

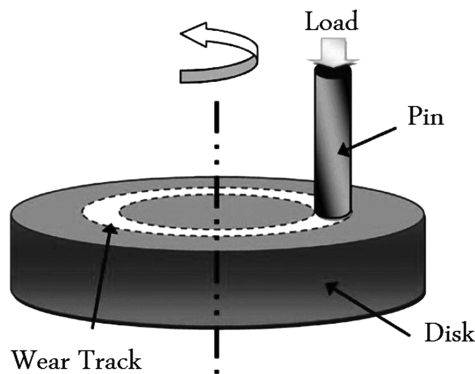


Figure 2: Schematic diagram of the abrasion wear test
Slika 2: Shematski prikaz preizkusa abrazijske obrabe

uncoated and TiB_2 coated) were subjected to metallographic studies, microhardness, tensile and wear tests.

Dry sliding wear tests were performed using pin-on-disk apparatus, under a load of 10 N and 20 N against a counterface steel disk of hardness 60 HRC. Cylindrical specimens of 6 mm diameter and 25 mm height were used as the test samples. Before the abrasion tests, each specimen was polished to $0.5 \mu\text{m}$. **Figure 2** shows a schematic diagram of the abrasion wear test. The experiment was carried out at room temperature with water as the lubricant. The wear loss was measured in the steady-state regime using a linear variable differential transducer of accuracy $1 \mu\text{m}$ at the end of 30 min. The wear rates were calculated from height-loss data. A set of three samples was tested in every experimental condition, and the average along with the standard deviation for each set of three tests was measured. The wear tests were conducted up to the total sliding distance of 2000 m. The tensile test samples were machined according to the ASTM E8M standard. Hardness measurements were carried out using a Shimadzu Microhardness tester with a load of 1 N for a period of 10 s. For each sample, five hardness tests on randomly selected regions were performed in order to eliminate the possible segregation effects and obtain a representative value of the matrix material hardness. During the hardness measurements, precaution was taken to make an indentation at a distance of at least twice the diagonal length of the previous indentation.

3 MODELING

3.1 Particle swarm optimization

The particle swarm optimization (PSO) was originally designed by Kennedy and Eberhart (Kennedy and Eberhart, 1995) and has been compared to genetic algorithms for efficiently seeking optimal or near-optimal solutions in large search spaces.³ It is a new search technique, which simulates preying behavior among birds.² In contrast to genetic algorithms, PSO does not need genetic operations such as crossover and mutation. Instead, it changes the individuals by their random velocities in the solution space.^{49–54} Compared to evolutionary

algebra, the solution group presents greater randomness and more benefits, such as faster searching speed, easy implementation and global optimization.³ In the original PSO with M particles, each particle is represented as a potential solution to a problem in a D -dimensional space and its position at the t -th iteration is denoted as:¹

$$X_i = (x_{i1}^t, x_{i2}^t, x_{iD}^t) \quad (1)$$

Each particle remembers its own previous best position and its velocity along each dimension as:^{49–52}

$$V_i = (v_{i1}^t, v_{i2}^t, v_{iD}^t) \quad (2)$$

The velocity and position of particle i at the $(t + 1)$ th iteration are updated by the following equations:³

$$V_{i,j}^{t+1} = wV_{i,j}^t + c_1 r_{1i,j}^t (p_{ij}^t - x_{ij}^t) + c_2 r_{2i,j}^t (Q_j^t - X_{i,j}^t) \quad (3)$$

$$X_{i,j}^{t+1} = V_{i,j}^{t+1} + X_{i,j}^t \quad (4)$$

where c_1 and c_2 are two positive constants, known as the acceleration coefficients; r_1 and r_2 are two uniformly distributed random numbers on the range (0.1) for the j -th dimension of particle i . Vector $p_i = (p_{i1}^t, p_{i2}^t \dots p_{iD}^t)$ is the position with the best fitness found so far for the i th particle, which is called the personal best (p_{best}) position. And vector $Q_i = (Q_1^t, p_2^t \dots p_D^t)$ records the best position discovered by the swarm so far, known as the global best (g_{best}) position. $x_{i,j}^t$, $v_{i,j}^t$ and $p_{i,j}^t$ are the j th dimension of the vector of x_i^t , v_i^t and p_i^t , respectively. The parameter w is the inertia weight used for the balance between the global and local search abilities. Usually, w decreases linearly with the iteration generations as:^{1–4}

$$w = w_{\text{max}} - \frac{t(w_{\text{max}} - w_{\text{min}})}{T} \quad (5)$$

where w_{max} and w_{min} are the maximum and minimum weights and usually set to 0.9 and 0.4, respectively. T is a predefined maximum number of iterations, and t represents the number of the current iteration.

3.2 Multi-strategy ensemble particle swarm optimization (MEPSO)

In MEPSO, all the particles are initially divided into two parts; we denote them as part I and part II, respectively. The two parts are considered to play different roles in the search of dynamic environments by using different strategies, which will be introduced as follows. The role of part I is considered to search the global optimum in the current environment as quickly as possible. Thus, similar operations as the standard PSO are adopted to guarantee good convergence. Furthermore, a Gaussian local search is introduced to enhance the local search ability of part I, which is designed as follows:

At every iteration, for each particle, it has the probability P_{ls} to perform the Gaussian local search defined as Eqs. (4) and (6), and has the probability $(1 - P_{\text{ls}})$ to perform the conventional search defined as Eqs. (3) and (4). The global best used in part I is the best solution

found by all particles, both in part I and part II. The Gaussian local search is defined as follows:

$$V_{i,j}^{t+1} = c_3 * \text{gaussrand} \tag{6}$$

where $i = 1, 2, \dots, m$, gaussrand is a random number generated from a standard normal distribution, c_3 is a positive constant. Although both strategies are designed for local search, the Gaussian local search adopted in part I of MEPSO is different from the quantum cloud defined in MQSO; the distribution in quantum cloud is uniform while Gaussian is not. The Gaussian local search strategy defined as Eq. (6) has been testified by many researches to be a good strategy to enhance the ability of elaborate search. By performing a local search with the probability P_{ls} , a particle can search for the optimum around its current position when it is on the process of "flying" to the best position found by the entire swarm.

Therefore, each particle has the chance to search for its neighborhood, and it might be favorable to find the optimum in dynamic multimodal environments. The role of part II is considered to extend the searching area of the algorithm, and to patrol around the part I to track the changed global optimum possibly "escaped" from the coverage of part I. To achieve this purpose, in part II, each particle has a probability 0.5 to fly to get closer to the personal best of a particle randomly chosen from part I, and has probability 0.5 to fly to get farther away from it. The operator is defined as Eq. (7), we call it differential mutation in this paper. It is implemented by changing the direction of a particle's velocity with a certain probability. The position of the particle is still renewed by Eq. (4):

$$V_{i,j}^{t+1} = wV_{i,j}^t \text{sgn}(r_1 - 0.5) + c_1 r_{2i,j}^t (p_{ij}^t - x_{ij}^t) + c_2 r_{3i,j}^t (G_j^t - X_{ij}^t) \tag{7}$$

$$\text{sgn} = \begin{cases} -1 & t < 0 \\ 0 & t = 0 \\ 1 & t > 0 \end{cases} \tag{8}$$

where G_j is the best solution found by particle a, which is chosen randomly from part I at each iteration; r_1, r_2, r_3 are uniformly distributed random numbers in the interval (0, 1); other parameters are the same as the ones described in Section PSO. The strategy of differential mutation may enhance the communication between part I and part II, extend the particle's search area, and prevent the algorithm from being premature.

In part II, particles fly in a way totally different to the standard PSO. There is no global attractor in part II, the position of each particle in part II is determined by the particle in part I via differential mutation strategy (each particle has a probability of 0.5 to fly to get closer to the personal best of a particle randomly chosen from part I, and has probability of 0.5 to fly to get farther away from it). The purpose of this strategy is to keep the particles in part II flying around part I to extend the coverage of the

particle population to avoid being trapped into a local optimum. The roles of the two parts in MEPSO are considered originally to be different. Part I is designed to enhance the algorithm's ability of exploitation, while part II is designed to enhance the algorithm's ability of exploration. The two parts work separately, but particles in these two parts are also interrelated. On the one hand, the personal best of particles randomly chosen in part I are used to compose the new velocities of the particles in part II, and then influence their relative position with respect to particles in part I. On the other hand, the best solution found by part II can be the global attractor of part I (if it is also the best of the entire swarm), which will guide the part I fly to the new best (maybe the changed optimum). The overall algorithm is summarized as follows.

Step1: Randomize the positions and velocities of all the particles in the search space. Set all the attractors to a randomized particle position. Divide all the particles into two parts. Set part I's attractor to be the best position of the entire swarm.

Step2: Evaluate the randomly chosen

Step3: IF the new value is different from the last iteration, re-evaluate the function values at each particle attractor in part I.

Step4: Re-randomize each particle in part II.

Step5: Update part I's attractor.

Step6: FOR each particle i in part I IF random number $< P_{ls}$ THEN, the random number within (0, 1), Apply Eq. (6) to renew the velocity, perform a local search

ELSE, Apply Eq. (3) to renew the velocity.

Step7: FOR each particle j in part II, Randomly choose a particle a from part I. Apply Eq. (7) to renew the velocity.//including operator of differential mutation

Step8: FOR each particle j both in part I and part II Apply Eq. (4) to renew the position.

Step9: Evaluate function at updated position. IF new value better than particle attractor value THEN, Particle attractor j : position and value of particle

Step10: IF new value better than part I's attractor value THEN, Part I's attractor: = position and value of particle

Step11: UNTIL number of function evaluations performed $> \text{max}$

There are mainly two parameters that should be set before the execution of the algorithm: the proportion of part I to the whole population P_{one} , the probability P_{ls} of performing a Gaussian local search. The first parameter may be used to control the contribution of part I and part II to the whole performance of the algorithm, and therefore, has an influence on the trade-off between the algorithm's performance on convergence and diversity maintenance. The second parameter may be used to control the proportion of particles in part I that perform the Gaussian local search other than the conventional strategy of PSO, and thus has an influence on the trade-off

between the algorithm's performance on local search and global search.

4 EXPERIMENTAL RESULTS

The execution of extrusion in this study results in compressive stresses and the fracturing of the hard ceramic particles within the deforming composites. **Figure 3** shows the light microphotographs of extruded volume fraction of Al6061–12.5 % B₄C composites. It should be noted that a combination of the semi-solid technique and extrusion in the fabrication of these composites leads to a reasonably uniform distribution of particles in the matrix and avoids clustering or agglomeration of the reinforcing phase. The presence of segregated B₄C particles can be easily recognized in the case of uncoated composites. Coated B₄C particles appear more homogeneous throughout the extruded matrix alloy. It is assumed that

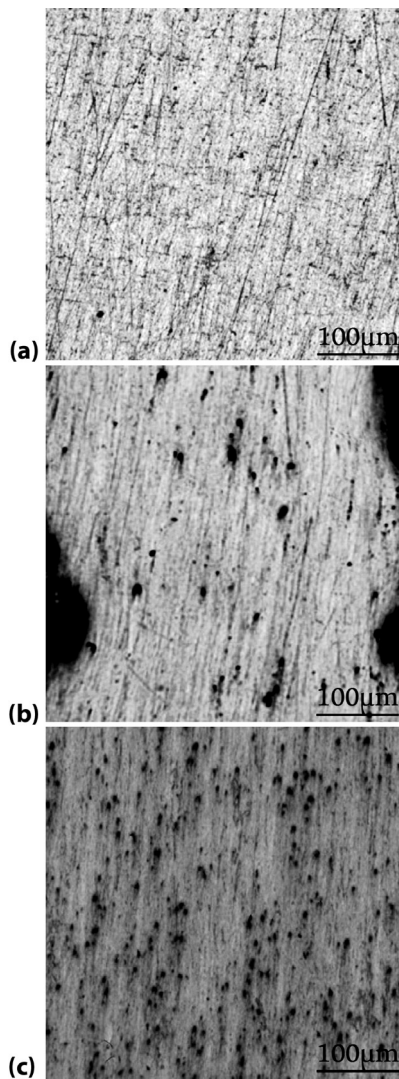


Figure 3: The light micrographs: a) unreinforced Al6061, b) Al6061–12.5 % uncoated B₄C, c) Al6061–12.5 % coated B₄C
Slika 3: Mikrostruktura: a) neojačan Al6061, b) Al6061–12,5 % neoplaščen B₄C, c) Al6061–12,5 % oplaščen B₄C

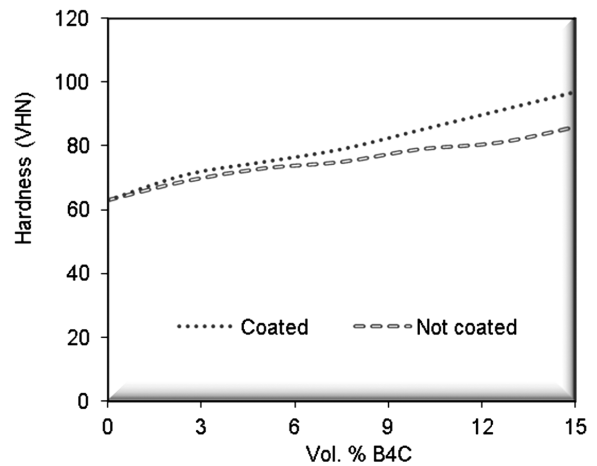


Figure 4: The influence of B₄C reinforcement on the hardness of the composites
Slika 4: Vpliv dodatka delcev B₄C na trdoto kompozita

TiB₂ coating improves the wetting kinetics in the liquid aluminum, which results in a uniform distribution of the coated B₄C particles.^{22–26}

The variation in the hardness of the extruded Al6061 alloy and its composites with the volume fraction of B₄C particles is presented in **Figure 4**. It is observed that the hardness of the composite samples increases with an increase in the B₄C content. However, coated composites exhibit a higher hardness compared to the uncoated ones. **Figures 5** and **6** show the results of the tensile strength in the extruded Al6061 alloy and its composites. In general, it is noted that both the yield strength and the ultimate tensile strength increase with the increasing the volume fraction of the incorporated B₄C particles for all the materials studied. The improvement in the tensile strength of the composites is the outcome of a higher dislocation density and plastic constraint in the matrix. The strain-hardening of the composites is expected to be influenced by the dislocation density, the dislocation-to-dislocation interaction and the constraint of the plastic

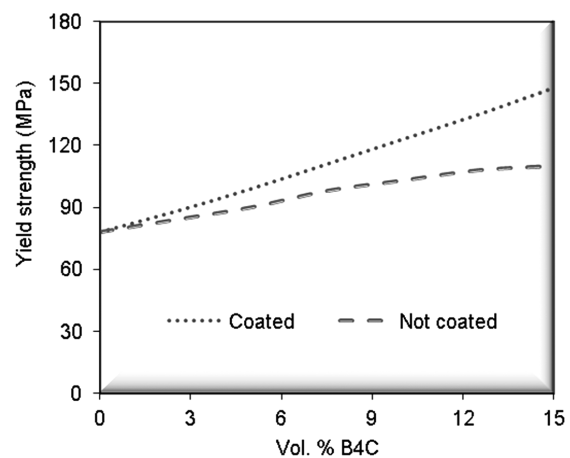


Figure 5: The influence of B₄C reinforcement on the yield strength of the composites
Slika 5: Vpliv dodatka delcev B₄C na mejo plastičnosti kompozita

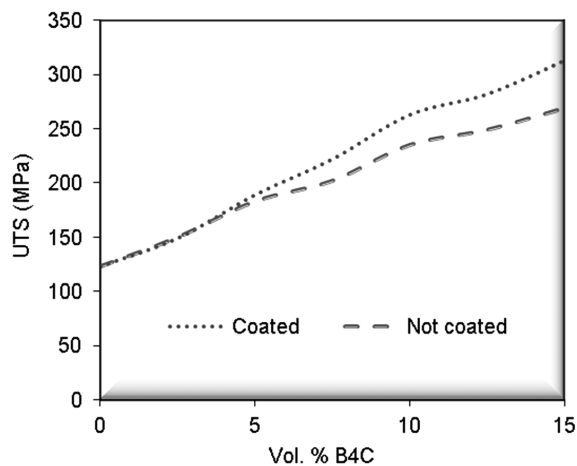


Figure 6: The influence of B₄C reinforcement on the UTS of the composites

Slika 6: Vpliv dodatka delcev B₄C na natežno trdnost kompozita

flow due to the resistance offered by the particles. The matrix could flow only with the movement of the B₄C particles or over the particles during plastic deformation.^{31–39}

Given the fact that the maximum solubility of B and C inside Al melt is not high, these two elements dissolve and saturate the melt rapidly in the case of uncoated composites, which leads to the nucleation of other products on impurity seeds or at the B₄C surface from the supersaturated melt. However, in the case of coated composites, most of the initial B₄C and Al remain unreacted, indicating the phases are conserved for desirable applications. The XRD pattern of the coated B₄C-reinforced composites is displayed in Figure 7. It can be seen that B₄C, TiB₂ and aluminum are present and no other reaction products are formed in the system. It is interesting to note that the rate of improvement in the yield strength and the ultimate tensile strength of the coated reinforced composites is higher when compared with the uncoated samples, which can be attributed to a number of reasons, including the absence of interfacial reactions in coated reinforced composites. In addition, a more uniform distribution of particles and a smaller

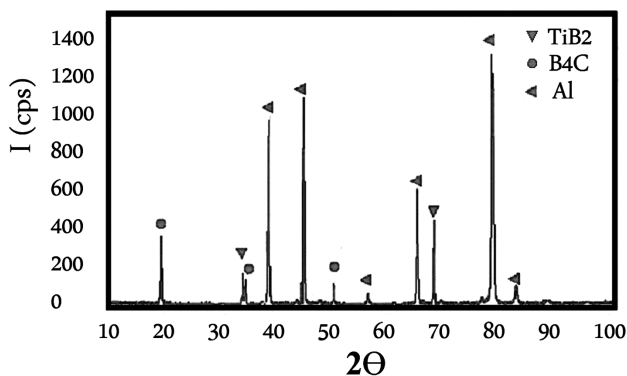


Figure 7: XRD pattern of the coated B₄C reinforced composites

Slika 7: Rentgenska difrakcija kompozita z oplaščenimi delci B₄C

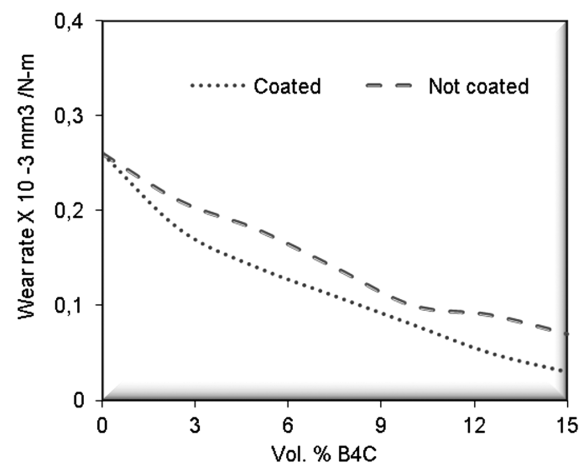


Figure 8: The influence of B₄C reinforcement on the wear rates of the composites

Slika 8: Vpliv delcev B₄C na hitrost obrabe kompozita

inter-particle distance in the case of coated composites cause the matrix to become considerably constrained and this results in a higher degree of improvement in flow stress and UTS.

Figure 8 shows the influence of B₄C reinforcement on the wear rates of the Al6061 alloy. It is clear that the wear rates of the Al6061 alloy decrease with the addition of the B₄C reinforcement. This improvement in the wear resistance of the composites can be attributed to the formation of mechanically mixed layers (MML) consisting of oxides of iron and aluminium during the sliding of composites on hard steel surfaces. It should be noted that coated composites exhibit a higher wear resistance than the Al6061 matrix alloy and the uncoated composites. The higher hardness, the uniform distribution of particles through the matrix alloy and the strong interfacial bond that exists between the matrix and the reinforcement increase the load-bearing capacity and minimize the matrix contact area in case of the coated B₄C reinforced composite. Figure 9 shows the worn surfaces of the unreinforced Al alloy and the composites. Extensive cracking and shearing are observed on the worn surfaces of the Al alloy. SEM micrographs indicate wider grooves and a greater extent of the damaged area on the worn surfaces of the uncoated samples, compared to the coated ones.

5 MODELING RESULTS

For MEPSO, the parameters used in Eqs. (4) and (7) are: $w = 0.25$, $c_1 = c_2 = 2.0$. Unless stated otherwise, the probability of a Gaussian local search P_{ls} is set to be 0.15, and the coefficient c_3 in Eq. (6) is set to be 0.3. The proportion of part I $P_{one} = 0.3$, and the proportion of part II $(1 - P_{one}) = 0.7$, i.e., the ratio of part I and part II was 3 : 7. When the dimensionality of the solution space increases, the problem becomes more and more difficult due to the increase in the number of local optima; therefore, the algorithms are more likely to be trapped into the local optimum. As can be seen, MEPSO has the

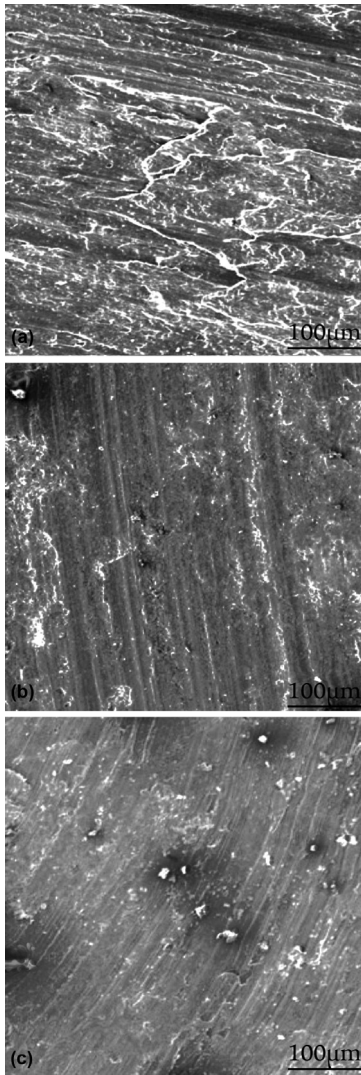


Figure 9: Worn surfaces of the unreinforced Al alloy and the composites: a) unreinforced Al6061 alloy, b) Al6061–10 % uncoated B₄C, c) Al6061–10 % coated B₄C

Slika 9: Obrabljena površina neojačane Al-zlitine in kompozitov: a) neojačana zlitina Al6061, b) Al6061–10 % neoplašččen B₄C, c) Al6061–10 % oplašččen B₄C

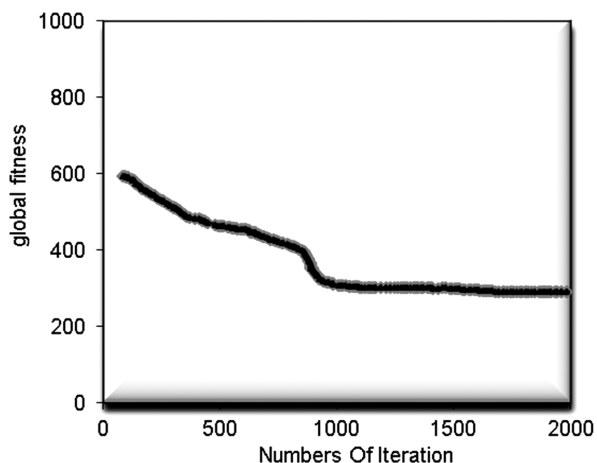


Figure 10: The effect of iteration number on the global fitness
Slika 10: Vpliv števila ponovitev na globalno zmogljivost modela

best performance in all the dimensionality conditions, and the offline error gap between the MEPSO and other algorithms becomes larger and larger as the dimensionality increases. In the following experiments, for MEPSO we use the method of re-evaluating five randomly chosen "sentry" particles to detect the change of the environments. When the changes have been detected, we re-evaluate each particle's best position and current position in part I, and then update each memory with the better position. The re-randomization mechanism is applied to all the particles in part II after the environment changes. The methods of detecting changes and handling outdated memories of the compared algorithms are the same as that adopted in¹⁻⁵. It is clear that MEPSO copes well with both unimodal and multimodal dynamic problems. A possible reason may stem from the ensemble of multiple strategies: from the experimental analysis, it can be observed that the mechanisms used in part I have a good effect on the convergence performance of the algorithm; while the mechanisms adopted in part II can extend the coverage of the particle population to avoid being trapped into the local optimum, and to enhance the ability of catching up with the changing optimum in dynamic multimodal environments. **Figure 10** shows the effect of iteration number on the global fitness of the developed model. The numbers of the iteration were selected to be 2000.

The value of P_{is} varies from 0.0 to 0.9. Good results are achieved for $0.1 = P_{is} = 0.2$ in various severity and multimodal environments. When $P_{is} > 0.4$, the performance gets rapidly worse as the value of P_{is} increases. It is obvious that when the value of P_{is} is set to be close to or equal to 0, the results are getting much worse than those attained for $0.1 = P_{is} = 0.2$. From the experimental results it is clear that, it is effective to perform a proper local search for the particles in part I. The value of P_{is} must not be too large or too small, i.e., $0.1 = P_{is} = 0.2$ is the best choice. What is more, the same conclusion can be drawn for various dynamic problem settings; in other words, the performance of MEPSO is rather robust to various dynamic problems with the parameter P_{is} setting range from 0.1 to 0.2. The final optimized parameters are 617.48 s stirring time, 644.26 r/min speed of stirrer, 31.43 μm particle size of B₄C, 11.53 % volume fractions of B₄C, 87.21 VHN hardness, 0.43 % porosity, 277.21 MPa UTS, 133.57 MPa yield strength, $0.06 \cdot 10^{-3} \text{ mm}^3/(\text{N m})$ wear rates and 5.73 % elongation. The results show that the novel technique implemented in this investigation has an acceptable performance. Therefore, this work shows the usefulness of an intelligent way to predict the performance of aluminum matrix composites using Multi-strategy ensemble particle-swarm optimization.

6 CONCLUSION

In MEPSO, the whole population of particles is divided into two parts: part I works as a standard PSO

enhanced with a Gaussian local search strategy, part II works as a patrol team around part I to extend the search area of the algorithm, and to catch up with the moving optimum. It is concluded that extrusion of the fabricated composites helps to reduce the B₄C particles size in both TiB₂ coated and uncoated B₄C reinforced composites. This can be attributed to fact that, the execution of the extrusion results in compressive stresses and therefore fracturing of the hard ceramic particles within the deforming composites. It should be noted that the particle distribution in the coated composites is much more uniform than the uncoated ones. The strong interfacial bond that exists between the matrix and the reinforcement in the case of coated B₄C reinforced composites contributes significantly to the improved wear resistance by increasing the load-transfer efficiency between the matrix and the reinforcement. Furthermore, a poor interfacial bond between the hard B₄C reinforcement and the soft matrix alloy will lead to the three-body abrasive wear phenomenon.

7 REFERENCES

- 1 J. J. Liang, A. K. Qin, P. N. Suganthan, S. Baskar, *IEEE Transactions on Evolutionary Computation*, 10 (2006), 281–295
- 2 M. O. Shabani, A. Mazahery, *Mater. Tehnol.*, 46 (2012) 6, 613–619
- 3 J. Kennedy, R. C. Eberhart, Particle swarm optimization, In: *Proceedings of the IEEE International Conference on Neural Networks*, vol. IV, Perth, Australia, 1995, 1942–1948
- 4 A. Mazahery, M. O. Shabani, *JOM*, 66 (2014) 5, 726–738
- 5 A. Mazahery, M. O. Shabani, *Powder Technology*, 225 (2012), 101–106
- 6 A. A. Tofigh, M. O. Shabani, *Ceramics International*, 39 (2013), 7483–7490
- 7 M. O. Shabani, A. Mazahery, *Appl. Math. Model.*, 36 (2012), 5455–5465
- 8 D. Beasley, D. R. Bull, R. R. Martin, *Evolutionary Comput.*, 1 (1993) 2, 101–125
- 9 R. Brits, *Niching Strategies for Particle Swarm Optimization*, Master's thesis, Department of Computer Science, University of Pretoria, Pretoria, South Africa, 2002
- 10 M. O. Shabani, A. Mazahery, *Metall. Mater. Trans. A*, 43 (2012), 2158–2165
- 11 A. Mazahery, M. O. Shabani, *Powder Technology*, 249 (2013), 530–535
- 12 A. Mazahery, M. O. Shabani, *JOM*, 64 (2012) 2, 323–329
- 13 J. Kennedy, R. C. Eberhart, *Swarm Intelligence*, Morgan Kaufman, 2001
- 14 J. Kennedy, R. Mendes, Population structure and particle swarm performance, In: *Proceedings of the IEEE World Congress on Evolutionary Computation*, Honolulu, Hawaii, 2002, 1671–1676
- 15 F. van den Bergh, A. P. Engelbrecht, *Information Science*, 176 (2006) 8, 937–971
- 16 C. Wang, Z. Zhong, E. Jiaqiang, *Powder Technology*, 219 (2012), 20–28
- 17 R. Bauri, M. K. Surappa, *Journal of Material Processing Technology*, 209 (2009), 2077–2084
- 18 M. O. Shabani, A. Mazahery, *Ceram. Int.*, 39 (2013), 5271–5279
- 19 J. Hashim, L. Looney, M. S. J. Hashmi, *J. Mater. Process. Technol.*, 123 (2002), 251–257
- 20 A. Mazahery, M. O. Shabani, *Powder Technology*, 217 (2012), 558–565
- 21 V. Kevorkijian, R. Hexemer, *Kovine zlitine tehnologije*, 32 (1998) 5, 397–402
- 22 M. O. Shabani, A. Mazahery, *Mater. Tehnol.*, 46 (2012) 2, 109–113
- 23 K. S. Vinoth, R. Subramanian, *Mater. Tehnol.*, 46 (2012) 5, 497–501
- 24 A. Mazahery, M. O. Shabani, *Composites: Part B*, 43 (2012), 1302–1308
- 25 S. K. Rhee, *J. Am. Ceram. Soc.*, 53 (1970), 386
- 26 M. O. Shabani, A. Mazahery, *Indian Journal of Engineering & Materials Sciences*, 19 (2012), 129–134
- 27 M. Razavi, M. R. Rahimipour, R. Kaboli, *Journal of Alloys and Compounds*, 460 (2008), 694–698
- 28 M. Demirel, M. Muratoglu, *Mater. Tehnol.*, 45 (2011) 5, 401–406
- 29 M. O. Shabani, A. Mazahery, *Trans Indian Inst Met.*, 65 (2012) 1, 77–83
- 30 M. Gupta, L. Lu, S. E. Ang, *J. Mater. Sci.*, 32 (1997), 1261–1267
- 31 V. Kevorkijian, B. Šuštaršič, M. Torkar, G. Chiarmetta, *Kovine zlitine tehnologije*, 32 (1998) 6, 539–543
- 32 A. Mazahery, M. O. Shabani, *Tribology Transactions*, 56 (2013), 342–348
- 33 C. J. Quaak, W. H. Kool, *Mater. Sci. Eng. A*, 188 (1994), 277–282
- 34 M. O. Shabani, A. Mazahery, *Archives of Metallurgy and Materials*, 56 (2011) 3, 671–675
- 35 A. J. Asthana, *Journal of Material Science and Engineering*, 35 (1998), 1959–1980
- 36 C. A. Leon, R. L. Drew, *J. of Mater. Sci.*, 35 (2000), 4763–4768
- 37 A. Mazahery, M. O. Shabani, *Journal of Materials Engineering and Performance*, 21 (2012) 2, 247–252
- 38 L. M. Tham, M. Gupta, L. Cheng, *Acta Materialia*, 49 (2001), 3243–3253
- 39 M. O. Shabani, A. Mazahery, *Composites: Part B*, 45 (2013), 185–191
- 40 A. A. Tofigh, M. R. Rahimipour, M. O. Shabani, M. Alizadeh, F. Heydari, A. Mazahery, M. Razavi, *Journal of Manufacturing Processes*, 15 (2013), 518–523
- 41 S. F. Moustafa, S. A. Badry, A. M. Sanad, B. Kieback, *Wear*, 253 (2002), 699–710
- 42 A. Mazahery, M. O. Shabani, *Russian Metallurgy (Metally)*, 7 (2011), 699–707
- 43 U. Cocen, K. Onel, *Composite Science Technology*, 62 (2002), 275–282
- 44 M. McKimpson, T. Scott, *Mater. Sci. Eng.*, 107 (1989), 93–106
- 45 A. Mazahery, M. O. Shabani, *Trans Indian Inst Met.*, 65 (2012) 2, 145–154
- 46 V. K. Varma, S. V. Kamath, V. V. Kutumabarao, *Material Science and Technology*, 17 (2000), 921–936
- 47 M. O. Shabani, A. Mazahery, *Powder Technology*, 249 (2013), 77–81
- 48 M. O. Shabani, A. Mazahery, *JOM*, 63 (2011) 8, 132–136
- 49 Y. G. Petalas, C. G. Antonopoulos, T. C. Bountis, M. Vrahatis, *Phys. Lett. A*, 373 (2009), 334–341
- 50 A. Mazahery, M. O. Shabani, *Metall and Mat Trans A*, 43 (2012), 5279–5285
- 51 C. H. Wu, N. Dong, W. H. Ip, C. Y. Chen, K. L. Yung, Z. Q. Chen, *Lecture Notes in Comput. Sci.*, 6024 (2010), 302–311
- 52 M. O. Shabani, M. Alizadeh, A. Mazahery, *Fatigue Fract Engng Mater Struct.*, 34 (2011), 1035–1040
- 53 S. Z. Zhao, P. N. Suganthan, *Engineering Optimization*, 43 (2011) 1, 1–17
- 54 K. Elsayed, C. Lacor, *Powder Technology*, 217 (2012), 84–99

TRIBO-CORROSION PROPERTIES OF A NiTi DENTAL WIRE

TRIBOKOROZIJSKE LASTNOSTI DENTALNE ŽICE NiTi

Petra Močnik, Tadeja Kosec

Slovenian National Building and Civil Engineering Institute, Dimičeva 12, 1000 Ljubljana, Slovenia
petra.mocnik@zag.si

Prejem rokopisa – received: 2013-06-13; sprejem za objavo – accepted for publication: 2013-10-04

NiTi-alloy archwires are used in dental medicine for tooth positioning. Failures are reported during the mounting and operation. It is supposed that these difficulties are results of a simultaneous presence of corrosion and mechanical wear. First, a corrosive medium was examined in order to simulate the conditions in the mouth. Different simulated body fluids were compared with natural saliva using electrochemical methods. The corrosion properties of the NiTi dental wire in the as-received state and without the surface oxide film were studied with electrochemical impedance spectroscopy. Tribo-corrosion tests of NiTi in artificial saliva were performed and a relation between the chemical and mechanical wear was studied. After the experiment, the surface was spectroscopically examined. The relation between the chemical and mechanical wear was determined.

Keywords: NiTi, simulated saliva, passive film, tribo-corrosion, electrochemical impedance spectroscopy

Žice zlitine NiTi se uporabljajo v dentalni medicini za oblikovanje zobnega loka. Med namestitvijo in uporabo se večkrat pojavijo pretrgi. Domneva se, da je vzrok sočasna korozija in mehanska obraba. Raziskava je bila najprej usmerjena v iskanje primerne korozivnega medija, ki nadomešča razmere v ustih. Z elektrokemijskimi metodami smo primerjali več različnih sintetičnih slin z vzorcem naravne sline. Korozijski preizkusi dentalne žice NiTi z oksidno plastjo (dostavljen vzorec) v primerjavi z žico brez oksidne plasti so bili izvršeni z elektrokemijsko impedančno spektroskopijo. Tribokorozijski preizkusi v umetni slini so pokazali odnos med kemijskim in mehanskim prispevkom obrabe. Po eksperimentu je bila površina spektroskopsko pregledana. Določena je bila odvisnost med kemijsko in mehansko obrabo.

Ključne besede: NiTi, umetna slina, pasivna plast, tribokorozijska, elektrokemijska impedančna spektroskopija

1 INTRODUCTION

A NiTi alloy is known as a shape-memory alloy. It is able to change its shape from a deformed to its original shape if it is heated or cooled in a certain temperature range. In general, the atomic composition of the alloy is 50 % Ni and 50 % Ti. A dental NiTi alloy wire is subjected to the mechanical and corrosive wear, known as tribo-corrosion processes. Tribo-corrosion is a complex process and its parameters include corrosion, deformation, friction and mechanical wear. The total wear of a material within a tribo-corrosion system is a combination of all these factors. Destructive effects of one factor on another one cannot be controlled and they are difficult to predict. The corrosion environment of dental wires includes several factors (saliva, food, drink), and, occasionally, also chemical abrasives (toothpaste, gels and mouthwashes). It is difficult to include all the factors and influences in the electrochemical experiments, so the research has been limited to the factor that is constantly present – the saliva.

In most cases the studies on a NiTi alloy are electrochemical researches.¹⁻⁵ There are some researches that investigate different surface finishes^{4,6-9} with the aim to improve the surface since nickel is known to be a potentially allergenic material. There are some studies that investigate the problems of pitting¹ and crevice corrosion^{2,3,6} on the NiTi alloy.

Since the NiTi alloy is primarily used for biomedical purposes, the electrochemical research of the material properties often uses a variety of simulated human fluids. For the studies of the biomaterial properties in the body, different simulated body fluids are used like: simulated body fluid (SBF),⁷ Hank's solution^{1,3,4,8} and solutions of NaCl with different concentrations.^{2,9} For the corrosion studies of dental materials, several different artificial salivas were used such as the artificial salivas according to Fusayama^{5,10,11} and Duffo et al.¹²

There are very few studies of the NiTi alloy with an emphasis on tribo-corrosion. Only tribological properties of NiTi alloys are reported.^{13,14} Zhang and Farhat¹³ found that the NiTi-alloy wear resistance is about 30 times greater than that of pure titanium, and about 10 times greater than that of pure nickel. Abedini and colleagues¹⁴ tested the tribological behaviour of a NiTi alloy in the austenitic and martensitic phase forms. They noted that plastic deformation dominates in the martensitic phase and fatigue wear dominates in the austenite phase.

The aim of the present study is to investigate the electrochemical properties of a NiTi alloy in an artificial saliva to learn about the corrosion properties of a dental wire and to define the effect of the wear on the corrosion properties of the dental wire.

2 EXPERIMENTAL WORK

The following types on the NiTi alloy were used in the study:

- a NiTi dental alloy (a 3M orthodontic wire, super-elastic, 0.48 mm × 0.64 mm, Orthoform III Ovoid, Upper) for EIS (electrochemical impedance spectroscopy) and tribo-corrosion;
- a NiTi sheet (alloy BB NiTi, 2 mm sheet, super-elastic, flat annealed, surface-oxide free (pickled), Memry GMBH) for the basic electrochemical study.

NiTi dental-wire samples were investigated for two different surface finishes, first in the as-received state (with the suppliers' finish) and later the surface was abraded with the 1200-grid SiC paper.

Before measuring, the samples were ultrasonically cleaned in ethanol, washed with distilled water and then well dried. For the selection of the most appropriate simulated saliva, natural saliva was compared to six different compositions of simulated saliva proposed by various authors. Duffo¹² (0.6 g/L NaCl, 0.72 g/L KCl, 0.22 g/L CaCl₂·2H₂O, 0.68 g/L KH₂PO₄, 0.856 g/L Na₂HPO₄·2H₂O, 0.06 g/L KSCN, 1.50 g/L KHCO₃, 0.03 g/L citric acid); Ericsson¹² (0.584 g/L NaCl, 0.34 g/L KH₂PO₄, 1.50 g/L KHCO₃, 0.029 g/L citric acid, 0.34 g/L Na₂HPO₄, 0.166 g/L CaCl₂, 0.014 g/L MgCl₂); Hank¹² (8.0 g/L NaCl, 0.4 g/L KCl, 0.6 g/L KH₂PO₄, 0.06 g/L Na₂HPO₄·12H₂O, 0.10 g/L MgCl₂·6H₂O, 0.35 g/L NaHCO₃, 0.06 g/L MgSO₄·7H₂O, 1.0 g/L glucose, 0.60 g/L Na₂HPO₄, 0.14 g/L CaCl₂); Fusayama¹¹ (0.4 g/L NaCl, 0.4 g/L KCl, 0.906 g/L CaCl₂·2H₂O, 0.69 g/L KH₂PO₄, 0.05 g/L Na₂S·9H₂O); simulated body fluid (SBF)¹⁵ (8.18 g/L NaCl, 0.22 g/L KCl, 0.13 g/L KH₂PO₄, 0.07 g/L Na₂SO₄, 0.35 g/L NaHCO₃, 0.36 g/L CaCl₂, 0.30 g/L MgCl₂); NaCl + lactic acid¹² (5.844 g/L NaCl, 9.008 g/L lactic acid).

The natural-saliva collection was conducted in two consecutive days. During collecting the saliva was stored in a refrigerator at 2 °C. The donor of the saliva did not eat any food or drink for 1 h before, and during the collection. The procedure took place more than 1 h after the last teeth cleaning. To stimulate the saliva secretion, the donor was asked to chew a parafilm and drink only water.

The electrochemical testing was executed in a three-electrode corrosion cell with a SCE reference electrode and a graphite counting electrode. After 2 h stabilization at the open-circuit potential (OCP) potentiodynamic measurements were performed starting at -0.25 V vs. the OCP and progressing up to +2.0 V at the scan rate of 1 mV/s. A Gamry Instruments potentiostat/galvanostat (ZRA Reference 600, USA, 2006) was used.

For EIS measurements an Autolab PGSTAT100 potentiostat/galvanostat, with a NOVA 1.6 module was used. The frequency scan ranged from 65 kHz to 1 mHz at 10 points per decade with an AC amplitude of ± 10 mV. The absolute impedance and phase angle were

measured at each frequency. The impedance measurements were carried out at the open-circuit potential (OCP) at different times of the immersion (2, 8, 24 and 72) h in the electrolyte. All the measurements were conducted in a Duffo simulated saliva. The impedance data were interpreted on the basis of the equivalent electrical circuits, using the Zview (Scribner) program for fitting the experimental data.

The tribo-corrosion tests were performed with a reciprocal tribometer (Tribotechnic, a pin-on-disc and reciprocating tribometer, 2009, France) in a Teflon cell with a platinum wire as the counter electrode and Ag/AgCl as the reference electrode. The counter body was a Al₂O₃ ball 6 mm. The length of the wear track was 10 mm, the sliding speed was 5 mm/s and the loads were 1 N and 2 N.

3 RESULTS AND DISCUSSION

3.1 Selection of an appropriate corrosion media

Figure 1 shows a potentiodynamic measurement of a NiTi alloy in different artificial saliva solutions and in natural saliva. The corrosion potential, E_{corr} , and the current density, j_{corr} , were defined by adjusting the tangents of the anodic and cathodic parts of the potentiodynamic curve in the Tafel region. The corrosion current density of the NiTi alloys in natural saliva was $46 \cdot 10^{-9}$ A cm⁻². The most similar result was obtained for the saliva proposed by Duffo,¹² where the current density was $70 \cdot 10^{-9}$ A cm⁻². Higher corrosion current densities were obtained for the other artificial salivas (**Table 1**). The current densities in the passive regions were similar in all the tested solutions, being approximately $3 \cdot 10^{-6}$ A cm⁻².

The breakdown potential value, E_b , was the same in Duffo's solution and in natural saliva, 1.1 V. The width of the passive area for the NiTi samples in natural saliva and in Duffo's solution were similar, 1.08 V for natural saliva and 1.06 V for Duffo's solution. All the other investigated solutions had their breakdown potentials at higher potential values and their widths of the passive areas differed from the values obtained in natural saliva. The highest values of the breakdown potential were measured in the solution of lactic acid with an addition of NaCl ($E_b = 1.40$ V) and in Fusayama's artificial saliva ($E_b = 1.28$ V).

After comparing the measurement results for the NiTi alloy in natural saliva with the results obtained in the artificial salivas, it is evident that the artificial saliva solution proposed by G. S. Duffo¹² shows the greatest similarity to natural saliva. The artificial saliva prepared with Duffo's procedure was used for further electrochemical measurements.

3.2 Electrochemical impedance spectroscopy

The electrochemical-impedance-spectroscopy results for the NiTi dental wire in a simulated saliva solution at

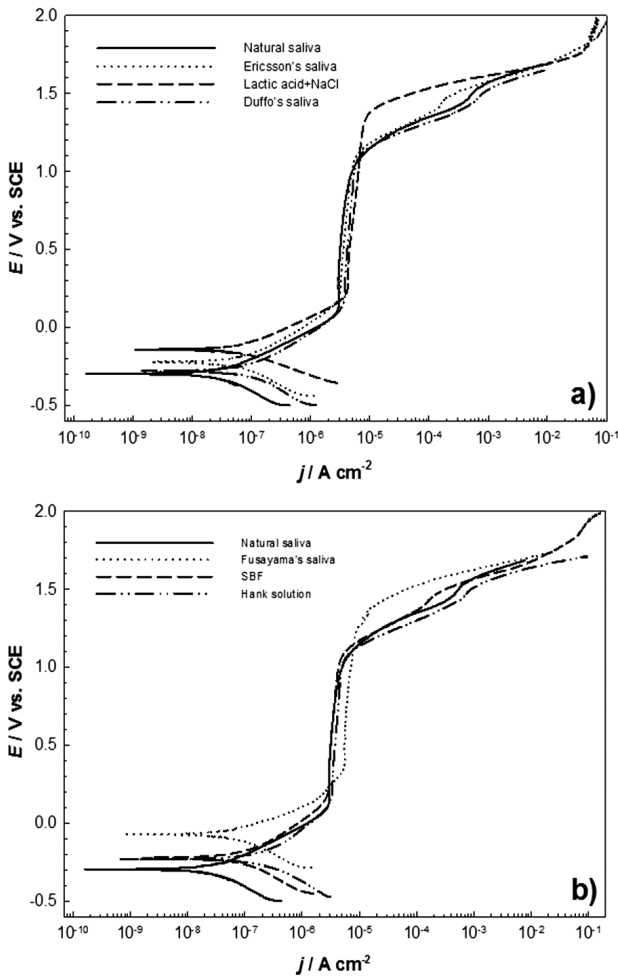


Figure 1: Potentiodynamic curves for the NiTi alloy in different simulated body solutions: a) Fusayama's saliva, SBF and Hank's solution compared to natural saliva, b) Ericsson's saliva, NaCl with the lactic acid and Duffo's saliva compared to natural saliva, at a scan rate 1 mV/s

Slika 1: Potenciodinamične krivulje za zlitino NiTi v različnih umetnih slinah: a) slina Fusayama, SBF in Hank primerjava z naravno slino, b) slina Ericsson, NaCl z mlečno kislino in Duffo-slina, primerjava z naravno slino, hitrost preleta 1 mV/s

Table 1: Electrochemical parameters for the NiTi alloy in different simulated saliva solutions compared with natural saliva

Tabela 1: Elektrokemijski parametri za zlitino NiTi v različnih raztopinah umetne sline v primerjavi z naravno slino

	E_{corr}/V	$j_{corr}/(A\ cm^{-2})$	E_b/V	$\Delta(E_b - E_{pp})/V$
Natural saliva	-0.30	$46 \cdot 10^{-9}$	1.10	1.08
Fusayama's saliva	-0.13	$78 \cdot 10^{-9}$	1.28	1.00
Ericsson's saliva	-0.21	$114 \cdot 10^{-9}$	1.10	0.90
SBF	-0.25	$81 \cdot 10^{-9}$	1.15	1.04
Hank's solution	-0.23	$147 \cdot 10^{-9}$	1.15	1.03
Lactic acid + NaCl	-0.16	$124 \cdot 10^{-9}$	1.40	1.20
Duffo's saliva	-0.32	$71 \cdot 10^{-9}$	1.10	1.06

different immersion times are presented as Nyquist plots and Bode diagrams in **Figures 2 and 3**.

The impedance spectra consist of a high-frequency intercept with the abscise axis and the main-frequency

semicircle. It can be seen at different immersion times on **Figures 2 and 3** that the impedance response increases with the time. There is a small difference in the profiles of the high- and medium- frequency regions, but a great difference in the responses at the lower frequencies.

The impedance spectra were fitted with the Randles equivalent circuit, as presented in **Figure 3**. The equivalent circuit consists of the resistance and capacitance elements due to the oxide film (RC) that are in the series with R_e , representing the electrolyte resistance.

R and Q represent the properties of the outer porous and passive film/solution interface reactions. The Q symbol signifies the possibility of a non-ideal capacitance (a constant-phase element, CPE) with n varying from 0.939 to 0.952 for the impedance data at different immersion times. The impedance of the CPE is given by:¹⁶

$$Q = Z_{CPE}(\omega) = [C(j\omega)^n]^{-1} \quad (1)$$

For $n = 1$, the Q element is reduced to a capacitor with the C capacitance and for $n = 0$, to a simple resistor.

The values of the fitted parameters of the equivalent circuit at four different immersion times and different potentials are presented in **Table 2**.

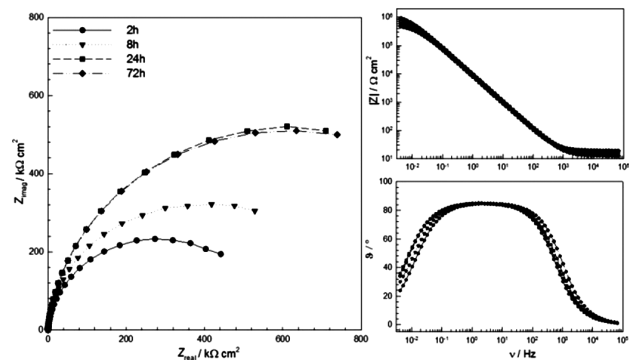


Figure 2: Nyquist and Bode plots for the NiTi dental wire in the as-received state at the OCP for different immersion times in the simulated saliva

Slika 2: Nyquistov in Bodejev diagram za dentalno žico NiTi v dostavljenem stanju pri OCP po različnih časih namakanja v umetni slini

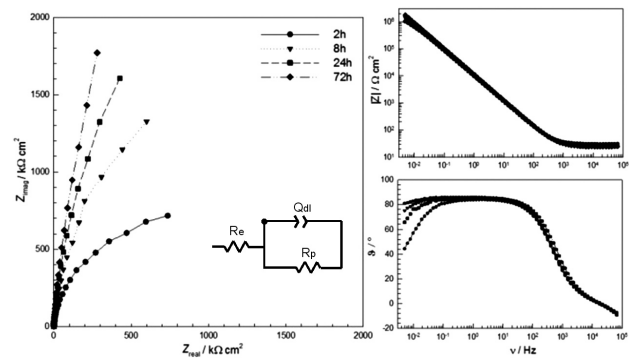


Figure 3: Nyquist and Bode plots for the NiTi dental wire without an oxide film at the OCP for different immersion times in the simulated saliva

Slika 3: Nyquistov in Bodejev diagram za dentalno žico NiTi brez oksidne plasti pri OCP po različnih časih namakanja v umetni slini

Table 2: Values of the fitted parameters of the equivalent circuit as a function of the applied potential at different immersion times

Tabela 2: Vrednosti prilagojenih parametrov nadomestnega vezja v odvisnosti od uporabljenega potenciala pri različnih časih namakanja

NiTi wire in the as-received state	<i>CPE</i>	<i>n</i>	<i>R_p</i> / (kΩ cm ²)	<i>C</i> / (F cm ⁻²)
2 h	2.25 · 10 ⁻⁵	0.939	517	2.64 · 10 ⁻⁵
8 h	2.10 · 10 ⁻⁵	0.941	704	2.49 · 10 ⁻⁵
24 h	1.91 · 10 ⁻⁵	0.941	1104	2.31 · 10 ⁻⁵
72 h	1.65 · 10 ⁻⁵	0.943	11250	1.99 · 10 ⁻⁵
NiTi without the oxide film	<i>CPE</i>	<i>n</i>	<i>R_p</i> / (kΩ cm ²)	<i>C</i> / (F cm ⁻²)
2 h	1.79 · 10 ⁻⁵	0.938	1470	2.22 · 10 ⁻⁵
8 h	1.64 · 10 ⁻⁵	0.947	4470	2.09 · 10 ⁻⁵
24 h	1.57 · 10 ⁻⁵	0.951	9330	2.03 · 10 ⁻⁵
72 h	1.50 · 10 ⁻⁵	0.952	20400	2.00 · 10 ⁻⁵

The *R_e* parameter has a value from 15 Ω cm² to 24 Ω cm² and it is ascribed to the electrolyte resistance. The *R* values are increasing with the immersion time, showing that the oxide film on the NiTi alloy has an increasing resistance. The *CPE*, denoted as *Q*, was recalculated using equation¹⁷ $C = [R^{1-n} Q]^{1/n}$ in order to compare the capacitance values for the NiTi dental alloy at different immersion times.

A decrease in the *C* value can be attributed to the thickening of the oxide layer. The thickening effect is larger in the case of the as-received oxide film than in the case of the oxide film naturally grown during the immersion in the simulated saliva. A similar effect was already observed in¹⁸⁻²⁰.

Based on equation:

$$d = (\epsilon) (\epsilon_0) (A) / C \tag{2}$$

where ϵ is the value for the dielectric constant, *d* is the thickness of the film, ϵ_0 is 8.85 · 10⁻¹⁴ F/cm and *A* is the surface area (cm²), the thickness of the oxide layer can be estimated. The decrease in capacitance points occurs with the increase in the thickness of the passive layer. This thickness growth is larger at the early immersion times at the OCP.

Assuming the value of 48 for the dielectric constant,²¹ the thickness determined with EIS can be calculated. The calculated thickness of the oxide film on the NiTi wire is approximately 1 nm and in the case when the oxide film was abraded during the 2 h immersion, the thickness is 2 nm.

The measured impedance spectra and the recalculated values show that the polarization resistance of the oxide films, immersed in a simulated saliva increases with the time of immersion. It is larger for the freshly polished oxide films on the NiTi wires than in the case of the as-received NiTi wires. Also, the impedance results show that the former oxide layer might be thinner and less protective than the oxide film formed during the immersion in a simulated saliva solution.

Even if the oxide layer on the NiTi wire is damaged, a quick repassivation is expected.

3.3 Tribo-corrosion

Due to a slightly more demanding form of the wire (the wire width of 0.64 mm) and the width of the wear track made with the 2 N force, which was up to 0.6 mm, the experiments with higher loads were not conducted. **Figure 4** shows a tribo-corrosion experiment on the dental NiTi wire worn by the 1 N and 2 N forces. The coefficients of friction (*COF*) were high, ≈ 0.7 , and the increase was intense in the first 50 s; after that the value of the *COF* was fairly constant. Near the end of the rubbing period, the *COF* value was registered and it was 0.75 for the load of 1 N and 0.65 for the load of 2 N. The *COF* fluctuations were smaller when the load of 2 N was applied. During the mechanical wear with 2 N load, the recorded potential was lower by 0.08 V than in the case of the test with the 1 N load. It was found that during the mechanical wear the potential and the coefficients of friction were stable and the fluctuation window was fairly narrow. These findings can also be attributed to the homogeneous surface. After the mechanical wear in the tribo-corrosion tests, the repassivation was fast, appro-

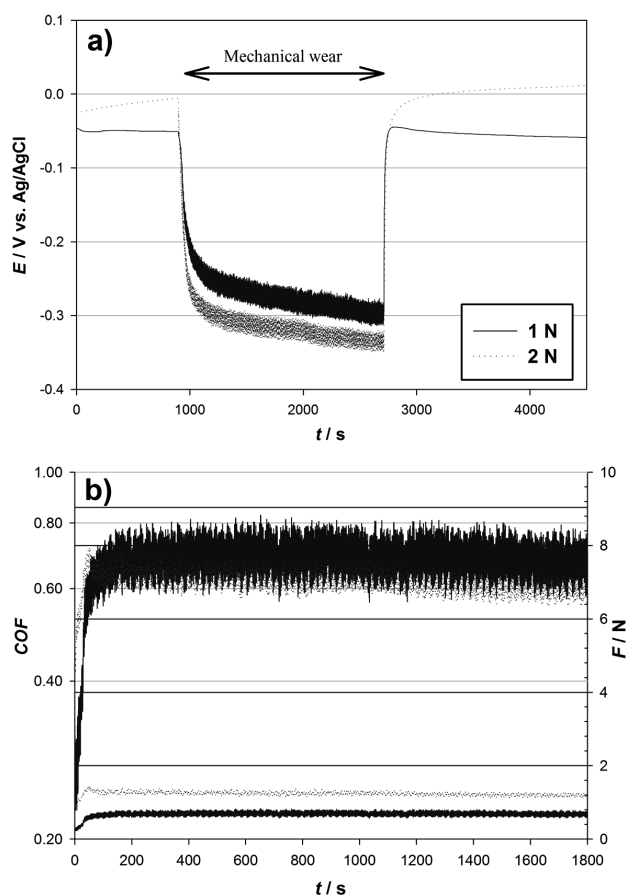


Figure 4: Monitoring of the: a) electrochemical potential, b) coefficient of friction and force vs. time during the tribo-corrosion test on the dental NiTi wire in a Duffo solution

Slika 4: Spremljanje: a) elektrokemijskega potenciala, b) koeficienta sile trenja v odvisnosti od trajanja tribokorozijskega preizkusa žice NiTi v Duffo-raztopini

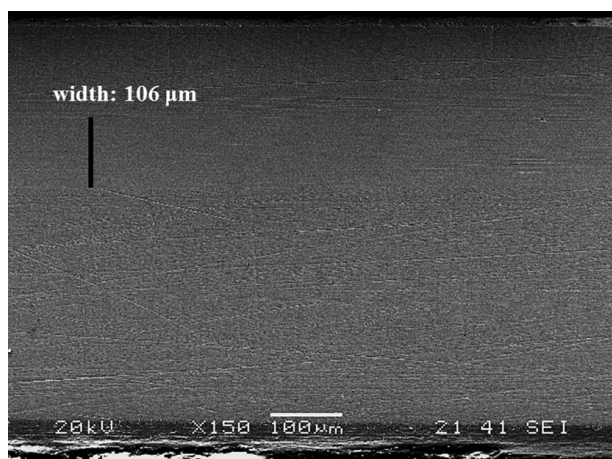


Figure 5: SEM image of the wear track of the NiTi dental wire after the tribo-corrosion test with the normal load of 1 N

Slika 5: SEM-posnetek sledi obrabe na dentalni žici NiTi po tribo-korozijskem preizkusu z obtežbo 1 N

ximately 30 s, showing fairly good repassivation properties of the NiTi dental alloy.

In **Figure 5**, a SEM image presents the wear track on the NiTi alloy after the tribo-corrosion test with the load of 1 N. The wear track is hardly visible, most likely due to the homogeneous surface and the large hardness of the NiTi alloy.¹³ The hardness of the NiTi dental alloy in the wear track was about 400 HV. The width of the wear track depending on the normal load was 106 μm for the 1 N load. In the case of the higher load of 2 N (not shown) the width of the wear track was about 135 μm.

We tried to define the prevailing wear mechanism by observing the characteristic changes in the surface topography and the microstructure of the thin zone below the rubbing surface. The wear particles were not found during the mechanical wear of the dental alloy. The wear track was smoothly worn, as already indicated by the small changes in the coefficient of friction. The SEM image did not give any additional information on the possible wear-mechanism properties. Since a considerable electrochemical change was detected by measuring the corrosion potential, one can assume that an oxidative wear as a tribo-corrosion phenomenon took place, combining the mechanical wear and oxidation.

4 CONCLUSIONS

A comparison between different solutions and natural saliva was made to study and determine realistic conditions. Furthermore, the corrosion and tribo-corrosion properties of a NiTi dental alloy in artificial saliva were studied.

Different solutions simulating the body fluids were tested with electrochemical techniques in order to find a solution that most closely represents the appropriate effects of natural saliva on the electrochemical properties of the NiTi alloy.

From the electrochemical impedance spectroscopy results it was clear that a NiTi-alloy archwire has a good corrosion resistance. By comparing two samples with different surfaces it could be concluded that the wire without the oxide film has better corrosion properties than the wire in the as-received state.

In the tribo-corrosion study it was found that the effect of the mechanical wear is fairly strong and the coefficients of friction are high. Heavy pressures on the surface accelerate the corrosion of the NiTi dental wire.

It can be concluded that the mechanical wear also has a great effect on the NiTi dental wire used in realistic conditions. It was evidenced that the NiTi alloy has good repassivation abilities.

5 REFERENCES

- A. Michiardi, C. Aparicio, J. A. Planell, F. J. Gil, Electrochemical behaviour of oxidized NiTi shape memory alloys for biomedical applications, *Surface & Coatings Technology*, 201 (2007), 6484–6488
- D. Vojtech, M. Voderová, J. Fojt, P. Novák, T. Kubásek, Surface structure and corrosion resistance of short-time heat-treated NiTi shape memory alloy, *Applied Surface Science*, 257 (2010), 1573–1582
- N. Figueira, T. M. Silva, M. J. Carmezim, J. C. S. Fernandes, Corrosion behaviour of NiTi alloy, *Electrochimica Acta*, 54 (2009), 921–926
- K. W. Ng, H. C. Man, T. M. Yue, Characterization and corrosion study of NiTi laser surface alloyed with Nb or Co, *Applied Surface Science*, 257 (2011), 3269–3274
- N. Schiff, B. Grosogeat, M. Lissac, F. Dalard, Influence of fluoride content and pH on the corrosion resistance of titanium and its alloys, *Biomaterials*, 23 (2002), 1995–2002
- L. Neelakantan, S. Swaminathan, M. Spiegel, G. Eggeler, A. W. Hassel, Selective surface oxidation and nitridation of NiTi shape memory alloys by reduction annealing, *Corrosion Science*, 51 (2009), 635–641
- X. M. Liu, S. L. Wu, P. K. Chu, C. Y. Chung, C. L. Chu, K. W. K. Yeung, W. W. Lu, K. M. C. Cheung, K. D. K. Luk, Effects of water plasma immersion ion implantation on surface electrochemical behavior of NiTi shape memory alloys in simulated body fluids, *Applied Surface Science*, 253 (2007), 3154–3159
- W. Cai, J. H. Sui, Effect of working pressure on the structure and the electrochemical corrosion behavior of diamond-like carbon (DLC) coatings on the NiTi alloys, *Surface & Coatings Technology*, 201 (2007), 5194–5197
- S. Rossi, F. Deflorian, A. Pegoretti, D. D’Orazio, S. Gialanella, Chemical and mechanical treatments to improve the surface properties of shape memory NiTi wires, *Surface & Coatings Technology*, 202 (2008), 2214–2222
- R. Zupančič, A. Legat, N. Funduk, Electrochemical and mechanical properties of cobalt-chromium dental alloy joints, *Mater. Tehnol.*, 41 (2007) 6, 295–300
- C. Rapijeko, S. Fouvry, B. Grosogeat, B. Wendler, A representative ex-situ fretting wear investigation of orthodontic arch-wire/bracket contacts, *Wear*, 266 (2009), 850–858
- G. S. Duffo, E. Quezada Castillo, Development of artificial saliva solution for studying the corrosion behavior of dental alloys, *Corrosion*, 60 (2004), 594–602
- C. Zhang, Z. N. Farhat, Sliding wear of superelastic TiNi alloy, *Wear*, 267 (2009), 394–400
- M. Abedini, H. M. Ghasemi, M. Nili Ahmadabadi, Tribological behavior of NiTi alloy in martensitic and austenitic states, *Materials and Design*, 30 (2009), 4493–4497

- ¹⁵ S. Kurz, A. W. E. Hodgson, S. Virtanen, V. Fervel, S. Mischler, Corrosion characterisation of passive films on CoCrMo with electrochemical techniques in saline and simulated biological solution, *European Cells and Materials*, 3 (2002), 26–27
- ¹⁶ I. D. Raistrick, J. R. MacDonald, D. R. Francschetti, J. R. MacDonald (ed.), *Impedance spectroscopy emphasizing solid materials and systems*, John Wiley&Sons, New York 1987
- ¹⁷ D. Kek-Merl, J. Lappalainen, H. L. Tuller, Electrical properties of nanocrystalline CeO₂ thin films deposited by in situ pulsed laser deposition, *Journal Electrochemical Society*, 153 (2006), J15–J20
- ¹⁸ I. C. Lavos-Valereto, S. Wolyneć, I. Ramires, A. C. Guastaldi, I. Costa, Electrochemical impedance spectroscopy characterization of passive film formed on implant Ti-6Al-7Nb alloy in Hank's solution, *Journal of Materials Science: Materials and Medicine*, 15 (2004), 55–59
- ¹⁹ M. Aziz-Kerrzo, K. G. Conroy, A. M. Fenelon, S. T. Farrell, C. B. Breslin, Electrochemical studies on the stability and corrosion resistance of titanium-based implant materials, *Biomaterials*, 22 (2001), 1531–1539
- ²⁰ J. E. G. Gonzalez, J. C. Mirza-Rosca, Study of the corrosion behavior of titanium and some of its alloys for biomedical and dental implant application, *Journal of Electroanalytical Chemistry*, 471 (1999), 109–115
- ²¹ M. Kwei Lee, C. F. Yen, J. J. Huang, Electrical characteristics of liquid-phase-deposited TiO₂ films on GaAs substrate with (NH₄)₂ S_x treatment, *Journal of the Electrochemical Society*, 153 (2006), F77–F80

EFFECT OF A NANO-CERAMIC MOLD COATING ON THE FLUIDITY LENGTH OF THIN-WALL CASTINGS IN Al4-1 ALLOY GRAVITY SAND CASTING

VPLIV NANOKERAMIČNEGA PREMAZA PEŠČENE FORME NA TEKOČNOST V TANKOSTENSKIH ULITKIH IZ ZLITINE Al4-1 PRI GRAVITACIJSKEM ULIVANJU

Mansour Borouni, Behzad Niroumand, Mohammad Hosein Fathi

Department of Materials Engineering, Isfahan University of Technology, 8415683111 Isfahan, Iran
m.mahmoudsalehi@ma.iut.ac.ir

Prejem rokopisa – received: 2013-06-27; sprejem za objavo – accepted for publication: 2013-10-29

The thin-wall casting of aluminum alloys provides new opportunities for aerospace industries in producing lightweight structures with good mechanical properties. The fluidity of molten metal is very important in producing sound castings, particularly thin-wall castings. In the gravity casting of thin-wall castings of the Al4-1 alloy, the melt that fills the mold with the effect of self-weight, does not have sufficient fluidity, so causing defects such as cold shut, misrun and shrinkage defects during the solidification. These defects reduce the quality and mechanical properties of the cast parts. The casting fluidity depends on many factors, such as temperature, melt composition, casting part shape and mold coating. This study reports the influence of a nano-ceramics mold coating, a micro-ceramic mold coating, a graphite mold coating and the section thickness of the part on the fluidity length of Al4-1 alloy castings. The results showed that by applying nano-ceramic mold coatings on the surface of a sand mold, the fluidity length and the surface quality of the castings can be improved.

Keywords: Al4-1 alloy, nano ceramic coating, micro ceramic coating, fluidity length, thin wall castings

Tankostenški ulitki iz aluminijevih zlitin so nova priložnost za letalsko industrijo pri proizvodnji lahkih ulitkov z dobrimi mehanskimi lastnostmi. Tekočnost staljene kovine je pomembna pri proizvodnji ulitkov brez napak, posebno še tankostenških. Pri gravitacijskem ulivanju tankostenških ulitkov iz zlitine Al4-1 talina zapolni formo zaradi lastne teže, če pa nima dovolj tekočnosti, to povzroči nastanek napak, kot so hladni zvari, slabo tečenje, napake zaradi krčenja pri strjevanju. Omenjene napake zmanjšujejo kvaliteto in mehanske lastnosti ulitkov. Livnost zlitine je odvisna od mnogih dejavnikov, kot so temperatura, sestava taline, oblika ulitka in prevleka forme. Predstavljen je vpliv nanokeramičnega premaza, mikrokeramičnega premaza, grafitnega keramičnega premaza in lokalne debeline na tekočnost v ulitkih iz zlitine Al4-1. Rezultati so pokazali, da je mogoče z uporabo nanokeramičnega premaza na peščeni formi izboljšati tekočnost in kvaliteto površine ulitka.

Ključne besede: zlitina Al4-1, nanokeramični premaz, mikrokeramični premaz, tekočnost, tankostenški ulitki

1 INTRODUCTION

Aluminum is one of the most important non-ferrous metals. Al-Si alloys are the most widely used aluminum alloys due to their castability, high strength-to-mass ratio, corrosion resistance, etc.¹ The industrial demand for thin-wall castings in aluminum alloys is of great importance in order to produce light components, which enable an increased payload and reduced energy consumption in aerospace applications. The Al4-1(Ak9pch) alloy is an aluminum-silicon alloy with 9–10.5 % silicon, 0.25–0.35 % manganese and 0.23–0.3 % magnesium. This alloy is used for reducing mass and good mechanical properties, and is employed for manufacturing many airplane and aerospace parts with complicated shapes and thin-wall castings.²⁻⁶

However, thin-wall castings of Al4-1 alloy can pose manufacturing problems associated with mold filling. The rapid cooling of thin-wall sections of the casting reduces the fluidity of the molten metal, which could cause the molten metal to prematurely freeze before it can completely fill the mold cavity, resulting in an incomplete fill or cold shuts. Hence, the fluidity of the

melt is an important concern in the foundry for thin-wall castings and the production of thin-wall castings is limited by the fluidity of the molten metal. The fluidity of aluminum alloys has a direct influence, not only on the material's castability, but also on the casting mechanical properties of the casting part. The fluidity of molten metals, in the foundry environment, is defined as the length the metal flows before it is stopped due to solidification. This is because the fluidity limits the geometry of a casting that can be successfully filled. The study of fluidity is particularly important for the aerospace and automotive industries in order to produce thinner and lighter products. Therefore, in recent years, many foundries and metal suppliers have invested time and money in studying the fluidity of their foundry alloys. Fluidity is a complex parameter that is affected by the properties of the molten metal and mold (such as the mold coating), the pouring conditions and the solidification mechanism.^{4,7-9} The mold coating significantly improves the fluidity. It also improves, indirectly, the mechanical properties of the cast products because the mold coating significantly increases the fluidity and,

hence, a lower casting temperature can be used.⁸ The surface roughness with the production of frictional forces reduces the flow of the melt, and consequently reduces the fluidity of the melt. In addition, various experiments show that the mold-coating materials will produce smooth surfaces and reduce the wetting characteristics of the mold at the metal-mold interface and reduce the friction and the melt-mold contact, therefore reducing the heat-transfer coefficient (HTC) at the metal-mold interface, and so the fluidity is substantially increased.^{8,10}

The most common application of nano-materials is nano-ceramic particles. Nano-ceramics are ceramic particles with dimensions in the nanometer range.¹¹ The nano-mold coating has a proper surface, anti-sticking and a low coefficient of friction. The roughness is related to the grain size of the mold coating. The apparent fluidity is represented by the flow distance in the test mold and was found to be increased significantly by the mold coating.^{6,12}

In this paper we investigate the effect of nano- and micro-ceramics and graphite mold coating on the fluidity length and the soundness of thin-wall castings of the aluminum alloy Al4-1 by gravity casting in a sand mold.

2 EXPERIMENTAL PROCEDURE

2.1 Materials

The standard as well as the actual chemical composition of the Al4-1 alloy are shown in **Table 1**. A 180 kg crucible resistance furnace was used to melt the alloy. At first, 170 kg of Al4-1 alloy was put into the furnace. Then, additions of 0.05 % of melt-mass beryllium to aluminium-5 % beryllium master alloy in the ingot form at the start of the melting treatment. Then the alloy was melted and heated to 740 °C and kept for 10 min, and a mobile rotary degassing system was used. The impeller, made of a graphite pipe, was immersed into the melt and argon was injected into the melt for 20 min through the

Table 1: Chemical composition of the Al4-1 alloy in mass fractions (w%)

Tabela 1: Kemijska sestava zlitine Al4-1 v masnih deležih (w%)

Elements	Standard	Actual
Si	9–10.5	10
Mn	0.25–0.35	0.3
Mg	0.23–0.3	0.3
Ti	0.08–0.15	0.1
Others	0.6	0.6
Al	Bal.	Bal.

Table 2: Composition of flux used in this research

Tabela 2: Sestava talil, uporabljenih pri tej raziskavi

Composition	Content (w%)
NaCl	45
KCl	45
LaF3	5
Other composition	5

pipe. Then a RE- containing flux was injected into the melt for 10 min through the pipe. The rotating speed of the impeller was maintained at 350 r/min. The main composition of the flux used in this experiment can be seen in **Table 2**. For melting qualification treatment, the addition of 0.05 % of melt mass strontium in rod form, to the aluminum-10 % strontium master alloy. The strontium master alloy was added to the melt approximately 3 min before the end of the fluxing, because it has the best effect and fewest losses.

The addition of 0.2 % of melt mass, titanium with Al-5Ti-1B master alloy in rod form, simultaneously with strontium master alloy 3 min before the end of the fluxing treatment. The titanium master alloy was added at the end stage of fluxing, because without the loss of grain refiner, refinement of the structure.^{5,13,14}

The sand molds were made from sodium-silicate bonded, CO₂-cured sand. After the preparation of the mold, a nano-ceramic (MM12), graphite or micron (ZR1) mold coating was applied to the sand mold surface using the spray gun and the mold surface was heated with a natural gas torch to harden the mold coating. The nano-ceramic mold coating MM12 was product by ItN Nanovation AG (Germany) in order to study the effects of mold coating and casting section thickness on the fluidity. The mold cavity was designed with four straight channels, 250 mm long, with rectangular cross-sections of (2, 4, 6, 8) mm thickness and 30 mm across. A mechanical drawing sample for fluidity test, a 3D model and one cast sample are shown in **Figure 1**.

The pouring basin that is shown in **Figure 2** was used for reducing the turbulence of the melt and to unify the velocity of the melt pouring. This basin was made using AFS (American foundry men society) supervision.¹⁵

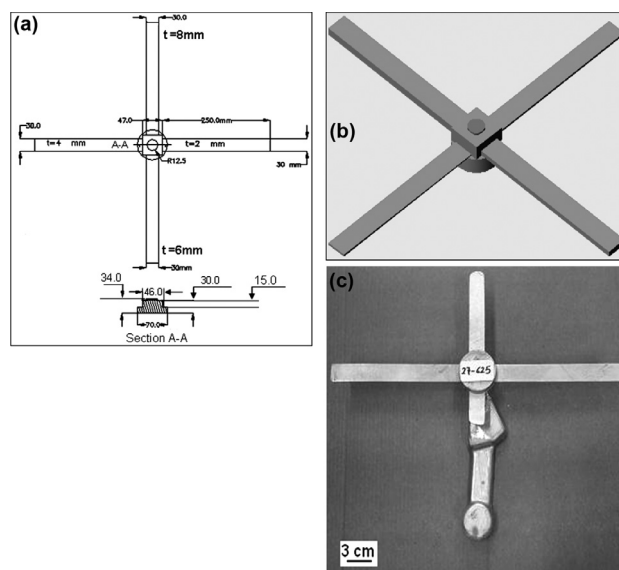


Figure 1: a) Mechanical drawing of sample for fluidity test, b) 3D model for fluidity test and c) one cast sample

Slika 1: a) Risba vzorca za preizkus tekočnosti, b) 3D-model za preizkus tekočnosti in c) ulit vzorec

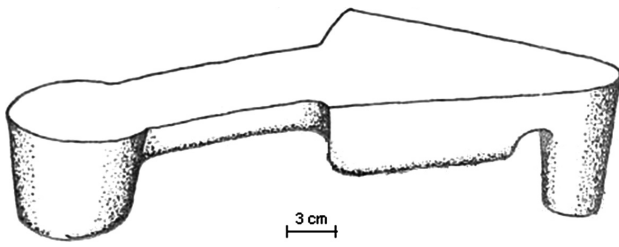


Figure 2: Pouring basin shape¹⁵
Slika 2: Oblika livne čaše¹⁵

2.2 Fluidity evaluation

In order to identify the effect of the mold coating and casting cross-sections on the fluidity, 12 samples were cast. The molten metal was poured manually from the furnace into the pouring basin with a ladle. The temperature of the metal was measured by the operator with a calibrated thermocouple (± 1 °C accuracy) in the ladle, before pouring into the basin. The aim was to pour the molten metal into the basin as fast as possible and to fill up the basin completely, in order to have the same initial metallostatic pressure head on the flowing metal.

Table 3 shows the casting conditions of the samples. In this study, a temperature of 625 °C was selected for pouring the melt after some preliminary tests, because at the mentioned temperature all of the channels have misrun. Therefore, trying with a change of the coating type, improves the fluidity length and the castability, for better filling of the channels. For a phase analysis of the MM12 coating, the amount of coating drying and powdered then carry out X-ray diffraction (XRD) using a Philips Xpert-MPD model on a coating and show that the mentioned coating contains ZrO_2 , SiO_2 and Al_2O_3 phases.

Table 3: Casting condition of various samples (for each condition, 3 samples were cast in a sand mold and 625 °C pouring temperature)

Tabela 3: Razmere pri ulivanju različnih vzorcev (za vsako stanje so bili uliti 3 vzorci v peščeno formo pri temperaturi ulivanja 625 °C)

Mold coating type	Sample
Without coating	1
Graphite coating	2
Micro-ceramic coating (ZR1)	3
Nano-ceramic coating (MM12)	4

3 RESULTS AND DISCUSSION

The beryllium element protects the melt from oxidation and burning of the active element such as magnesium.² The strontium element modifies the eutectic silicon phase morphology and changes the needle-like to a fine fibrous morphology, consequently the mechanical properties and, especially, the elongation was improved. The fine fibrous eutectic modifies the hypoeutectic Al–Si alloys that occur when elements such as strontium and sodium are added, and this has been explained based on observations of increased twinning. The increased den-

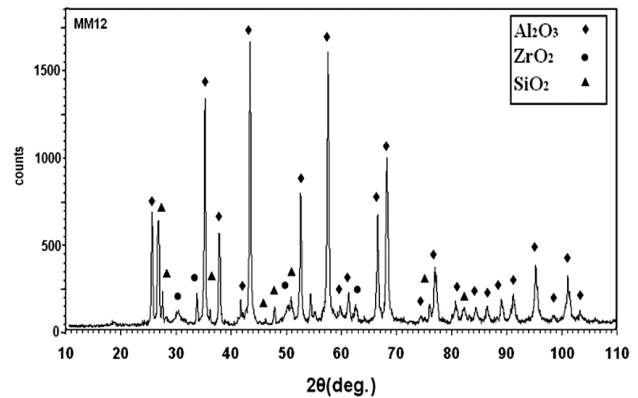


Figure 3: XRD pattern of nano-ceramic coating (MM12) used in this study

Slika 3: XRD-posnetek nanokeramičnega premaza (MM12), uporabljenega v tej študiji

sity of twinning is believed to result from an impurity-induced twinning (IIT) mechanism that promotes further growth by encouraging the formation of a perpetuating twin plane re-entrant edge (TPRE).^{16–18}

The chemical compositions of the nano-ceramic coating (MM12) and micro-ceramic coating (ZR1) are shown in Table 4. The XRD patterns of the nano-ceramic coating (MM12) and the micro-ceramic coating (ZR1) powders are shown in Figures 3 and 4.

Table 4: Chemical composition of MM12 and ZR1 coatings used in this study

Tabela 4: Kemijska sestava premazov MM12 in ZR1, uporabljenih v tej študiji

Composition	Al_2O_3	ZrO_2	SiO_2	H_2O	Others
Content (w/%)	30	7	1	60	2

With reference to the XRD analysis shown in Figure 3, the nano-ceramic coating used in this research particularly contains Al_2O_3 , ZrO_2 and SiO_2 . Based on the broadening of the most prominent peak in the XRD profile, a

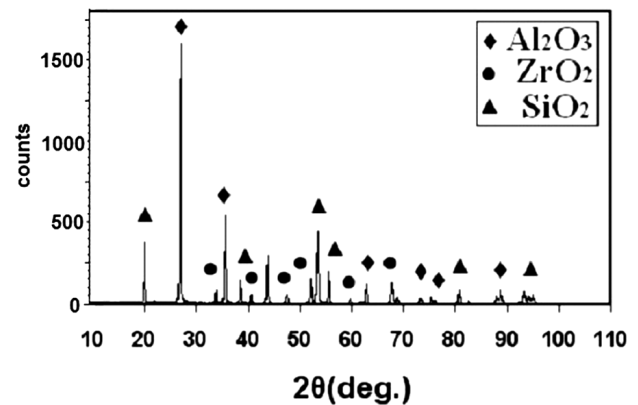


Figure 4: XRD pattern of micro-ceramic coating (ZR1) used in this study

Slika 4: XRD-posnetek mikrokeramičnega premaza (ZR1), uporabljenega v tej študiji

mean crystallite dimension D was calculated using Scherer's formula:¹⁹

$$D = \frac{0.9\lambda}{\beta \cdot \cos \theta} \quad (1)$$

where λ stands for the X-ray radiation wavelength (here 0.15406 nm), β stands for the line broadening at half the maximum intensity in radians. β calculated by equation (2):²⁰

$$\beta^2 = \beta_M^2 - \beta_S^2 \quad (2)$$

$\beta_M = \beta$ in nano-ceramic coating pattern XRD (MM12)

$\beta_S = \beta$ in micro-ceramic coating pattern XRD (ZR1).

Here, $\beta_{Al_2O_3} = 0.0053$, $\beta_{ZrO_2} = 0.0012$, $\beta_{SiO_2} = 0.0058$, K is a shape factor, for the case of a sphere $K = 0.9$, and θ is the Bragg angle.¹⁹ $\theta_{Al_2O_3} = 28.78^\circ$, $\theta_{ZrO_2} = 16.91^\circ$ and $\theta_{SiO_2} = 13.38^\circ$, therefore, $D_{Al_2O_3} = 30$ nm, $D_{ZrO_2} = 120$ nm and $D_{SiO_2} = 25$ nm.

The melting temperature of bulk Al_2O_3 is 2015 °C. The melting temperature of the Al_2O_3 nano-particles (25 nm) should be similar to the bulk counterparts, because the size effect becomes significant only when the particle size is less than 10 nm.²¹ Therefore, no sintering of the nano-coating occurs.

Figure 5 shows a SEM micrograph of the micro-ceramic coating ZR1 and the nano-ceramic coating

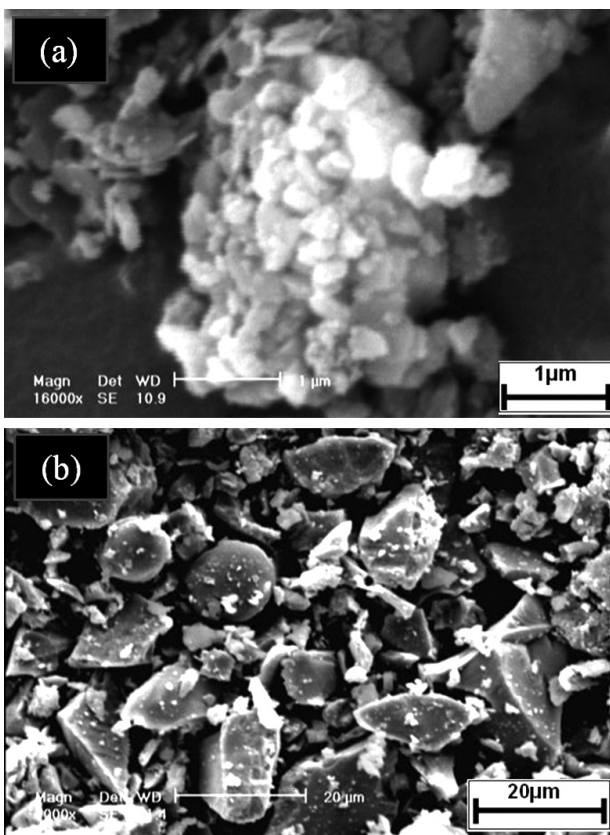


Figure 5: SEM micrographs of: a) micro-ceramic coating ZR1 and b) nano-ceramic coating MM12 used in this study

Slika 5: SEM-posnetka: a) mikrokeramičnega premaza ZR1 in b) nanokeramičnega premaza MM12, uporabljena v tej študiji

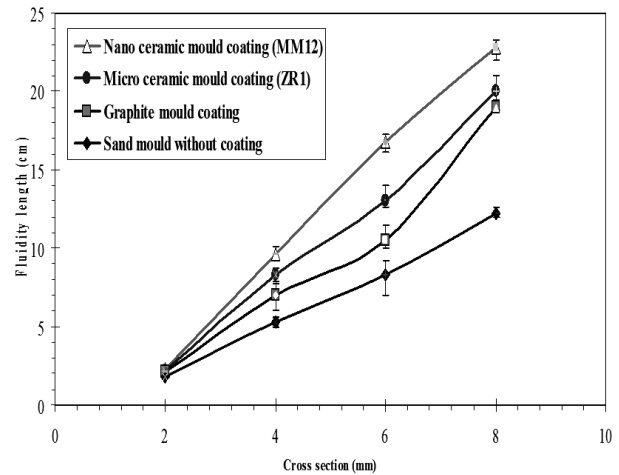


Figure 6: Fluidity length versus cross-section channel
Slika 6: Tekočnost v odvisnosti od prereza kanala

MM12. The phase particles of the ZR1 coating have an average size of approximately 2–20 μm. The ZR1 and MM12 coatings have nearly similar compositions, but different particle sizes. The micro-ceramic coating with a similar composition to the nano-ceramic coating was used to study the influence of the particle size coating on the surface quality of the cast parts and the fluidity length.

Figure 6 shows the effect of the cross-section and the mold coating type on the fluidity length of the melt. With an increasing cross-section of the channel, the fluidity of melt was improved. The fluidity in the mold with the nano-ceramic mold coating was a maximum and the fluidity in the mold with the micro-ceramic coating and graphite coating was better than in sand mold without coating.

The surface roughness was measured using a Mahr-Perthometer M2 roughness tester device. The nano-mold coating had a very smooth surface, hence it reduced the friction forces and the fluidity was improved. Figure 7 shows the relationship between the mold coating and the surface roughness. This figure show that the nano-ceramic mold coating (MM12) has a minimum roughness, and hence the fluidity length in the mold with this

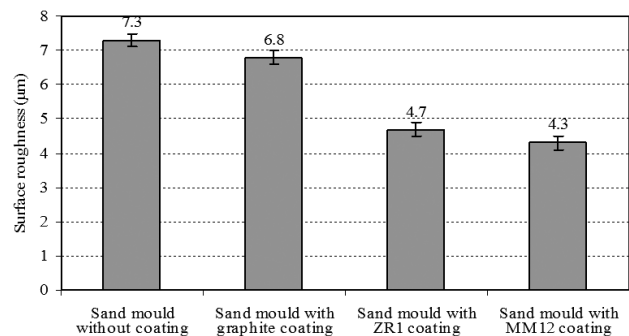


Figure 7: Surface roughness versus mold coating
Slika 7: Hrapavost površine pri različnih premazih forme

coating is better than the mold with micro-coating, graphite coating and a mold without coating.

Research has shown that the wetting angle between the Al melt and ZrO_2 and Al_2O_3 is 70° and 152° , respectively.¹² Thus, the wetting angles are large, and consequently the wettability of the mold when using molten aluminum is very low and the fluidity in the thin section can be improved.¹² The completely proper characteristics of the mold with nano-ceramic coatings can be for the following reasons:^{12,22,23}

1. Thermal and chemical stability, because of ionic and covalent bonds of the ceramics. After the experiment, the composition analysis performed on the inner surface of the coating mold and in the alloy samples achieved, indicated that no chemical reaction occurred between the alloy melt and the mold materials, and therefore no gas is produced and this increases the fluidity.
2. Best flow of melt into mold, because this reduces the coefficient friction and the surface roughness of the mold by smooth and clean surfaces with the nano-mold coating, consequently the melt easily fills the mold and improves the fluidity.
3. Large wetting angle between the aluminum melt and the particles of the coating, which reduces the wettability of the mold coating with the aluminum melt, and consequently it easily fills the mold.
4. Crystal lattice misfit between the melt and the coating materials that inhibits the nucleation of the aluminum melt on a nano-mold coating and consequently there is easy melt flow and an enhancement of the fluidity.

4 CONCLUSIONS

1. By applying a graphite mold coating, a micro-ceramic mold coating and a nano-ceramic mold coating on a sand mold surface, because the coat operates the insulation role and reduces the roughness of the mold surface, this increases the fluidity and castability of melt.
2. The melt fluidity and the castability in the sand mold with a nano-ceramic coating has the best result in comparison with the sand mold with a micro-ceramic mold coating, a graphite mold coating and a sand mold without coating.
3. By increasing the cross-section of the channel, because it reduces the cooling rate and the surface tension, this improves the fluidity length and the castability.
4. Mold coating significantly improves the fluidity, and hence a lower casting temperature can be used. Therefore, casting defects were reduced and indirectly mechanical properties could be improved.

Acknowledgements

The authors are grateful for support of this research by Isfahan University of Technology (IUT).

5 REFERENCES

- ¹ E. Taghaddos, M. M. Hejazi, R. Taghiabadi, S. G. Shabestari, Effect of iron-intermetallics on the fluidity of 413 aluminum alloy, *Journal of Alloys and Compounds*, 468 (2009) 1–2, 539–545
- ² V. S. Zolotarevsky, N. A. Belov, *Casting Aluminum Alloy*, 1st ed., Elsevier Science, 2007
- ³ W. R. Osório, L. R. Garcia, P. R. Goulart, A. Garcia, Effects of eutectic modification and T4 heat treatment on mechanical properties and corrosion resistance of an Al-9wt%Si casting alloy, *Materials Chemistry and Physics*, 106 (2007) 2–3, 343–349
- ⁴ M. Di Sabatino, L. Arnberg, A review on the fluidity of Al based alloys, *Metallurgical Science and Technology*, 22 (2004) 1, 9–15
- ⁵ N. Hongjun, B. Sun, H. Jiang, W. Ding, Effects of rotating impeller degassing on microstructure and mechanical properties of the A356 scraps, *Materials Science and Engineering A*, 352 (2003) 1–2, 294–299
- ⁶ K. R. Ravi, R. M. Pillai, K. R. Amaranathan, B. C. Pai, M. Chakraborty, Fluidity of aluminum alloys and composites: A review, *Journal of Alloys and Compounds*, 456 (2008) 1–2, 201–210
- ⁷ *Casting Design Handbook*, ASM, 1962
- ⁸ M. Di Sabatino, Fluidity of aluminum foundry alloys, Thesis submitted to the Norwegian University of Science and Technology (NTNU) in partial fulfillment of the requirements for the degree of Philosophiae Doctor, Trondheim, 2005
- ⁹ Y. D. Kwon, Z. H. Lee, The effect of grain refining and oxide inclusion on the fluidity of Al-4.5Cu-0.6Mn and A356 alloys, *Materials Science and Engineering A*, 360 (2003) 1–2, 372–376
- ¹⁰ P. R. Beeley, *Foundry Technology*, Butterworth Scientific, 1972
- ¹¹ A. N. Goldstein (ed.), *Handbook of Nanophase Materials*, Marcel Dekker Inc., 1997
- ¹² L. Feng, Y. Gencang, Solidification of superalloy in a SiO_2 - ZrO_2 - B_2O_3 coating mould, *Journal of Non-Crystalline Solids*, 290 (2001) 2–3, 105–114
- ¹³ J. E. Gruzleski, B. M. Closset, *The Treatment of Liquid Aluminium-Silicon Alloys*, American Foundrymen's Society, Inc., 1990
- ¹⁴ *Metals Handbook Aluminium and Aluminium Alloys*, 1992
- ¹⁵ *Metalcasters' Reference and guide*, first edition, AFS, August 1972
- ¹⁶ S. Zulu, A. Hellowell, *Solidification processing*, (1987), 4–47
- ¹⁷ S. D. McDonald, K. Nogita, A. K. Dahle, Eutectic grain size and strontium concentration in hypoeutectic aluminium-silicon alloys, *Journal of Alloys and Compounds*, 422 (2006) 1–2, 184–191
- ¹⁸ K. Nogita, H. Yasuda, M. Yoshiya, S. D. McDonald, A. Takeuchi, Y. Suzuki, The role of trace element segregation in the eutectic modification of hypoeutectic Al-Si alloys, *Journal of Alloys and Compounds*, 489 (2010) 2, 415–420
- ¹⁹ P. N. Prasad, *Nanophotonics*, John Wiley & Sons Inc., 2004
- ²⁰ B. D. Cullity, *Elements of X-Ray Diffraction*, 2nd ed, Addison-Wesley, 1978
- ²¹ J. Y. Huang, In Situ Observation of Quasimelting of Diamond and Reversible Graphite-Diamond phase Transformations, *Nano Letters*, 7 (2007) 8, 2335–2340
- ²² M. Sherif, El. Eskandarany, *Journal of Alloys and Compounds*, 296 (2000), 175–182
- ²³ G. J. Li, X. X. Huang, J. K. Guo, Fabrication, microstructure and mechanical properties Al_2O_3 /Ni nanocomposites by a chemical method, *Materials Research Bulletin*, 38 (2003) 11–12, 1591–1600

INFLUENCE OF THE THERMO-MECHANICAL TREATMENT ON THE EXFOLIATION AND PITTING CORROSION OF AN AA5083-TYPE ALLOY

VPLIV TERMO-MEHANSKE OBDELAVE ZLITINE AA5083 NA LUŠČENJE IN JAMIČASTO KOROZIJO

Akram Halap¹, Miljana Popović¹, Tamara Radetić¹, Veselin Vaščić²,
Endre Romhanji¹

¹Department of Metallurgical Engineering, Faculty of Technology and Metallurgy, University of Belgrade, Karnegijeva 4, 11120 Belgrade, Serbia

²Freelance Consultant

akram_halap@yahoo.com, endre@tmf.bg.ac.rs

Prejem rokopisa – received: 2013-07-18; sprejem za objavo – accepted for publication: 2013-10-04

Exfoliation and pitting corrosion were tested on an AA5083-type alloy sheet, after applying different thermo-mechanical treatments. Hot-rolled plates were laboratory cold rolled with 16–54 % reductions, and subsequently annealed for 2 h in the temperature range from 220 °C to 280 °C. The performed tests have shown that an unacceptable exfoliation and a corrosion susceptibility were developed after the 54 % deformation and low-temperature annealing at 220 °C. However, no severe exfoliation was observed after the cold rolling with low deformations, independent of the applied annealing temperature. The pitting corrosion was less aggressive, and the highest degree of the pitting attack was not experienced for the tested alloy. A slight tendency to pitting was detected after the high cold deformation and high-temperature annealing for the samples with recrystallized but significantly flattened grain structures.

Keywords: AA5083 alloy, thermo-mechanical treatment, exfoliation, pitting

Luščenje in jamičasta korozija sta bili preizkušeni na pločevini iz zlitine AA5083 po različnih termo-mehanskih obdelavah. Vroče valjane plošče so bile v laboratoriju hladno valjane z redukcijo 16–54 %, nato žarjene 2 h v območju temperature od 220 °C do 280 °C. Preizkusi so pokazali nesprejemljivo luščenje in občutljivost za korozijo po 54-odstotni deformaciji in nizki temperaturi žarjenja 220 °C. Močnejšega luščenja ni bilo opaziti po hladnem valjanju z majhno deformacijo, neodvisno od uporabljene temperature žarjenja. Jamičasta korozija je bila manj agresivna in močne jamičaste korozije ni bilo pri preizkušeni zlitini. Rahla tendenca po nastajanju jamic se je pokazala pri veliki hladni deformaciji in visoki temperaturi žarjenja pri vzorcih, ki so bili rekristalizirani in so imeli močno sploščeno strukturo.

Ključne besede: zlitina AA5083, termo-mehanska obdelava, luščenje, jamica

1 INTRODUCTION

Al-Mg alloys found a wide range of applications, especially in the construction of transportation means due to the attractive strength-to-weight ratio, good weldability and formability as well as high corrosion resistance.¹⁻⁴ However, the Al-Mg alloys with more than 3 % Mg, due to a limited room-temperature solubility of Mg in an Al matrix ($w(\text{Mg}) = 1.9 \%$), can be sensitized due to the formation of a continuous film of the β -phase (Mg_2Al_3) at the grain boundaries, and become susceptible to intergranular corrosion (IGC).⁵⁻⁹ Generally, the susceptibility to the IGC is influenced, in a complex manner, by the structure features of a material,^{10,11} and an optimization of the overall thermo-mechanical treatment is the key point in producing a corrosion-resistant material.¹⁰ One of the manifestations of the IGC is a specific lamellar type of corrosion, with a blister-surface appearance, known as exfoliation. It is a form of the IGC that occurs on the surfaces of the wrought aluminum alloys¹²⁻¹⁴ with highly flattened grain structures. Another common corrosion type, also associated with a specific surface appearance, is pitting corrosion. It is a form of an extremely localized corrosion¹⁵ that leads to a creation of

small holes or pits in the structure, usually covered by the corrosion products. These types of corrosion were often observed and analyzed on 2xxx and 7xxx type alloys, used in aircraft industries, and due to their importance a major attention was paid to the investigation of these alloys.^{16,17}

The objective of this work was to study the exfoliation and pitting corrosion on a moderate-strength non-heat treatable AA5083-type-alloy sheet, after applying different thermo-mechanical treatments (TMTs). Exfoliation and pitting corrosion appeared to be very important manifestations of a sea-water attack in Al-Mg-based alloys,¹⁸ therefore, marine-grade alloys should be subjected to the corrosion testing defined in ASTM B 928/B 928M-04a standard,¹⁹ including intergranular, exfoliation and pitting corrosion assessments.

2 EXPERIMENTAL WORK

Material. The material used in this study was an industrially manufactured hot-rolled thick plate 7.4 mm, supplied by Impol-Seval Aluminium Rolling Mill. The chemical composition is listed in **Table 1**.

The as-received hot-rolled plates were laboratory cold rolled to 3.5 mm and inter-annealed for 3 h at 350 °C. These samples were further cold rolled with different degrees of deformation ranging from 16 % to 54 %, and then finally annealed for 2 h in the temperature range of 220–280 °C and air cooled.

Table 1: Chemical composition of the tested alloy in mass fractions (w/%)

Tabela 1: Kemijska sestava preizkusne zlitine v masnih deležih (w/%)

Mg	Mn	Cu	Fe	Si	Zn	Cr	Ti	Sr
5.13	0.718	0.013	0.337	0.11	0.513	0.008	0.0254	0.003

Corrosion testing. Susceptibility to exfoliation and pitting corrosion was determined with a visual inspection using the ASSET method (the method for a visual assessment of the exfoliation-corrosion susceptibility of AA5xxx-series Al alloys), described in ASTM G66 standard.

Brinell hardness was measured on the samples processed in the manner described above, as well as the grain aspect ratio, calculated after revealing the grain structure using Barker's etchant and a microstructure analysis with an optical microscope.

3 RESULTS

Exfoliation and pitting-corrosion susceptibility were ranked after a visual inspection according to ASTM G66 standard. The following letters were used to describe the degrees of pitting corrosion: N – no appreciable attack, or A, B and C levels of attack (A and B denote acceptable corrosion, C denotes susceptibility to corrosion). In

case of exfoliation (besides N) the ratings are as follows: A, B, C and D levels of attack (A and B denote acceptable exfoliation, C and D denote susceptibility to exfoliation). A combination of two letters was used in the case when the surface morphology could not be described with only one letter due to a mixed- or boundary-type surface appearance like the ones on the photographs given in ASTM G66 standard.

The ratings of the exfoliation and pitting-corrosion-attack dependence on the applied TMTs, i.e., the cold-rolling reductions and annealing temperatures, are shown in **Figures 1a** and **1b**. The results for the general IGC susceptibility of the tested alloy (expressed as a mass loss per unit area, according to ASTM G67 standard), considered elsewhere,²⁰ are also attached. The results shown in **Figure 1a** indicate that the C level denoting unacceptable exfoliation appeared after the 54 % cold deformation and low-temperature annealing at 220 °C. However, after a prior low deformation of 16 %, the exfoliation was absent, even after a low-temperature annealing at 220 °C, and not related to the IGC susceptibility that was very pronounced in this case, as shown in **Figure 1a**.

The most detrimental pitting-corrosion susceptibility, described as the C-type surface appearance, was not recognized for the tested alloy. However, after a higher degree of the cold-rolling reduction, 54 %, and the final annealing at 260 °C and 280 °C, the B level of the pitting susceptibility was identified (**Figure 1b**). The same B level of the pitting attack was noticed after the 30 % deformation and the annealing at the highest temperature of 280 °C.

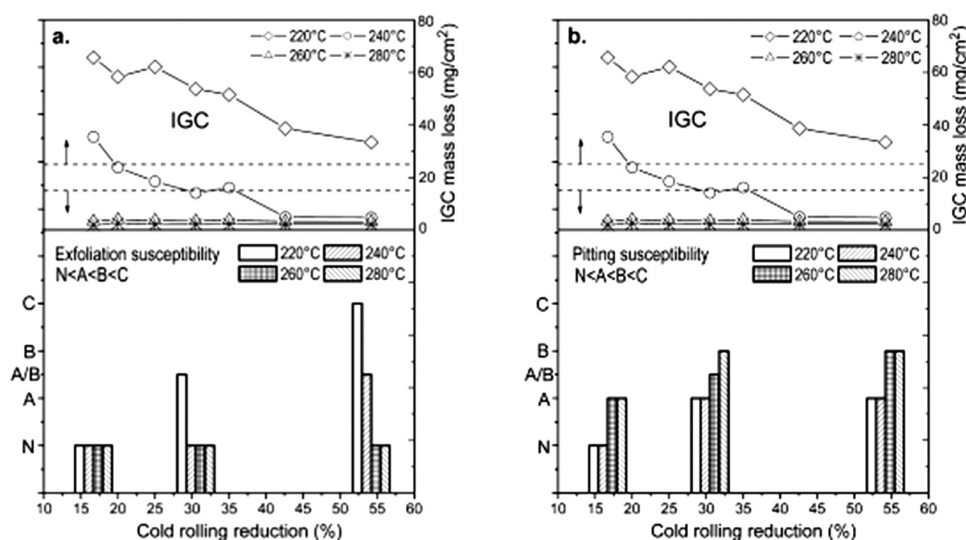


Figure 1: Ratings of the: a) exfoliation and b) pitting corrosion levels (according to ASTM G66 standard) for the cold rolled (16–54 %) and subsequently annealed (220–280 °C) specimens. The appropriate data for the IGC susceptibility is also shown. The values below the lower dashed line (IGC = 15 mg/cm²) indicate the IGC resistance, while the ones above the upper line (IGC = 25 mg/cm²) indicate the IGC susceptibility.

Slika 1: Ocena: a) luščenja in b) jamičaste korozije (skladno z ASTM G66-standardom) za hladno valjane (16–54 %) in kasneje žarjene (220–280 °C) vzorce. Prikazani so tudi ustrezni podatki za občutljivost IGC. Vrednosti pod spodnjo črtkano črto (IGC = 15 mg/cm²) izkazujejo odpornost proti IGC, medtem ko vrednosti nad zgornjo črto (IGC = 25 mg/cm²) izkazujejo občutljivost za IGC.

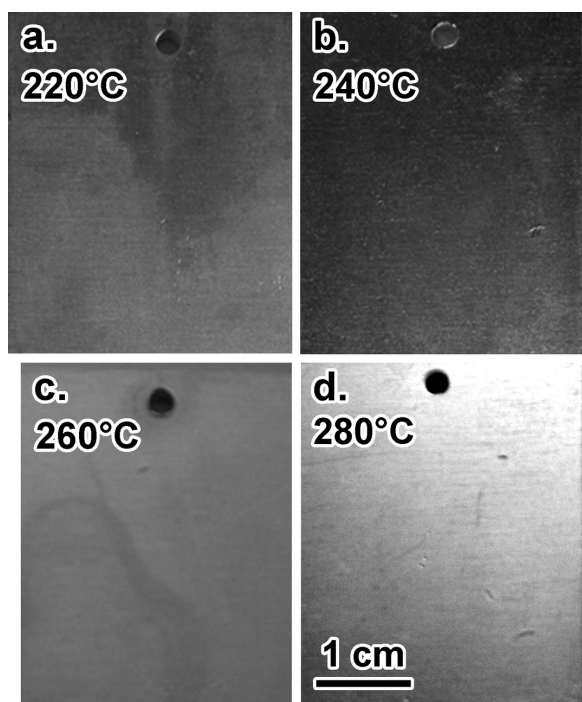


Figure 2: Surface appearance for the samples deformed with the 16 % reduction and annealed for 2 h at different temperatures

Slika 2: Videz površine vzorcev, deformiranih s 16-odstotno redukcijo in žarjenih 2 h pri različnih temperaturah

Illustrations of the surface appearances for the samples subjected to the ASSET test, used for the exfoliation and pitting assesment, are shown on **Figures 2 and 3**. **Figure 2** shows the surfaces of the specimens cold rolled with a low-degree deformation, showing no corrosion and no influences of the final annealing temperature.

However, a severe C-type exfoliation was detected on the surfaces of highly deformed samples (54 %) subsequently annealed at a low temperature (220 °C), as shown in **Figure 3a**. The B-level pitting corrosion was observed after the 54 % deformation and annealing at 260 °C or 280 °C as shown in **Figures 3c and 3d**.

The results of the hardness measurements shown in **Figure 4** revealed that an increase in the cold-rolling reduction up to ≈ 35 % caused a hardness increase. In the cases of higher cold-rolling reductions of > 35 %, the hardness level stayed almost unchanged (ranging from 85–100 HB), except for the samples annealed at 280 °C. For those samples, a steep decrease in the hardness was observed after a 20 % pre-deformation. However, after the annealing at 260 °C a less steep but continuous drop in the hardness occurred when the prior cold deformation was increased to over 30 %.

In order to correlate the corrosion behavior and the microstructure of the tested alloy, the grain structures of the samples cold rolled with 16 % and 54 % reductions and annealed at 220 °C 2 h and 280 °C 2 h, were revealed as shown in **Figures 5a to 5d**. In the case of the prior 54 % cold deformation, the grains were elongated after the annealing at both temperatures, independently

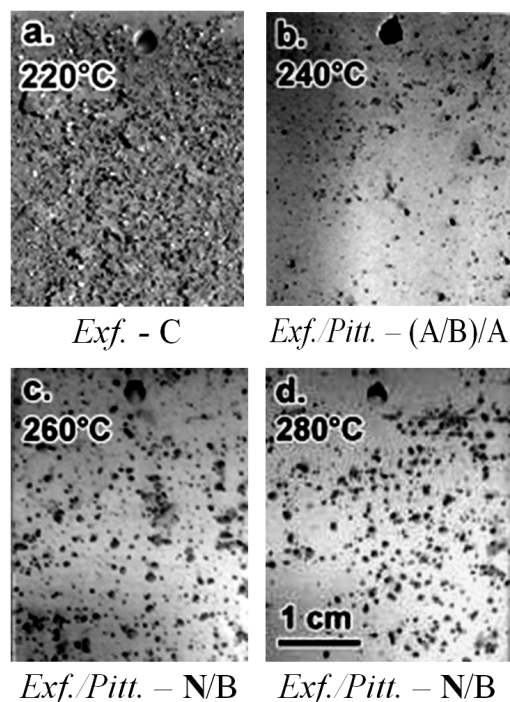


Figure 3: Surface appearance for the samples deformed with the 54 % reduction and annealed for 2 h at different temperatures

Slika 3: Videz površine vzorcev deformiranih s 54-odstotno redukcijo in žarjenih 2 h pri različnih temperaturah

of the recrystallization processes that occurred after the annealing at 280 °C 2 h (the recrystallization is indicated by the hardness drop in **Figure 4**).

The grain aspect ratio was calculated for the prior cold deformations of (16, 30 and 54) %, for the whole range of the annealing temperatures, as shown in **Figure 6**. It was found that the appropriate grain aspect ratios were around 5.5 for the sample annealed at 220 °C 2 h and 5.7 for the sample annealed at 280 °C 2 h after the 54 % deformation.

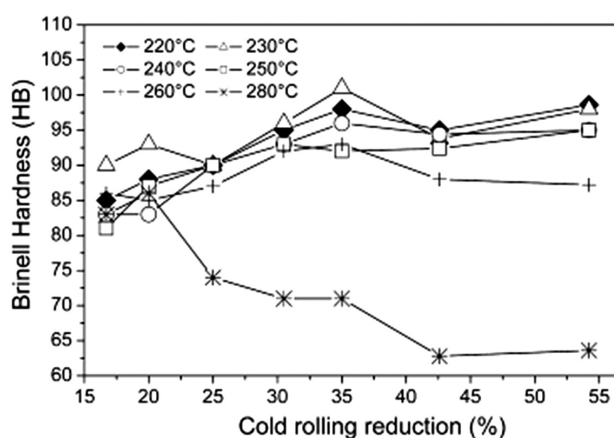


Figure 4: Influence of cold-rolling reductions on the hardness of the samples subsequently annealed for 2 h in the temperature range of 220–280 °C

Slika 4: Vpliv redukcije pri hladnem valjanju na trdoto vzorcev, kasneje žarjenih 2 h v območju 220–280 °C

After the 16 % deformation the grains were less elongated, with the grain aspect ratio being 1.7 for the samples annealed at 220 °C 2 h and 3.5 for the samples annealed at 280 °C 2 h. After the 30 % pre-deformation the grain aspect ratio was from 2.3 to 4.4 for the tested range of temperatures. Generally, the grain aspect ratio significantly increased with the increase in the annealing temperature.

4 DISCUSSION

Previous studies^{12-14,21} have shown that the grain structure developed under different thermo-mechanical treatments (TMTs) can have an important role in developing the exfoliation corrosion of the high-strength alloys such as 2xxx or 7xxx series of Al alloys. The basic influence of TMTs is related to the grain flatness or grain aspect ratio enabling a specific long surface path for the IGC, and a formation of corrosion products on a few surface planes with a higher specific volume. In this way the expansion tendency creating the compressive stress can lift the surface grains and form surface blisters. On the other hand, it is already known that the general IGC susceptibility is mostly controlled with the alloy composition and the distribution of grain-boundary precipitates.²²

In this work, the harmful C level of exfoliation was experienced only after the 54 % cold-rolling deformation and the subsequent low-temperature annealing at 220 °C (Figures 1a and 3a). In this case the recovery degree was supposed to be low, as it was indicated by the hardness level after the annealing at 220 °C (Figure 4). The microstructural observations of these samples showed that the grains were highly elongated (Figure 5c) with the grain aspect ratio of ≈ 5.7 (Figure 6). For the samples with the lower grain aspect ratio of ≈ 2.3 after the 30 %

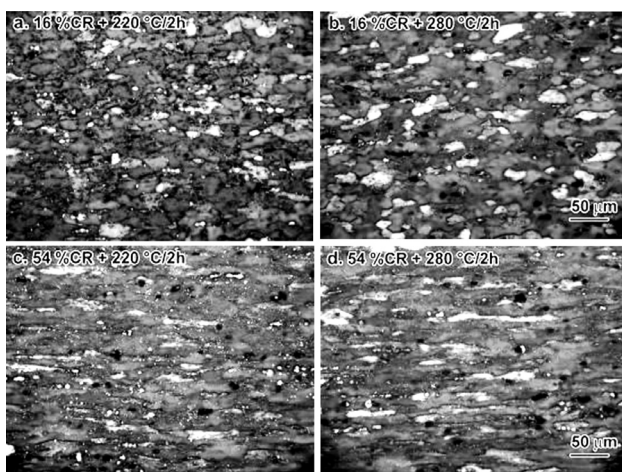


Figure 5: Grain structures of the samples deformed with the: a), b) 16 % and c), d) 54 % cold-rolling reductions and annealed for 2 h at: a), c) 220 °C and b), d) 280 °C

Slika 5: Zrnata struktura vzorcev po hladnem valjanju, deformiranih s: a), b) 16 % in c), d) 54 % redukcijo ter žarjenih 2 h pri: a), c) 220 °C in b), d) 280 °C

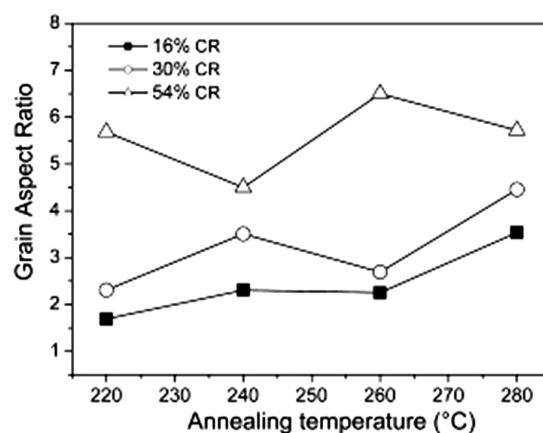


Figure 6: Grain aspect ratios for the samples cold rolled with (16, 30 and 54) % reductions and subsequently annealed for 2 h at 220 °C and 280 °C

Slika 6: Razmerje dolžine proti višini zrn pri hladno valjanih vzorcih z redukcijo (16, 30 in 54) % ter kasneje žarjenih 2 h pri temperaturah 120 °C in 280 °C

deformation, or ≈ 1.7 after the 16 % deformation, no unacceptable exfoliation level of attack was observed or it was completely absent (Figure 1a). This indicates the grain-flatness importance in the case of the exfoliation-type corrosion. It should also be emphasized that for the 16 % deformed samples, the general IGC susceptibility was at the highest level (Figure 1a), but obviously the grain flatness was low and exfoliation could not develop at all. The grain aspect ratio seemed to increase with the increasing annealing temperature (Figure 6), but in spite of this, no detrimental level of the exfoliation attack took place (Figure 1a). It was assumed that the general IGC susceptibility was reduced to such an extent that it suppressed exfoliation, i.e., any type of intercrystalline corrosion. Therefore, after the low-temperature annealing, the 54 % deformed sample with a non-recrystallized structure and the grain aspect ratio of 5.5 was prone to exfoliation, while the recrystallized structure with the grain aspect ratio of 5.7 (after the annealing at 280 °C) was completely resistant to exfoliation, as the IGC was suppressed too. It was supposed that an improvement of the corrosion properties with the annealing-temperature variations can be basically related to the β -phase precipitation, i.e., the change of a continuous film after the low-temperature annealing to a discontinuous discrete β -phase morphology after the high-temperature annealing at 260 °C and 280 °C, as discussed elsewhere.²⁰ Therefore, in practice, the exfoliation-corrosion control should be considered in a limited range of the structure states that are also fully resistant to the IGC. However, according to our results the tendency to the exfoliation-type corrosion in all the circumstances was related to a flattened-grain structure, i.e., it was suppressed in the case of the structure with a grain aspect ratio below a certain critical value.

On the other hand, in the case of a lower grain aspect ratio or a structure with less elongated grains, the pitting

ing-type corrosion is thought to be the active process of the intercrystalline corrosion.^{12,13} In this experiment, no unacceptable C-level pitting was detected (**Figures 1b, 3c and 3d**) according to the fact that under the applied cold deformations and heat treatments no equiaxed grain structure was developed (**Figure 5**). The appearance of a severe but not harmful B-level pitting corrosion, observed after the annealing at 260 °C and 280 °C of the 54 % deformed samples (**Figures 1b and 3b**), could be related to a high degree of the recovery or recrystallization process. This is in a good agreement with the hardness drop (**Figure 4**) and cannot be related to the development of a less flattened or equiaxed grain structure enabling the pitting corrosion with the progress in the intercrystalline corrosion over the shorter paths around the grains.^{12,13}

Using the results shown in **Figure 1b** it was difficult to correlate the degree of the pitting-corrosion attack and the general intergranular-corrosion (IGC) susceptibility as the pitting was even stronger for the samples showing a high IGC resistance (indicated by a very low mass loss in **Figure 1b**).

5 CONCLUSION

The exfoliation and pitting corrosion of an AA5083-type alloy sheet were considered after applying different thermo-mechanical treatments (TMTs): cold-rolling deformations from 16 % to 54 % and the final annealing for 2 h at 220–280 °C.

The results of the corrosion testing, performed according to ASTM G66 standard, showed that the exfoliation-type corrosion can be significantly affected by varying the applied TMTs. A detrimental or unacceptable exfoliation-corrosion level was experienced after high cold-rolling deformations ($\approx 50\%$) and low-temperature annealing (at 220 °C) together with a highly elongated grain structure. However, in the case of the high-temperature annealing and a certain grain flatness, the exfoliation could not develop as the general IGC was suppressed too.

No harmful level of pitting corrosion was detected as the equiaxed grain structure was not developed after applying different TMTs. However, a moderate pitting attack was noticed after the annealing at high temperatures on the samples with recrystallized but highly flattened grain structures and with a very low IGC susceptibility.

Acknowledgements

The authors are grateful to the Ministry of Education, Science and Technological Development, Republic of

Serbia, and Impol-Seval Aluminium Mill, Sevojno, for supporting this research under contract TR 34018.

6 REFERENCES

- ¹Transport and Aluminium, The Aluminium Association-IAI, 2008
- ²G. M. Raynaud, Ph. Gomiero, Aluminium Alloys for the Marine Market, Aluminium and its Alloys, 79 (1996), 73
- ³K. Baumann, M. Bertram, P. Kistler, In: M. Pekguleryuz (ed.), Conf. Proc.: Light Metals in Transport Applications, Canadian Institute of Mining, Metallurgy and Petroleum, 2007, 325–338
- ⁴T. Summe, The Aluminum Advantage – Commercial Vehicle Applications, SAE, Automotive Aluminum – The Performance Advantage, from www.autoaluminum.org
- ⁵M. Popović, E. Romhanji, Mater. Sci. Eng., A492 (2008), 460–467
- ⁶M. Popović, E. Romhanji, B. Minov, D. Glišić, SCC susceptibility and formability in relation to different TMTs of an Al-6.8 wt% Mg alloy sheet, In: J. Hirsch, B. Skrotzki, G. Gottstein (eds.), Conf. Proc. ICAA11: Aluminium Alloys – Their Physical and Mechanical Properties, Wiley-VCH Verlag GmbH & Co. KGaA, Weinheim, 2 (2008), 2155–2162
- ⁷A. L. Davenport et al., Mater. Sci. Forum, 519–521 (2006), 641–646
- ⁸J. C. Chang, T. H. Chuang, Metall. Mater. Trans., 30A (1999), 3191–3199
- ⁹J. L. Searles, P. I. Gouma, R. G. Buchheit, Mater. Sci. Forum, 396–402 (2002), 1437–1442
- ¹⁰L. Tan, T. R. Allen, Corrosion Science, 52 (2010), 548–554
- ¹¹M. Popović, T. Radetić, E. Romhanji, Precipitation of the β -phase and Corrosion Behavior of an Al-6.8 wt.% Mg Alloy, Proc. of 13th International Conference on Aluminum Alloys ICAA13, H. Weiland, A. D. Rollett, W. A. Cassada (eds.), John Wiley & Sons, Inc., Hoboken, NJ, USA 2012, 363–370
- ¹²M. J. Robinson, Corrosion Science, 22 (1982), 775–790
- ¹³M. J. Robinson, N. C. Jackson, Corrosion Science, 41 (1999), 1013–1028
- ¹⁴M. J. Robinson, N. C. Jackson, British Corrosion Journal, 34 (1999), 45–49
- ¹⁵D. W. Hoepfner, C. A. Arriscorreta, International Journal of Aerospace Engineering, Article ID 191879, (2012), 1–29
- ¹⁶D. A. Jones, Principles and Prevention of Corrosion, 2nd ed., Prentice-Hall, Inc., Upper Saddle River, NJ 1996
- ¹⁷B. W. Lifka, Corrosion of aluminum alloys, Corrosion Engineering Handbook, P. A. Schweitzer, Marcel Dekker, New York 1996, 129–133
- ¹⁸H. Bushfield, M. Cruder, R. Farley, J. Towers, Marine Aluminum Plate – ASTM Standard Specification B 928 and the Events Leading to its Adoption, 2003, available from: www.boatdesign.net/...what-best-marine-alluminum-alloy-5083-alloy
- ¹⁹ASTM standard B 928/B 928M-04a: Standard Specification for High Magnesium Aluminum-Alloy Sheet and Plate for Marine Service and Similar Environments
- ²⁰T. Radetić, A. Halap, M. Popović, E. Romhanji, Effect of the thermo-mechanical treatment on IGC susceptibility of AA 5083 alloy, In: J. Granfield (eds.), Light Metals 2014: Proceedings of TMS 2014 Annual Meeting, J. Wiley & Sons, Hoboken, NJ, USA 2014, 297–302
- ²¹D. McNaughtan, M. Worsfold, M. J. Robinson, Corrosion Sci., 45 (2003), 2377–2389
- ²²J. R. Davis, Corrosion of Aluminum and Aluminum Alloys, ASM International, Metals Park, Ohio 1999, 101

STRUCTURAL AND ELECTRICAL STUDIES OF FULLERENE (C60) DISPERSED POLYMER ELECTROLYTES

ŠTUDIJ STRUKTURNIH IN ELEKTRIČNIH LASTNOSTI POLIMERNEGA ELEKTROLITA Z DISPERGIRANIM FULERENOM (C60)

Amit Saxena^{1,2}, Pramod Kumar Singh², Bhaskar Bhattacharya²

¹Department of Physics, Hindustan College of Science and Technology, Farah, Mathura- 281122, India

²Material Research Laboratory, School of Engineering and Technology, Sharda University, G. Noida 201310, India
saxena.electronics@gmail.com, b.bhattacharya@sharda.ac.in

Prejem rokopisa – received: 2013-07-18; sprejem za objavo – accepted for publication: 2013-10-29

In this work we report on a modification of the optical and electrical properties of a polymer electrolyte film (PEO : NaI) by doping with C60. Light microscopy was used to study the surface morphology of the polymer electrolyte film doped with C60. For the electrical properties, complex impedance spectroscopy (CIP) was used and the conductivity was calculated. The dielectric, modulus and transference numbers were calculated and explained in detail to support the electrical conductivity data.

Keywords: polymer electrolyte, light microscopy (LM), conductivity, dielectric constant, ion transference number

V tem delu poročamo o spremembi optičnih in električnih lastnosti polimerne elektrolitske plasti (PEO : NaI) po dopiranju s C60. Študij morfologije površine elektrolitske polimerne plasti je bil izvršen s svetlobno mikroskopijo (LM). Za električne lastnosti je bila uporabljena kompleksna impedančna spektroskopija (CIP), prevodnost pa je bila izračunana. Dielektričnost, moduli in transportno število so bili izračunani in podrobno razloženi za podporo podatkov električne prevodnosti.

Ključne besede: polimerni elektrolit, svetlobna mikroskopija (LM), prevodnost, dielektrična konstanta, transportno število

1 INTRODUCTION

Ion-conducting polymers, obtained by polymer-salt complexation, are becoming increasingly important because of their application in solid-state polymer batteries, fuel cells, etc. Many good ion-conducting polymer electrolytes have been developed by complexing polymers (for example, PEO) with salts like lithium perchlorate, lithium triflate, sodium chloride, sodium iodide, etc.¹⁻⁴ To enhance the conductivity of the polymer electrolyte, various approaches have been adopted, like (a) changing the type of complexing polymer (b) the use of polymers with different chain lengths (c) the use of different complexing salts and (d) modifying the degree of crystallinity by the use of plasticizers and copolymerization.⁵⁻⁸ However, the doping of fullerene (C60) with a polymer electrolyte is a relatively a new approach to enhance the optical and electrical properties of polymeric films. In this paper we report an important observation regarding a change in the physical and electrical properties of polymer films doped with fullerene (C60).⁹⁻¹¹

2 EXPERIMENTAL

2.1 Material Preparation

Composite polymer films with a thickness varying between 200 μm to 300 μm were synthesized using the standard "solution cast" technique.¹²

Before the preparation of the polymer film, the fullerene is prepared in the laboratory. To obtain this fullerene, soot is collected by the burning of phenolphthalein, which is dissolved in benzene and stirred continuously for approximately 5 h. Finally, the solution was filtered. A wine-coloured solution was obtained, which was characterized by NMR to confirm the formation of C60. The NMR results showed the formation of fullerenes (methanofullerene) (**Figure 1**) with a small chain attached with the ball. The obtained structure was similar to that required for doping in polymer electrolyte films. Finally, PEO (Mw: 2 000 000) and NaI were weighed separately in the required amounts. These weighed components were then dissolved in distilled methanol. Different weights of prepared fullerene were added to this combination. After this the solution was stirred for a long time to achieve uniform mixing and complexation. Then, the mixture was poured into polypropylene/Teflon moulds for casting in ambient, room conditions. The solvent was then slowly evaporated at room temperature. Finally, the film was dried under vacuum to eliminate any traces of solvents. The as-prepared films were subjected to different characterizations.

The polymer (PEO) and salt (NaI) molar ratio was maintained at 0.065¹³ and the amount of C60 dispersed in the complex matrix was expressed in mass fractions. The composition is represented as (PEO : NaI) + w(C60).

2.2 Material Characterisation

The surface morphology of the composite polymer film was studied with an optical microscope. In order to evaluate the ionic conductivity of the polymer electrolyte film, impedance spectroscopic techniques were used. The conductivity of the polymer films was evaluated from the bulk resistance calculated by ac complex impedance spectroscopy over a frequency range of 100 Hz to 1 MHz. The transference numbers (tion) of the C60-doped polymer electrolyte composite sample were measured using Wagner's polarization method.⁴ In this method the sample is placed between two electrodes in such a way that it minimizes the contact resistance. In an ideal case one of the electrodes is blocking, whereas the other is non-blocking. In the present case we used stainless-steel electrodes. A DC potential is applied across the sample in such a way that mobile ion species move towards the non-blocking electrode and a small polarization current flows and, finally, the sample becomes polarized. The initial total current I_i and the final residual current I_f are use to evaluate the ionic transference number.⁷

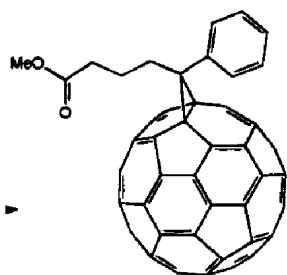


Figure 1: Chemical structure of methanofullerene C61 (CO₂Me)[C₆H₆]

Slika 1: Kemijska struktura metanofulerena C61 (CO₂Me)[C₆H₆]

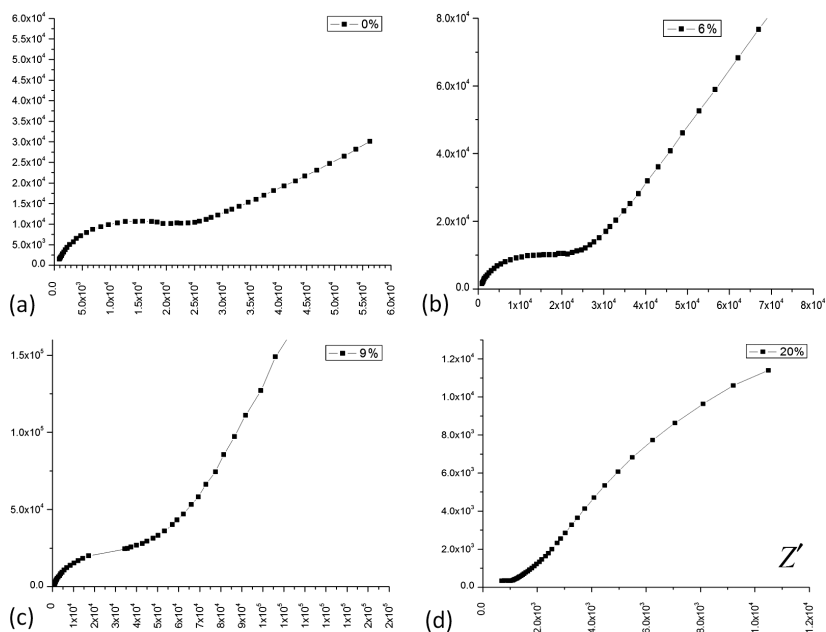


Figure 3: Complex impedance spectra of (PEO : NaI) + w(C60) film at room temperature: a) 0 %, b) 6 %, c) 9 %, d) 20 %

Slika 3: Kompleksni spekter impedance za plast (PEO : NaI) + w(C60) pri sobni temperaturi: a) 0 %, b) 6 %, c) 9 %, d) 20 %

3 RESULTS AND DISCUSSION

3.1 NMR

The samples were investigated in the NMR study. The result confirms the formation of methanofullerene. **Figure 1** shows the structure of methanofullerene C61 (CO₂Me) [C₆H₆].⁹

3.2 Surface Morphological Study

3.2.1 Morphology

Typical light micrographs of the composite polymer electrolyte system (PEO : NaI) + w(C60) are shown in **Figure 2**.

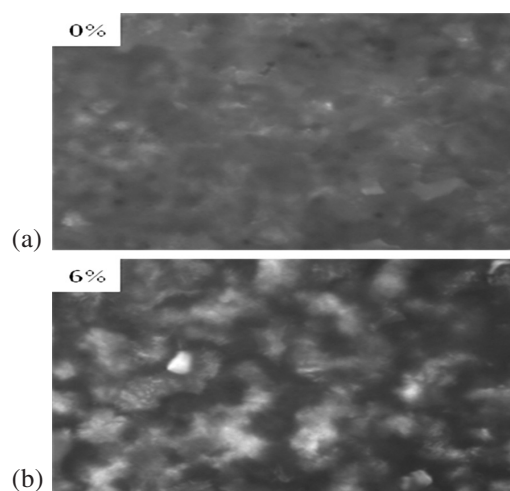


Figure 2: Light micrographs of (PEO : NaI) + w(C60) composite polymer electrolyte system: a) 0 % and b) 6 %

Slika 2: Mikrostruktura polimernega elektrolitskega kompozitnega sistema (PEO : NaI) + w(C60): a) 0 % in b) 6 %

The spherulites are observed (Figure 2a) in the pure polymer complex (i.e., for $w(\text{C60}) = 0$). The dark boundaries observed between the spherulites show the partial amorphous phase of the films. The morphological pattern of the film changed upon the addition of different amounts of the dispersoid. This effect is well shown in Figure 2b. Several dark spots are visible in the case of doping with $w = 6\%$ of C60. This indicates that a larger addition of dispersoid will make more amorphous phase of the films.¹³

3.3 Electrical Properties Study

3.3.1 Complex Impedance Spectroscopy (CIS)

A CIS analysis of the C60 dispersed polymer electrolyte films was performed to determine the change in the electrical properties. The impedance patterns for the different compositions of the films are shown in Figure 3.

It is clearly shown in the figure that as the concentration of the dispersoid increases the impedance pattern of the sample is changed. This impedance graphs are used to calculate the bulk resistance (R_b) of the sample.¹⁰ It is clear from Figure 3 that the value of the bulk resistance is decreased as the concentration of C60 is increases. Now by using the values of bulk resistance, the area and the thickness of the film we are able to calculate the conductivity of the sample.

3.3.2 DC conductivity

The electrical conductivity of the composite polymer films as a function of doping concentration was calculated. Figure 4 shows the change in the conductivity in the polymer electrolyte film doped with C60.

Figure 4 shows that the conductivity decreases with the doping of the dispersoid C60. The minimum of the conductivity was seen at 9% of doping, but the value suddenly increases to a maximum of 7.9×10^{-7} S/cm when doping with $w(\text{C60}) = 20\%$

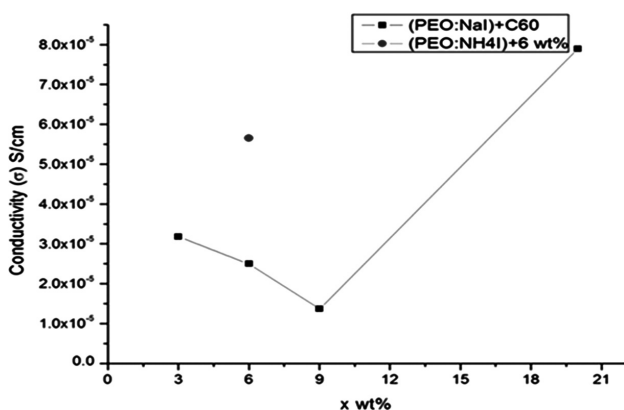


Figure 4: Variation in conductivity of (PEO : NaI) + $w(\text{C60})$ at room temperature

Slika 4: Spreminjanje prevodnosti (PEO : NaI) + $w(\text{C60})$ pri sobni temperaturi

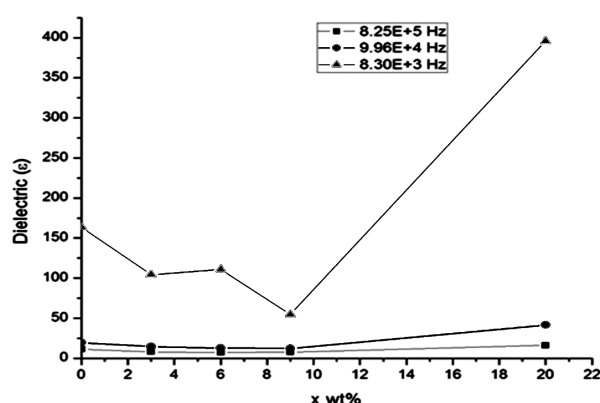


Figure 5: Variation in dielectric of (PEO : NaI) + $w(\text{C60})$

Slika 5: Spreminjanje dielektričnosti (PEO : NaI) + $w(\text{C60})$

3.3.3 Dielectric Constant

The frequency-dependent dielectric constant (ϵ) is calculated for different mass fractions of dispersoid and shown in Figure 5. It is clear that the dielectric decreases as the doping of C60 begins, but at 6% of doping the dielectric increases.

Two increases in the dielectric constant are clearly seen in Figure 5, at 6% and 20%. This result for the dielectric supports the change in the conductivity.^{10,14}

3.4 Dielectric relaxation study

A dielectric formulism is useful in retrieving many particulars about the conductivity behaviour of any material. The dielectric constant is a measure of the stored charge. The frequency dependence of the real (ϵ') and imaginary (ϵ'') parts of the dielectric constants are shown in Figure 6.

ϵ' and ϵ'' are calculated by using the following relations:

$$\epsilon' = \frac{Z''}{\omega CZ^2} \quad \text{and} \quad \epsilon'' = \frac{Z'}{\omega CZ^2}$$

where Z'' is the imaginary part of the impedance, ω is the angular frequency and C is the capacitance of the empty measuring cell for the electrode area A and the sample thickness L . The capacitance is calculated using the relation:

$$C = \frac{\epsilon_0 A}{L}$$

At lower frequency the high value is due to the polarization of the electrode.¹⁵ But at high frequency, the periodic reversal of the electric field is so fast that the ion diffusion in the electric field is not feasible. Hence, the charge accumulation at the electrode decreases, leading to a decrease in ϵ' and ϵ'' .¹⁶

3.4.1 Modulus Formalism

The sudden change in ϵ' and ϵ'' values at lower frequency is possibly due to the contribution of the elec-

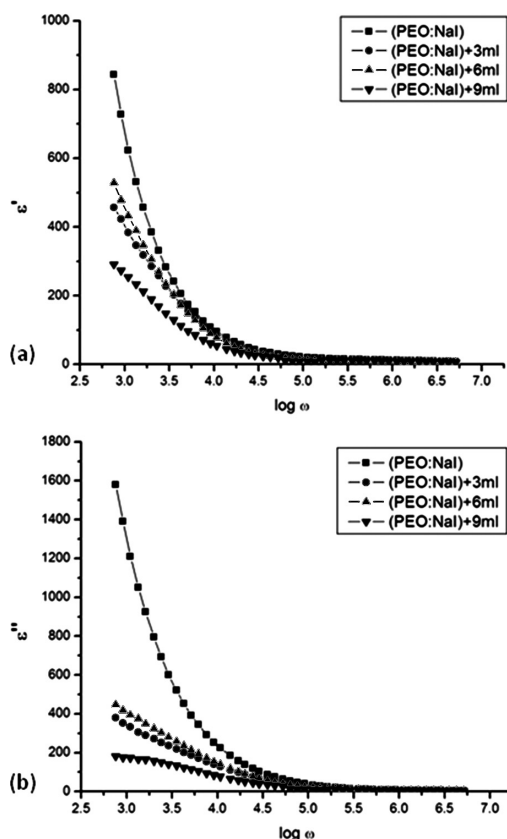


Figure 6: a) Variation in real part of dielectric constant (ϵ') with $w(\text{C60})$, b) variation in imaginary part of dielectric constant (ϵ'') with $w(\text{C60})$

Slika 6: a) Spreminjanje realnega dela dielektrične konstante (ϵ') z $w(\text{C60})$, b) spreminjanje navideznega dela dielektrične konstante (ϵ'') z $w(\text{C60})$

trode polarization effect. Hence, ionic conduction relaxation is not properly analysed in the dielectric formulism. Here, the modulus is calculated to overcome this problem and widely used to analyse the relaxation phenomenon for different compositions.

The values of M' and M'' were calculated using the following relations:

$$M' = \frac{\epsilon'}{\epsilon'^2 + \epsilon''^2} \quad \text{and} \quad M'' = \frac{\epsilon''}{\epsilon'^2 + \epsilon''^2}$$

where M' and M'' are the real and imaginary parts of the electrical modulus.

Figure 7 shows the modulus as a function of $\lg \omega$ for different $w(\text{C60})$. The peaks at a very high frequency are invariably present in all the complexes and the height of the peaks changes with the dispersoid (C60) concentration. This indicates that a relaxation phenomenon is occurring.^{17,18}

The M' shows a increasing trend with frequency whereas the peaks are observed in the M'' spectra in the higher frequency region. The peak in the modulus formulism confirms the ionic conduction in the system.^{19,20}

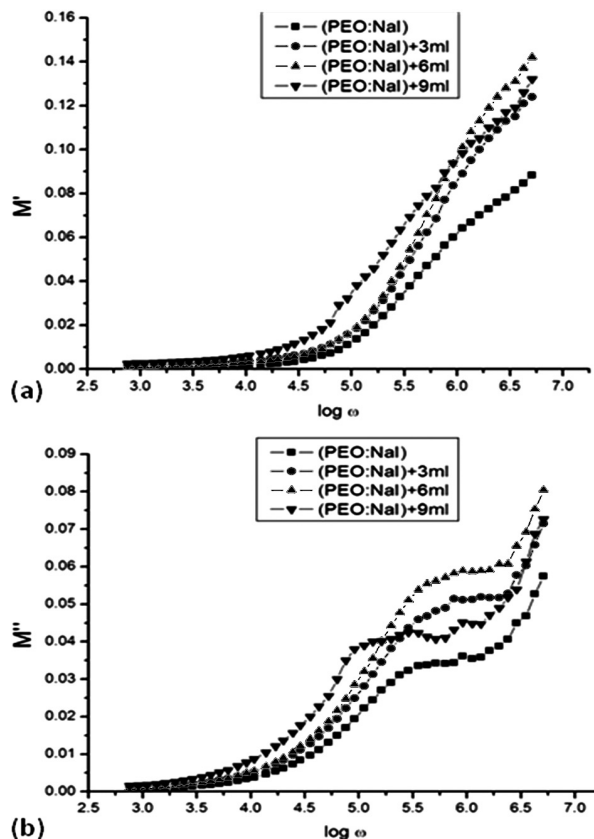


Figure 7: a) Variation in M' with $w(\text{C60})$, b) variation in M'' with $w(\text{C60})$

Slika 7: a) Spreminjanje M' z $w(\text{C60})$, b) spreminjanje M'' z $w(\text{C60})$

3.4.2 Transference Number (t_{ion})

This parameter will show the conductivity due to ions in polymer electrolyte films. The t_{ion} of the prepared films are calculated by dc polarization method. In this method, the dc current is observed as a function of time on the application of a fixed dc voltage (0.25 V) across the sample electrodes. The t_{ion} was calculated using the relation:

$$T_{ion} = \frac{I_{initial} - I_{final}}{I_{initial}}$$

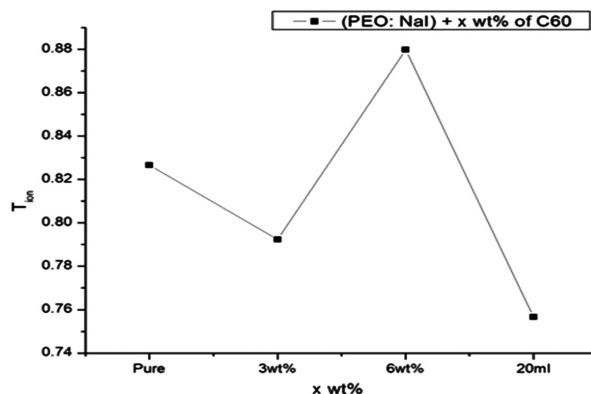


Figure 8: Variation in t_{ion} with $w(\text{C60})$

Slika 8: Spreminjanje transportnega števila z $w(\text{C60})$

Figure 8 shows a plot of σ vs different $w(\text{C60})$ doped with polymer electrolyte. In this plot it is clear that the ionic conductivity in the polymer electrolyte film initially decreases, but the 6 % dispersed film shows a high ionic conductivity. As the concentration of dispersed C60 is further increased the ionic conductivity of the film decreases. It may be concluded from the plot that the higher doping of C60 makes the polymer film more electronically conductive than ionically conductive.

3.4.3 Concentration and Mobility

The conductivity of polymer electrolytes depends upon the charge-carrier concentration (n), the charge on the carrier (e), and the number of charge carrier. Hence, when the charge concentration is changed by doping, the conductivity is also expected to change. In polymer-salt complexes, the charge-carrier concentration is not directly proportional to the doping concentration. To analyse the origin of the conductivity changes in the present system, the concentration factor (n) and the mobility factor (μ) were calculated with respect to the added $w(\text{C60})$. **Figure 9** shows these changes graphically.

The mobility variation data (**Figure 9a**) are approximately following the trend of the conductivity. This con-

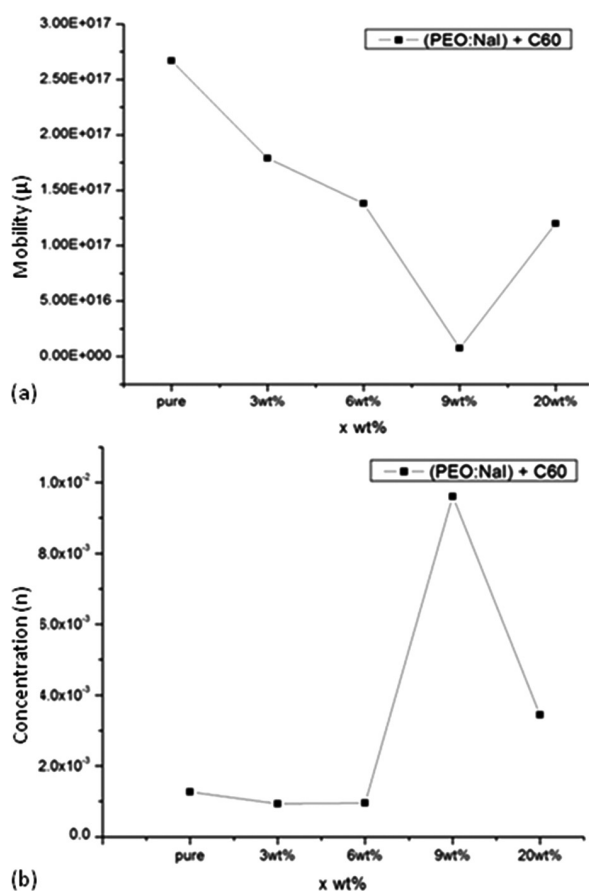


Figure 9: Variation of: a) mobility (μ) and b) concentration (n) of (PEO : NaI) + $w(\text{C60})$

Slika 9: Spreminjanje: a) mobilnosti (μ) in b) koncentracije (n) (PEO : NaI) + $w(\text{C60})$

firm that ion-pair formation and re-dissociation theory applicable to polymer-salt complexes¹⁰ are also applicable in the present system. The decrease in the mobility may be due to electrostatic hindrance in the movement and because of the increased weight of the charge carriers.^{21–23}

Figure 9b shows the variation in the concentration of the charge carrier on the doping of different $w(\text{C60})$. It initially attains a minimum (at 9 %) value, followed by a maximum (at 20 %). Many theories explaining this phenomenon can be found in literature. The change in the conductivity can be correlated with a change in the charge-carrier concentration (**Figures 4 and 9b**).

4 CONCLUSION

A fullerene-based polymer electrolyte was prepared by a standard solution cast technique. The ionic conductivity $\approx 7.95 \times 10^{-7}$ S/cm and the ionic transference number, ≥ 0.87 , indicate that the prepared film is mixed conductor. Parameters such as the charge-concentration factor (n) and the mobility factor (μ) were studied with respect to the fullerene concentration. The relationship between the charge concentration factor (n) and the mobility factor (μ) with respect to the fullerene $w(\text{C60})$ is established. At low frequency, the variation of the dielectric constant with frequency suggests an electrode interface polarization process. At a low frequency the high value of the dielectric constant and loss is due to electrode polarization.

Acknowledgement

This work was supported by the DST project (SR/S2/CMP-0065/2010) of the government of India. The Indian Institute of Goat Research Center, Farah, Mathura is also acknowledged for support with taking the LM images of the samples.

5 REFERENCES

- J. R. MacCallum, C. A. Vincent (eds.), *Polymer Electrolyte Reviews* 1-2, Elsevier, Science Publishers Ltd., New York 1989, 1991
- R. Saumya, K. Thakur Awalendra, R. N. P. Chaudhary, *Ionics*, 14 (2008), 255–262
- D. E. Fenton, J. M. Parker, P. V. Wright, *Polymer*, 14 (1973), 589
- H. Al-Ahmad, A. M. Zihlif, *Journal of Thermoplastic Composite Materials*, 26 (2013), 263–275
- T. J. Pinnavaia, G. W. Beall, *Polymer-Clay Nanocomposites*, John Wiley and Sons, New York 2001, chap. 2
- D. K. Pradhan, B. K. Samantaray, *Xpress polymer Letter*, 2 (2008), 630–638
- A. Chandra, P. K. Singh, S. Chandra, *Solid State Ionics*, 15 (2002), 154–155
- P. Kumar, P. K. Singh, B. Bhattacharya, *Ionics*, 17 (2011), 721–725
- C. Wang, Zhi-Xin Guo, Fu. Shoukuan, *Progress in Polymer Science*, 29 (2004), 1079–1141
- J. Suboco, A. Valozhyn, M. Zenker, *Rev. Adv. Mater. Sci.*, 14 (2007), 193–196

- ¹¹ W. Kratschmer, L. D. Lamb, D. R. Huffman, *Nature*, 347 (1990), 354–358
- ¹² P. K. Singh, B. Bhattacharya, R. K. Nagarale, *Journal of Applied Polymer Science*, 118 (2010) 5, 2976–2980
- ¹³ A. Saxena, P. K. Singh, B. Bhattacharya, *Mater. Tehnol.*, 47 (2013) 6, 799–802
- ¹⁴ K. Munindra, T. Tiwari, N. Shrivastava, *Carbohydrate Polymer*, 88 (2012), 54–60
- ¹⁵ R. Mishra, N. Baskaran, K. J. Rao, *Solid State Ionics*, 112 (1998), 261–273
- ¹⁶ S. Havriliak Jr., S. J. Havriliak, *Dielectric and Mechanical Relaxation in Materials: Analysis, Interpretation and Application to Polymers*, *Polymer International*, 45 (1998), 127–128
- ¹⁷ A. Ltaief, J. Davenas, P. Alcouffe, *Thin Solid Films*, 511–12 (2006), 498–505
- ¹⁸ T. Heiser, U. Giovanella, S. Ould-Saad, M. Pa, *Thin Solid Films*, (2006), 371–376
- ¹⁹ K. Tasaki, A. Venkatesan, P. Pugazhendhi, R. O. Loutfy, *Prepr. Pap. - Am. Chem. Soc., Div. Fuel Chem.*, 49 (2004) 2, 530–531
- ²⁰ S. Ramesh, A. K. Arof, *Material Science and Engineering B*, 85 (2001), 11–15
- ²¹ D. F. Vieira, C. O. Avellaneda, A. Pawlicka, *Electrochimica Acta*, 53 (2007), 1404–1408
- ²² P. K. Singh, B. Bhattacharya, *Optoelectronics and Advanced Materials- Rapid Communication*, 7 (2013), 157–160
- ²³ V. K. Singh, A. Annu, U. Singh, P. Singh, B. Bhattacharya, P. K. Singh, *Journal of Optoelectronics and Advanced Materials*, 15 (2013), 927–931

EFFECT OF TUNNELING DEFECTS ON THE JOINT STRENGTH EFFICIENCY OBTAINED WITH FSW

VPLIV TUNELSKIH NAPAK NA UČINKOVITOST TRDNOSTI SPOJA, IZDELANEGA Z DRSNO MEŠALNIM VARJENJEM

Sebastian Balos, Laposava Sidjanin

Faculty of Technical Sciences, Department of Production Engineering, Trg Dositeja Obradovica 6, 21000 Novi Sad, Serbia
sebab@uns.ac.rs

Prejem rokopisa – received: 2013-08-14; sprejem za objavo – accepted for publication: 2013-09-13

In this paper, an attempt was made to study the effects of various types of tunneling defects in friction stir welding (FSW). Two types of welding tool were used, one with a threaded and the other with a polygonal pin. To enable the formation of tunneling defects, the shoulder-to-pin-volume ratio was larger than 1 for both tools, while the ratio of rotation speed to welding speed was optimized as well. Tunneling defects were tested on EN-AW 5052 H32 and H38 alloys, having the thicknesses of 3 mm and 8 mm. It was found that the threaded tool produced a single or double triangular, as well as crack-shaped tunnel. The polygonal tool produced a multiple triangular tunnel (the material flows toward the weld face) with a complex shape or a crack-type tunnel with a complex shape. The most unfavorable tunnel obtained with the polygonal tool was the crack-shaped one, resulting in the 62 % and 46 % joint yield and ultimate tensile-strength efficiency. The corresponding values for the threaded tool were 40 % and 36 %. The hardness efficiencies did not follow the trends of the proof and ultimate tensile strengths due to the prevention of the tunneling during indentation. Another effect on the hardness is the presence of microcracks that may influence the apparent decrease in the hardness in spite of the detected grain-refinement effect in the nugget. These effects influence the hardness distribution in the weld, shifting the maximum hardness value into the thermo-mechanical zone.

Keywords: friction stir welding, aluminium alloy, tunneling defect, joint strength efficiency

Članek predstavlja študij vpliva različnih vrst tunelskih napak pri drsno mešalnem varjenju (FSW). Uporabljeni sta bili dve vrsti varilnega orodja, eno z navoji in drugo s poligonalnim nastavkom. Da bi preprečili nastanek tunelske napake, je bilo razmerje med nosilcem in nastavkom večje od 1 pri obeh orodjih, medtem ko je bila optimirana tudi rotacija glede na hitrost varjenja. Tunelska napaka je bila preizkušena po EN-AW 5052 na zlitinah H32 in H38, debelih 3 mm in 8 mm. Ugotovljeno je bilo, da orodje z navoji povzroči enojni, dvojni trikotni tunel, kot tudi tunel v obliki razpoke. Poligonalno orodje povzroči več kompleksnih tunelov s trikotnim prerezom (material steče proti čelu zvara) ali kompleksnih vrst tunelov v obliki razpok. Najbolj nezaželen tunel, dobljen s poligonalnim orodjem, je bil v obliki razpoke, kar je povzročilo 62-odstotni in 46-odstotni izkoristek spoja oziroma učinkovitost natezne trdnosti. Ustrezne vrednosti pri orodju z navoji so bile 40 % in 36 %. Učinkovitost trdote ni sledila tem usmeritvam in končni natezni trdnosti zaradi izogibanja tunelom med merjenjem trdote. Nadaljnji vpliv na trdoto imajo mikrorazpoke, ki lahko povzročijo navidezno zmanjšanje trdote, kljub odkritemu zmanjšanju zrn v jedru zvara. Ti pojavi vplivajo na razporeditev trdote v zvaru in potiskajo vrednosti največje trdote v termomehansko območje.

Ključne besede: drsno mešalno varjenje, aluminijeva zlitina, tunelska napaka, učinkovitost trdnosti spoja

1 INTRODUCTION

Friction stir welding (FSW) is a solid-state metal-joining process that uses the third body (a specialized tool) to join two or more workpieces.¹ FSW has attracted considerable interest due to a number of advantages over arc-welding processes.² It has been shown that FSW may be suitable for joining materials that are difficult to join using conventional welding techniques such as 7XXX and 2XXX aluminium alloys.³⁻⁷ Furthermore, Mg-alloys and dissimilar materials have been successfully welded with FSW.⁸⁻¹³

The microstructure and, therefore, the performance of the FSW welds strongly depend on the tool geometry as well as on the welding parameters such as the tool rotation and welding speeds. One of the main differences between the traditional arc-welding methods and FSW is the existence of the thermo-mechanically affected zone (TMAZ) near the heat-affected zone (HAZ) and the nugget.¹⁴ The nugget takes the central place in the joint

region. It is the most severely deformed region, often containing the equiaxed grains as the result of a dynamic recrystallization.¹⁴ As the result of its position and the fact that the tool directly influences it, the nugget, together with the region above and under the nugget, may represent the zone where defects can occur.¹⁵ One of the most critical types of the FSW defect is the tunneling. The tunneling defect occurs when the material flow around the tool pin is not adequate, resulting in an irregular weld filling.¹⁶⁻¹⁸ In accordance with the results presented by Radisavljevic et al.¹⁵, the ratio between the rotation and the welding speeds must be optimized. At the same time, an additional influencing factor might be the ratio between the pin volume and the reservoir in the tool shoulder (a concave shoulder volume) that should not exceed one in order to enable the material to pile up as a result of a pin indentation. In this work, an attempt was made to study the influence of the tunneling-defect shape and size on the mechanical properties of FSW joints, using two types of aluminium alloy.

2 EXPERIMENTAL PROCEDURE

Al-Mg plates in the half-hard condition (EN-AW 5052-H32) with a thickness of 3 mm and in the full-hard condition (EN-AW 5052-H38) with a thickness of 8 mm were used in this study. The chemical compositions of the plates, determined with an optical emission spectrometer ARL 3580, are given in **Table 1**. The mechanical properties of the workpiece materials, determined with a ZDM 5/91 tensile testing machine, are given in **Table 2**. The tensile properties were determined as the average of three specimens. The sample dimensions were 300 mm × 65 mm, forming a welded sample of 300 mm × 130 mm. The samples were tightly placed in a steel fixture with a backing plate into a 130 mm wide groove and secured with clamps (**Figure 1**). The fixture was fitted on an adapted Prvomajska UHG universal milling machine



Figure 1: Test setup
Slika 1: Preizkusni sestav

Table 1: Chemical composition of EN-AW 5052 aluminium alloys (mass fractions, w%)

Tabela 1: Kemijska sestava aluminijeve zlitine EN-AW 5052 (masni deleži, w%)

	Cu	Mn	Mg	Si	Fe	Zn	Ti	Al
EN-AW 5052-H32	0.04	0.11	2.46	0.19	0.73	0.061	0.010	balance
EN-AW 5052-H38	0.03	0.29	2.33	0.19	0.29	0.011	0.022	balance

Table 2: Mechanical properties of EN-AW 5052-H32 and H38

Tabela 2: Mehanske lastnosti EN-AW 5052-H32 in H38

	Proof strength $R_{p0.2}$ %/MPa	Ultimate tensile strength R_m /MPa	Elongation %	Vickers hardness Number HV5
EN-AW 5052-H32	157 ± 3	214 ± 2	19 ± 1	67 ± 1
EN-AW 5052-H38	204 ± 7	245 ± 3	12 ± 1	90 ± 2

Table 3: Chemical composition of the X38CrMoV5-1 tool steel (w%)

Tabela 3: Kemijska sestava orodnega jekla X38CrMoV5-1 (w%)

C	Si	Mn	P	S	Cr	Mo	V	Fe
0.37	1.01	0.38	0.017	0.0005	4.85	1.23	0.32	balance

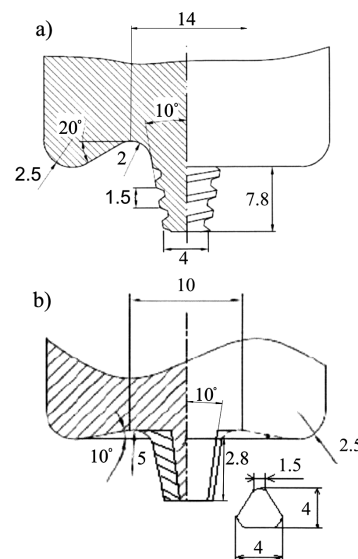


Figure 2: a) Threaded and b) polygonal tools
Slika 2: Orodje: a) z navoji, b) poligonalno orodje

Table 4: FSW parameters

Tabela 4: Parametri FSW

Sample	Rotation speed r/min	Welding speed mm/min	Rotation to welding speed r/mm	Tool rotation direction	Material flow direction
EN-AW 5052-H32; thickness 3 mm; polygonal-type tool					
1	1230	17	72.35	right	–
2	1230	12	102.50	right	–
3	1230	23	53.48	right	–
4	925	68	13.60	right	–
5	925	91	10.16	right	–
EN-AW 5052-H32; thickness 8 mm; threaded-type tool					
6	645	5	129.00	left	Up
7	645	5	129.00	right	Down
8	645	12	53.75	right	Down
9	645	49	13.16	right	Down

with a power of 5.2 kW. In this study, two different types of tool were used: plates 3 mm were welded with a polygonal-type tool, while plates 8 mm were welded with a threaded-type tool (**Figure 2**). Both tools were made of X38CrMoV5-1 (H11) hot-work tool steel, having a chemical composition as shown in **Table 3**. The chemical composition of the FSW tool material was measured with an optical emission spectrometer ARL 2460. The FSW tools were used in a heat-treated condition to 53 HRC. The tool concave-shoulder volume (reservoir) is larger than the pin volume in both tools used, stimulating the formation of a tunneling defect. For the polygonal-type tool, the shoulder-to-pin-volume ratio was 5.3 and for the threaded type it was 1.1, both being more than sufficient to store the piled up material as a result of the tool-pin indentation. Furthermore, the welding parameters were set to enable the formation of various types of the tunneling defect (**Table 4**). These parameters were set according to the results presented by Radisavljevic et

al.¹⁵, where the welding speeds were in the range of 6.45–8.22 r/mm and the tool rotation direction was able to prevent the tunneling defect.

The mechanical properties of the FSW workpieces were determined with the tensile, root-bending and hardness tests as well as with a metallographic examination. The tensile and bending tests were carried out with a WPM ZDM 5/91 mechanical testing machine, according to EN 895 and EN 910 standards, respectively. The hardness was determined with a VEB HPO-250 Vickers testing machine, with a load 5 kg. The hardness measurements were done on the workpiece material (an average of five indentations) before and after the welding, to obtain the hardness profiles for the 1.5 mm distance between the indentations. The metallographic examinations were done with a light microscope Leitz Orthoplan, after a standard metallographic preparation. The metallographic preparation consisted of grinding (sandpaper, the grit of 220 to 2000), polishing (a diamond paste with (6, 3, 1 and ¼) µm particle sizes) and etching with Keller's reagent (2 mL HF, 3 mL HCl, 5 mL HNO₃, 190 mL H₂O).

3 RESULTS

3.1 Tensile properties

The tensile properties of FSW samples are presented in **Figure 3**. In Samples 1–5, it can be seen that the highest joint efficiencies are obtained with the higher tool rotation speed. Within this rotation speed, the highest joint proof-strength (PS) efficiency was obtained with a high end-welding speed, while the highest joint ultimate-tensile-strength (UTS) efficiency was obtained with the lowest welding speed. The lowest efficiencies were obtained with the lower tool rotation speed and the higher welding speed. A similar result was obtained with the EN-AW 5052-H38 alloy with a thickness of 8 mm, welded with a conceptually different tool, see Samples 6–9.

3.2 Root-bending test

In **Figure 4**, the root-bending-test results are shown. It can be seen that the highest angle of the first crack was

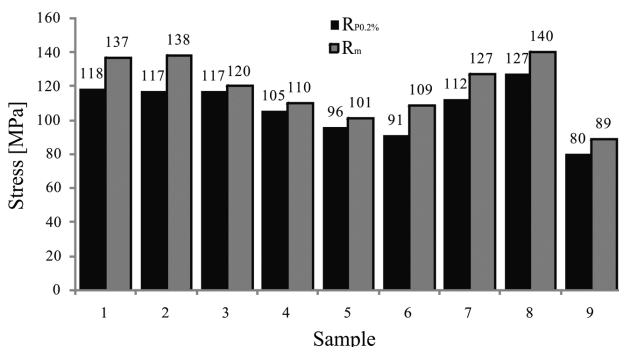


Figure 3: Joint proof and the ultimate tensile strengths of the tested samples

Slika 3: Preizkus spoja in končna natezna trdnost vzorcev

obtained on Sample 1 (a base-material thickness 3 mm), while the lowest angle was obtained on Sample 6 (an base-material thickness 8 mm). On samples 1–8, the fracture did not occur up to 180°, while on Sample 9, the fracture occurred at 134°.

3.3 Hardness results

The Vickers-hardness (HV5) profiles of the representative samples are shown in **Figure 5**. In **Figures 5a** and **5b**, the hardness profiles for Samples 1 and 2 are shown, depicting the highest and the lowest tensile properties of the welded plates 3 mm. On the other hand, in **Figures 5c** and **5d**, the hardness profiles for Samples 8 and 9 are shown, depicting the highest and the lowest tensile pro-

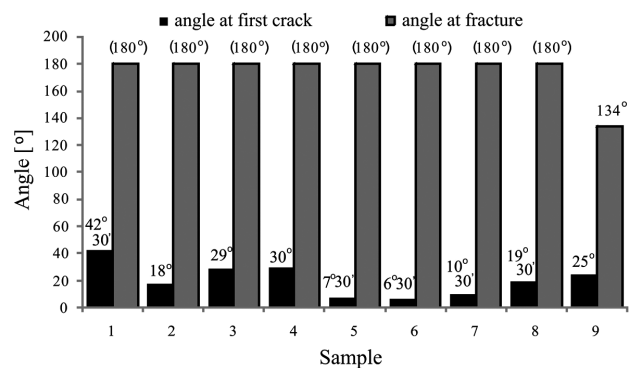


Figure 4: Results of the bending test. The values in parentheses represent the samples where no fracture occurred.

Slika 4: Rezultati upogibnega preizkusa. Vrednosti v oklepajih so za vzorce, kjer ni prišlo do zloma.

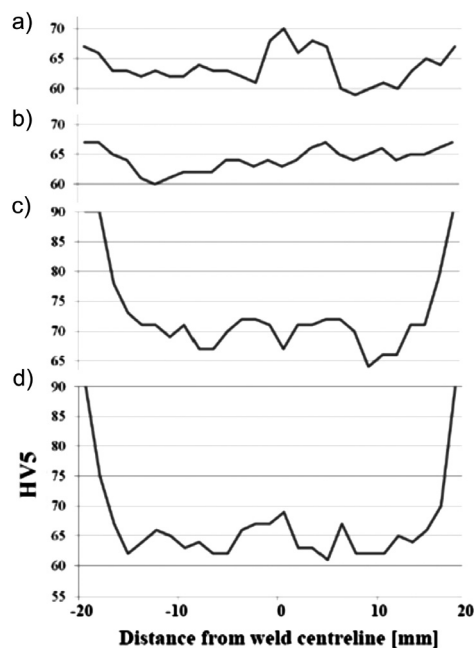


Figure 5: HV5 hardness profiles in relation to the distance from the centerline: a) sample 1, b) sample 5, c) sample 8, d) sample 9

Slika 5: Profil trdote HV5 v odvisnosti od razdalje od središča: a) vzorec 1, b) vzorec 5, c) vzorec 8, d) vzorec 9

erties of the welded plates 8 mm. In **Figures 5a, 5c and 5d** (Samples 1, 8 and 9) a common FSW hardness profile may be observed, while for Sample 5 (**Figure 5b**), an irregular profile was obtained. For Sample 1, the maximum hardness in the nugget (the weld centerline) is higher than that of the base material. For the other samples, all the hardnesses of the weld, in the thermo-mechanical zone and the heat-affected zone, are lower than that of the base material, indicating an insufficient grain refinement in certain FSW zones.

3.4 Macro and microstructure

The weld cross-sections of the specimens are shown in **Figure 6**, more exactly, in **Figures 6a to 6e**, the weld cross-sections presented were obtained with the polygonal tool, while the ones from the second column, **Figures 6f to 6i**, were obtained with the threaded tool. From these results it can be seen that with the polygonal tool, two types of the tunneling defect were achieved: a triangular (a closed tunneling defect) and a crack-shaped defect (an open tunneling defect). Tunnels might occur in a single (**Figure 6b**, Sample 2), double (**Figures 6a**

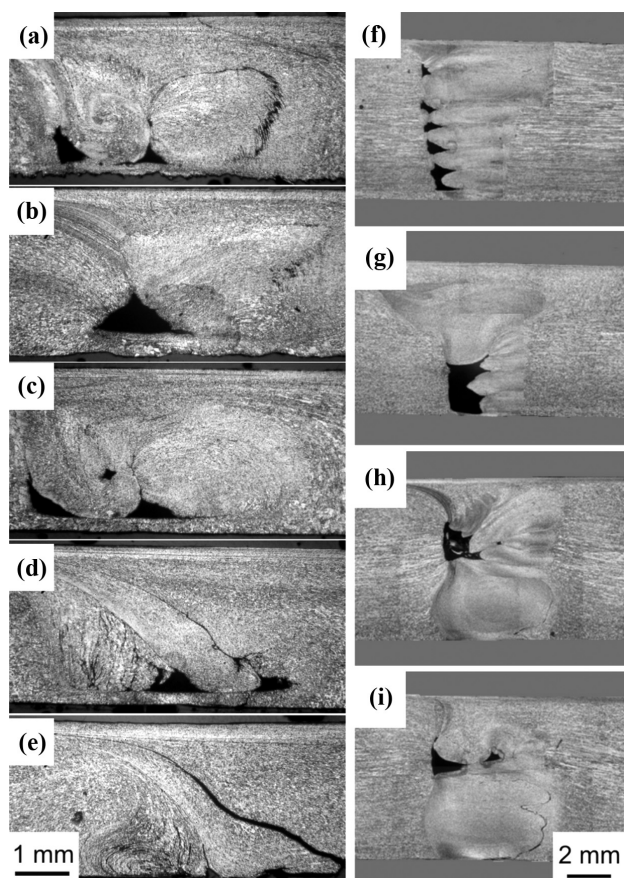


Figure 6: Weld cross-sections showing the tunnel profiles: a) sample 1, b) sample 2, c) sample 3, d) sample 4, e) sample 5, f) sample 6, g) sample 7, h) sample 8, i) sample 9

Slika 6: Prerezi zvara, ki prikazujejo profil tunela: a) vzorec 1, b) vzorec 2, c) vzorec 3, d) vzorec 4, e) vzorec 5, f) vzorec 6, g) vzorec 7, h) vzorec 8, i) vzorec 9

and **6d**, Samples 1 and 4) or even triple configuration (**Figure 6c**, Sample 3). The crack-type tunneling defect obtained consisted of one longer and three smaller cracks (**Figure 6e**, Sample 5).

On the other hand, when the threaded-type tool was used, the tunneling defects with a more complex shape were obtained. The threaded-type tool with the material flow direction towards the tool (up) creates multiple tunnels, closely following the tool pin geometry. Such tunneling defects are spread across the whole weld cross-section. The material flow towards the weld root results in a complex-shaped tunneling defect in the weld center or at the bottom (**Figure 6f to 6i**). Furthermore, a combination of the complex-shaped tunneling defect and the crack-shaped tunneling defect occurred on Sample 9 (**Figure 6i**).

The microstructures of the representative welded samples are shown in **Figure 7**. In **Figures 7a to 7c**, the Sample 5 FSW zones are presented, while in **Figures 7d to 7f**, the Sample 9 FSW zones are shown. It can be seen that the base-material microstructures, EN-AW 5052-H32 and H38 shown in **Figures 7a and 7d**, correspond to the typical cold-rolled alloy, with a clearly visible deformed grain structure in the rolling direction. On the other hand, the heat-affected zones (HAZs) (**Figures 7b and 7e**, both on the left of the micrograph) show coarsened recrystallized structures. In the thermo-mecha-

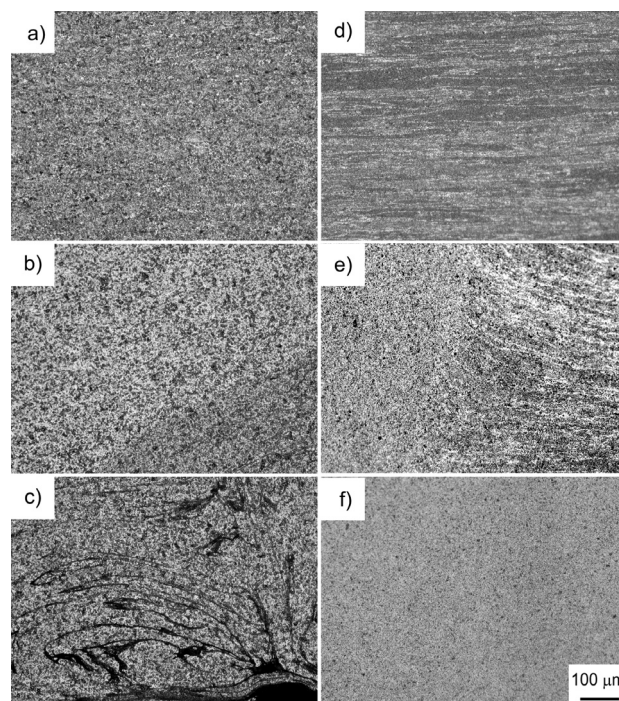


Figure 7: Microstructures of samples 5 and 9: a) sample 5: base material, b) sample 5: HAZ/TMAZ zone, c) sample 5: nugget, d) sample 9: base material, e) sample 9: HAZ/TMAZ zone, f) sample 9: nugget

Slika 7: Mikrostruktura vzorcev 5 in 9: a) vzorec 5: osnovni material, b) vzorec 5: področje HAZ/TMAZ, c) vzorec 5: jedro, d) vzorec 9: osnovni material, e) vzorec 9: področje HAZ/TMAZ, f) vzorec 9: jedro

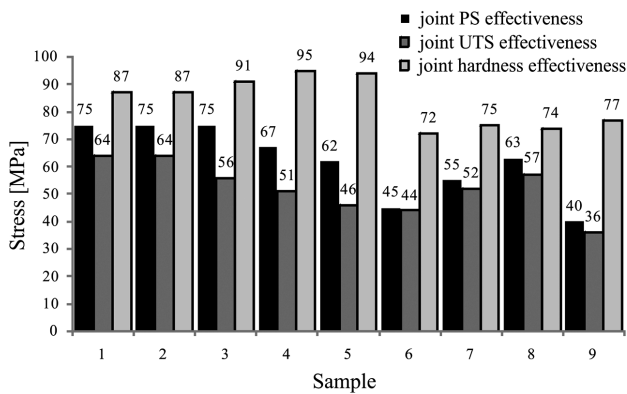


Figure 8: Joint PS, UTS and hardness effectiveness

Slika 8: Učinkovitost spoja PS, UTS natezne trdnosti in trdote

nical zones (TMAZs), shown in **Figures 7b** and **7e** (both to the right of the micrograph), finer microstructures are formed as a result of the local deformation. The main difference between **Figures 7c** and **7f**, where the nugget is depicted, is the occurrence of an intensive cracking, seen on Sample 5. In the Sample 9 nugget (**Figure 7f**), the microstructure is finer than that of the base material, HAZ and TMAZ.

4 DISCUSSION

4.1 Joint effectiveness to microstructure correlation

Joint PS, UTS and hardness effectiveness are given in **Figure 8**. According to the joint effectiveness shown in **Figure 8**, it can be seen that the joint UTS effectiveness is the lowest, followed by the joint PS effectiveness. The joint UTS effectiveness is lower than the values obtained by Radisavljevic et al. (by up to 80.1 %) ¹⁵, which is the result of the tunneling-type defect, as depicted in **Figure 4**. On the other hand, the joint hardness effectiveness matches the values obtained by Radisavljevic et al. ¹⁵ This is the result of the measuring method, according to which the indentations were made in the tunnel-free region of the weld, as well as the method of calculation. Namely, the maximum hardness was taken into account. However, although there is a correlation between the proof strength and the ultimate tensile strength, these two parameters cannot be correlated to the hardness effectiveness. Nevertheless, the hardness distributions may be correlated to the microstructures obtained, **Figures 6** and **7**, especially for the representative Samples 5 and 9. In Sample 5, the hardnesses of the nugget, TMAZ and HAZ are all similar, which is in contrast to the hardness values for Sample 9. There the nugget has a higher hardness than in the case of TMAZ and HAZ. As shown in **Figure 7**, the Sample 5 nugget contains a number of cracks that might have influenced the values that are similar to the ones for TMAZ and HAZ. On the other hand, in Sample 9, a crack-free nugget was obtained and, consecutively, higher hardnesses were measured than

those for TMAZ and HAZ. Such a hardness distribution is the result of the grain refinement in the nugget. The nugget-hardness values are lower compared to the base material, which might be influenced by two factors: the grain refinement and the recrystallization.

4.2 Influence of the tunnel shape

The mechanical properties of the joints and their efficiencies clearly vary in accordance with the type of the FSW tool geometry. The two types of the FSW tool have different influences on the joint properties. It can be seen that the polygonal tool (Samples 1–5) produces joints with higher mechanical properties than the threaded tool (Samples 6–9) in spite of the higher shoulder-to-pin-volume ratio of 5.3 versus 1.1. The higher mechanical properties are influenced by the tunnel obtained. Namely, the polygonal tool produces triangular-shaped tunnels or crack-shaped tunnels that are the least optimal. The most optimum sample obtained with the polygonal-type tool is Sample 1 with a double tunnel, while the lowest mechanical properties were found for Sample 5 with a crack-shaped tunnel. Regarding the threaded-tool samples, the mechanical properties of Sample 8 are the highest, while the lowest mechanical properties were found for Sample 9. On Sample 9, a combination of a tunnel and a crack-shaped tunnel was found, which proved to have a more adverse effect on the mechanical properties compared to Sample 6, where multiple tunnels were found, closely following the tool-pin profile. The relatively high welding speeds applied in this study clearly did not contribute to the joint quality, regardless of the tool type.

5 CONCLUSIONS

According to the presented results, the following conclusions can be drawn:

- The UTS efficiency of the joints with the tunneling defect was lower by 25–82 % than that of the joints without the tunneling defect.
- The efficiency of the joint PS is higher than that of the ultimate tensile strength, while the hardness efficiency is higher than the joint PS efficiency.
- The tunnel profile is influenced by the pin geometry and pin direction determining the material flow direction.
- The polygonal-type tool produces a triangular tunnel shape, in single and multiple forms, as well as a crack-type tunneling defect.
- The threaded-type tool produces a triangular and complex-shaped tunnel, depending on the material flow direction. If the material flows towards the weld root a complex-shaped tunnel is formed with superior mechanical properties. The only exception is the combination of a complex-shaped and crack-type tunnel. In the case of an upward material flow,

multiple triangular tunneling defects are formed that are very unfavorable with respect to mechanical properties.

- The lowest mechanical properties both in terms of the tensile strength and bending were obtained with the tunneling defects associated with cracks.
- The highest joint efficiency was obtained with the polygonal-pin profile.
- The pin-to-concave-shoulder-volume ratio greatly influences the occurrence of the tunneling defect.

Acknowledgements

The authors are grateful to Mr. Michael A. Maier for his technical assistance.

6 REFERENCES

- ¹W. M. Thomas, E. D. Nicholas, J. C. Needham, M. G. Murch, P. Templesmith, C. J. Dawes, International Patent Application No. PCT/GB92/02203, GB Patent Application No. 9125978.8 (Dec. 1991) and U.S. patent No. 5, 460, 317, (Oct. 1995)
- ²H. Khodaverdizadeh, A. Mahmoudi, A. Heidarzadeh, E. Nazari, *Materials and design*, 35 (2012), 330
- ³G. İpekoglu, B. G. Kiral, S. Erim, G. Çam, *Mater. Tehnol.*, 46 (2012) 6, 627–632
- ⁴L. Fratini, G. Buqa, D. Palmeri, J. Hua, R. Shivpuri, *Science and Technology of Welding and Joining*, 11 (2006), 412
- ⁵R. S. Mishra, Z. Y. Ma, *Materials science and engineering A*, 50 (2005) 1/2, 1
- ⁶P. L. Threadgill, A. J. Leonard, H. R. Shercliff, P. J. Withers, *International materials review*, 54 (2009) 2, 49
- ⁷L. Magnusson, L. Kallman, Mechanical Properties of Friction Stir Welds in Thin Sheet of Aluminium 2024, 6013 and 7475, Proc. of the 2nd International Symposium on Friction Stir Welding, Gothenburg, Sweden, 2000, 26–28
- ⁸N. Afrin, D. L. Chen, X. Cao, M. Jahazi, *Materials science and engineering A*, 472 (2008), 179
- ⁹G. M. Xie, Z. Y. Ma, L. Geng, *Materials science and engineering A*, 486 (2008), 49
- ¹⁰S. M. Chowdhury, D. L. Chen, S. D. Bhole, X. Cao, *Materials science and engineering A*, 527 (2010), 6064
- ¹¹T. Debroy, H. K. D. H. Bhadeshia, *Science and Technology of Welding & Joining*, 15 (2010) 4, 266
- ¹²O. Frigaard, A Process Model for FSW of Age Hardening Aluminium Alloys, Ph.D. Thesis, Norwegian University of Science and Technology, 1999
- ¹³J. Quyang, R. Kovacevic, *Journal of Materials Engineering and Performance*, 11 (2002), 51
- ¹⁴K. V. Jata, S. L. Semiatin, Continuous Dynamic Recrystallization During FSW of High Strength Aluminium Alloys, *Scripta Materialia*, 43 (2000), 743
- ¹⁵I. Radisavljevic, A. Zivkovic, N. Radovic, Avoidance of tunnel type defects in FSW welded Al 5052-H32 plates, *Welding & Welded Structures*, 1 (2012) 1, 5–11
- ¹⁶R. Nandan, T. Debroy, H. Bhadeshia, Recent Advances in Friction Stir Welding: Process, Weldment structure and Properties, *Progress in Materials Science*, 53 (2008), 980
- ¹⁷H. Bhadeshia, Joining of Commercial Aluminium Alloys, Proc. of the International Conference on Aluminium, Bangalore, India, 2003, 195–204
- ¹⁸K. Kumar, S. V. Kailas, The Role of Friction Stir Welding Tool on Material Flow and Weld Formation, *Material Science and Engineering*, 485 (2008), 367

THE INFLUENCE OF LAMINATION AND CONDUCTIVE PRINTING INKS ON SMART-CARD OPERABILITY

VPLIV LAMINACIJE IN PREVODNIH TISKARSKIH BARV NA DELOVANJE PAMETNIH KARTIC

**Miloje Đokić¹, Vasa Radonić², Vladan Mladenović³, Anton Pleteršek⁴,
Urška Kavčič⁵, Aleš Hladnik¹, Vesna Crnojević-Bengin², Tadeja Muck¹**

¹Faculty of Natural Sciences and Engineering, University of Ljubljana, Snežniška 5, 1000 Ljubljana, Slovenia

²Faculty of Technical Sciences, University of Novi Sad, Trg Dositeja Obradovića 6, 21000 Novi Sad, Serbia

³Cetis, d. d., Čopova ulica 24, 3000 Celje, Slovenia

⁴ams R&D, d. o. o., Tehnološki park 21, 1000 Ljubljana, Slovenia

⁵Valkarton Rakek, d. o. o., Partizanska cesta 7, 1381 Rakek, Slovenia
miloje.djokic@gmail.com

Prejem rokopisa – received: 2013-08-15; sprejem za objavo – accepted for publication: 2013-10-24

In this paper a novel design of UHF RFID antennas for smart cards is proposed. Smart cards usually include HF RFID antennas produced by means of hot foil stamping or etching – a subtractive process. Making HF antennas using printing – an additive process – is difficult, because it necessitates the printing of three layers: that of conductive lines (a coil), followed by a dielectric layer and once again a conductive layer. On the other hand, the printing of UHF antenna requires only the single-layer printing of conductive lines, i.e., antenna, thus enabling a more rational printing.

After designing, simulating and testing a folded UHF dipole antenna for RFID applications, the impact of three different conductive printing inks, reading distance and card deformation on the backscattered signal power was studied. A three-way analysis of variance (ANOVA) was implemented to aid in the interpretation of the measurement results obtained on both non-laminated and laminated cards. It was demonstrated that smart cards with screen-printed UHF antennas can be fabricated using the proposed design optimization, so achieving good card readability.

Keywords: smart cards, printed antenna, antenna design, lamination, conductive printing inks, UHF RFID, analysis of variance

V članku je predlagana nova izvedba UHF RFID-anten za pametne kartice. Pametne kartice navadno vključujejo HF RFID-antene, izdelane na podlagi vročega tiska s folijo ali z jedkanjem (subtraktivni proces). Izdelava HF-anten v tisku (aditivni proces) je težavna, saj mora biti tisk izveden v treh plasteh – tisk prevodnih linij (tuljava), dielektrične plasti in nato ponovno prevodne plasti. Po drugi strani pa je želen enoplastni tisk prevodnih linij UHF-antene, kar omogoča racionalnejši tisk.

Po načrtovanju, simulaciji in preizkušanju dipolne UHF-antene za RFID-aplikacije je bil preučevan vpliv treh prevodnih tiskarskih barv, razdalje odčitavanja in deformacije kartic na moč povratnega signala. Pri razlagi dobljenih rezultatov meritev nelaminiranih in laminiranih kartic je bila uporabljena trosmerna analiza variance (ANOVA). Izkazalo se je, da je mogoče izdelati pametne kartice s tehniko sitotiska z opisano optimizacijo izvedbe UHF-antene, kar omogoča dobro čitljivost kartic.

Ključne besede: pametne kartice, tiskana antena, izvedba antene, laminacija, prevodne tiskarske barve, UHF RFID, analiza variance

1 INTRODUCTION

Printed flexible electronics is becoming more viable with recent technological developments, opening up possibilities to integrate radio frequency (RF) functions into clothing or moving objects to monitor various parameters of interest. Printed electronics that combine electronic components with different printing technologies allows the production of miniature low-cost electronic systems.

The first connection between printing technology and conventional electronics appeared in the 1980s when Teng and Vest made metal conductors for solar cells using inkjet printing.¹ This opened up the possibility to produce various electronic components using different printing techniques. Generally, two printing techniques are the most common, i.e., screen printing²⁻⁸ and inkjet printing,⁹⁻¹² but others such as flexography,¹³ gravure printing¹⁴ and pad printing¹⁵ are also used. Conventional printing techniques, such as screen printing or gravure

printing, are characterized by high production speed, high resolution and the possibility of using a number of different conductive inks, so these techniques are suitable for the mass production of precise electronics.¹¹ Printed electronics has many advantages, including a simple production process, the reduced consumption of raw materials and high productivity (especially in roll-to-roll processes). One of the major applications of printed electronics is radio-frequency identification (RFID). RFID is an automatic identification technology that uses a wireless non-contact radio frequency to transfer data for the purposes of automatically identifying and tracking the tags attached to objects. RFID systems are widely used in various real-life applications, such as access control or smart-card systems, public transport and logistics.¹⁶⁻¹⁸ RFID systems consist of at least of a reader, which receives the feedback signals sent back from the tags, and the tags themselves. The simplest, passive tags consist of an antenna and an integrated

circuit (IC). An integrated controller and a memory in the IC chip enable the activity of the tag and contain electronically stored information. The second part of the tag is the antenna that receives and transmits the radio signals.

Since the mechanical and electrical characteristics of antennas depend on the materials used, several experimental studies have recently been carried out to investigate the effects of conductive pastes,³ to compare different printed materials¹⁹ and to look at the influence of substrate folding.¹² The effects of different materials used in the production of UHF RFID antennas on their performance have been analysed.¹⁹ It has been shown that the conductive material used to print the antenna has a significant influence on the antenna's return loss. A similar study has confirmed that a conductive silver-based paste outperformed all the other types of conductive pastes and provided a performance similar to that of its copper equivalent.³

This paper presents a novel design for UHF RFID smart cards, realized using the basic functionality offered by printing technology. The impacts of different conductive inks that are used to print the UHF antenna are investigated. In addition, the influence of the lamination process and card deformation on the performance of the cards is investigated in detail.

2 THEORETICAL

The reading range in the free space of an RFID system operating at wavelength λ depends on the reader power density (P_{TX}^{rdr}), the antenna gain (G_{rdr}) and the tag antenna gain (G_{tag}). The power received by the tag (P_{RX}^{tag}) at distance r from the reader is estimated using the Friis equation:²⁰

$$P_{RX}^{tag} = P_{TX}^{rdr} G_{rdr} G_{tag} \left(\frac{\lambda}{4\pi r} \right)^2 \quad (1)$$

The transmitted signal power is denoted by TX , while the received signal is denoted by RX . We can define the gain of the tag antenna G_{tag} and the backscatter transmission loss T_b using the relationships from the Friis equation, as expressed in equations Eq. 2 to 4:

$$P_{TX}^{tag} = P_{TX}^{rdr} G_{rdr} G_{tag} \left(\frac{\lambda}{4\pi r} \right)^2 T_b \quad (2)$$

$$P_{RX}^{rdr} = P_{TX}^{tag} G_{tag} G_{rdr} \left(\frac{\lambda}{4\pi r} \right)^2 \quad (3)$$

$$P_{RX}^{rdr} = P_{TX}^{rdr} T_b G_{rdr}^2 G_{tag}^2 \left(\frac{\lambda}{4\pi r} \right)^4 \quad (4)$$

The backscattered modulated signal received by the reader is therefore proportional to r^{-4} . Nevertheless, the communication between the passive tag and the reader is forward link limited, since the power to power on the IC (P_{min}^{tag}) is by at least 6 orders of magnitude higher than the

minimum power (P_{min}^{rdr}) required to demodulate the backscattered signal. The forward limited range in free space ($R_{forward}$) follows from Eq. 5:

$$R_{forward} = \left(\frac{\lambda}{4\pi} \right) \sqrt{\frac{P_{TX}^{rdr} G_{rdr} G_{tag}}{P_{min}^{tag}}} \quad (5)$$

A simple estimation for a reader with the power $P_{TX} = 500$ mW, a tag in the form of a $\lambda/2$ dipole, with gain $G_{tag} = 2.2$ dBi and minimum power needed to turn on the IC $P_{min}^{tag} = 100$ μ W, gives a forward range of 2.4 m in free space. Until this point, a perfect matching between the antenna and load (IC) has been assumed with the power-transfer coefficient $\tau = 1$. Generally speaking, the power-transfer coefficient is defined by Eq. 6:

$$\tau = \frac{4R_{chip} R_{ant}}{|Z_{chip} + Z_{ant}|^2} \quad (6)$$

where the impedance of the chip (Z_{chip}) and the antenna (Z_{ant}) is the sum of the resistance and the reactance. The transfer coefficient is a maximum when the reactance of the chip and antenna cancel each other. In this case, referred to as conjugate matching, the transfer coefficient is equal to 1. In all other cases, the transfer coefficient is lower.

The effective gain (G_{eff}) of the tag antenna (the ability to increase the power or amplitude of the signal) can be defined as follows⁶:

$$\tau G_{eff} = D\eta\tau \quad (7)$$

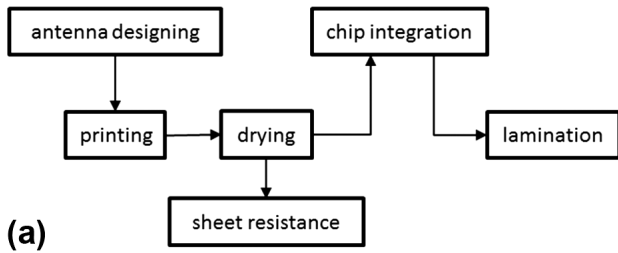
where D is the directivity of the antenna, η is the antenna efficiency and τ is the power transfer efficiency.

3 EXPERIMENTS

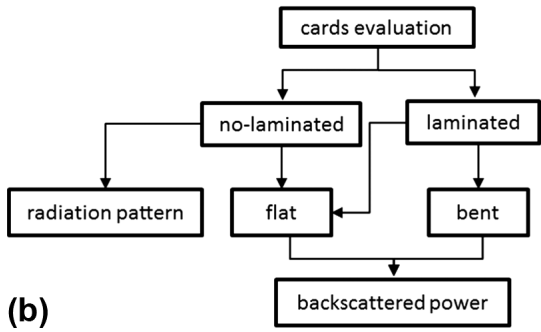
The block diagram of the smart-card fabrication process is shown in **Figure 1a**. First, the UHF antenna was designed using the EM simulator CST Microwave Studio and then printed and dried. In the next step, the chips were assembled and the lamination performed to fabricate a final smart card. The fabricated cards were experimentally tested following the process shown in **Figure 1b**. The characteristics of the flat non-laminated antenna were measured in an anechoic chamber, while the backscattering characteristics of the smart cards were evaluated in a real environment using an ams-R902 reader. Furthermore, the effect that bending has on the initial planar topology in the case of the laminated cards was also investigated. Multifactorial analysis of variance (ANOVA) was implemented to aid in the interpretation of the measurement results obtained for both non-laminated and laminated cards.

3.1 Antenna design and simulation

The novel design configuration of the proposed folded dipole antenna is shown in **Figure 2**. The antenna



(a)



(b)

Figure 1: a) Block diagrams of smart-card fabrication, b) testing and measurement process

Slika 1: a) Blokovna diagrama izdelave pametnih kartic, b) procesa preizkušanja in merjenja

is designed to operate according to the UHF standard with a central operating frequency of 868 MHz. In addition, the dipole is folded in order to fit the standard credit-card size, with a negligible reduction in antenna efficiency. The antenna was designed for a thick polycarbonate film 120 μm (grammage: 120 g/m^2 ; surface roughness, ISO 4288: 2.3 μm) with a relative permittivity of $\epsilon_r = 3.2$ and a dissipation factor 0.0019. All the simulations were performed using CST Microwave Studio. For the conductive material, 16 μm silver was used and the conductor losses were modelled using the bulk conductivity for silver.

As the number and thickness of the dielectric layers during lamination affects the characteristics of the antennas, initially the antenna dimensions were determined for

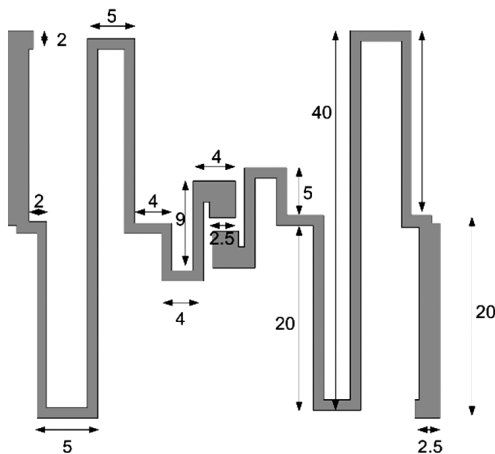


Figure 2: Proposed folded dipole antenna (mm)

Slika 2: Nova izvedba dipolne antene (mm)

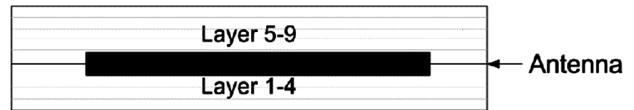


Figure 3: Cross section of the laminated card with antenna placed inside

Slika 3: Prečni prerez laminirane kartice z vključeno anteno v vmesni plasti

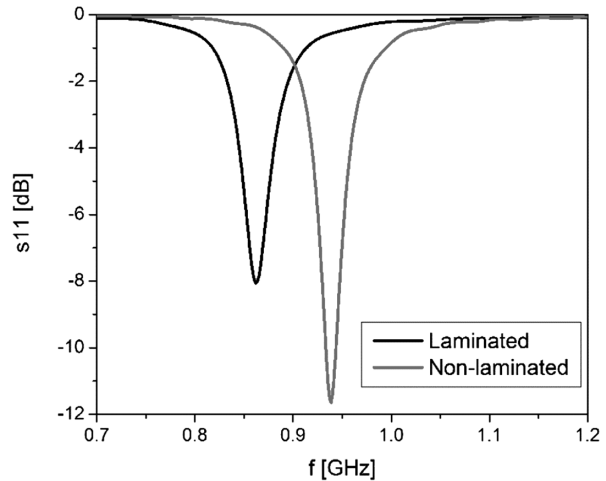


Figure 4: Simulated return losses of the laminated and non-laminated antennas

Slika 4: Simulacija izgube povratnega signala laminirane in nelaminirane antene

the laminated case. Nine dielectric layers were used in the simulation, with the antenna placed between the fourth and fifth layers (Figure 3).

The dimensions of the antenna are carefully optimized in order to obtain the central frequency of 868 MHz. The final antenna dimensions are shown in Figure 2, with all the marked dimensions in mm. The total antenna size is only 37 mm \times 41 mm. Figure 4 compares the simulated return loss of the laminated and non-laminated antennas. It is clear that the lamination process significantly influences the resonant frequency of the antenna,

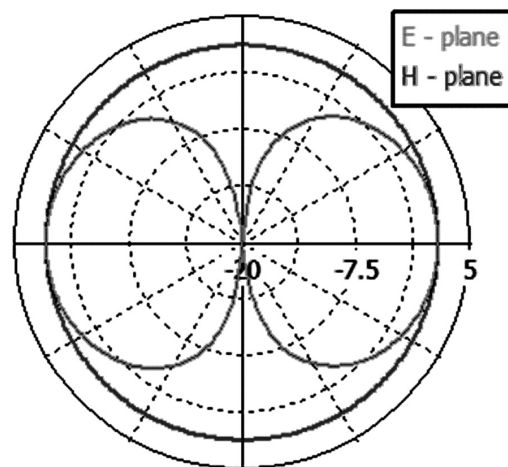


Figure 5: Simulated radiation pattern of the laminated antenna

Slika 5: Simulacija sevalnega diagrama laminirane antene

due to changes in the effective dielectric constant of the substrate.

The simulated radiation patterns of the proposed laminated dipole antenna in the E - and H -planes are shown in **Figure 5**. The total antenna gain is above 1.9 dBi.

3.2 Printing and drying

Antenna samples were printed using the Siasprint Novaprint-P screen printer with a monofilament polyester plain weave mesh with 120 l/cm and a theoretical ink volume of 16.3 cm³/m². For printing, three different silver conductive printing inks were used:

- SC-CRSN2442 SunTronic 280 Thermal Drying Silver Conductive Ink,
- DP-DuPont 5064H Silver Conductor,
- UV-Electra Polymers ELX 30.

Inks denoted as SC and DP require thermal drying, while UV is an ultraviolet curing ink. The characteristics of the used inks are summarized in **Table 1**.

After printing, the optimal drying process for each ink was determined. The optimal drying was determined as the point where the sheet resistance of the printed samples became constant and did not get any lower with a longer drying time, higher temperature or higher or longer UV exposure. In accordance with the SC and DP printing inks' specifications, drying in an infra-red (IR) tunnel was performed. The best results – the lowest sheet resistance – were obtained when the samples passed the IR tunnel seven times (at 72 °C for 30 s). The UV printed samples were optimally cured when twice passed through a UV tunnel with a dose of 700 mJ/cm².

3.3 Sheet resistance

The resistance, R , of the printed conductive lines was measured using a DT-890G digital multimeter on the test element, as shown in **Figure 6**, between points 1 and 2. The nominal length, L , between points 1 and 2 was 22 mm and the line width, W , was set to 3 mm. The resistance was measured after 24 h of conditioning with a 50 % relative humidity at 23 °C. The nominal number of

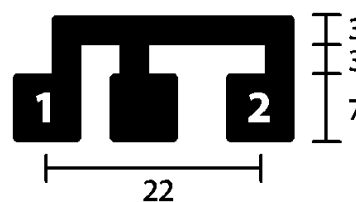


Figure 6: Test element for resistance measurements
Slika 6: Preizkusni element za merjenje upornosti

squares N_{sq} and the final sheet resistance R_{sh} of the conductive ink layer (m Ω) can be calculated using Eq. 8 and Eq. 9, respectively. The measured resistances for the different inks are shown in **Table 1**.

$$N_{sq} = \frac{L}{W} = 10.3 \quad (8)$$

$$R_{sh} = \frac{R}{N_{sq}} \quad (9)$$

3.4 Chip integration

In our study, NXP strap chips were used. The main chip characteristics are as follows: operating frequency 840–960 MHz, impedance 22 – j195 Ω and Q -factor 9. The chips were assembled with isotropic conductive glue based on silver particles (Bison, Netherlands) after the drying process. After chip integration, tags were dried in a thermal oven at 120 °C for 30 min.

3.5 Lamination

The lamination process was used to fabricate the final smart cards. It was separated into two phases: first the "heat phase", where nine foil layers were assembled at a temperature of 199 °C and a pressure of 300 N/cm² for a fixed period of 19 min. In the second phase, the "cold phase", the assembled foils were exposed to 25 °C and a pressure of 500 N/cm² for 18 min. Finally, cutting into final cards sized according to ISO/IEC 7810 standard was carried out. The final prototype of the laminated smart card is shown in **Figure 7**.

Table 1: Properties of investigated printing inks

Tabela 1: Lastnosti tiskarskih barv

Printing ink	Solids (%)	Recommended drying condition	Specified resistance* R_{sh} (spec.)/m Ω (layer thickness)	Measured resistance** R_{sh} (meas.)/m Ω
SC CRSN2442 SunTronic 280	69–71	100–130 °C over 30–90 s in the hot zone	10–32 (25 μ m)	118.12
DP DuPont 5064H	63–66	140 °C over 120 s in the hot zone	≤ 6 (25 μ m)	567.96
UV Electra Polymers ELX 30	approx. 75	1000–1500 mJ cm ⁻²	300–500 (15 μ m)	653.72

*Sheet resistance from the product specification

**Sheet resistance measured on printed samples using the DT-890G digital multimeter. An average thickness of 15 μ m was determined on the prints' cross-sections with a scanning electron microscope.

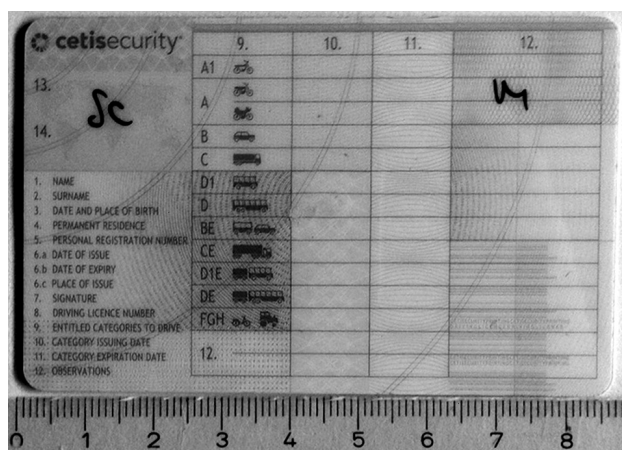


Figure 7: Final laminated smart card prototype
Slika 7: Končni prototip laminirane pametne kartice

4 RESULTS AND DISCUSSION

4.1 Non-laminated antenna measurements

The return loss of the fabricated non-laminated SC antenna was measured and the comparison of the simulated and measured return losses for the non-laminated antenna is given in **Figure 8**, with a photograph of the fabricated circuit shown in an inset. Despite the small size of the antenna, good agreement is observed and the fundamental resonance occurs at 940 GHz, as predicted, with a reflection better than -10 dB.

Figure 9 shows the comparison of the simulated and measured radiation patterns for the non-laminated antenna. The pattern measurements were taken in an anechoic chamber using a vector network analyser and the measured patterns agree well with the simulated ones, except for some ripple, which is ascribed to reflections in the chamber.

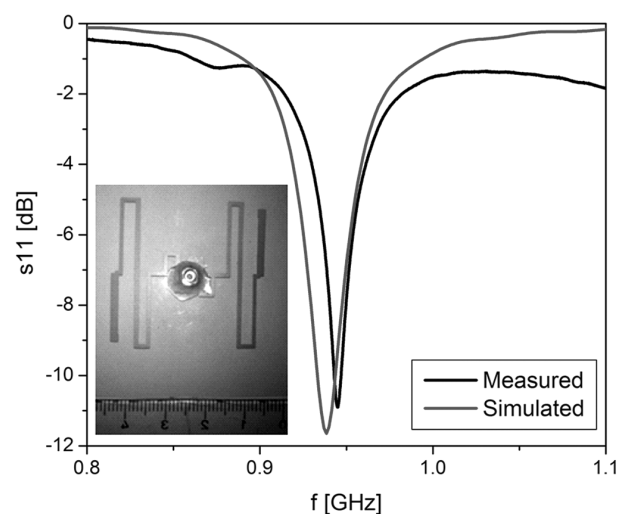


Figure 8: Comparison of simulated and measured return losses for the non-laminated antenna with inset photograph of the fabricated circuit
Slika 8: Primerjava simulirane in izmerjene povratne izgube signala za nelaminirano anteno z vključeno sliko natisnjene vezja

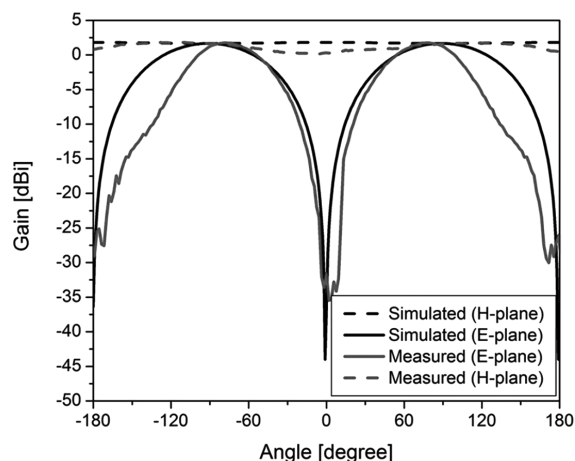


Figure 9: Comparison of simulated and measured radiation patterns in *E*-plane and *H*-plane for non-laminated antenna

Slika 9: Primerjava simuliranega in izmerjenega sevalnega diagrama v *E*-ravnini in *H*-ravnini za nelaminirane antene

4.2 Card evaluation

The realized readability of the cards with RFID tags was measured in a real environment using an IDS-R902 reader that consists of the reader electronics and an A0025 circularly polarized patch antenna (Poynting GmbH, Dortmund, Germany) with gain of 6.5 dBi emitting UHF EM radiation at frequency $f = 868$ MHz. The reader electronics measures the intensity of the modulated backscattered signal.

The cards with UHF RFID tags were evaluated by measuring the backscattered power (dBm), moving the tag in a straight line perpendicular to the reader in 2 cm increments, starting at 2 cm from the emitting antenna up to the estimated free space working distance (**Figure 10**).

Multifactorial (multiway) analysis of variance (ANOVA) was implemented to aid in the interpretation of the measurement results obtained for both non-laminated and laminated cards. The impact of the three selected factors on the response – backscattered power – was

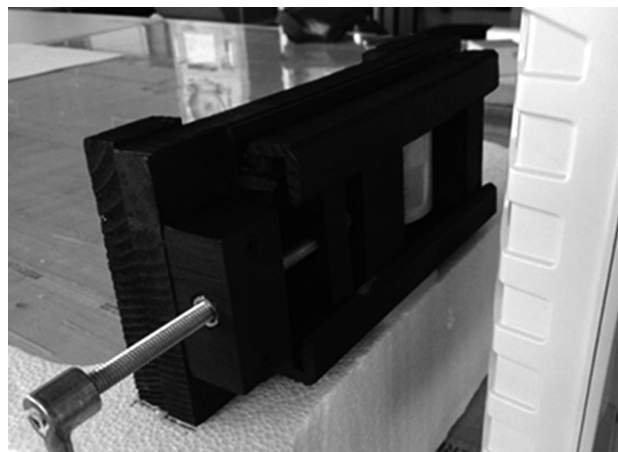


Figure 10: Measurement of the backscattered power

Slika 10: Merjenje moči povratnega signala

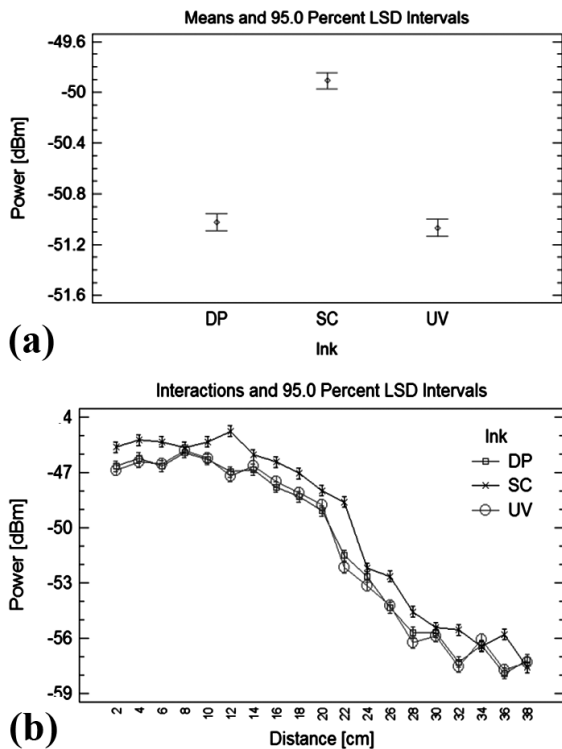


Figure 11: Non-laminated cards: a) effect of ink type and b) ink-type/reading distance interaction on the backscattered signal power
Slika 11: Nelaminirane kartice: a) vpliv vrste tiskarske barve in b) interakcije vrsta tiskarske barve/razdalja odčitavanja na moč povratnega signala

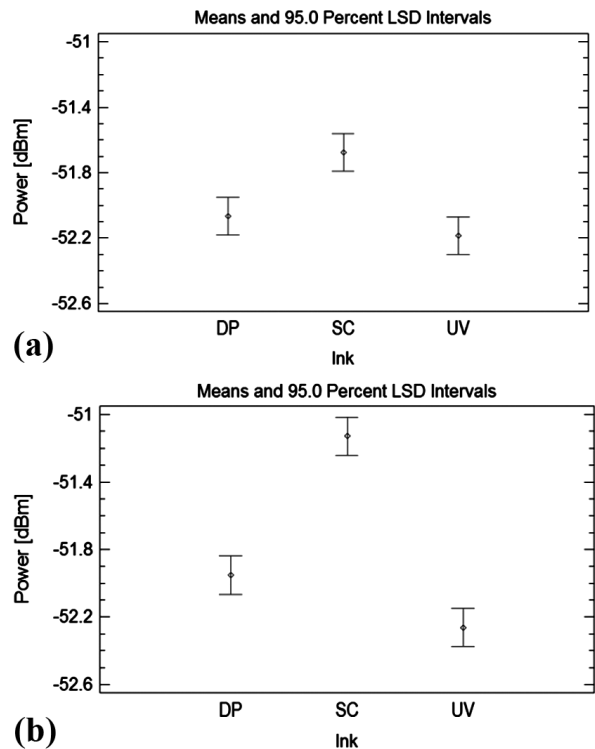


Figure 13: Laminated cards effect of ink type on backscattered power for: a) flat and b) bent cards
Slika 13: Laminirane kartice: vpliv vrste tiskarske barve na moč povratnega signala za: a) ravne in b) upognjene kartice

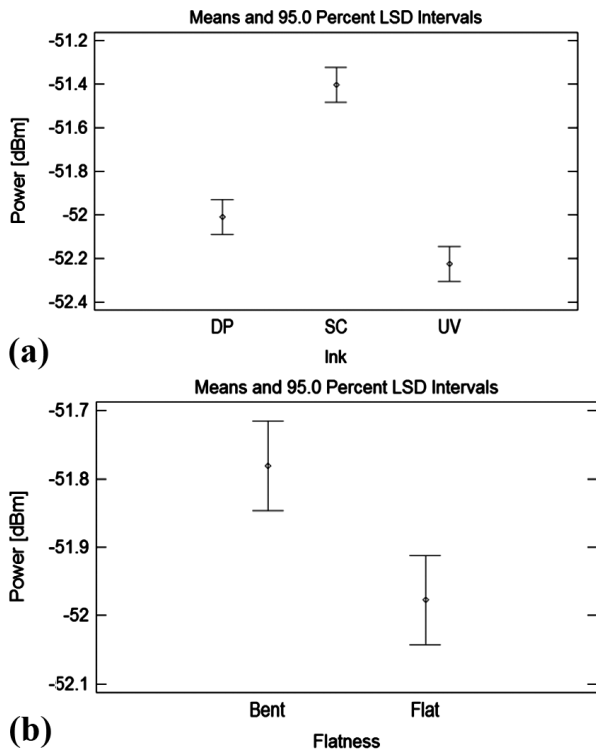


Figure 12: Laminated cards: a) effect of ink type and b) flatness on backscattered signal power
Slika 12: Laminirane kartice: a) vpliv vrste tiskarske barve in b) ploskosti na moč povratnega signala

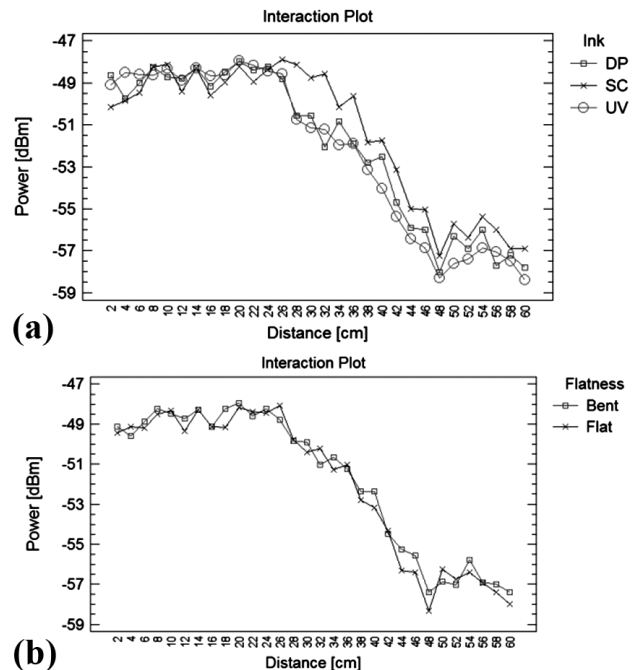


Figure 14: Laminated cards: a) effects of interactions – ink-type/reading distance and b) flatness/reading distance on backscattered power
Slika 14: Laminirane kartice: a) vpliv interakcije vrsta tiskarske barve – razdalja odčitavanja in b) ploskost – razdalja odčitavanja na moč povratnega signala

studied: ink type, reading distance and flatness, the later one only for the laminated cards (flat or bent). The cards were bent to a final deformed position: 2.6 cm height, 3 cm width, 1.73269 cm radius and an angle of 240° subtended by an arc. The results of the statistical analysis at $\alpha = 0.05$ (i.e., a 95 % confidence level) are presented in **Figures 11a, 12a, 12b, 13a** and **13b**. The analyses were made on nine samples for each of the various cards (non-laminated, flat laminated and bent laminated).

4.3 Non-laminated cards

All of the examined non-laminated cards were flat, so here only two factors – ink type and reading distance – were analysed. As shown in the ANOVA table (**Table 2a**), both factors have a statistically significant effect (P -value < 0.05) on the response. The very small interaction effect (F -ratio_{AB} = 6.16) is merely due to an extremely strong impact of the reading distance and can be neglected. **Figure 11a** and the multiple range test data (**Table 2b**) clearly show that the SC ink behaves in a substantially different manner compared to the other two inks: the mean backscattered signal power of the UHF RFID cards with the applied SC ink is -49.9 dBm, while the mean responses with the DP and UV inks are -51.0 dBm and -51.1 dBm, respectively. The difference in the responses between the latter two inks is not statistically significant (**Table 2b**), since the corresponding mean values form the same homogeneous group (a). The ink type/reading distance diagram (**Figure 11b**) also supports the above findings.

4.4 Laminated cards

In addition to the impacts of the ink type and reading distance, the flatness of the substrate was studied in the case of the laminated cards. As shown in **Table 3a**,

Table 2: Non-laminated cards: a) ANOVA table and b) multiple range test results for ink type; SS = Sum of Squares, Df = Degrees of Freedom, MS = Mean Square

Tabela 2: Nelaminirane kartice: a) ANOVA tabela in b) rezultati preizkusov večkratnih primerjav za vrsto tiskarske barve; SS = vsota kvadratov, Df = stopinje prostosti, MS = povprečje kvadratov

a)	Source	SS	Df	MS	F-Ratio	P-Value
MAIN EFFECTS						
	A:Ink	302.14	2	151.07	187.25	0.0000
	B:Distance	20749.4	18	1152.74	1428.83	0.0000
INTERACTIONS						
	AB	178.831	36	4.96753	6.16	0.0000
	RESIDUAL	781.763	969	0.806773		
	TOTAL (corr.)	22063.8	1025			

b)	Method: 95.0 percent Duncan				
Ink	Count	LS Mean	LS Sigma	Homogen. groups	
UV	323	-51.0687	0.049978	a	
DP	342	-51.0228	0.048569	a	
SC	361	-49.9094	0.047274	b	

reading distance has by far the strongest effect on the backscattered power, followed by the effects of the ink type and flatness. The impact of the three ink types on the response (**Figure 12a**) is similar to that found with the non-laminated cards, the only difference being that the mean response with the UV ink (-52.2) is now statistically higher compared to the one with the DP ink (-52.0) (**Table 3b**). The detected backscattered power with the flat cards is generally lower than with the bent cards (**Figure 12b**).

The compared maximum reading distances of the non-laminated and laminated cards showed a significant difference (presented in **Figures 11b** and **14a**). Since the antenna is designed for laminated cards, the lamination process increases the reading distance from 40 cm to 60 cm.

To find out how flatness affects the measured backscattered power, we ran two more ANOVAs, separately for the flat and for the bent cards. The results (**Figure 13**) indicate that the differences in the effects of the DP, UV and SC inks on the response become more pronounced with bending (**Figure 13**).

It is clear that the readability of the cards depends on the conductivity of the printing ink used for printing the antenna. Antennas printed with SC ink ($R_{sh} = 118.12 \text{ m}\Omega$) had 5 to 6 times higher conductivity than those with DP and UV inks and, as a consequence, the cards printed

Table 3: Laminated cards: a) ANOVA table, b) multiple range test results for ink type and c) flatness; SS = Sum of Squares, Df = Degrees of Freedom, MS = Mean Squares

Tabela 3: Laminirane kartice: a) ANOVA tabela, b) rezultati preizkusov večkratnih primerjav za vrsto tiskarske barve in c) ravnoležnosti; SS = vsota kvadratov, Df = stopinje prostosti, MS = povprečje kvadratov

a)	Source	SS	Df	MS	F-Ratio	P-Value
MAIN EFFECTS						
	A:Ink	65.2691	2	32.6346	54.48	0.0000
	B:Distance	6701.27	29	231.078	385.79	0.0000
	C:Flatness	5.2215	1	5.2215	8.72	0.0034
INTERACTIONS						
	AB	171.159	58	2.95101	4.93	0.0000
	AC	9.20544	2	4.60272	7.68	0.0005
	BC	33.2657	29	1.14709	1.92	0.0036
	ABC	44.609	58	0.769121	1.28	0.0912
	RESIDUAL	215.633	360	0.598981		
	TOTAL (corr.)	7245.63	539			

b)	Method: 95.0 percent Duncan				
Ink	Count	LS Mean	LS Sigma	Homogen. groups	
UV	180	-52.2244	0.057686	a	
DP	180	-52.0094	0.057686	b	
SC	180	-51.4033	0.057686	c	

c)	Method: 95.0 percent Duncan				
Flatness	Count	LS Mean	LS Sigma	Homogen. groups	
Flat	270	-51.9774	0.0471	a	
Bent	270	-51.7807	0.0471	b	

with SC ink had a better readability or a higher back-scattered power (dBm) of the return signal. The maximum reading (working) distance showed no significant differences between the applied inks. Furthermore, the maximum reading distance was higher for the laminated cards, with an approximately 20 cm increase, regardless of the ink used.

With card deformation, we are assuming that the bending increases the reading distance range. This can be seen from **Figure 14b**, where the strength of the modulated backscattered signal is improved after bending. The result of the performed analysis shows that the printed card printed with SC inks outperforms all the other printed cards in terms of the backscattered power.

5 CONCLUSIONS

In the present study, a novel folded UHF RFID antenna that requires only single-layer printing has been proposed and implemented in the smart-card design. Despite the small size of the antenna, good readability was achieved. Through optimizing the antenna design, more rational printing for low-cost mass production can be possible.

We showed that a higher ink conductivity increases the backscattered power and that the novel design of the UHF antenna is appropriate for final laminated smart cards, while the lamination process increases the maximum reading distance.

By the end of our research, we had shown that smart cards with screen-printed UHF antennas can be realized. The main effect on the final tag's operability is that of the quality of the conductive ink itself, while bending can improve the strength of the modulated backscattered signal. The study of chip contacting, especially the glue/ink interactions and the influence of the mechanical strength of smart cards, will be the topic of our future research.

Acknowledgments

Urška Kavčič acknowledges assistance from the European Social Fund ("Operation part-financed by the European Union, European Social Fund").

6 REFERENCES

- ¹ K. F. Teng, R. W. Vest, Metallization of solar cells with ink jet printing and silver metallo-organic inks, *IEEE Transaction on Components, Hybrids and Manufacturing Technology*, 11 (1988), 291–297
- ² D. Y. Shin, Y. Lee, C. H. Kim, Performance characterization of screen printed radio frequency identification antennas with silver nanopaste, *Thin Solid Films*, 517 (2009), 6112–6118
- ³ K. Janeczek, M. Jakubowska, G. Koziol, A. Młozniak, A. Araz'na, Investigation of ultra-high-frequency antennas printed with polymer pastes on flexible substrates, *IET Microwaves, Antennas & Propagation*, 6 (2012), 549–554
- ⁴ T. Elsherbeni, K. E. Mahgoub, L. Sydanheimo, L. Ukkonen, F. Yang, Laboratory scale fabrication techniques for passive UHF RFID tags, *Antennas and Propagation Society International Symposium (APSURSI)*, 2010 IEEE, Toronto, 2010
- ⁵ K. Janeczek, M. Jakubowska, A. Młozniak, G. Koziol, Thermal characterization of screen printed conductive pastes for RFID antennas, *Materials Science and Engineering B: Solid-State Materials for Advanced Technology*, 177 (2012), 1336–1342
- ⁶ U. Kavčič, L. Pavlovič, M. Pivar, M. Đokić, B. Batagelj, T. Muck, Printed electronics on recycled paper and cardboards, *Inf. MIDEM*, 43 (2013) 1, 50–57
- ⁷ U. Kavčič, M. Maček, T. Muck, M. Klanjšek Gunde, Readability and modulated signal strength of two different ultra-high frequency radio frequency identification tags on different packaging, *Package. Technol. Sci.*, 25 (2012) 7, 373–384
- ⁸ U. Kavčič, M. Maček, T. Muck, Impact study of disturbance on readability of two similar UHF RFID tags, *Inf. MIDEM*, 41 (2011) 3, 197–201
- ⁹ X. Nie, H. Wang, J. Zou, Inkjet printing of silver citrate conductive ink on PET substrate, *Applied Surface Science*, 261 (2012), 554–560
- ¹⁰ A. Kanso, E. Arnaud, T. Monediere, M. Thevenot, E. Beaudrouet, C. Dossou-yovo, R. Noguera, Inkjet printing of Coplanar Wire-Patch antenna on a flexible substrate, *15th International Symposium on Antenna Technology and Applied Electromagnetics*, Toulouse, 2012, 1–4
- ¹¹ J. Li, B. An, J. Qin, Y. Wu, Nano copper conductive ink for RFID application, *International Symposium on Advanced Packaging Materials*, Xiamen, 2011, 91–93
- ¹² V. Radonic, K. Palmer, G. Stojanovic, V. Crnojevic-Bengin, Flexible Sierpinski Carpet Fractal Antenna on a Hilbert Slot Patterned Ground, *International Journal of Antennas and Propagation*, Vol. 2012, Article ID 980916, 2012, doi: 10.1155/2012/980916
- ¹³ L. B. Keng, W. L. Lai, C. W. A. Lu, B. Salam, Processing and characterization of flexographic printed conductive grid, *Electronics Packaging Technology Conference*, Singapore, 2011, 517–520
- ¹⁴ D. A. Alsaïd, E. Rebrosova, M. Joyce, M. Rebros, M. Z. Atashbar, B. Bazuin, Gravure Printing of ITO Transparent Electrodes for Applications in Flexible Electronics, *Journal of Display Technology*, 8 (2012), 391–396
- ¹⁵ S. L. Merilampi, P. Ruuskanen, T. Björninen, L. Sydänheimo, L. Ukkonen, Characterization of UHF RFID tags fabricated directly on convex surfaces by pad printing, *International Journal of Advanced Manufacturing Technology*, 53 (2011), 577–591
- ¹⁶ Z. J. Tang, Y. G. He, Y. Wang, Broadband RFID tag antenna with quasi-isotropic radiation performance, *AEU-International Journal of Electronics and Communications*, 65 (2011), 859–863
- ¹⁷ D. M. Dobkin, *The RF in RFID, Passive UHF RFID in Practice*, Elsevier, 2008
- ¹⁸ K. Finkenzeller, D. Muller, *RFID Handbook: Fundamentals and Applications in Contactless Smart Cards, Radio Frequency Identification and Near-Field Communication*, 3rd edition, John Wiley & Sons, Inc., 2010
- ¹⁹ A. Syed, K. Demarest, D. D. Deavours, Effects of antenna material on the performance of UHF RFID tags, *IEEE International Conference on RFID*, Grapevine, 2007, 57–62
- ²⁰ C. A. Balanis, *Antenna Theory: Analysis and Design*, 3rd edition, John Wiley & Sons, Inc., 2005

CHARACTERIZATION OF THE SUBSTRATES FROM TWO CULTURAL-HERITAGE SITES AND A PREPARATION OF MODEL SUBSTRATES

KARAKTERIZACIJA GRADBENIH MATERIALOV IZ DVEH OBJEKTOV KULTURNE DEDIŠČINE IN PRIPRAVA MODELNIH MATERIALOV

**Sabina Kramar¹, Vilma Ducman¹, Snezana Vucetic², Edo Velkavrh³,
Miroslava Radeka⁴, Jonjaua Ranogajec²**

¹Slovenian National Building and Civil Engineering Institute, Dimičeva 12, 1000 Ljubljana, Slovenia

²University of Novi Sad, Faculty of Technology, Bulevar Cara Lazara 1, 21000 Novi Sad, Serbia

³Saning International, d. o. o., Kranj, Ulica Mirka Vadnova 1, 4000 Kranj, Slovenia

⁴University of Novi Sad, Faculty of Technical Sciences, Trg Dositeja Obradovica 6, 21000 Novi Sad, Serbia
sabina.kramar@zag.si

Prejem rokopisa – received: 2013-09-11; sprejem za objavo – accepted for publication: 2013-10-09

In this study the microstructural characteristics of the materials selected from two cultural-heritage sites (the Dornava Manor, Slovenia, and the Bač Fortress, Serbia) and of the model samples – the control and aged ones – were investigated. The samples were characterized by means of mercury intrusion porosimetry (MIP) and total-specific-area analysis (BET). A good agreement was achieved between the samples of the brick and mortar from the Bač Fortress, or the samples of the natural stone and render from the Dornava Manor, and the corresponding model samples.

Keywords: cultural heritage, microstructure, brick, natural stone, mortar, frost resistance

Prispevek obravnava mikrostrukturne lastnosti izbranih materialov iz dveh objektov kulturne dediščine (dvorec Dornava v Sloveniji in trdnjava Bač v Srbiji) ter modelnih materialov – kontrolnih in staranih. Vzorce smo preiskali z živosrebrno porozimetrijo in plinsko sorpcijo. Med vzorci iz objektov kulturne dediščine in modelnimi vzorci smo dosegli dobro ujemanje, tako v primeru opeke in malte s trdnjave Bač kot naravnega kamna in ometa z dvorca Dornava.

Ključne besede: kulturna dediščina, mikrostruktura, opeka, naravni kamen, malta, zmrzljinska obstojnost

1 INTRODUCTION

Within the scope of the 7th FP HEROMAT project (*Protection of cultural heritage objects with multifunctional advanced materials* ENV-NMP.2011.3.2.1-1 NMP) the main goal is to develop the consolidants and multifunctional photocatalytic coatings for cultural-heritage sites in order to conserve degraded materials and to prevent their further degradation. To meet the set goals and develop the basis for further applications, the following steps were implemented: (i) an analysis of the microstructure of the substrates from the two studied facilities (the Dornava Manor, Slovenia, and the Bač Fortress, Serbia); (ii) the preparation of a model substrate, simulating the substrates from such sites for the preliminary testing of the newly developed products; (iii) an analysis of the microstructure of the model substrate before and after the ageing procedure, and a comparison of this substrate with the substrates from the two selected sites.

The Dornava Manor Complex, with its accompanying park, is one of the most important monuments of the late Baroque period in Slovenia. Because of a long exposure to a strong degradation and inappropriate restoration procedures, the stone elements of the exterior, i.e., the

statues and ornaments of the garden, the balustrades and the main building, show only a faint picture of the past. The Bač Fortress, Serbia (currently included in the UNESCO Tentative List) is the best preserved brick-built medieval fortress in Vojvodina. This, first a Hungarian and later on an Ottoman stronghold, has been in ruins for centuries as a result of various physical, chemical and biological degradation processes. Its physical integrity has been substantially lost, but the preserved elements indicate the sophisticated architecture of the fortification school of the high Gothic style, with the elements of the early Italian Renaissance.

Among the most active causes for the weathering of the historical monuments exposed to the outdoor environment is frost. A common degradation phenomenon of the porous materials such as mortars, stone and brick is a loss of cohesion of the binder-aggregate/grain system. This process is usually followed by a deposition and formation of new products, a loss of mechanical strength, a loss of the material from the surface, and chromatic alterations.¹ The cohesion recovery between these particles, released by the binder loss, can be achieved through an application of consolidants.²

Porosity and pore-size distribution can have a major effect on the durability of porous materials, influencing

the effectiveness of a consolidation, the depth of a consolidant, etc.^{3,4} No consolidation action can be reasonably justified without having access (directly or by deduction) to the information on all these aspects.⁵

Taking into consideration the fact that porosity is the most important factor with regard to the absorption and fluid transport in porous materials, the present study focuses on the characterization of the porosity and pore-size distribution as well as determining the specific surface area. In this study the microstructural characteristics of the selected materials from the Dornava Manor and the Bač Fortress are determined. In order to assess the changes that occur in the microstructure after a freeze/thaw cycles, model substrates were prepared. The samples were characterized with mercury intrusion porosimetry (MIP) and total-specific-area analysis (BET).

2 EXPERIMENTAL WORK

2.1 Materials and sample preparation

Four substrates were selected among various materials from the two historical sites: (i) sandstone (designated as Stone Dornava) and (ii) a render sample from the Dornava Manor (designated as Render Dornava); (iii) lime mortar with a carbonate aggregate (designated as Mortar Bač) and (iv) a brick from the Bač Fortress (designated as Brick Bač).

Based on the mineralogical and petrographic analyses, a quartzitic-micaceous sandstone from the Dornava Manor was recognised as the Vunduški sandstone outcropping in the eastern part of Slovenia. As a model stone, a bulk sample of the Vundušek sandstone (from the Middle-Miocene geological period) was taken from the Jelovice quarry, located near the town of Majšperk, in the eastern part of Slovenia. Samples were cut having a dimension of 5 cm × 5 cm × 1 cm and designated as Model Stone or Model Stone F, where F means that the sample was exposed to freezing and thawing.

The model render was prepared on the basis of a petrographic analysis of render sample DOR 137 from the Dornava Manor. A silicate gravel fraction of 0–4 mm was obtained from the Hoče quarry (Slovenia) and sieved in order to get a grading curve for the aggregate similar to that of the analyzed render. In order to weaken the mechanical properties of the cement part of the model samples, a Portland cement (CEM I 42.4, Lafarge) mixed with tuff (Ecotrass, Saning, d. o. o.) was used. The traditionally prepared slaked lime from the local producers was also used. The substrates were prepared by combining together coarse and fine renders in order to achieve the appropriate thickness. On an approximately 3.5 cm thick coarse layer, a 3–4 mm thick layer of fine render was applied. Steel moulds with the dimensions of 16 cm × 4 cm × 4 cm and 15 cm × 15 cm × 4 cm were used for the preparation of the models that were then cut out to the dimensions required for the testing. The samples were cured at 100 % relative humidity at room tempe-

perature for a minimum of 14 d before the cutting was performed.

The model bricks were prepared by hand in the traditional way, using an old crushed brick and the clay from a pit situated near the Bač Fortress. Based on the mineralogy and chemical composition of the examined historical-brick samples, the optimum formulation for the raw-material mixture and firing temperature was determined. The clay material was based mainly on quartz and carbonates such as dolomite and calcite. The raw material was hand-moulded in the laboratory. The moulds were filled and then air-dried for a period of two weeks. When an adequate strength was obtained, the model bricks were fired in a laboratory kiln (T max of 980 °C). The prepared model-brick samples were then exposed to a laboratory degradation, followed by a characterization procedure. Samples with the dimensions of 5 cm × 5 cm × 1 cm were prepared.

For the preparation of the model mortar, the following components were used: lime putty, micronized quicklime, sand and water (the hot-lime-mix method). The selected components provided a mineralogical and chemical composition that was as close as possible to the characterized historical mortars. All the mortars were prepared in the traditional way, in a wooden dish. The prepared mortars were moulded in specially designed moulds. The interior surfaces of the moulds were coated with TFE-fluorcarbon (Teflon) that did not affect the setting of the mortar, also preventing any damage to the mortar surfaces. During the first weeks, carbonation was achieved in a moist room and after that all the samples (5 cm × 5 cm × 1 cm) were placed in a chamber with a constant flow of CO₂ (accelerated carbonation).

2.2 Methods

The freeze/thaw cycling was performed according to standard EN 12371:2010. All the samples were exposed to 50 cycles of freezing and thawing, where one cycle consists of (1) a sample being in water for 5.5 h and at 15 °C, (2) sucking the water from the chamber so that the temperature reaches –4 °C within 2 h, (3) cooling down over the next 4 h to –10 °C, and (4) pouring the water again into the chamber.

The porosity and pore-size distribution of the investigated samples were determined by means of mercury intrusion porosimetry (MIP). Small blocks, approximately 1 cm³ in size, were dried in an oven for 24 h at 105 °C, and then analysed using a Micromeritics Auto-pore IV 9500 Series pore-size analyzer. The samples were analysed in the range of 0–414 MPa, using solid penetrometers.

On the basis of the BET (Brunauer-Emmet-Teller) method, the total specific area of a sample surface was determined with nitrogen adsorption at 77 K within a relative pressure range of 0.05 to 0.3 using a Micromeritics ASAP-2020 analyzer. Prior to the performance of these measurements, the samples (2 to 3 small blocks

Table 1: Comparison of the porosity and specific surface (the average of 2 measurements) of the samples from Dornava Manor and Bač Fortress with the corresponding values for the model substrates (before and after the ageing (F – exposure to freezing/thawing))**Tabela 1:** Primerjava poroznosti in specifične površine (povprečje 2 meritev) vzorcev iz dvorca Dornava in vzorcev iz trdnjave Bač z ustreznimi vrednostmi modelnih podlag pred staranjem in po njem (F – izpostavitve zmrzovanju in odtajanju)

	Brick Bač	Model brick	Model brick F	Mortar Bač	Model mortar	Model mortar F
Porosity (%)	42.0 ± 4.4	45.6 ± 0.4	43.5 ± 0.8	40.3 ± 0.8	32.2 ± 4.1	29.6 ± 0.6
BET (m ² /g)	5.4 ± 0.9	2.03 ± 0.7	5.0 ± 1.4	2.8 ± 0.3	2.3 ± 0.2	1.8 ± 0.2
	Stone Dornava	Model stone	Model stone F	Render Dornava	Model render	Model render F
Porosity (%)	9.8 ± 0.2	13.4 ± 1.2	17.1 ± 2.8	26.7 ± 1.6	38.6 ± 1.0	27.8 ± 0.2
BET (m ² /g)	1.9 ± 0.3	2.3 ± 0.5	3.5 ± 0.1	10.3 ± 0.5	4.8 ± 0.4	9.3 ± 0.3

with a weight of approximately 1 g) were being degassed for at least 3 h.

3 RESULTS AND DISCUSSION

The results of the porosity and BET specific-surface tests are presented, for the all prepared samples, in **Table 1**, from which it can be seen that there is a very good agreement between the samples from the historical sites and the model samples obtained, in the case of the brick and mortars, from the Bač Fortress, and a fairly good agreement with the stone and render from the Dornava Manor. For example, the overall porosity of the Brick Bač sample was 42.0 %, whereas it was 45.6 % for the model-brick sample. In the case of the Mortar Bač sample it was 40.3 % compared to 32.2 % for the model-mortar sample. The porosity of the Stone Dornava sample was found to amount to 9.8 % compared to 13.4 % for the model-stone sample, whereas the porosity of the original render from Dornava reached 26.7 % and that of the model-render sample was 38.6 %.

After an exposure to the freeze/thaw cycling, only a slight increase in the porosity of the model-stone sample was observed. On the other hand, the sample's average pore diameter increased significantly, shifting from 0.04 μm to 0.26 μm (**Figure 1**). The pore-size distribution was unimodal, with an intrusion peak at 2 μm. The BET surface-area values also increased. The pressure caused by freezing range from 14 MPa to 138 MPa, with a

decrease in the temperature of between -1.1 °C and -12.5 °C.⁶ During the ageing test performed within the scope of this study, the temperature fell by up to -10 °C. The temperature range considered critical for a deterioration of natural stone is from about -4 °C to -15 °C.⁶ A stone with a higher quantity of smaller pores is more prone to frost deterioration as well as salt crystallisation, although stone damage is more specifically influenced by nanopores in the case of salt crystallisation, and by micropores in the case of frost damage.⁷

The porosity of the model-render sample reduced significantly after the freeze/thaw cycling, whereas the change in the average pore size was not significant (0.04 μm and 0.06 μm). The main intrusion peak after the freeze/thaw cycling shifted from 1 μm to 0.15 μm (**Figure 2**). A significant increase in the BET surface area of the render was observed after the freeze/thaw cycling. Both of these phenomena can be ascribed to the dissolution/precipitation processes that occur due to the water exposure in the freezing/thawing test.

The overall porosity of the model-brick sample decreased slightly after the freeze/thaw cycling tests, which can be attributed to the natural re-carbonation of the calcium hydroxide inside the porous media, thus also contributing to an improvement in the durability.⁸ Additionally, the average pore diameter also decreased (from 0.57 μm to 0.21 μm). However, a certain increase was observed in the case of bigger pores – there are three peaks above 10 μm, representing either pores or cracks. This could mean that the brick might be susceptible to

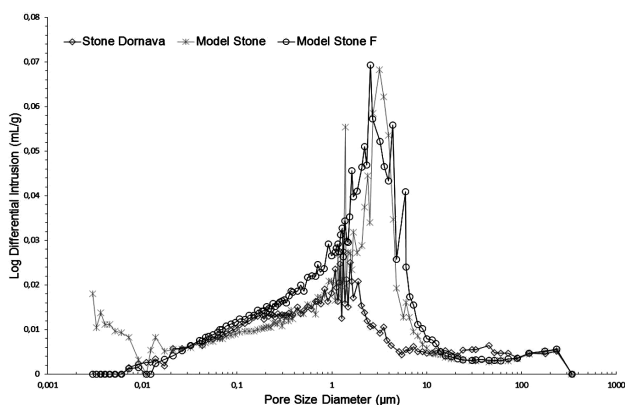


Figure 1: Pore-size distributions for the samples of natural stone
Slika 1: Porazdelitev velikosti por v vzorcih naravnega kamna

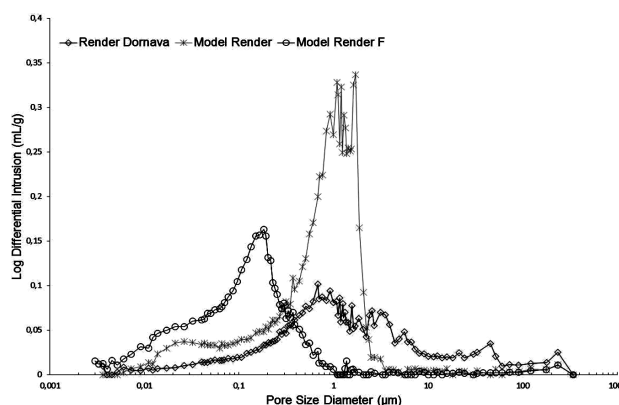


Figure 2: Pore-size distributions for the samples of render
Slika 2: Porazdelitev velikosti por v vzorcih ometa

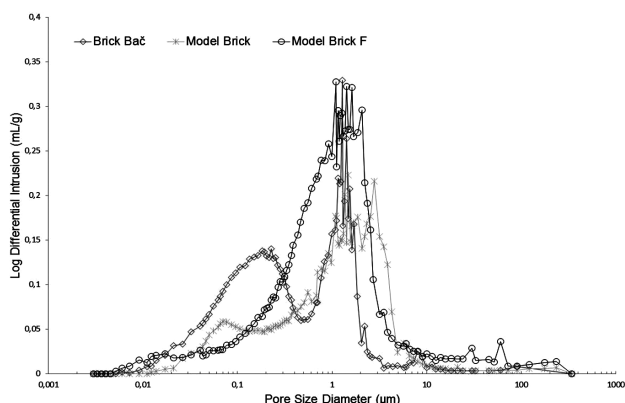


Figure 3: Pore-size distributions for the samples of brick
Slika 3: Porazdelitev velikosti por v vzorcih opeke

freezing. The values of the BET surface area increased significantly after the ageing. The pore-size distribution of Brick Bač and model-brick samples was bimodal, but after the freeze/thaw cycling it became unimodal (**Figure 3**).

The values of the porosity and the average pore diameter for the model-mortar sample decreased after the freeze/thaw cycling, most probably due to the dissolution/reprecipitation processes inside the pores. The pore-size distribution of the control sample was bimodal – this distribution was observed for a significant number of historical mortars⁹, becoming unimodal after the ageing¹⁰ (**Figure 4**). The values of the BET surface area increased significantly after the freeze/thaw cycling, indicating a deleterious effect of freezing on the mortar.

4 CONCLUSIONS

Samples of the selected substrates from the two monuments and model substrates – the control and aged ones, were investigated by means of mercury intrusion porosimetry (the total porosity, the average pore diameter, the pore-size distribution) and gas sorption (the BET surface area). A good agreement between the samples from the historical sites and the model samples was obtained for the brick and mortars from the Bač Fortress as well as for the natural stone and render from the Dornava Manor.

On the basis of these results, the selected model substrates will be used with newly developed materials in order to test and otherwise scrutinize them before applying them to the valuable substrates belonging to cultural-heritage sites.

Acknowledgements

This work was financially supported by the European Commission under the 7th FP HEROMAT project

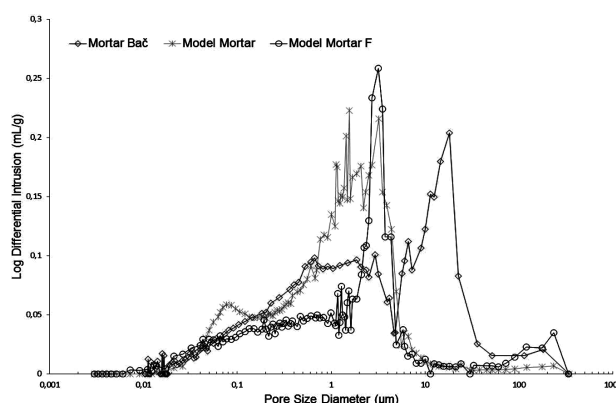


Figure 4: Pore-size distributions for the samples of mortar
Slika 4: Porazdelitev velikosti por v vzorcih malt

(*Protection of cultural heritage objects with multifunctional advanced materials*, ENV-NMP.2011.3.2.1-1 NMP).

5 REFERENCES

- L. Toniolo, A. Paradisi, S. Goidanich, G. Pennati, Mechanical behaviour of lime based mortars after surface consolidation, *Construction and Building Materials*, 25 (2010) 4, 1553–1559
- G. Borsoi, M. Tavares, R. Veiga, A. Santos Silva, Microstructural Characterization of Consolidant Products for Historical Renders: An Innovative Nanostructured Lime Dispersion and a More Traditional Ethyl Silicate Limewater Solution, *Microsc. Microanal.*, 18 (2012) 5, 1181–1190
- S. P. Gupta, Consolidation of historic porous stone by impregnation with silica acid-esters, *World Journal of Science and Technology*, 1 (2011) 3, 17–21
- P. Lopez-Arce, L. S. Gomez-Villalba, L. Pinho, M. E. Fernandez-Valle, M. Alvarez de Buergo, R. Fort, Influence in the porosity and relative humidity on consolidation of dolostone with calcium hydroxide nanoparticles: effectiveness assessment with non-destructive techniques, *Materials Characterization*, 61 (2010), 168–184
- J. Delgado-Rodriguez, Consolidation of decayed stones. A delicate problem with few practical solutions, *Historical Constructions*, P. B. Lourenço, P. Roca (Eds.), Guimarães, (2001), 3–14
- A. Goudie, H. Viles, *Salt weathering hazards*, J. Wiley and Sons, Chichester 1997, 235
- J. E. Lindquist, K. Malaga, B. Middendorf, M. Savukoski, M. P. Pétursson, Frost resistance of natural stone, the importance of micro- and nano-porosity, Geological Survey of Sweden, External research project report, published online at: http://www.sgu.se/dokument/fou_extern/Lindqvist-et-al_2007.pdf
- P. Lopez-Arce, D. Benavente, J. García-Guinea, Durability improvement of ancient bricks by cementation of porous media, *J. Am. Ceram. Soc.*, 88 (2005) 9, 2664–2672
- A. Klisinska-Kopacz, R. Tišlova, G. Adamski, R. Kozłowski, Control of the porosity structure to produce Roman cement mortars compatible with the historic substrate, *Proceedings of the 11th International Congress on Deterioration and Conservation of Stone*, Torun, Poland, 2008, 931–938
- A. Izaguirre, J. Lanás, J. I. Álvarez, Ageing of lime mortars with admixtures: Durability and strength assessment, *Cement and Concrete Research*, 40 (2010) 7, 1081–1095

LONG-TERM DURABILITY PROPERTIES OF POZZOLANIC CEMENT MORTARS

DOLGOROČNA OBSTOJNOST PUCOLANSKE CEMENTNE MALTE

Lina Završnik, Jerneja Strupi Šuput, Sabina Kramar

Slovenian National Building and Civil Engineering Institute, Dimičeva ulica 12, 1000 Ljubljana, Slovenia
lina.završnik@zag.si

Prejem rokopisa – received: 2013-09-23; sprejem za objavo – accepted for publication: 2013-10-30

Within the scope of this study, the durability properties of mortar prepared with pozzolanic cement were examined. The physical-mechanical properties of the mortars were determined after their exposure to various aggressive media (a sodium sulphate water solution, a magnesium sulphate water solution, seawater, and a water solution of NO_3^{2-} , SO_4^{2-} , and NH_4^-) and freeze/thaw cycling. Additionally, the depth of carbonation of the mortars was determined. The results showed that the mortar containing pozzolanic cement was sulphate resistant, but when it was exposed to a solution of NO_3^{2-} , SO_4^{2-} , and NH_4^- its strength was significantly reduced. On the other hand, the mortar was found to be sensitive to freezing/thawing, as its compressive strength decreased by 50 %, and its flexural strength by as much as 90 %. Due, especially, to its lack of resistance to freezing/thawing, the use of the investigated pozzolanic cement mortar is limited to indoor applications.

Keywords: pozzolanic cement, durability, sulphate attack, frost resistance, carbonation

V prispevku obravnavamo trajnostne lastnosti malte, pripravljene iz pucolanskega cementa. Določili smo fizikalno-mehanske lastnosti malte po izpostavitvi različnim agresivnim medijem (vodni raztopini natrijevega sulfata, vodni raztopini magnezijevega sulfata, morski vodi, vodni raztopina ionov NO_3^{2-} , SO_4^{2-} , NH_4^-) in cikličnemu zmrzovanju in odtaljevanju. Poleg tega smo določili tudi globino karbonatizacije. Na podlagi rezultatov ugotavljamo, da je malta s pucolanskim cementom odporna proti sulfatom, medtem ko se njena trdnost po izpostavitvi raztopini ionov NO_3^{2-} , SO_4^{2-} in NH_4^- močno zmanjša. Prav tako preiskana malta nima zmrzlinke obstojnosti, saj se njena tlačna trdnost zmanjša za 50 %, upogibna pa za 90 %. Na osnovi rezultatov ugotavljamo, da je malta zaradi slabe zmrzlinke obstojnosti uporabna le za notranje površine.

Ključne besede: pucolanski cement, obstojnost, sulfatna korozija, obstojnost proti zmrzali, karbonatizacija

1 INTRODUCTION

Over the past decade there has been a clearly perceptible trend towards the replacement of Portland cement, by up to 80 %, with various mineral additives, such as ground granulated blast furnace slag, natural (volcanic ash) and synthetic pozzolans (fly ashes, microsilica, rice husk ash), and ground limestone.¹⁻⁴ An important reason for the use of blended or pozzolanic cements lies in their good resistance to attack by chemical agents, especially seawater, and by sulphate-rich water.⁵⁻⁷ In addition, the replacement of Portland cements with pozzolans has environmental benefits, since in this way waste materials can be used, thus contributing to the reduced use of naturally occurring raw materials, and less energy is consumed in their production compared with the production of cement clinker, reducing greenhouse-gas emissions and the overall CO_2 footprint.

The most widely used cement-replacement material is coal combustion fly ash. In the EU, the replacement of up to 33 % of the Portland cement with fly ash is permitted for a range of cement types, whereas in the case of pozzolanic cement a limit of 55 % has been specified (EN 197-1:2011).⁸ The performance of concrete with added fly ash is frequently better than that of concrete mixed with Portland cement only. Although the pozzolanic reaction is slow, and can cause a significant decrease in early-age strengths, the use of fly ash in cement

results in a generally improved workability, a higher late-age strength and increased durability, as well as improved sulphate resistance, and reductions in the heat of hydration and in the risk of the occurrence of an alkali silica reaction and efflorescence.^{4,7,9} There are some situations, however, where the performance of concrete with added fly ash may not be so good, e.g., when such concrete is subjected to freeze-thaw actions. In this case concerns have been raised regarding the concrete's durability, especially when the fly ash is used at higher content levels.¹⁰ Two main classes of fly ash can be defined: siliceous fly ash (low calcium fly ash; < 10 % CaO), which has been widely used as a replacement for cement, and calcareous fly ash (high calcium fly ash; > 10 % CaO). Calcareous fly ashes show a more rapid strength gain during early ages than in the case of concretes made with siliceous fly ashes.¹¹ This is because calcareous fly ashes usually exhibit a higher rate of reaction during early ages than siliceous fly ashes. Since a negative cement performance has been frequently connected with the presence of lime and sulphates, the limits of the existing standards are very strict, so that most calcareous fly ashes are rejected as unsuitable.¹¹ However, the large amounts of calcareous fly ashes that are produced have resulted in a pressing need for their utilization, especially if sustainability issues are to be adequately resolved in the construction industry.

In the present investigation the durability properties of mortars prepared with pozzolanic cement have been investigated. The pozzolanic cement used in the study was a mix of calcareous fly ash and Portland cement clinker designated as CEM IV/B-W 32.5 N according to EN 197-1:2011⁸. The physical-mechanical properties of mortars made using this type of cement were determined after the latter had been exposed to different aggressive media, as well as to freeze/thaw cycling.

2 EXPERIMENTAL

2.1 Materials and methods

A pozzolanic cement CEM IV/B-W 32.5 N (Lafarge Cement, d. o. o., Trbovlje, Slovenia) and CEN standard sand were used for the preparation of mortars. A cement: aggregate:water ratio of 1 : 3 : 0.6 was used, except for the investigation of the resistance to freezing/thawing and carbonation. The properties of the samples of fresh mortar (consistence EN 1015-3:2001¹², bulk density EN 1015-6:1999¹³, air content EN 1015-7:1999¹⁴) for the investigation of the resistance to freezing/ thawing and carbonation are given in **Table 1**.

In order to evaluate the sulphate resistance of the pozzolanic cement mortar, samples having dimensions of 10 mm × 10 mm × 60 mm were cured for 21 d in deionized water. After this, some of the samples were exposed to a 4.4 % Na₂SO₄ water solution or a 3.73 % MgSO₄ water solution, whereas the remaining samples were left in the deionized solution. In order to compare the influence of the different curing media, another set of samples was cured in saturated lime water for 21 d, after which they were exposed to a 4.4 % Na₂SO₄ water solution, whereas the remaining samples were left in the saturated lime water. Compressive and flexural strengths according to EN 196-1:2005¹⁵ were determined after (14, 28 and 56) d. The resistance of the investigated mortars to sulphate attack was investigated and evaluated using the Koch-Steinegger test.¹⁶

In order to assess the influence of various aggressive media on the long-term durability of pozzolanic cement mortar, samples having dimensions of 40 mm × 40 mm × 160 mm were cured for 28 d in saturated lime water. After this, some of the samples were exposed to a 4.4 % Na₂SO₄ water solution, as well as to seawater, and to a (NO₃²⁻, SO₄²⁻, NH₄⁻) water solution, whereas the remaining samples were left in the saturated lime water. The compressive and flexural strengths of the mortar samples were determined according to EN 196-1:2005¹⁵, after 1 and 2 years.

In order to investigate the resistance to freezing/thawing of the pozzolanic cement mortar (in the absence and presence of de-icing salt) an air-entraining admixture was added to the mortar (Cementol Eta S, and Cementol Eta EM, produced by TKK Srpenica). The amount of air-entraining admixture used in the preparation of the mortar samples was determined by the consistence of the fresh mortar (EN 1015-3:2001)¹², by keeping a flow value (175 ± 5) mm (**Table 1**). For the investigation of the resistance to freezing/thawing in the absence of de-icing salt, mortar samples having dimensions of 40 mm × 40 mm × 160 mm were cured for 28 d in water at (20 ± 1) °C. After this, some of the samples were exposed to freeze/thaw cycling, whereas the remaining samples were left in the water at (20 ± 1) °C. Freeze/thaw cycling was performed according to the standard SIST 1026:2008.¹⁷ All the samples were exposed to 50 cycles of freezing/thawing, where one cycle consisted of 4 h at (-20 ± 2) °C and 4 h at (20 ± 2) °C.

The flexural and compressive strengths of the prepared mortar samples were determined according to EN 196-1:2005¹⁵ after 50 cycles. In the case of freeze/thaw cycling in the presence of the de-icing salt solution (3 % NaCl), samples having dimensions of 200 mm × 200 mm × 50 mm were cured for 7 d at (20 ± 2) °C at a RH of (65 ± 5) %, and their resistance to freezing/thawing was assessed according to SIST 1026:2008.¹⁷

The carbonation of the mortar samples was assessed on mortar prisms having dimensions of 40 mm × 40 mm × 160 mm, according to EN 13295:2004.¹⁸ The samples were cured for 24 h in a mould, wrapped in film. After de-moulding, the samples were cured for 48 h, wrapped in film, and then for 25 d at (21 ± 2) °C and at a RH of (60 ± 10) %. After this, they were placed in a chamber containing CO₂ 1 %, at a RH of (60 ± 10) %. The depths of the carbonation were determined by spraying a phenolphthalein indicator solution onto the freshly broken surface. Another set of samples was exposed to the natural environment, i.e., to outdoor conditions in a sheltered area. The depth of carbonation was determined after (28, 56, 90, 180 and 270) d, using the phenolphthalein indicator solution.

3 RESULTS AND DISCUSSION

3.1 Resistance to the investigated aggressive media

The compressive and flexural strengths of the mortar specimens that had been immersed in the sodium sulphate solution and the magnesium sulphate solution were

Table 1: Properties of the samples of fresh mortar for resistance to freezing/thawing and carbonation

Tabela 1: Odpornost vzorcev sveže malte proti zmrzovanju/odtaljevanju in karbonatizaciji

Additive – cement (%)	Water/cement ratio	Consistence (mm), EN 1015-3:2001 ¹²	Bulk density (kg/m ³), EN 1015-6:1999 ¹³	Air content (%), EN 1015-7:1999 ¹⁴
–	0.5	174	2180	3.6
0.15 (Cementol Eta S)	0.5	175	2100	4
0.6 (Cementol Eta EM)	0.47	171	2105	7.4

determined and compared with those of the samples that had been immersed in deionised or saturated lime water. A difference in the initial strengths was observed, which depended upon which solution, i.e., deionised water or saturated lime water, had been used to cure the specimens prior to the test. The lower initial strengths obtained in the case of the deionised water suggest that the latter behaves as an aggressive solution, if compared to the saturated lime water.

According to the Koch-Steiniger test,¹⁶ the criterion that can be used to classify a material as resistant or durable in a specific aggressive medium is that the corrosion index (i.e., the relative strength of the aggressive-solution-stored samples to the water-stored samples) must be higher than 0.7. As can be seen from **Figures 1** and **2**, the corrosion index for the mortar samples that were exposed to the investigated aggressive media was always above 0.7, in the case of both flexural and compressive strength. The corrosion index is slightly higher in the case of the magnesium sulphate solution. These results suggest that the pozzolanic cement mortar could be classified as durable or resistant to a sodium sulphate solution, as well as to a magnesium sulphate solution. This can be mainly attributed to the pozzolanic reaction, where the reactive siliceous and aluminous phases in the fly ash react with portlandite to form new C-S-H- or C-AS-H-type phases, provoking a refinement in the pore structure, and thus impeding the penetration and movement of potentially aggressive ions.^{6,19}

The flexural and compressive strengths of the mortar samples, measured after long-term exposure to the investigated aggressive media, are shown in **Figures 3** and **4**. The results indicate that the mortar containing pozzolanic cement continued to be sulphate resistant after 2 years of exposure, but when it was exposed to seawater or a solution of NO₃²⁻, SO₄²⁻, and NH₄⁻ its strength was significantly reduced. This could be due to

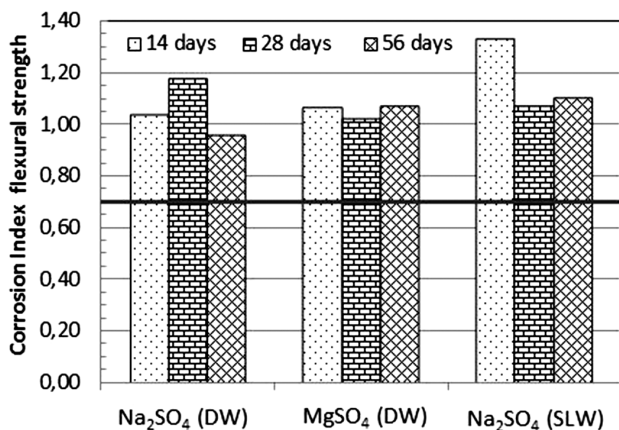


Figure 1: Corrosion index (flexural strength) for the mortar samples exposed to various solutions (DW – deionised water, SLW – saturated lime water)

Slika 1: Korozijski indeks (upogibna trdnost) za vzorce malte, izpostavljene različnim raztopinam (DW – deionizirana voda, SLW – nasičena apnena voda)

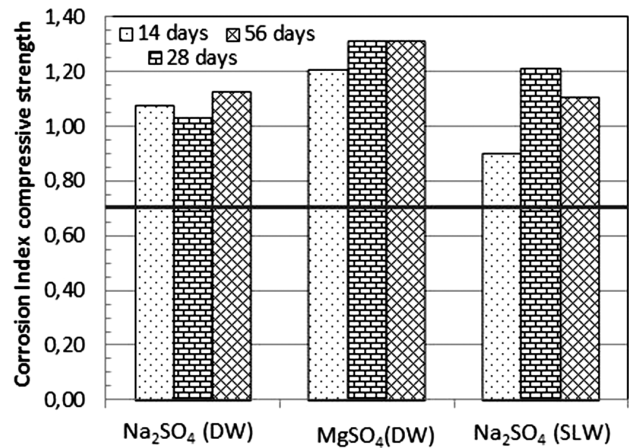


Figure 2: Corrosion index (compressive strength) for the mortar samples exposed to various solutions (DW – deionised water, SLW – saturated lime water)

Slika 2: Korozijski indeks (tlačna trdnost) za vzorce malte, izpostavljene različnim raztopinam (DW – deionizirana voda, SLW – nasičena apnena voda)

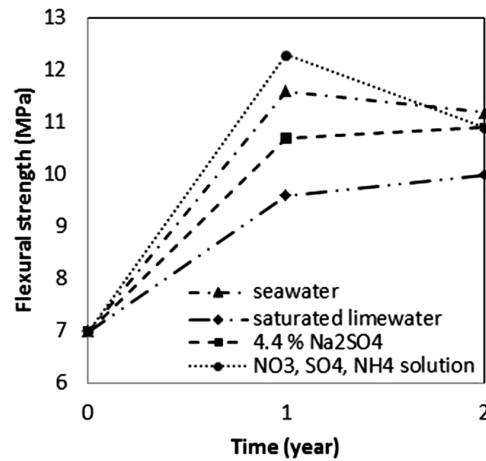


Figure 3: Flexural strength of the investigated mortar samples after long-term exposure to the investigated aggressive media

Slika 3: Upogibna trdnost preiskovanih malt po dolgotrajni izpostavitvi preiskovanim agresivnim medijem

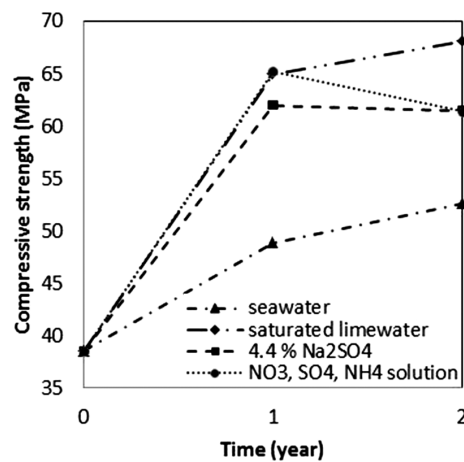


Figure 4: Compressive strength of the investigated mortar samples after long-term exposure to the investigated aggressive media

Slika 4: Tlačna trdnost preiskovanih malt po dolgotrajni izpostavitvi preiskovanim agresivnim medijem

the removal of calcium hydroxide, the hardened cement paste will be decalcified, causing the pH value to decrease.²⁰

3.2 Resistance to freezing/thawing

The results showed (Table 2) that, after the freeze/thaw cycling, the compressive strength of the investigated mortar samples decreased by more than 50 %, and their flexural strength by as much as 90 %. The observed decrease in strengths was higher in the case of the mortar with a higher air content.

In the presence of de-icing salt the loss of material exceeded the requirement according to the standard SIST 1026:2008¹⁷ (0.35 mg/mm²) already after 10 cycles of freezing/thawing. It was, however, higher in the case of the mortar with a higher air content, as the loss of material was 2.32 mg/mm² and, in the case of the mortar with a lower air content, 1.58 mg/mm². Thus, the investigated mortar is non-resistant to frost action, despite the addition of an air-entraining admixture. In general, the freeze-thaw durability of fly ash concrete, when a fly ash content of more than 20 % is used, is similar to or worse than that of Portland cement concretes, which could be attributed to compatibility problems between the fly ash and the air entraining agents.¹⁰

Table 2: Strengths of the investigated mortar samples after freeze/thaw cycling

Tabela 2: Trdnost preiskovanih malt po cikličnem zamrzovanju/odtaljevanju

Additive – sample (%)	Flexural strength (N/mm ²)		Compressive strength (N/mm ²)	
	cured in water	freeze/thaw cycling	cured in water	freeze/thaw cycling
0.15 (Cementol Eta S)	7.7	1.3	52.1	31.2
0.6 (Cementol Eta EM)	9.3	0.5	57.3	23.1

3.3 Carbonation

The depth of carbonation of the mortar samples exposed to the accelerated carbonation was 10.2 mm after 56 d, and 15.4 mm after 90 d. On the other hand, the mortar samples that were exposed to the natural environment showed a reduced depth of carbonation, which amounted to 3.1 mm after 56 d, 3.9 mm after 90 d, and 6.1 mm after 270 d.

It has been reported that the carbonation of concrete increases significantly with increased fly ash content, i.e., when the fly ash content is higher than 30 %, as a large amount of fly ash delays the hydration and the increase of porosity.²¹ However, when the binder used in the mortar samples contained just 10 % of fly ash, the carbonation level was equal to that of the samples containing Portland cement only, or was slightly higher.

On the other hand, when the concrete incorporated calcareous fly ash, carbonation was reduced in comparison with the siliceous fly ash.²¹

4 CONCLUSIONS

The investigated pozzolanic cement CEM IV/B-W 32.5 N is resistant to the selected sulphate solution, whereas both of the selected (NO₃²⁻, SO₄²⁻, NH₄⁻) solution and seawater had a negative effect, since the strengths of the tested mortar samples reduced over a period 1–2 years. However, there was a difference in the initial strengths, depending upon which solution, i.e., deionised water or saturated lime water, was used to cure the samples prior to testing. Deionised water behaves as an aggressive solution when compared to saturated lime water. On the other hand, the mortar was found to be sensitive to freezing/thawing in both the presence and the absence of de-icing salt, as its compressive strength decreased by 50 %, and its flexural strength by as much as 90 %. When exposed to a selected natural environment the mortar samples showed a reduced depth of carbonation with respect to the accelerated carbonation test.

Due, especially, to its lack of resistance to freezing/thawing, the use of the investigated pozzolanic cement mortar is limited to indoor applications.

Acknowledgements

This study was financially supported by the Metrology Institute of the Republic of Slovenia.

5 REFERENCES

- K. Sobolev, Mechano-chemical modification of cement with high volumes of blast furnace slag, *Cement and Concrete Composites*, 27 (2005) 7–8, 848–853
- B. Lothenbach, G. Le Saout, E. Gallucci, K. Scrivener, Influence of limestone on the hydration of Portland cements, *Cement and Concrete Research*, 38 (2008), 848–860
- V. Ramasamy, Compressive strength and durability properties of rice husk ash concrete, *KSCE Journal of Civil Engineering*, 16 (2012) 1, 93–102
- S. Donatello, A. Palomo, A. Fernández-Jiménez, Durability of very high volume fly ash cement pastes and mortars in aggressive solutions, *Cement and Concrete Composites*, 38 (2013), 12–20
- R. O. Yusuf, T. A. Salawudeen, Pozzolanic properties of calcareous clay in blended cement pastes, *Global Jour. of Eng. Techn.*, 2 (2009) 2, 161–166
- C. Samanta, M. K. Chatterjee, Sulfate resistance of Portland-pozzolanic cements in relation to strength, *Cement and Concrete Research*, 12 (1982), 726–734
- I. Janotka, L. Krajčiči, Sulphate resistance and passivation ability of the mortar made from pozzolan cement with zeolite, *Journal of Thermal Analyses and Calorimetry*, 94 (2008) 1, 7–14
- EN 197-1:2011, Cement. Composition, specifications and conformity criteria for common cements, 2011
- W. Ma, W. P. Brown, Hydrothermal reactions of fly ash with Ca(OH)₂ and CaSO₄·2H₂O, *Cement and Concrete Research*, 27 (1997) 8, 1237–1248

- ¹⁰ A. Knutsson, Freeze/thaw durability of concrete with fly ash, Master of Science Thesis, Chalmers University of Technology, Gothenburg, 2010, 99
- ¹¹ I. Papayianni, E. K. Anastasiou, An investigation of the behaviour of raw calcareous fly ash in mortar mixtures, *Coal Combustion and Gasification Products*, 2 (2010), 9–14
- ¹² EN 1015-3:2001, Methods of test for mortar for masonry - Part 3: Determination of consistence of fresh mortar (by flow table), 2001
- ¹³ EN 1015-6:1999, Methods of test for mortar for masonry - Part 6: Determination of bulk density of fresh mortar, 1999
- ¹⁴ EN 1015-7:1999, Methods of test for mortar for masonry - Part 7: Determination of air content of fresh mortar, 1999
- ¹⁵ EN 196-1:2005, Methods of testing cement — Part 1: Determination of strength, 2005
- ¹⁶ A. Koch, H. Steinegger, A rapid test for cements for their behaviour under sulphated attack, *Zement-Kalk-Gips*, 7 (1960), 317–324
- ¹⁷ SIST 1026:2008, Concrete-part 1: Specification, performance, production and conformity – Rules for the implementation of SIST EN 206-1 (Revised edition), 2008
- ¹⁸ EN 13295:2004, Products and systems for the protection and repair of concrete structures - Test methods - Determination of resistance to carbonation, 2004
- ¹⁹ G. R. de Sensale, Effect of rice-husk ash on durability of cementitious materials, *Cement and Concrete Composites*, 32 (2010) 9, 18–25
- ²⁰ U. Schneider, S. W. Chen, Behaviour of high performance concrete (HPC) under ammonium nitrate solution and sustained load, *ACI Materials Journal*, 96 (1999) 1, 47–51
- ²¹ J. Khunthongkeaw, S. Tangemsirikul, T. Leewat, A study on carbonation depth prediction for fly ash concrete, *Construction and Building Materials*, 20 (2006), 744–753

ESTIMATION OF THE EFFECTIVE BORON-DIFFUSION COEFFICIENT IN THE Fe₂B LAYERS GROWN ON GRAY CAST IRON

DOLOČANJE EFEKTIVNEGA KOEFICIENTA DIFUZIJE BORA PRI RASTI PLASTI Fe₂B NA SIVEM LITEM ŽELEZU

Boudjema Bouarour¹, Mourad Keddami¹, Omar Allaoui²

¹Laboratoire de Technologie des Matériaux, Département de Sciences des Matériaux, Faculté de Génie Mécanique et Génie des Procédés, USTHB, B.P N°32, 16111, El-Alia, Bab-Ezzouar, Algiers, Algeria

²Laboratoire de Génie des Procédés, Université Amar Tellidji de Laghouat, B.P. 37 G, 03000 Laghouat, Algeria
keddami@yahoo.fr

Prejem rokopisa – received: 2013-09-29; sprejem za objavo – accepted for publication: 2013-10-09

The present work evaluates the effective diffusion coefficient of boron in the Fe₂B layers grown on a substrate from gray cast iron. The boride layers were generated using powder-pack boriding in the temperature range of 1173–1273 K for (2, 4, 6 and 8) h of treatment. First, the diffusion coefficient of boron in Fe₂B (free of chemical stresses) was obtained through solving the mass-balance equation at the (Fe₂B/substrate) interface using the experimental values of parabolic-growth constants taken from the literature.

Second, a simple equation was derived to evaluate the effective diffusion coefficient of boron in Fe₂B by considering the effect of chemical stresses. The estimated values of boron activation energies were 154.8 kJ/mol and 164.8 kJ/mol with and without the presence of chemical stresses. Furthermore, the calculated values of effective diffusion coefficients were found to be sensitive to the change in the boriding temperature and to the increase in the upper boron concentration in Fe₂B.

Keywords: boriding, chemical stresses, kinetics, Fick's law, effective diffusion coefficient, incubation time

To delo ocenjuje efektivni koeficient difuzije bora v plasteh Fe₂B, zraslih na podlagi iz sivega litega železa. Boridne plasti so nastale med boriranjem v prahu v škatli, v temperaturnem območju 1173–1273 K in trajanju (2, 4, 6 in 8) h. Najprej je bil določen koeficient difuzije bora v Fe₂B (brez kemijskih napetosti) z rešitvijo enačbe za masno ravnotežje (Fe₂B/podlaga) na stiku z uporabo eksperimentalnih vrednosti za konstanto parabolične rasti, dobljeno v literaturi.

Nato je bila izpeljana enostavna enačba za oceno efektivnega koeficienta difuzije bora v Fe₂B z upoštevanjem kemijskih napetosti. Določeni sta bili vrednosti aktivacijske energije bora 154,8 kJ/mol in 164,8 kJ/mol s kemijskimi napetostmi in brez njih. Ugotovljeno je bilo tudi, da so izračunane vrednosti efektivnega koeficienta difuzije občutljive za spremembo temperature boriranja in za naraščanje koncentracije bora v Fe₂B.

Ključne besede: boriranje, kemijske napetosti, kinetika, Fickov zakon, efektivni koeficient difuzije, čas inkubacije

1 INTRODUCTION

Boriding is a well-known thermochemical treatment for creating boride layers with interesting properties by saturating the surface layer of a material with boron. It is used to improve the surface hardness, the frictional wear, the fatigue endurance and the corrosion resistance of ferrous and non-ferrous alloys. It can be performed between 1123 K and 1323 K to form iron borides on the material surface with the treatment times varying from 0.5 h to 10 h¹. Different boriding methods exist in practice. However, the powder-pack boriding has the advantages of simplicity, flexibility with respect to the powder composition, minimum equipment and cost-effectiveness.²⁻⁴

The boriding temperature, the time duration, the boron potential of the medium and the chemical composition of the substrate are the key parameters controlling the morphology, the growth kinetics and the microstructural nature of boride layers.⁵⁻⁷

The present model considers the effect of chemical stresses when evaluating the effective diffusion coefficient of boron in the Fe₂B layers grown on a gray-cast-

iron substrate. In this context, some recent reference studies regarding the evaluation of the effective diffusion coefficient of boron in Fe₂B were reported for borided AISI 1018 and AISI 4140 steels and borided Armco iron.⁸⁻¹⁰

Certain reference works^{11,12} report on the chemical stresses resulting from the composition gradient similar to those caused by the thermal stresses in an isotropic medium. Diffusion-induced stresses (or chemical stresses) are then built up due to the composition inhomogeneity during mass transfer. Diffusion-induced stresses also change the mechanical properties of metal systems during mass transfer. Larché and Cahn¹³⁻¹⁵ investigated the stresses arising from the inhomogeneities of materials. Consequently, chemical stresses enhance both the diffusion coefficient and the concentration.¹⁶

The objective of this work was to evaluate the diffusivity of boron in Fe₂B (with and without the presence of chemical stresses) in the temperature range of 1173–1273 K by applying a kinetic model of a monolayer configuration of Fe₂B grown on gray cast iron.

2 MATHEMATICAL MODEL

A schematic non-linear concentration profile of boron in the Fe₂B layer is depicted in **Figure 1** where the boron potential allows the formation of Fe₂B on the surface of the material.

$C_{up}^{Fe_2B}$ denotes the upper boron concentration in Fe₂B, $C_{low}^{Fe_2B}$ ($= 59.2 \times 10^3 \text{ mol m}^{-3}$) represents the lower boron concentration in Fe₂B and $t_0(T)$ is the boride incubation time depending on the boriding temperature. C_{ads} is defined as the effective boron concentration¹⁷. Distance u is the layer depth at the (Fe₂B/substrate) interface as a function of treatment time t . C_0 is the boron solubility in the matrix. The upper boron concentration in Fe₂B is between $59.2 \times 10^3 \text{ mol m}^{-3}$ and $60 \times 10^3 \text{ mol m}^{-3}$ since this phase exhibits a narrow composition range as pointed out by Massalski¹⁸.

When building a mathematical model of the problem, the following assumptions are made:

- The growth kinetics is controlled by the boron diffusion in the Fe₂B layer
- The growth of the Fe₂B boride layer is a consequence of the boron diffusion perpendicular to the sample surface
- The solid solution of boron in the matrix behaves ideally (i.e., the activity coefficient of boron in the solid solution is independent on the concentration)
- The Fe₂B iron boride nucleates after a certain incubation time
- The boride layer is thin in comparison to the sample thickness
- Local equilibrium is held at the (Fe₂B/substrate) interface
- A planar morphology is assumed for the (Fe₂B/substrate) interface
- The volume change during the phase transformation is neglected

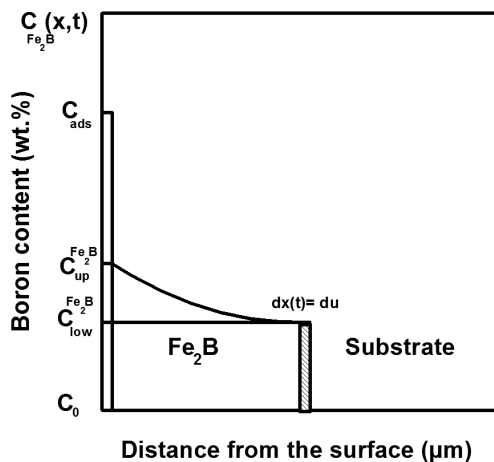


Figure 1: Schematic non-linear concentration profile of boron in the Fe₂B layer

Slika 1: Shematični prikaz nelinearnega profila koncentracije bora skozi plast Fe₂B

- A uniform temperature is assumed throughout the sample
- No effect of the alloying elements on the boron diffusion is assumed
- The pressure effect on the boron effective diffusion coefficient in Fe₂B is ignored

The initial condition of the diffusion problem is expressed with Equation (1):

$$C_{Fe_2B}(x,0) = C_0 \quad (1)$$

The boundary conditions of the diffusion problem are given with Equations (2) and (3):

$$C_{Fe_2B} \left\{ x \left[t = t_0(T) \right] = 0, t_0(T) \right\} = C_{up}^{Fe_2B} \quad (2)$$

for $C_{ads} > 59.2 \times 10^3 \text{ mol m}^{-3}$

$$C_{Fe_2B} \left\{ x(t=t) = u, t \right\} = C_{low}^{Fe_2B} \quad (3)$$

for $C_{ads} < 59.2 \times 10^3 \text{ mol m}^{-3}$

for $0 \leq x \leq u$.

The Fick's second law of diffusion¹⁹ relating to the change in the boron concentration throughout the Fe₂B layer with time t and location $x(t)$ is:

$$\frac{\partial C_{Fe_2B}(x,t)}{\partial t} = D_B^{Fe_2B} \frac{\partial^2 C_{Fe_2B}(x,t)}{\partial x^2} \quad (4)$$

where $D_B^{Fe_2B}$ is the diffusion coefficient of boron in Fe₂B free of chemical stresses and $C_{Fe_2B}(x,t)$ is the boron concentration. The boron concentration along the boride layer, which is the solution of the Fick's second law (Equation (4)) in a semi-infinite medium, is consistent with **Figure 1**. Its expression is given with Equation (5):

$$C_{Fe_2B}(x,t) = C_{up}^{Fe_2B} + \left(\frac{C_{low}^{Fe_2B} - C_{up}^{Fe_2B}}{u} \right) \cdot \text{erf} \left(\frac{x}{2\sqrt{D_B^{Fe_2B} \cdot t}} \right) \quad (5)$$

for $0 \leq x \leq u$.

The continuity equation at the (Fe₂B/substrate) interface is expressed with Equation (6):

$$w_{Fe_2B} \left[\frac{dx}{dt} \right]_{x=u} = -D_B^{Fe_2B} \left[\frac{\partial C_{Fe_2B}}{\partial x} \right]_{x=u} \quad (6)$$

with $w_{Fe_2B} = [0.5 \times (C_{up}^{Fe_2B} + C_{low}^{Fe_2B}) - C_0]$.

Boride layer thickness u follows the parabolic-growth law expressed with Equation (7), where k represents the parabolic-growth constant at the (Fe₂B/substrate) interface:

$$u = k \sqrt{t - t_0(T)} \quad (7)$$

where $[t - t_0(T)]$ is considered as the effective growth time of the Fe₂B layer^{9,10,20-22}. According to Brakman et al.²³, boride incubation time $t_0(T)$ is decreased as the temperature goes up. The $\beta(T)$ parameter, which takes

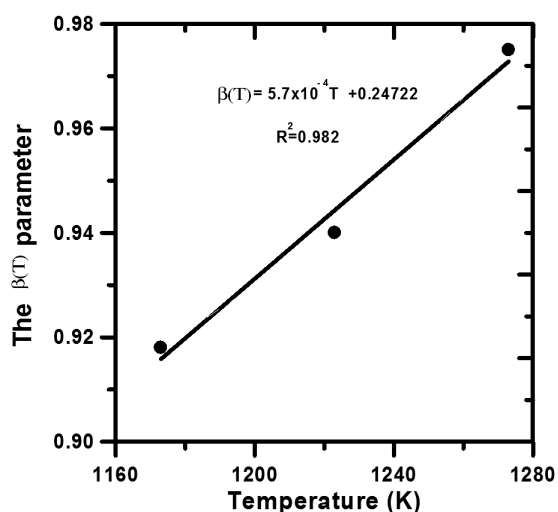


Figure 2: Temperature dependence of the $\beta(T)$ parameter
Slika 2: Temperaturna odvisnost parametra $\beta(T)$

into account the effect of the boride incubation time, is given with Equation (8):

$$\beta(T) = k\sqrt{1 - \frac{t_0(T)}{t}} \quad (8)$$

The $\beta(T)$ parameter can be approached with a linear relationship (Equation (9)), illustrated also in **Figure 2** (with a correlation factor = 0.982):

$$\beta(T) = (5.7 \times 10^{-4} T + 0.24722) \quad (9)$$

By derivation of Equation (5) with respect to distance $x(t)$ and Equation (7) with respect to time t , Equation (6) can be rewritten²⁴ as follows:

$$\begin{aligned} & [0.5(C_{\text{up}}^{\text{Fe}_2\text{B}} + C_{\text{low}}^{\text{Fe}_2\text{B}}) - C_0]k = \\ & = 2\sqrt{\frac{D_{\text{B}}^{\text{Fe}_2\text{B}}}{\pi}} \cdot \frac{(C_{\text{low}}^{\text{Fe}_2\text{B}} - C_{\text{up}}^{\text{Fe}_2\text{B}})}{\text{erf} \frac{k\beta(T)}{2\sqrt{D_{\text{B}}^{\text{Fe}_2\text{B}}}}} \cdot \exp\left(-\frac{\beta^2(T)k^2}{4D_{\text{B}}^{\text{Fe}_2\text{B}}}\right) \cdot \beta(T) \quad (10) \end{aligned}$$

To evaluate the diffusion coefficient of boron in Fe_2B $D_{\text{B}}^{\text{Fe}_2\text{B}}$ (free of chemical stresses), it is necessary to use the Newton-Raphson routine²⁵ to solve the problem.

For this purpose, a computer program was written in Matlab (version 6.5) to find the roots of Equation (10). By ignoring the pressure effect on diffusion, the effective diffusion coefficient of boron in Fe_2B (see reference¹⁰ for more details) can be evaluated from Equation (11) as follows:

$$D_{\text{B}}^{\text{eff}} = D_{\text{B}}^{\text{Fe}_2\text{B}} \left[1 + \frac{2C_{\text{Fe}_2\text{B}}(x,t)\bar{V}^2 E}{9RT(1-\nu)} \right] \quad (11)$$

where $D_{\text{B}}^{\text{eff}}$ and $D_{\text{B}}^{\text{Fe}_2\text{B}}$ are the diffusion coefficients of boron in Fe_2B with and without the chemical stresses, respectively. The origin of Equation (11) can be found elsewhere in^{13–15}.

Since the solid solution of boron in the matrix is ideal, the second term in Equation (11) is positive regardless of \bar{V} . Partial molar volume \bar{V} is taken to be equal to $(1.01 \times 10^{-5} \text{ m}^3 \text{ mol}^{-1})$.²⁶

$E = 290 \text{ GPa}$ and $\nu = 0.3$ are the Young's modulus and Poisson's ratio of the Fe_2B layer, respectively^{27,28}. Taking the mean value of the boron concentration throughout the Fe_2B layer¹⁰, i.e.,

$C_{\text{Fe}_2\text{B}}(x,t) = [0.5 \times (C_{\text{up}}^{\text{Fe}_2\text{B}} + C_{\text{low}}^{\text{Fe}_2\text{B}})]$, Equation (11) yields:

$$D_{\text{B}}^{\text{eff}} = D_{\text{B}}^{\text{Fe}_2\text{B}} \left[1 + \frac{\bar{V}^2 (C_{\text{up}}^{\text{Fe}_2\text{B}} + C_{\text{low}}^{\text{Fe}_2\text{B}}) E}{9RT(1-\nu)} \right] \quad (12)$$

3 RESULTS AND DISCUSSION

To evaluate the diffusion coefficient of boron in Fe_2B using Equation (10), the experimental results found in the reference work²⁹ in terms of the parabolic growth constants at the (Fe_2B / substrate) interface and boride incubation times were used. The chemical composition (in mass fractions) of the gray cast iron (class 30, ASTM A48) to be borided is the following: (3.44–3.45 % C, 1.7–1.77 % Si, 0.5–0.6 % Mn, 0.2 % Cr, 0.45–0.5 % Cu). The boriding process was performed on the gray cast iron under an argon atmosphere in a conventional furnace at three temperatures (1173, 1223 and 1273) K and for variable times (2, 4, 6 and 8) h. The boriding medium is composed of boron carbide (B_4C) as the boron source and KBF_4 as the activator. Fifty measurements were taken on different cross-sections of the borided samples of the gray cast iron to estimate the thickness of the Fe_2B layer. As the input data, the model uses the following parameters: the time, the temperature, the upper and lower boron concentrations in the Fe_2B iron boride and the experimental values of the parabolic

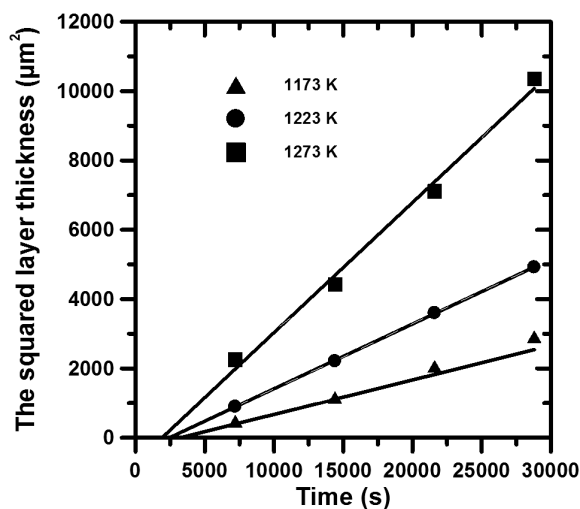


Figure 3: Evolution of the squared value of the Fe_2B layer thickness versus the boriding time at different temperatures

Slika 3: Razvoj kvadratne vrednosti debeline plasti Fe_2B v odvisnosti od časa boriranja pri različnih temperaturah

growth constants at the (Fe₂B/substrate) interface. The effective diffusion coefficient of boron in Fe₂B was estimated on the basis of Equation (12). **Figure 3** shows the squared value of the experimental boride-layer thickness as a function of the boriding time, according to Equation (13):

$$u^2 = k^2 [t - t_0(T)] \quad (13)$$

The squared values of parabolic-growth constants (k^2) are obtained from the slopes of the straight curves using the least-square method. The intercept with the abscissa determines the boride incubation time at each temperature.

Table 1 gives the experimental values of parabolic-growth constants k in the temperature range of 1173–1273 K, along with the corresponding boride incubation times deduced from **Figure 3**.

Table 1: Experimental values of parabolic-growth constants at the Fe₂B/substrate interface with the corresponding boride incubation times

Tabela 1: Eksperimentalne vrednosti konstant parabolične rasti na stiku Fe₂B/podlaga z ustreznimi inkubacijskimi časi boriranja

T/K	Experimental parabolic-growth constant $k/\mu\text{m s}^{-0.5}$	Incubation boride time (s)
1173	0.3150	3200
1223	0.4321	2428
1273	0.6122	1902

Table 2 lists the simulated values of $D_B^{\text{Fe}_2\text{B}}$ and D_B^{eff} obtained at each boriding temperature using Equations (10) and (12), for the upper value of the boron content in Fe₂B¹⁰ being equal to $59.80 \times 10^3 \text{ mol m}^{-3}$.

Table 2: Computed values of the boron-diffusion coefficients for Fe₂B and the effective diffusion coefficients of boron in Fe₂B, for the upper boron content in the Fe₂B phase equal to $59.80 \times 10^3 \text{ mol m}^{-3}$

Tabela 2: Izračunane vrednosti koeficientov difuzije bora v Fe₂B in efektivni koeficienti difuzije bora v Fe₂B za zgornjo vsebnost bora v Fe₂B fazi $59,80 \times 10^3 \text{ mol m}^{-3}$

T/K	$D_B^{\text{Fe}_2\text{B}}/(\text{m}^2 \text{ s}^{-1})$ using Eq.(10)	$D_B^{\text{eff}}/(\text{m}^2 \text{ s}^{-1})$ using Eq.(12)
1173	6.31×10^{-12}	3.67×10^{-10}
1223	11.881×10^{-12}	6.64×10^{-10}
1273	23.86×10^{-12}	12.82×10^{-10}

When incorporating the effect of chemical stresses on the boron diffusion, the effective diffusion coefficient of boron in Fe₂B is increased with the boriding temperature. So, the dependence between the diffusivity of boron in Fe₂B and the boriding temperature can be expressed with the Arrhenius equation. The temperature dependence of the diffusivity of boron in Fe₂B is then depicted in **Figure 4**. The activation energy of boron (with and without the presence of chemical stresses) can be easily obtained from **Figure 4**.

As a result, the diffusion coefficient of boron in Fe₂B in the temperature range of 1173–1273 K is given with:

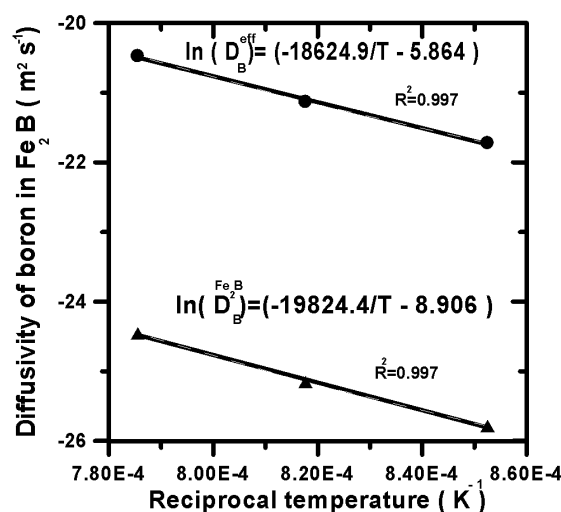


Figure 4: Temperature dependence of the diffusivity of boron in Fe₂B
Slika 4: Temperaturna odvisnost difuzivnosti bora v Fe₂B

$$D_B^{\text{eff}} = 1.35 \times 10^{-4} \exp \frac{-164.8 \text{ kJ/mol}}{RT} \text{ m}^2/\text{s} \quad (14)$$

The effective diffusion coefficient of boron in Fe₂B is also determined as:

$$D_B^{\text{eff}} = 2.8 \times 10^{-3} \exp \frac{-154.8 \text{ kJ/mol}}{RT} \text{ m}^2/\text{s} \quad (15)$$

where R is the universal gas constant (8.314 J/mol K) and T represents the absolute temperature. The boron activation energy obtained in this work, in the absence of chemical stresses, was compared with the values found in the literature^{29–34}.

Table 3 shows a comparison of the boron activation energies (in the absence of chemical stresses) obtained from different borided materials. The reported values in **Table 3** differ from each other depending on different factors such as the chemical composition of the substrate, the boriding method and the kinetic approach used to estimate the boron activation energy.

Table 3: Comparison of the boron activation energies (in the absence of chemical stresses) for borided ferrous alloys

Tabela 3: Primerjava aktivacijskih energij bora (pri odsotnosti kemijskih napetosti) za primere boriranja zlitin železa

Material	Boron activation energy (kJ mol ⁻¹)	Reference
Armco iron	151	30
Armco iron	157	31
AISI H13	186.2	32
AISI 1045	169.6	33
Gray cast iron	177.4	29
Gray cast iron	175	34
Gray cast iron	164.8	Present work

It is seen that the calculated value of the boron activation energy (154.8 kJ mol⁻¹) under chemical stresses is lower than the one for 164.8 kJ mol⁻¹ due to an enhancement of the boron diffusion. The temperature dependence of the computed values of the effective

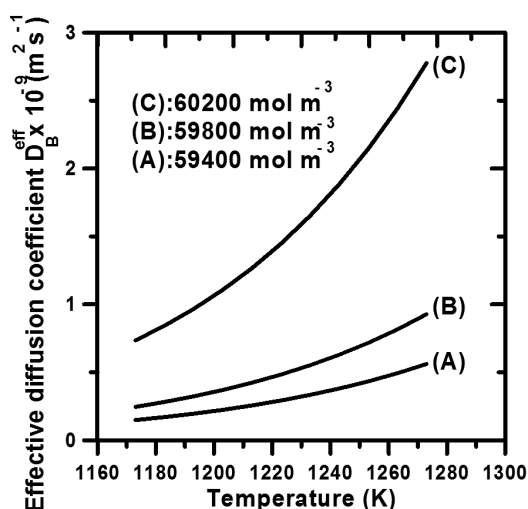


Figure 5: Temperature dependence of the computed values of the effective diffusion coefficient of boron in Fe_2B for the increasing values of $C_{\text{up}}^{\text{Fe}_2\text{B}}$

Slika 5: Temperaturna odvisnost izračunanih vrednosti efektivnega koeficienta difuzije bora v Fe_2B pri naraščajočih vrednostih $C_{\text{up}}^{\text{Fe}_2\text{B}}$

diffusion coefficient of boron in Fe_2B for the increasing values of the upper boron contents in Fe_2B is shown in **Figure 5**.

With the presence of chemical stress, the diffusion of boron atoms is accelerated with an increase in the boriding temperature since the diffusion process is a thermally activated phenomenon. At a given value of the upper boron content in Fe_2B , the computed values of $D_{\text{B}}^{\text{eff}}$ are affected by the change in the boriding temperature.

The variation in the calculated values of the effective diffusion coefficient of boron in Fe_2B as a function of the

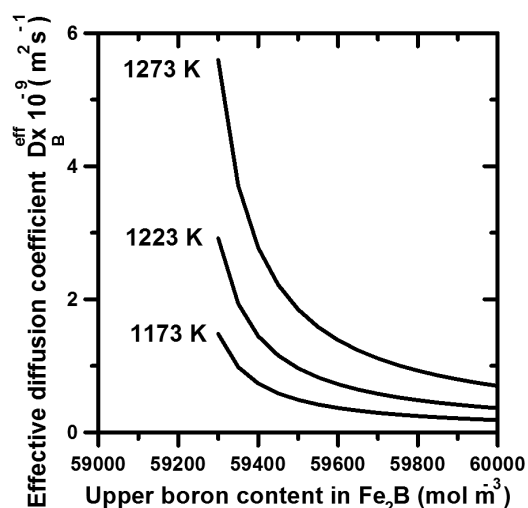


Figure 6: Variation in the calculated values of effective diffusion coefficients of boron in Fe_2B as a function of the upper boron content in the same phase for different boriding temperatures

Slika 6: Spreminjanje izračunanih vrednosti efektivnega koeficienta difuzije bora v Fe_2B v odvisnosti od zgornje vsebnosti bora v isti fazi pri različnih temperaturah boriranja

upper boron content in the same phase ($C_{\text{up}}^{\text{Fe}_2\text{B}}$) is displayed in **Figure 6** for different boriding temperatures. The effective diffusion coefficient of boron in Fe_2B is decreased with an increase in the upper boron content in Fe_2B . It can be explained with the saturation of the material surface with the active boron atoms for longer boriding times. It is concluded that the calculated values of the effective diffusion coefficients of boron in Fe_2B vary notably with the upper boron content in Fe_2B at a fixed boriding temperature.

4 CONCLUSION

In the present work, the diffusion coefficient of boron in the Fe_2B layers grown on gray cast iron was estimated through the mass-balance equation at the (Fe_2B /substrate) interface under certain assumptions. The model included the effect of boride incubation times by forming the Fe_2B layers. Afterwards, the boron effective diffusion coefficient in Fe_2B was evaluated by applying a simple equation based on the elasticity theory.

A lower value of the boron activation energy under chemical stresses was obtained ($154.8 \text{ kJ mol}^{-1}$) for an upper boron content in Fe_2B equal to $59.80 \times 10^3 \text{ mol m}^{-3}$. This result is a consequence of the chemical stresses enhancing the boron diffusion through the Fe_2B layers.

In addition, it is also shown that the calculated values of the boron effective diffusion coefficient in Fe_2B vary notably with the boriding temperature. The values of the boron effective diffusion coefficients in Fe_2B are found to be decreased with an increase in the upper boron content in Fe_2B at a given boriding temperature.

The model can be reformulated to be applied to a bilayer configuration ($\text{FeB} + \text{Fe}_2\text{B}$) as an extension of the present work to estimate the boron diffusion coefficients for the FeB and Fe_2B layers in borided ferrous alloys, incorporating the effect of chemical stresses.

5 REFERENCES

- 1 A. K. Sinha, *J. Heat Treat.*, 4 (1991), 437
- 2 M. Keddad, S. M. Chentouf, *Applied Surf. Sci.*, 255 (2005), 393–399
- 3 B. Selcuk, R. Ipek, M. B. Karamis, V. Kuzucu, *J. Mater. Process. Technol.*, 103 (2000), 310–317
- 4 S. Taktak, *Mater. Des.*, 28 (2007), 1836–1843
- 5 G. Palombarini, M. Carbucicchio, *J. Mater. Sci. Lett.*, 3 (1984), 791–794
- 6 C. Martini, G. Palombarini, M. Carbucicchio, *J. Mater. Sci.*, 39 (2004), 933–937
- 7 Y. Gencer, *Surf. Eng.*, 27 (2011), 634–638
- 8 M. Ortiz-Dominguez, I. Campos-Silva, G. Ares De Parga, J. Martínez-Trinidad, *Kovove Mater.*, 50 (2012), 115–123
- 9 M. Keddad, B. Bouarour, Z. Nait Abdellah, R. Chegroune, *MATEC Web of Conferences*, 3 (2013), 01012, <http://dx.doi.org/10.1051/mateconf/20130301012>
- 10 Z. Nait Abdellah, M. Keddad, A. Elias, *International Journal of Materials Research*, 104 (2013), 260–265

- ¹¹ J. C. M. Li, *Metall. Trans. A*, 9A (1978), 1353–1380
- ¹² S. Prussin, *J. Appl. Phys.*, 32 (1961), 1876–1881
- ¹³ F. C. Larché, J. W. Cahn, *Acta Metall.*, 33 (1985), 331–357
- ¹⁴ F. C. Larché, J. W. Cahn, *J. Res. Natl. Bur. Stand.*, 89 (1984), 467–500
- ¹⁵ F. C. Larché, P. W. Voorhees, *Defect Diffus. Forum*, 129–130 (1996), 31–36
- ¹⁶ J. L. Chu, S. Lee, *J. Appl. Phys.*, 75 (1994), 2823–2829
- ¹⁷ L. G. Yu, X. J. Chen, K. A. Khor, *Acta Mater.*, 53 (2005), 2361–2368
- ¹⁸ T. B. Massalski, *Binary Alloys Phase diagrams*, 2nd ed., ASM International Metals Park, OH 1990
- ¹⁹ J. Crank, *The Mathematics of Diffusion*, Clarendon, Oxford 1975
- ²⁰ I. Campos-Silva, M. Ortiz-Domínguez, O. Bravo-Bárceñas, M. A. Donu-Ruiz, D. Bravo-Bárceñas, C. Tapia-Quintero, M. Y. Jiménez-Reyes, *Surf. Coat. Technol.*, 205 (2010), 403–412
- ²¹ M. Keddad, *Appl. Surf. Sci.*, 257 (2011), 2004–2010
- ²² Z. Nait Abdellah, M. Keddad, A. Elias, *Acta Physica Polonica A*, 122 (2012), 588–592
- ²³ C. M. Brakman, A. J. W. Gommers, E. J. Mittemeijer, *J. Mater. Res.*, 4 (1989), 1354–1370
- ²⁴ Z. Nait Abdellah, M. Keddad, R. Chegroune, B. Bouarour, L. Haddour, A. Elias, *Matériaux et Techniques*, 100 (2012), 581–588
- ²⁵ W. H. Press, B. P. Flannery, S. A. Teukolsky, *Numerical recipes in Pascal: the art of scientific computing*, Cambridge University Press, 1989
- ²⁶ S. P. Timoshenko, J. N. Goodier, *Theory of Elasticity*, Third Edition, McGraw-Hill, New York 1970
- ²⁷ I. N. Frantzevich, F. F. Voronov, S. A. Bakuta, *Elastic constants and elastic modulus for metals and non-metals: Handbook*, First Ed., Naukova Dumka Press, Kiev 1982
- ²⁸ D. Golanski, A. Marczuk, T. Wierzchon, *J. of Mater. Science Letters*, 14 (1995), 1499–1501
- ²⁹ I. Campos-Silva, N. López-Perrusquia, M. Ortiz-Domínguez, U. Figueroa-López, O. A. Gómez-Vargas, A. Meneses-Amador, G. Rodríguez-Castro, *Kovove Mater.*, 47 (2009), 75–81
- ³⁰ I. Campos, J. Oseguera, U. Figueroa, J. A. García, O. Bautista, G. Keleminis, *Mater. Sci. Eng. A*, 352 (2003), 261–265
- ³¹ I. Campos-Silva, M. Ortiz-Domínguez, H. Cimenoglu, R. Escobar-Galindo, M. Keddad, M. Elías-Espinosa, N. López-Perrusquia, *Surf. Eng.*, 27 (2011), 189–195
- ³² K. Genel, *Boriding Vacuum*, 80 (2006), 451–457
- ³³ I. Campos, O. Bautista, G. Ramirez, M. Islas, J. De La Parra, L. Zuniga, *Appl. Surf. Sci.*, 243 (2005), 429–436
- ³⁴ I. Campos-Silva, M. Ortiz-Domínguez, M. Keddad, N. López-Perrusquia, A. Carmona-Vargas, M. Elias-Espinosa, *Appl. Surf. Sci.*, 255 (2009), 9290–9295

OPTIMIZATION OF THE SECONDARY COOLING IN A CONTINUOUS CASTING PROCESS WITH DIFFERENT SLAB CROSS-SECTIONS

OPTIMIZACIJA SEKUNDARNEGA HLAJENJA PRI KONTINUIRNEM ULIVANJU SLABOV Z RAZLIČNIMI PREREZI

Tomas Mauder, Josef Stetina

Brno University of Technology, Faculty of Mechanical Engineering, Technicka 2, Brno, Czech Republic
mauder@fme.vutbr.cz

Prejem rokopisa – received: 2013-09-30; sprejem za objavo – accepted for publication: 2013-10-28

Although the continuous casting of steel began almost 60 years ago, its production still suffers from many serious defects in the final structure. Cracks in the solidifying slab are mainly caused by variable thermal conditions and mechanical stresses. It is well known that the secondary cooling zone has an important effect on the internal and surface quality. Thus, the optimal control of the cooling intensity in secondary cooling is inevitable in order to obtain high-quality products. Nowadays, the control of the slab temperature via numerical temperature-field models is a common practice for controlling the quality of the slabs. This leads to cooling regulation according to the actual casting speed, casting temperature, cross-section of casting slab, chemical composition of steel, etc. Unfortunately, the actual practice in many steelworks is that the cooling regulation is determined as a simple linear function of the casting speed. In order to deal with this problem, the fuzzy-optimization algorithm and numerical model of the temperature field were created. Their combination can provide instructions for how to control the secondary cooling and obtain high-quality of steel. This paper mainly describes the differences between the optimal cooling of different slab cross-sections (width between 800 mm and 1600 mm, thickness between 180 mm and 250 mm). The results show that the proper setting of secondary cooling cannot be done without a consideration of all the main casting factors.

Keywords: secondary cooling, fuzzy optimization, temperature field, continuous casting

Čeprav je kontinuirano ulivanje jekla poznano že skoraj 60 let, se v proizvodnji še vedno pojavljajo številne resne napake slabov. Razpoke pri strjevanju slaba so v glavnem posledica spremenljivih toplotnih razmer in mehanskih napetosti. Znano je, da ima sekundarna hladilna cona pomemben učinek na kakovost notranjosti in površine. Zato je za visoko kakovost proizvoda neizogibna optimalna kontrola intenzivnosti sekundarnega hlajenja. Danes se zagotavlja kontrola slabov z uporabo numeričnih modelov temperaturnega polja. To vodi do regulacije ohlajanja, skladno z dejansko hitrostjo ulivanja, temperaturo ulivanja, prereza ulitega slaba, kemijske sestave jekla itd. Da bi obvladali te težave, sta bila postavljena algoritem mehke optimizacije in numerični model temperaturnega polja. Njuna kombinacija lahko da napotke, kako kontrolirati sekundarno hlajenje in zagotoviti veliko kvaliteto jekla. Ta članek opisuje razlike med optimalnim ohlajanjem različnih prerezov slabov (širine med 800 mm in 1600 mm in debeline med 180 mm in 250 mm). Rezultati kažejo, da pravilna nastavitve sekundarnega hlajenja ni mogoča brez upoštevanja glavnih dejavnikov pri ulivanju.

Ključne besede: sekundarno hlajenje, mehka optimizacija, temperaturno polje, kontinuirano ulivanje

1 INTRODUCTION

Nowadays, more than 95 % of the world's steel production is being produced by continuous casting (CC).^{1,2} Using CC molten steel is formed into semi-finished products such as slabs, blooms and billets. The CC installation is divided into three parts. The water-cooled mold (primary cooling zone), secondary cooling where the steel is transported by rollers and cooled down by groups of nozzles, and the tertiary cooling zone where the surface is cooled down by free convection and radiation only. The importance of the intensity of cooling in the secondary cooling is well known and has been discussed in many papers.^{1,3,4} These papers give the casting recommendations and possible mathematical tools which can be applied in the real system.

Unfortunately, the practice in many steel works does not reflect the actual state of the art in this field and the regulation of the secondary cooling is far from optimum. There can be many reasons for this. Some steel workers

are not progressive enough; many papers are rather theoretical and the validation is not sufficient; mathematical models and optimization algorithms are often less general than is necessary; etc.

This paper deals with optimal cooling curves in the secondary cooling zone for different slab cross-sections (width 800–1600 mm, thickness 180–250 mm). These cooling curves were found by using a combination of numerical modeling and the optimization technique. The next section describes the modeling concept, but for a detailed description we recommend our previous work.^{5,6}

2 DESCRIPTIONS OF THE MATHEMATICAL ALGORITHMS

The mathematical part of the research is created by two models. The first model is a numerical model of the temperature field based on the governing equation of transient heat conduction, also called the Fourier-Kirchhoff equation:^{1,5}

$$\frac{\partial H}{\partial \tau} + v \frac{\partial H}{\partial z} = \nabla(k_{\text{eff}}(T)\nabla T) \quad (1)$$

where k_{eff} (W/mK) is the effective thermal conductivity, T (K) is the temperature, H (J/m³) is the volume enthalpy, τ (s) is time and v (m/s) is the casting speed and z (m) is the direction of casting. This model represents a unique combination of numerical modeling and a large number of experimental measurements.⁷ The model is able to predict the temperature distribution in the whole slab, the solid shell thickness and the position of the metallurgical length (the distance below the meniscus). Its results are validated by measurements in the real casting process. In order to speed up the computational time, the model could run in a parallel GPU (Graphic Processing Unit) architecture.⁸

The second model is the optimization/regulation algorithm based on fuzzy logic. The model is created with the aim to optimize the parameters of the casting for a given particular grade of steel, cross-sections of the slab, casting temperature, casting speed, etc. **Figure 1** shows a block scheme of the connection between the regulator and the numerical model. The fuzzy regulator is subordinated to the numerical model and in every time iteration the regulator progressively tunes the cooling parameters as the closed-loop system.

The optimization strategy is to keep the surface and core temperatures in the specific ranges corresponding with the hot ductility of the steel.⁹ The reason for this is to avoid surface and core defects.

The presented concept creates a very general approach to optimally control any CC process (geometry of the slab, steel grades, caster geometry, casting limitation such as allowed casting speed, water flows in secondary cooling, etc.). Moreover, the algorithm can be used for both off-line and on-line regulation. The example of an optimal result is shown in **Figure 2** for the steel grade S355J0H. **Figure 2** shows the temperature distribution at the slab surface in different positions and the temperature distribution in the slab core. The black boxes are the recommended temperature intervals at the slab surface to ensure the good surface quality of the steel.

The most important indicator of iterative optimization algorithms is usually the number of evaluations of

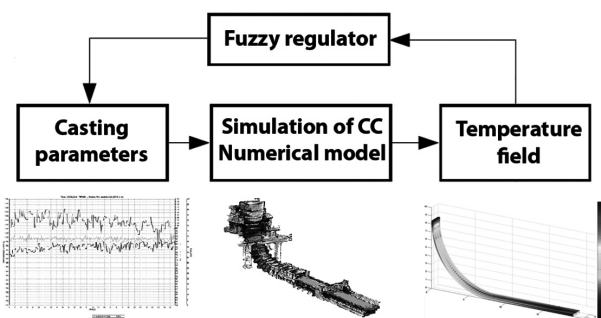


Figure 1: Block scheme of the regulation approach
Slika 1: Shematski prikaz načina regulacije

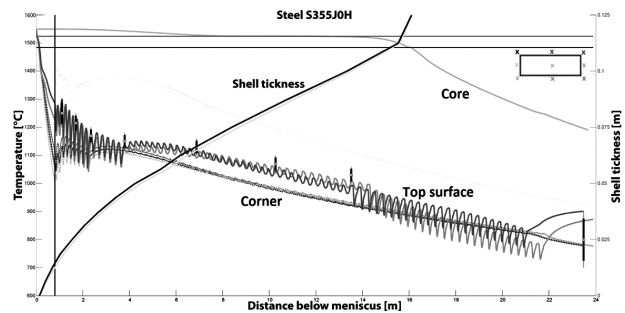


Figure 2: Temperatures distribution after fuzzy regulation
Slika 2: Razporeditev temperature po mehki regulaciji

the problem. The evaluation of the numerical model is very time consuming and therefore each repetition can significantly prolong the computation. Our algorithm was able to find the optimal parameters in less than 30 evaluations, on average. The tests were run several times for the different grades of steels and with completely random initial states and the number of evaluations never exceeded 50. The results shown in **Figure 2** were obtained after 27 evaluations.

3 RELATIONSHIP BETWEEN CASTING SPEED AND COOLING INTENSITY

The steelmakers operating with CC of slabs are forced by their customers to cast different slab cross-sections. The width of the slab is generally from 800 mm to 1600 mm and thickness of slab from 180 mm to 250 mm, depending on the caster installation. Each slab cross-section has typical defects. In order to avoid these defects the caster should be set-up with a consideration of the slab cross-section.

The casting process is influenced by many parameters, but only a few of them can be controlled in reasonable ranges. For instance, controlling the casting temperature is not really possible and the safety protocols restrict the water flows through the mold. The typical control parameters are the casting speed and the cooling intensity in the secondary cooling zone.

The goal of the optimization is to set the casting speed as high as possible and still keep the good quality of the cast steel. Controlling the surface quality can be achieved by the presented temperature intervals in certain points (the black boxes in **Figure 2**, the so-called control points), while the inner quality is influenced by the position of the metallurgical length. Thus, there are two optimization constraints: the limitation of the metallurgical length and the artificial value, the so-called maximum error (the sum of temperature residuums in the controlled points).

The search for the optimal relationship between the casting speed and the cooling intensity is simply based on a gradual increase of the casting speed (from 0.7 m/min to 1.3 m/min). The algorithm for every value of the casting speed is able to find a corresponding cooling

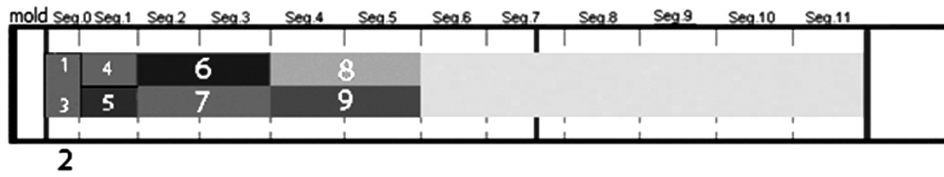


Figure 3: Position of cooling circuits
Slika 3: Položaj hladilnih tokokrogov

intensity. From the optimization results the data where the metallurgical length exceeded the given limit (from 14 m to 24 m) and where the maximum error exceeded 100 °C were discarded.

4 RESULTS AND DISCUSSION

The results were calculated for a casting machine SMS Demag. The caster specifications are in Table 1. The number of independent cooling circuits is nine, placed according to Figure 3. The examined grade of steel is typical low-carbon steel from Steel Group 4 No. 4038 specified by the chemical composition in Table 2.

Table 1: Slab caster machine specification

Tabela 1: Lastnosti naprave za ulivanje slabov

Ladle capacity	180 t
Tundish capacity	40 t
Mold level control	Berthold mould level measuring system
Torch cutting machine type	
Slab Marking Machine type	
Caster Machine has 9 cooling loops and electrical mold oscillation system	
Width	650–1880 mm
Length short slab	4.5–4.75 m
Length long slab	9.1–9.9 m

Table 2: Chemical composition of examined steel (w/%)

Tabela 2: Kemijska sestava preiskovanega jekla (w/%)

C	Si	Mn	Cr
0.190	0.250	1.350	0.035
Ni	Mo	Cu	Al
0.045	0.035	0.045	0.040
Nb	Ti	V	
0.005	0.005	0.005	

The optimal cooling curves were calculated for the three frequently cast slab cross-sections, 1600 mm × 250 mm, 1200 mm × 200 mm, and 800 mm × 180 mm. The results are shown (Figures 4 to 7) for the cooling circuits on the top surface where the risk of the occurrence of cracks is higher than on the bottom surface.

The metallurgical length and temperature intervals on the surfaces restrict the allowed casting speed range for all the simulated slab cross-sections. For instance, the slab cross-section 1600 mm × 250 mm has a recommended casting speed interval of between 0.7 m/min and 1.0 m/min. This result was expected, but the casting

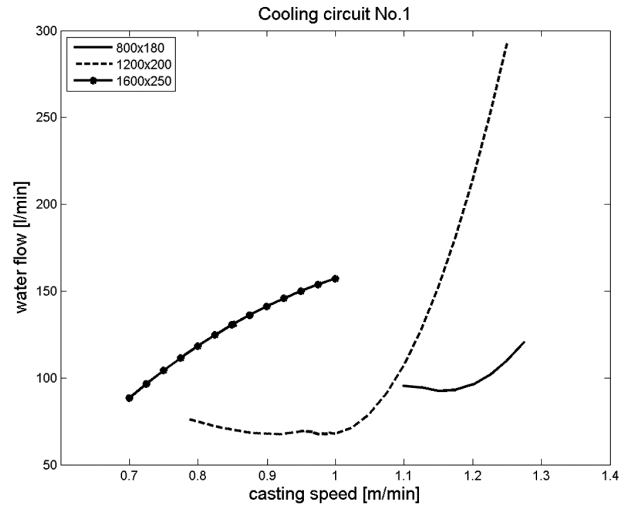


Figure 4: Optimal cooling curves for cooling circuit No. 1
Slika 4: Optimalne krivulje hlajenja za hladilni krog št. 1

limits are slightly different than the casting limits presented by the casting equipment. The most flexible casting range is for the 1200 mm × 200 mm slab, while the most critical interval is for the 800 mm × 180 mm slab, and it probably needs special treatment. There are more reasons for this, but we should realize that this caster was mainly designed to cast larger cross-sections.

The second problem is the shape of the cooling curves. The initial hypothesis that the linear relationship between the casting speed and cooling intensity is not suited is clearly seen from Figures 4 to 7. The cooling results were fitted by both linear and quadratic regression. The results with the higher value of the

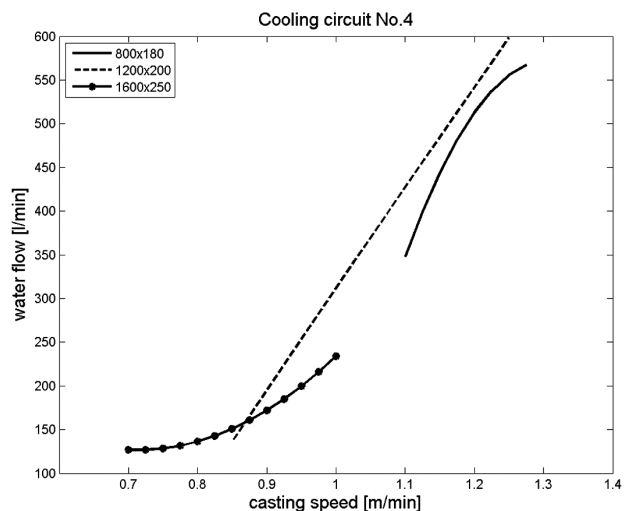


Figure 5: Optimal cooling curves for cooling circuit No. 4
Slika 5: Optimalne krivulje hlajenja za hladilni krog št. 4

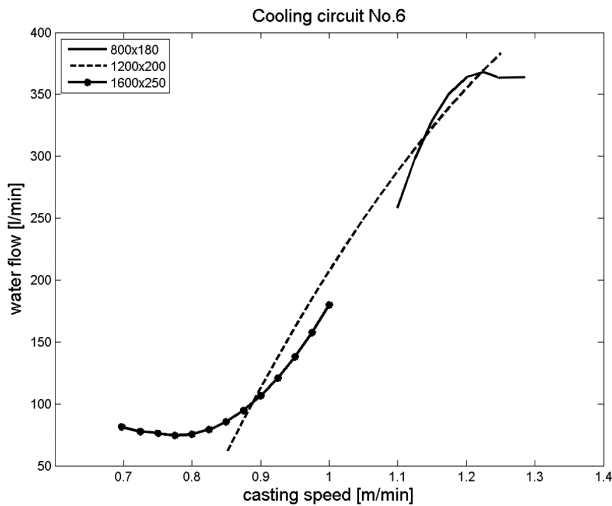


Figure 6: Optimal cooling curves for cooling circuit No. 6
Slika 6: Optimalne krivulje hlajenja za hladilni krog št. 6

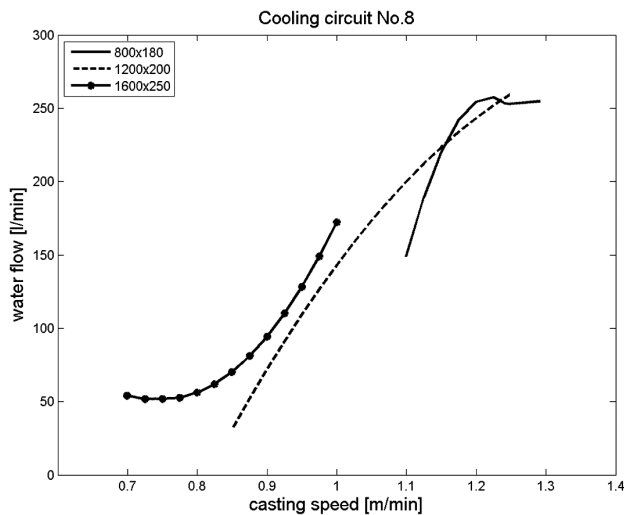


Figure 7: Optimal cooling curves for cooling circuit No. 8
Slika 7: Optimalne krivulje hlajenja za hladilni krog št. 8

coefficient of determination were chosen. Only for the cooling circuit No. 5 and for the slab cross-section 1200 mm × 200 mm the linear regression has better results than the quadratic. But the rest of them were clearly non-linear.

5 CONCLUSION

The problem of optimally cast steel for different slab cross-sections can be efficiently solved using the described algorithm. The algorithm based on numerical

modeling with fuzzy logic is very robust and is easily adaptable to any grade of steel, caster and slab geometry, etc. The results show that the casting of steel slabs should be made according to more casting indicators than just the casting speed. The cooling behavior is different for the different slab cross-sections and the steelmaker should take into account this fact. Otherwise the steel product will still be cast with the surface and the core defects.

Acknowledgement

The authors gratefully acknowledge the financial support of project ED0002/01/01 - NETME Centre, project NETME CENTRE PLUS (LO1202), Junior research project FSI-J-13-1977, project No. CZ.1.07/2.3.00/20.0188, HEATEAM - Multidisciplinary Team for Research and Development of Heat Processes and project GAP107/11/1566 founded by the Czech Science Foundation.

6 REFERENCES

- ¹ J. P. Birat et al., The Making, Shaping and Treating of Steel: Casting Volume, 11th edition, The AISE Steel Foundation, A. W. Cramb, Pittsburgh, PA, USA 2003, 1000 p.
- ² A. Flick, Ch. Stoiber, Trends in Continuous Casting of Steel – Yesterday, Today and Tomorrow, In METEC InSteelCon 2011 Proceedings, Düsseldorf, Germany, TEMA Technologie Marketing AG, 2011, 8
- ³ Y. Ito, et al., Development of Hard Secondary Cooling by High Pressure Water Spray, In METEC InSteelCon 2011 Proceedings, Düsseldorf, Germany, TEMA Technologie Marketing AG, 2011, 5
- ⁴ A. A. Ivanova, V. A. Kapitanov, A. V. Kuklev, Method of calculating the optimum parameters for the air-mist cooling of a continuous-cast slab, *Metallurgist*, 56 (2012), 173–179
- ⁵ T. Mauder, C. Sandera, J. Stetina, A Fuzzy-Based Optimal Control Algorithm for a Continuous Casting Process, *Mater. Tehnol.*, 46 (2012) 4, 325–328
- ⁶ T. Mauder, C. Sandera, J. Stetina, M. Masarik, A Fuzzy Logic Approach for Optimal Control of Continuous Casting Process, In METAL 2012 Conference proceedings, Ostrava, Czech Republic, 2012, 35–40
- ⁷ M. Raudensky, M. Hnizdil, J. Hwang, S. Lee, S. Kim, Influence of Water Temperature on The Cooling Intensity of Mist Nozzles in Continuous Casting, *Mater. Tehnol.*, 46 (2012) 3, 311–315
- ⁸ L. Klimes, J. Stetina, Parallel dynamic solidification model of continuous steel casting on GPU, Proceedings of 22nd Conference on metallurgy and materials, Ostrava, 2013, 34–39
- ⁹ G. S. Jansto, Steelmaking and Continuous Casting Process Metallurgy Factors Influencing Hot Ductility Behavior of Niobium Bearing Steels, In METAL 2013 Conference proceedings, Ostrava, 2013, 32–39

UNSTEADY MODEL-BASED PREDICTIVE CONTROL OF CONTINUOUS STEEL CASTING BY MEANS OF A VERY FAST DYNAMIC SOLIDIFICATION MODEL ON A GPU

PREDVIDEVANJE KONTROLE KONTINUIRNEGA LITJA NA PODLAGI NERAVNOTEŽNEGA MODELA Z ZELO HITRIM DINAMIČNIM MODELOM STRJEVANJA NA GPU

Lubomir Klimes, Josef Stetina

Brno University of Technology, Faculty of Mechanical Engineering, Energy Institute, Technická 2896/2, 616 69 Brno, Czech Republic
klimes@fme.vutbr.cz, stetina@fme.vutbr.cz

Prejem rokopisa – received: 2013-10-01; sprejem za objavo – accepted for publication: 2013-10-07

The aim of the paper is to develop and test a model-based predictive control system for continuous casting of steel billets with an emphasis on unsteady casting situations, often accompanied by abrupt changes in the casting speed. A very fast dynamic solidification model was developed for this purpose. This fully 3D model runs on graphics processing units, GPUs, and it is significantly faster than the recently used commercial models. Therefore, a scenario approach can be utilized, which means that the control system, in real time, predicts and evaluates the thermal behavior of cast billets for various scenarios of the control strategy. The concept of the effective casting speed was utilized for the proposed control strategies. The results show that the developed control system can provide an effective control of the casting process and brings new control possibilities for continuous steel casting.

Keywords: continuous casting, model-based predictive control, effective casting speed, dynamic solidification model, GPU, computing

Namen prispevka je razvoj in preizkušanje nadzornega sistema kontinuirnega ulivanja gredic, ki temelji na modelu napovedovanja, z upoštevanjem neenakomernih razmer pri litju, pogosto spremljanih z nenadnimi spremembami hitrosti ulivanja. Za ta namen je bil razvit zelo hiter dinamičen model strjevanja. To je popoln 3D-model, ki teče na grafičnih procesnih enotah GPU in je bistveno hitrejši kot pred kratkim uporabljeni komercialni modeli. Zato se lahko uporabi scenarijski način, kar pomeni, da sistem nadzora v realnem času napoveduje in ocenjuje toplotno vedenje litih gredic pri različnih scenarijih strategije kontrole. Za predlog nadzornih strategij je bil uporabljen koncept učinkovite hitrosti ulivanja. Rezultati kažejo, da razviti sistem nadzora ponuja učinkovito metodo nadzora procesa litja in prinaša nove možnosti nadzora pri kontinuirnem ulivanju jekla.

Ključne besede: kontinuirno ulivanje, napovedovanje na osnovi modela, efektivna hitrost litja, dinamični model strjevanja, GPU, računalništvo

1 INTRODUCTION

Recently, the optimum control of continuous casting has been among the main objectives of steelmakers around the world. A proper control, especially in the secondary cooling with water or air-mist cooling nozzles, is an essential issue directly related to productivity and quality. Various techniques and approaches can be used for this purpose. An experimental setup of a casting machine is seldom used due to a large complexity of the problem and due to fallible results. Instead, many researchers and steelmakers use numerical dynamic solidification models. These systems enable the calculations of the temperature field of a cast blank and its solidification and they can be, therefore, used for the casting control,^{1,2} its optimization³⁻⁵ and for investigating the thermal behavior.^{6,7}

The crucial issue of dynamic solidification models in relation to casting control is their computational demands limiting their wider use in the production control process. In particular, a dynamic solidification model usually computes the transient heat transfer and the temperature distribution of an entire cast blank in specified

points, in the so-called computing grid. This procedure generates a large amount of calculations (in order of billions) determining the transient temperature field of cast blanks. The recently used commercial dynamic solidification models use the state-of-the-art CPU computing and perform these calculations within tens of minutes. Nevertheless, tens of minutes are rather long times to utilize the solidification models for the real-time control or optimization of a casting process. However, a new computing approach has recently become available for highly parallelizable problems. This technique, called the GPGPU (general-purpose computing on graphics processing units), utilizes the computing on graphics cards, GPUs. A GPU, though primarily intended for the use in computer graphics and gaming, consists of a large number (from hundreds to thousands) of rather simple processors allowing a huge computing performance that can be used for solving various scientific and technical problems. The GPGPU has been mainly used for the simulations of molecular dynamics,⁸ image processing⁹ and Monte Carlo simulations.¹⁰ In spite of this, only a few papers relating to heat-transfer problems have been pub-

lished¹¹ by researchers and none of these covers continuous casting. However, Klimes and Stetina^{12,13} recently published papers on the use of the GPGPU for a parallel dynamic solidification model of continuous casting on a GPU and the results show that the GPGPU can greatly enhance the computing performance of solidification models, allowing a significant reduction in the computing time and, therefore, new opportunities for the use of solidification models in the optimum casting control have become available.

Based on the literature review, researchers have recently used various approaches to the optimum control of the continuous casting process: frequently by applying PI or PID controllers,¹ probabilistic metaheuristics (e.g., simulated annealing²), heuristic searches,³ fuzzy logic techniques⁴ or mathematical programming methods⁵. However, several issues may appear when these methods are used or intended for a practical use in steelworks. One of the most important issues of PI and PID controllers is that they regulate a process according to the history of that process. Considering a system delay, it means that the regulation may react improperly. Heuristic methods and, particularly, the approaches via mathematical programming suffer from huge computational demands, usually because of the repeated computations of the model. This issue can, therefore, significantly prolong the regulation process and, for this reason, the use of these methods is often limited in a real-time regulation.

Due to the above reasons and encouraged by the computational performance of the developed parallel dynamic solidification model running on a GPU, the aim was to propose a new control approach for continuous casting. For this purpose the model-based predictive-control (MPC) approach was selected. One of the features of the MPC is that it uses a model as a numerical sensor to predict the future evolution of a controlled process under certain conditions.

2 PARALLEL DYNAMIC SOLIDIFICATION MODEL RUNNING ON A GPU

Nowadays, commercial dynamic solidification models for continuous steel casting utilize the state-of-the-art computing on central processing units (CPUs). These models usually solve heat transfer and solidification of cast blanks in discretized points (in a number of hundreds of thousands or millions) and these models require tens of minutes to compute the stationary state under constant casting conditions.¹² These models are, therefore, rather awkward for a fast and real-time regulation due to time-consuming computations. However, many computational problems with a possibility to be parallelized can be computed more efficiently with the use of GPGPU techniques and graphics processing units (GPUs).¹⁴ The GPGPU divides a computational problem into independent parts that can be computed concurrently in a parallel manner. For this reason a GPU

consists of many simple computing units that are designed to process an identical code, but on different data. The number of units depends on the type of the GPU, generally varying between several hundreds and several thousands.

The transient heat transfer and the solidification of cast blanks can be modeled with the Fourier-Kirchhoff equation:

$$\frac{\partial H}{\partial t} = \nabla \cdot (k \nabla T) + v_z \frac{\partial H}{\partial z} \quad (1)$$

where H is the volume enthalpy (J m^{-3}), T is the temperature (K), t is the time (s), k is the thermal conductivity ($\text{W m}^{-1} \text{K}^{-1}$), v_z is the casting speed (m s^{-1}) and z is the spatial coordinate (m) in the direction of casting. The mass-transfer and fluid-flow phenomena inside a blank are usually neglected, but they can also be considered, e.g., with the use of the effective heat-conductivity approach. The volume enthalpy that appears in Equation (1) is used to include the latent heat released during the solidification.¹⁵ This thermodynamic function can be defined as:

$$H(T) = \int_0^T \left(\rho c - \rho L_f \frac{df_s}{d\theta} \right) d\theta \quad (2)$$

where ρ is the density (kg m^{-3}), c is the specific heat ($\text{J kg}^{-1} \text{K}^{-1}$), L_f is the latent heat (J kg^{-1}) and f_s is the solid fraction (1).

The developed parallel dynamic solidification model for continuous casting of steel billets (**Figure 1**) based on Equation (1) and the necessary initial and boundary conditions was created using the control-volume method and explicit time discretization.^{12,13} The heat withdrawal from the mould, within the secondary cooling zones with the cooling nozzles and other casting conditions, can be adjusted through the initial and boundary conditions. The explicit discretization in time is an essential condition for the parallel model, allowing it to run on GPUs. Basically, the calculations related to various control volumes are solved concurrently by various computing units of a GPU.^{12,13} The CUDA C/C++ computing architecture was

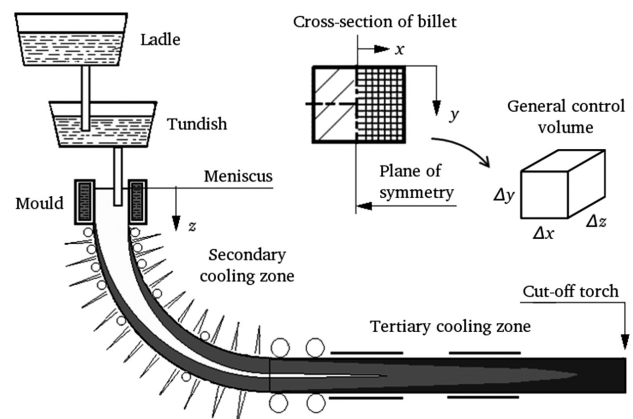


Figure 1: Billet caster and the mesh definition

Slika 1: Naprava za ulivanje gredic in določanje mreže

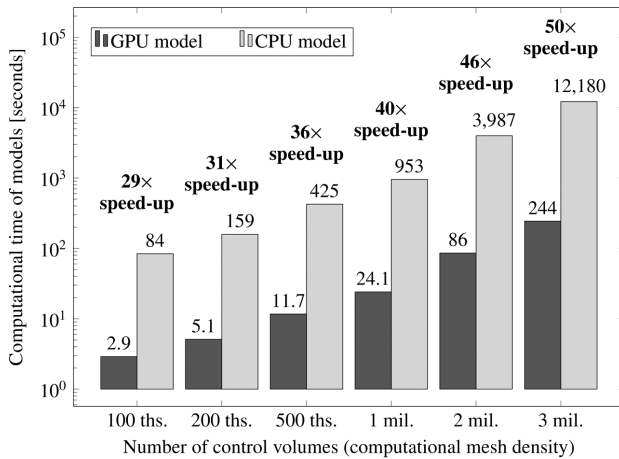


Figure 2: Comparison of computational performances between GPU and CPU dynamic solidification models

Slika 2: Primerjava računskih zmogljivosti med GPU in CPU pri dinamičnih modelih strjevanja

used for the development of the presented solidification model.¹⁶

A comparison of the computing performances between the developed parallel solidification model running on a GPU and an identical model utilizing the state-of-the-art computing on a CPU is shown in **Figure 2**. The results are presented for various numbers of control volumes (i.e., for various computational mesh densities) and identical casting conditions.¹² GPU NVIDIA Tesla C2075 having 448 computing units was used as the representative of GPUs. The CPU model was run on a computer with Intel Core 2 Quad CPU with 4 cores, each having a frequency of 2.4 GHz. As can be seen from **Figure 2**, the GPGPU computing can greatly enhance the computational performance of the solidification models. For the mesh with 100000 control volumes, the GPU model processes the computations in only about 3 s which is 30-times faster than in the case of the model running on a CPU. Moreover, with an increasing mesh density the parallelism and the computational performance of the GPU become more significant: in the case of 3 million control volumes, the model running on a GPU is even about 50-times faster than the CPU model. In this case, the GPU model performs all the computations with a very fine mesh in only 4 min. On the contrary, the CPU model needs more than 200 min to do the same job. These results unambiguously prove the benefits of the parallel GPU solidification model, opening new possibilities for its real-time use in continuous-casting control.

3 MODEL-BASED PREDICTIVE CONTROL FOR CONTINUOUS CASTING

3.1 Model-based predictive control systems

On the basis of the literature review, the model-based predictive control approach^{17,18} was chosen to be utilized with the developed GPU model for the optimum control

of continuous casting process. Though primarily utilized in the petroleum industry, the model-based predictive control has been recently used in many engineering applications, mainly due to a rapid development of computers and their performance.^{17–19} The main principle of the general model-based predictive control (MPC) system is as follows: in defined consecutive time instants with the measurements of the current and past process outputs and with the past values of the control inputs, the control inputs for the current and future instants are determined with the model, so that these control inputs minimize the differences between the predicted controlled outputs and the required reference values, the so-called set-points over a certain control horizon¹⁷. In other words, the MPC utilizes the model of the process to predict the behavior of the system resulting from the changes in the inputs and to evaluate the consequences of these modifications. This is actually an opposite to the PI and PID controllers that control and regulate the process according to the known behavior in the past. A very illustrative comparison between the PI and PID versus the MPC is as follows: the PI and PID controlling is like driving a car using the rear-view mirror. On the other hand, the MPC approach, in the context of driving a car, is like the normal driving using the windshield of the car.¹⁷

Inspired by the described idea of the MPC, we propose an MPC system for the continuous casting of steel utilizing the developed, very fast GPU model. The scenario approach and the effective casting speeds are then used for determining the control inputs.

3.2 Proposal of the model-based predictive control system for continuous steel casting

The main idea of the proposed MPC system for continuous steel casting is based on using the developed parallel GPU model as a numeric sensor of the real casting machine. However, due to the developed, very

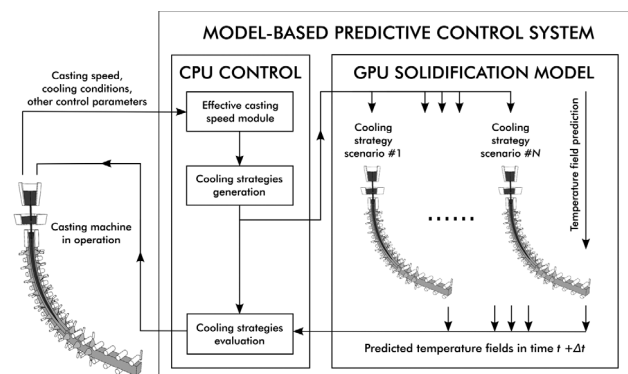


Figure 3: Concept of the model-based predictive control system for continuous casting using a very fast dynamic solidification model running on a GPU

Slika 3: Zasnova kontrolnega sistema napovedovanja na osnovi modela pri kontinuirnem ulivanju z uporabo modela zelo hitrega dinamičnega modela strjevanja, ki teče na GPU

fast dynamic solidification model running on a GPU, the concept of the MPC can be extended and modified. The entire concept of the control system is presented in **Figure 3**. The main idea is to use the scenario approach. It means that in every time step the MPC system retrieves the actual casting parameters (e.g., the casting speed, the casting temperature, etc.) from the casting machine. The control system then generates several control strategies, the so-called control scenarios in order to control the process. Each of these scenarios represents a possible control of the casting machine, particularly the cooling setup (i.e., the water-flow volume) of the cooling nozzles in the cooling circuits within the secondary zone. The control scenarios are generated making use of the experiences provided by the experts, the traditional relationships between the water-flow volume through the nozzles and the casting speed, and the concept of the effective casting speed²⁰. The control system then predicts the future thermal behavior of cast billets for a certain future-time horizon and for all the generated control scenarios. This task can be performed in real time (between tens of seconds and several minutes depending on the number of scenarios) solely due to the very fast GPU dynamic solidification model. The control system consequently analyses the results of the scenario thermal behaviors and chooses the resultant control strategy used for the real casting process. The main objective of the resultant control strategy is to ensure that the surface temperatures of cast billets fit the predefined temperature intervals (to avoid subcooling or overcooling because of a low ductility of steel²¹ resulting in surface defects, e.g., cracks) and that the metallurgical length fits the defined range.^{3,4} The control loop is, thereby, closed and the procedure is repeated in the next time instant.

3.3 Effective casting speed

The concept of the effective casting speed was adopted for the determination of the control cooling strategies in secondary cooling.²⁰ When the actual cast-

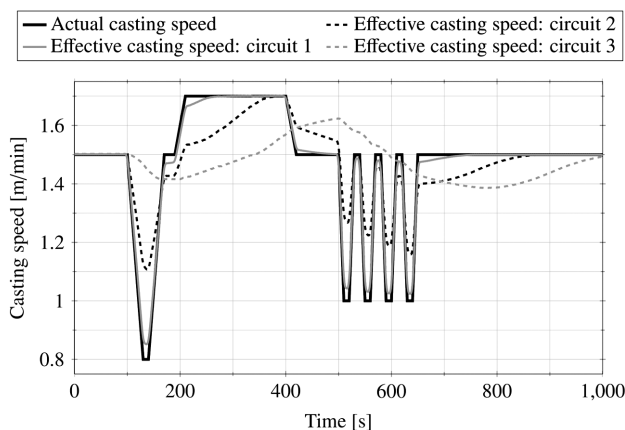


Figure 4: Concept of the effective casting speed

Slika 4: Zasnova učinkovite hitrosti litja

ing speed rapidly varies in time (e.g., due to a change of tundishes), the determination of the water-flow volume through the nozzles as a function of the actual casting speed may result in inappropriate cooling, particularly in the cooling circuits far from the mould.²⁰ Researchers and steelworkers usually tend to use the dependencies of the water-flow volume in the cooling circuits as the quadratic functions of the casting speed.²⁰ The mentioned problem can be overcome with the use of the effective casting-speed approach, based on considering the dwell time that a blank divided into slices spends in each of the cooling circuits. The effective casting speed $v_{e,i}$ for the i -th cooling circuit (m min⁻¹) can be calculated as:

$$v_{e,i} = \varepsilon_i v_{a,i} + (1 - \varepsilon_i) v_z \quad (3)$$

where ε_i is the weight coefficient (1), v_z is the actual casting speed (m min⁻¹) and the average casting speed $v_{a,i}$ for the i -th cooling circuit (m min⁻¹) is determined as:

$$v_{a,i} = \frac{n_i L_i}{\sum_{j=1}^{n_i} t_{r,i,j}} \quad (4)$$

where n_i is the number of slices, L_i is the distance from the mould (m) and $t_{r,i,j}$ is the residential time (s).²⁰ **Figure 4** shows the effective casting speed for the fluctuating actual casting speed and for the casting machine with three cooling circuits within the secondary cooling zone.

As can be seen from **Figure 4**, the effective casting-speed approach can be suitably used for the characterization of the fluctuating casting conditions. Particularly in the cooling circuits far from the mould, the effective casting speed has a smoothness effect, which fairly corresponds to the reality.

4 USE OF THE CONTROL SYSTEM, RESULTS, DISCUSSION

The developed MPC system was tested for the control of the secondary cooling in the case of a temporary change in the casting speed, e.g., due to the change of tundishes. The dynamic solidification model was configured for a caster with 6 cooling circuits within the secondary cooling incorporating 180 JATO cooling nozzles of several types. The caster casts 200 mm × 200 mm steel billets, normally with the casting speed of 1.5 m/min. The temporary drop in the casting speed from 1.5 m/min to 0.8 m/min was assumed for 6 min as depicted in **Figure 5** where the effective casting speeds for each of the cooling circuits are presented as well.

The aim of the control was to determine the cooling strategy of the cooling nozzles within the secondary cooling so that the surface temperatures on the cast billets would be maintained as close as possible to the surface temperatures in the case when no change is made to the casting speed. Thereby, the steady-state surface

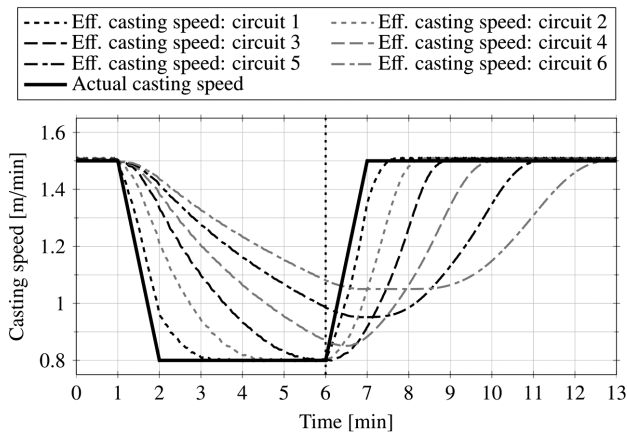


Figure 5: Actual casting speed and the corresponding effective casting speeds for all the cooling circuits

Slika 5: Dejanska hitrost litja in ustrezne hitrosti litja za vse hladilne kroge

temperatures were considered as the optimum target temperatures. The resultant surface temperatures on the top (small-radius) surface of the control process are shown in **Figure 6**. These temperatures for the cooling circuits 4, 5, 6 are plotted for the time when 5 min have elapsed from the beginning of the change in the casting speed (depicted by the vertical dotted line in **Figure 5**) and when the actual casting speed begins to increase from 0.8 m/min back to 1.5 m/min.

As for the described control problem of the temporary change in the casting speed, the developed model-based control system generated 15 cooling scenarios for the cooling strategy within the secondary cooling. These scenarios were generated taking into account the effective casting speeds. The system then predicted the future thermal behavior (calculating the complete temperature distribution) for all these cooling scenarios. The computations were performed for a computational mesh with 1 million control volumes and all these computations for all the cooling scenarios were performed within 1 min

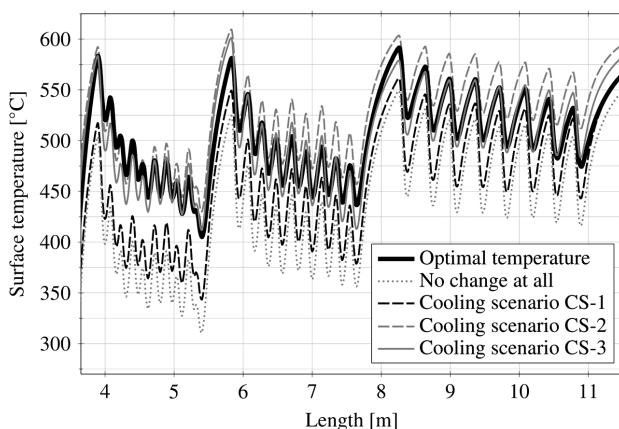


Figure 6: Surface temperatures on the top (small-radius) surface resulting from the use of the MPC system

Slika 6: Temperature površine na vrhu gredic (manjši polmer), ki so dobljene z uporabo MPC-sistema

using GPU NVIDIA Tesla C2075. The temperature distributions for three representative scenarios (denoted as CS-1, CS-2, and CS-3) are plotted in **Figure 6** together with the optimum steady-state temperature distribution and with the temperature distribution for the case when no change in the cooling strategy is performed. As can be seen from **Figure 6**, when no change in the cooling strategy is considered, a significant subcooling occurs within the secondary cooling. Further, the generated cooling strategy CS-1 is also rather inappropriate due to the subheating, mainly occurring within the fourth cooling circuit. Similarly, the cooling strategy CS-2 is also rather inconvenient owing to the overheating, especially in the fifth and sixth cooling circuits. But in the case of the cooling strategy CS-3, the distribution of the temperature is very close to the target temperature distribution in all three cooling circuits plotted in **Figure 6**. The cooling scenario SC-3 can, therefore, be considered as the optimum cooling strategy for the investigated situation.

5 CONCLUSION

The paper presents a proposal for a model-based predictive control system for the continuous casting of steel. The system is based on the dynamic solidification model as the numerical sensor for predicting the future thermal behavior of cast billets under specific casting conditions. The control system utilizes the developed very fast dynamic solidification model that runs on graphics processing units, GPUs. The solidification model, using the concepts of the scenario-based cooling strategies and the effective casting speed was then used for the optimum control of continuous casting. The control system was tested for the case of a temporary drop in the casting speed and the results show that the proposed system is a promising tool for solving these control problems. The next research will aim at tuning up the developed control system and testing it in various production control situations in the continuous casting of steel.

Acknowledgement

The presented research was supported by project GACR P107/11/1566 of the Czech Science Foundation, by the NETME Centre, ED0002/01/01, by the NETME CENTRE PLUS (LO1202), and by the BUT project FSI-J-13-1977 for young researchers. The principal author, the former holder of the Brno PhD Talent Financial Aid sponsored by the Brno City Municipality, also gratefully acknowledges the financial support.

6 REFERENCES

- ¹ B. Petrus, K. Zheng, X. Zhou, B. G. Thomas, J. Bentsman, Real-time model based spray-cooling control system for steel continuous casting, *Metallurgical and Materials Transactions B*, 42 (2011) 1, 78–103

- ² M. S. Kulkarni, A. S. Babu, Managing quality in continuous casting process using product quality model and simulated annealing, *Journal of Materials Processing Technology*, 166 (2005) 2, 294–306
- ³ N. Cheung, A. Garcia, The use of a heuristic search technique for the optimization of quality of steel billets produce by continuous casting, *Engineering Applications of Artificial Intelligence*, 14 (2001) 2, 229–238
- ⁴ T. Mauder, C. Sandera, J. Stětina, A fuzzy-based optimal control algorithm for a continuous casting process, *Mater. Tehnol.*, 46 (2012) 4, 325–328
- ⁵ T. Mauder, J. Novotny, Two mathematical approaches for optimal control of the continuous slab casting process, *Proc. of 16th International Conference on Soft Computing MENDEL*, Brno, 2010, 395–400
- ⁶ L. Klimes, J. Stetina, P. Bucek, Impact of casting speed on the temperature field of continuously cast steel billets, *Mater. Tehnol.*, 47 (2013) 4, 507–513
- ⁷ Y. J. Xia, F. M. Wang, C. R. Li, J. L. Wang, Simulation of thermo-mechanical behaviour during continuous casting process based on MiLE method, *Journal of Central South University*, 19 (2012) 9, 2403–2410
- ⁸ J. A. Baker, J. D. Hirst, Molecular dynamics simulations using graphics processing units, *Molecular Informatics*, 30 (2011) 6–7, 498–504
- ⁹ K. E. A. van der Sande, T. Gevers, C. G. M. Snoek, Empowering visual categorization with the GPU, *IEEE Transactions on Multimedia*, 13 (2011) 1, 60–70
- ¹⁰ Y. Uejima, T. Terashima, R. Maezono, Acceleration of a QM/MM-QMC simulation using GPU, *Journal of Computational Chemistry*, 32 (2011) 10, 2264–2272
- ¹¹ W. S. Fu, W. H. Wang, S. H. Huang, An investigation of natural convection of three dimensional horizontal parallel plates for a steady to an unsteady situation by a CUDA computation platform, *International Journal of Heat and Mass Transfer*, 55 (2012) 17–18, 4638–4650
- ¹² L. Klimes, J. Stetina, Parallel dynamic solidification model of continuous steel casting on GPU, *Proc. of 22nd Conference on Metallurgy and Materials METAL*, Brno, 2013, 6
- ¹³ L. Klimes, J. Stetina, Transient heat transfer problem with phase changes solved by means of GPGPU with CUDA and MATLAB, *Proc. of 19th International Conference on Soft Computing MENDEL*, Brno, 2013, 397–402
- ¹⁴ J. D. Owens, M. Houston, D. Luebke, S. Green, J. E. Stone, J. C. Phillips, *GPU computing*, *Proceedings of the IEEE*, 96 (2008) 5, 879–899
- ¹⁵ L. Klimeš, P. Charvat, M. Ostry, Challenges in the computer modeling of phase change materials, *Mater. Tehnol.*, 46 (2012) 4, 335–338
- ¹⁶ N. Wilt, *CUDA Handbook: A comprehensive guide to GPU programming*, 1st ed., Addison-Wesley, 2013
- ¹⁷ P. Tatjewski, *Advanced Control of Industrial Processes: Structures and Algorithms*, Springer, London 2007
- ¹⁸ A. Ivanova, Model predictive control of secondary cooling modes in continuous casting, *Proc. of 22nd Conference on Metallurgy and Materials METAL*, Brno, 2013, 6
- ¹⁹ S. J. Qin, T. A. Badgwell, A survey of industrial model predictive control technology, *Control Engineering Practice*, 11 (2003) 7, 733–764
- ²⁰ Z. Dou, Q. Liu, B. Wang, X. Zhang, J. Zhang, Z. Hu, Evolution of control models for secondary cooling in continuous casting process of steel, *Steel Research International*, 82 (2011) 10, 1220–1227
- ²¹ S. G. Jansto, Steelmaking and continuous casting process metallurgy factors influencing hot ductility behaviour of niobium bearing steels, *Proc. of International Conference on Metallurgy and Materials METAL*, Brno, 2013, 7

DSC/TG OF Al-BASED ALLOYED POWDERS FOR P/M APPLICATIONS

DSC/TG PRAHOV NA OSNOVI Al PRIMERNIH ZA P/M UPORABO

Borivoj Šuštaršič¹, Jože Medved², Srečko Glodež³, Marko Šori³, Albert Korošec⁴

¹Institute of Metals and Technology, Lepi pot 11, 1000 Ljubljana, Slovenia

²OMM, NTF, University of Ljubljana, Aškerčeva 12, 1000 Ljubljana, Slovenia

³University of Maribor, FNM, Koroška cesta 160, 2000 Maribor, Slovenia

⁴Talum, Tovarna aluminija d. d., Tovarniška cesta 10, 2325 Kidričevo, Slovenia

borivoj.sustarsic@imt.si

Prejem rokopisa – received: 2013-11-13; sprejem za objavo – accepted for publication: 2014-04-16

Al-based alloyed powders, appropriate for the sintering procedure (powder metallurgy, P/M) contain the alloying elements with a high solid solubility in Al, enabling reaction and liquid-phase sintering. They are surface oxidised because of a high affinity of Al to oxygen. Besides, this type of powders contains a polymeric lubricant (wax), which reduces the friction on die walls during automatic die compaction into the final compact shape of a product. This lubricant has to be removed slowly during the first stage of sintering in order to prevent deformations and cracking of the product. Consequently, its sintering is very complex. Generally, these powders are sintered in pure nitrogen with a low dew point. The optimum sintering conditions are generally determined on the basis of light and scanning electron microscopy. The investigation can also be completed very successively with differential scanning calorimetry and thermo gravimetry. The first one allows an insight into the endo- and exothermic reactions, taking place during the heating and cooling of a compacted metal powder, and the second one allows an insight into the processes, connected with the mass loss (a reduction, a lubricant removal, etc.) or mass increase (an oxidation). The DSC/TG of three commercial Al-based alloyed powders was performed in the frame of our investigations. The results were compared with the theoretical thermodynamic-based calculations and the optimum sintering conditions were proposed.

Keywords: Al-based alloyed powders, sintering, differential scanning calorimetry and thermo gravimetry (DSC/TG)

Legirani prahovi na osnovi Al, primerni za sinter postopek (P/M, metalurgija prahov), vsebujejo zlitinske elemente z veliko topnostjo v trdnem Al, kar omogoča reakcijsko sintranje v prisotnosti tekoče faze. Zaradi velike afinitete aluminija do kisika so na površini oksidirani. Poleg tega vsebujejo ti prahovi polimerno mazivo, ki zmanjšuje trenje na stenah orodja med avtomatskim stiskanjem prahu v končno oblikovan izdelek. To mazivo moramo v prvi fazi procesa sintranja počasi odstraniti, sicer bi lahko prišlo do nepopravljive deformacije ali celo pokanja izdelka. Zato je njihovo sintranje zelo zahtevno. Navadno se sintrajo v čisti dušikovi atmosferi z nizko temperaturo rosišča. Poleg fizikalno-kemijske karakterizacije sintranih izdelkov s svetlobno in elektronsko mikroskopijo je za določitev optimalnih pogojev sintranja zelo uporabna diferencialna vrstična kalorimetrija, kombinirana s termogravimetrijo (DSC/TG). Prva omogoča vpogled v endo- in eksotermne reakcije, ki potekajo med segrevanjem in ohlajanjem kompaktnega kovinskega prahu, druga pa s temi procesi povezano izgubo (redukcija, odstranitev maziva itd.) ali prirastek (oksidacija) mase. V okviru naših raziskav smo izvedli DSC/TG treh komercialno dosegljivih prahov na osnovi Al, ugotovljene reakcije smo primerjali z napovedmi teoretične termodinamike in predlagali optimalne pogoje sintranja teh prahov.

Ključne besede: prahovi zlitine na osnovi Al, sintranje, diferencialna vrstična kalorimetrija s termogravimetrijo

1 INTRODUCTION

Al-based alloyed powders, appropriate for the sintering procedure (powder metallurgy, P/M) contain the alloying elements (Cu, Zn, Mg, etc.) with a high solid solubility in Al enabling reaction and liquid-phase sintering. Generally, these powders are surface oxidised because of a high affinity of Al to oxygen. Besides, these types of powders contain mass fraction approximately $w = 1.5\%$ of a polymeric lubricant, which reduces the friction on die walls during automatic die compaction (ADC) into the final compact shape of a product. This lubricant has to be removed slowly during the first stage of sintering in order to prevent deformations and cracking of the product. Therefore, its sintering is very complex. Generally, these types of powders are sintered in pure nitrogen (N_2 , 5.9) with a low dew point (below $-40\text{ }^\circ\text{C}$). The optimum sintering conditions are commonly determined on the basis of light (LM) and scanning electron microscopy combined with a microchemical

analysis based on the measurement of the dispersed kinetic energy of X-rays (an energy dispersive X-ray spectrometer – SEM/EDS).¹ The investigation can also be completed very successively with heating microscopy, as well as differential scanning calorimetry and thermo gravimetry (DSC/TG). The DSC method allows an insight into exothermic/endergonic reactions, and the TG method allows an insight into the mass increase/decrease occurring during the heating/cooling of a compact, respectively.

DSC is an effective and widely used method of the thermal analysis (TA) of metallic and other materials. It is a modern, completely automated and highly improved version of an older method known as differential thermal analysis (DTA) where the temperature differences between the investigated and the standard (neutral, usually alumina) samples are measured. The temperature differences are the consequence of the heat release/consume of the exothermic/endergonic reactions associated with different physical and chemical processes (melting, soli-

dification, evaporation, oxidation, reduction, solid-state transformations, etc.) occurring during the heating and cooling of the investigated sample. The actual difference between the DTA and DSC methods is a more precise determination of the released or consumed heat. With the DSC method it is possible to determine the released or consumed heat much better because the specific heats and their temperature dependencies of the investigated samples are considered. The new DSC devices also have a significantly higher number of temperature sensors (thermocouples) in a very small space of the measuring cell and an improved calibration system of the thermal buoyancy, enabling a much better measuring of temperature gradient dT/dt ($^{\circ}\text{C/s}$). The measuring cell is usually placed on a very precise balance. This also enables thermogravimetry (TG) and a simultaneous tracking of the mass changes due to different reactions. Modern DSC/TG devices enable experimental work with a controlled heating/cooling rate in different stationary or flow atmospheres. They enable the heating up to very high temperatures (for the metals, generally, up to 1600°C ; the maximum of 2400°C is also possible). Mass changes are the results of the changes in the investigated sample (a wax removal, an evaporation, etc.) or its reaction with the selected atmosphere (hydrogen, oxygen, water vapour, etc.).

The DSC/TG analyses of three commercial² Al-based alloyed powders were performed in the frame of our investigations. The results were compared with the theoretical thermodynamic-based calculations (ThermoCalc)³ and the optimum sintering conditions were proposed. Our experiments were performed with a Netzsch STA (simultaneous thermal analysis) device, Germany.^{4,5}

2 EXPERIMENTAL WORK

The actual chemical compositions of the selected commercial Al powders are given in **Table 1**. From this table one can notice that the first AlCuSiMg-based alloy (A) is of type 2xxx (2014), the second alloy (B) is a special hypereutectoid Al-Si-based alloy with a high Si content and additions of Cu and Mg. The third alloy (C) is an AlZnMgCu-based alloy of 7xxx family type (7075). The powders were compacted on an ADC mechanical press (Dorst, Germany, 60 kN) with a 450 MPa pressure into standard tensile-test specimens (DIN ISO 2740).⁶ Thirty-five (35) pieces of each alloy were prepared for

further experiments and investigations. From three (3) characteristic specimens (with the average green density) samples of approximately 5 g were cut off for the DSC/TG experiments. As already mentioned, the experiments were performed with a Netzsch STA 449C Jupiter⁵ device installed at the Laboratory for Thermodynamics of Materials, Department for Metallurgy and Materials, University of Ljubljana. This equipment enables a simultaneous performance of differential scanning calorimetry and thermogravimetry with the selected heating/cooling rate and atmosphere conditions. In our case the samples were heated/cooled at the constant rate of 5°C/min in a stationary atmosphere of Ar (the purity of 5.9), as well as in a flow atmosphere (10 mL/h) of pure nitrogen (5.9). The samples were heated up to the maximum temperature of 650°C and then cooled down. The calibration (determination of the base line) of the device as well as the evacuation of the cell were performed every time before the start of an analysis.

Table 1: Actual average chemical compositions of the selected powders in mass fractions (w/%)

Tabela 1: Povprečna kemijska sestava izbranih prahov v masnih deležih (w/%)

Designation	Cu	Si	Mg	Zn	Al	Remarks
Chemical composition	w/%					
Alloy A	4.5	0.62	0.48	–	bal	0.08 % Fe
Alloy B	2.7	15.0	0.58	–	bal	
Alloy C	1.6	–	2.40	5.8	bal	0.29 % Sn

The average bulk chemical compositions of the powders were determined with a classical Agilent 720 ICP-OES (ion coupled plasma - optical emission spectroscopy) instrument with a limit of detection ($< 0.001\%$ of an individual element). However, the microchemical compositions of individual powder particles were determined with SEM/EDS (a JEOL FE HR JSM-6500F and Oxford EDS INCA Energy 450, X-Sight LN2 detector).

The compacted tensile-test specimens were also sintered at the selected sintering conditions. The obtained mechanical properties are given in **Table 2**. They are in accordance with the expectations and the powder-producer specifications.²

The standard metallographic samples of the powders and sintered materials were prepared for the microstructural and microchemical investigations under LM and SEM/EDS. In this article, the description is focused

Table 2: Average mechanical properties of the materials after the ADC and sintering of the tensile-test specimens made of the selected Al-based powders

Tabela 2: Povprečne mehanske lastnosti materialov, dobljene po stiskanju in sintranju nateznih preizkušancev iz izbranih Al-prahov

Alloy	Green density	Sintered density	Hardness HB _{2,5/31,25}	Tensile strength	Yield strength	Young's modulus	Elongation %
	g/cm ³			MPa			
A	2.62	2.60	65	202	156	3834	2.23
B	2.52	2.62	104	239	219	4399	0.70
C	2.61	2.73	102	325	250	4102	3.90

mainly on DSC/TG investigations and analyses. The description of the other investigations can be found elsewhere.¹

3 RESULTS AND DISCUSSION

This article will only focus on some general characteristics and the most important findings. An additional description of the results of the investigations can be found elsewhere.¹ **Figure 1** shows the typical measuring protocol and the results of the DSC analysis obtained for both experimental conditions during the investigation of alloy A. The heating/cooling program is recorded with a fine dotted line. One can notice that the resulting DSC curve for the analysis performed with stationary Ar is almost the same as the one performed with a flow of nitrogen. Only small differences can be noticed. They can be ascribed to the fluctuations in the sample composition, solubility of gas in the melt, possible formation of nitrides/oxides and variations of the used experimental conditions. The sole large exothermic (exo) and equivalent endothermic (endo) peaks can be ascribed to the melting and solidification of the alloy, respectively. The exo peak connected with the solidification is sharper for the nitrogen-flow experiment. Other changes are less distinctive and can be observed only in the magnified mode. The cooling parts of the DSC curves have no visible additional peaks, which means that, during the melting, the homogeneous alloy was completely formed, without any significant precipitation of the secondary phases during the cooling of the sample.

Figure 2 shows the heating part of the DSC curve in the magnified mode obtained with the DSC analysis of alloy A. In the temperature region between 100 °C and 500 °C there is a number of small less recognizable endo peaks. The first one at 138 °C (i.e., 141 °C; the data for the experiments in stationary Ar is given in parentheses) can be associated with the beginning of the melting of the polymer wax, but the later peaks at ((261), 322 (328), (348) and 440 (442)) °C are the results of the evapora-

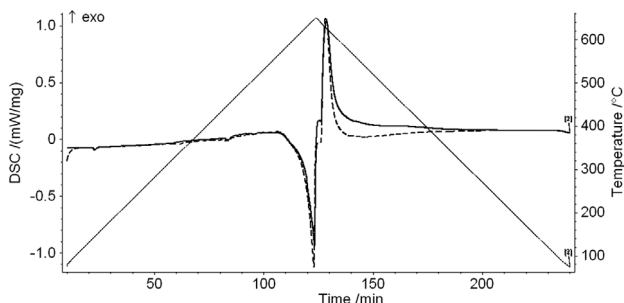


Figure 1: Measuring protocol of the DSC analysis of alloy A (heating/cooling is shown with a fine dotted line), a comparison of the DSC curves obtained during the experiments performed in stationary Ar (dashed line) and in a flow of N₂ (full line)

Slika 1: Merilni protokol DSC-analize zlitine A (segrevanje/ohlajanje – fina pikčasta črta); primerjava DSC-krivulj, izdelanih v stacionarnem argonu (črtkana črta) in pretoku dušika (polna črta)

tion of the multicomponent lubricant system. A constant slight ascent of the DSC curve in this temperature region can also be noticed. This is the result of the exothermic nature of the wax removal (burning). Simultaneously, at the temperatures above 400 °C, above the solvus line of the complex alloying system, one can also expect the beginning of the formation of the final solid solution (α -Al) because of the increased diffusion of the alloying elements into the aluminium. The SEM/EDS microchemical analyses of loose powders showed¹ that not all the individual (pre-alloyed) powder particles are of the same chemical compositions, but they are of different compositions forming the final mixtures with the average compositions given in **Table 1**. For example, SEM/EDS analyses¹ showed that alloy A consisted of the powder particles of pure Al, alloys Al-10Si-Mg (but Mg was not detected) and Cu-5Al. Alloy B consisted of the powder particles made of the Al-3Si, Al-27Si-1Mg-6Cu and Si-Al-based alloys, and, finally, alloy C consisted of the particles of pure Al and the particles of the Al-Zn-Mg-Cu alloy (approximately $w(\text{Al}) = 79\%$, $w(\text{Mg}) = 5\%$, $w(\text{Cu}) = 4\%$, $w(\text{Zn}) = 12\%$). Thus, the endo peaks at approximately (452, 486, 482 (484) °C and 506 (509)) °C can be associated with the diffusion of the alloying elements and the formation of the α -Al solid solution. EDS analyses also showed that alloy B had the most oxidised particles (a high Si content) and alloy C was the least oxidised of all.

The theoretical calculation of the thermodynamic equilibrium with ThermoCalc³ predicts the formation of the first melt at 525 °C (**Figure 3**). On the experimental DSC curve, it is visible at 534 °C. However, the real large endo peak caused by the melting starts at 567.8 (573.2) °C and finishes at approximately 640 °C when the melting of the alloy is completed. ThermoCalc predicts the two-phase region (α -Al+L) between 525 °C and 638 °C (**Figure 3**). This is in a relatively good agreement with the experimental results of the DSC analysis. From these results one can find that the optimum liquid-phase sintering temperature is somewhere in the middle of the α -Al+L region. This is in a good agreement with the powder producer that recommends, for

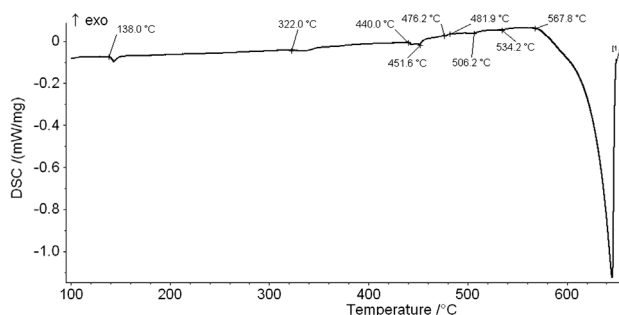


Figure 2: Heating part of the DSC curve of alloy A, protective atmosphere of N₂ 5.9, flow of 10 mL/h, 1 × vacuum, $T_{\text{max}} = 650$ °C, 5 °C/min
Slika 2: DSC segrevalna krivulja zlitine A, zašč. atm. N₂ 5,9, pretok 10 mL/h, 1 × vakuum, $T_{\text{maks.}} = 650$ °C, 5 °C/min

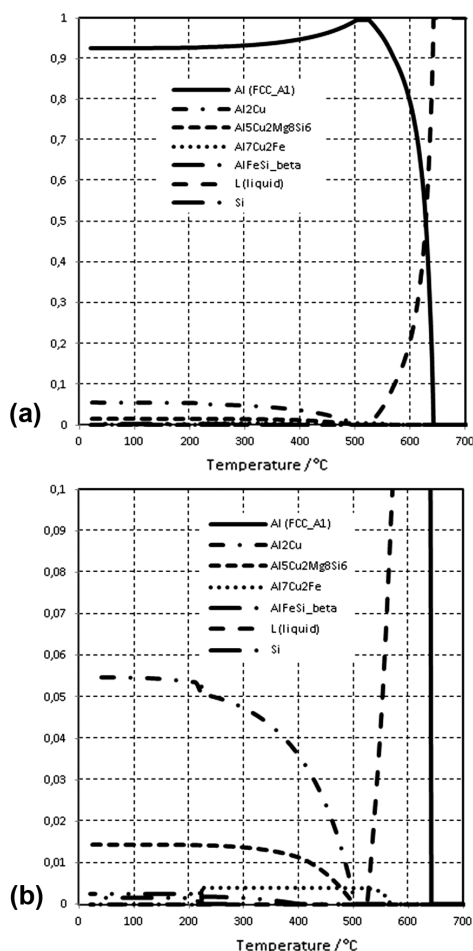


Figure 3: a) Theoretical equilibrium thermodynamic phase stability of alloy A and b) detail of the diagram up to a fraction of 0.1 mol, calculated with ThermoCalc³

Slika 3: a) Teoretična ravnotežna termodinamska stabilnost faz zlitine A in b) detajl v diagramu do 0,1 molskega deleža, izračunano z orodjem ThermoCalc³

alloy A, a sintering temperature between 590 °C and 600 °C. In this case most of the intermetallic phase is already dissolved in the solid solution of Al and a small amount of the liquid needed is also present.

The thermodynamic analysis with ThermoCalc also shows (Figure 3) that, in the equilibrium, alloy A contains solid crystals of the homogeneous solid solution of α -Al from room temperature up to 638 °C and mainly intermetallic phase Al₂Cu (the θ phase) up to 501 °C. As already mentioned, the first liquid appears at 525 °C.

The theory also predicts possible formations of phases Al₅Cu₂Mg₈Si₆ (up to 500 °C), Al₇Cu₂M (M = Fe, up to 565 °C), β AlFeSi (up to 223 °C) and Si up to 396 °C. From this analysis one can conclude that alloy A is a typical precipitation-hardening alloy. Therefore, an improvement in the mechanical properties of this alloy can be achieved with a combination of homogenization annealing at the temperature of a complete solid solution (for example, 500 °C, 20 min), fast cooling and natural (T4) or artificial ageing (T6, for example, 150 °C, 15 min). The optimization of the ageing parameters can be performed with the help of theoretical and experimental CCT (continuous-cooling temperature) diagrams. The optimum process parameters (temperature/time) of ageing lead to an alloy with a fine uniform dispersion of the precipitates of the intermetallic phases in the α -Al solid solution. In the case of high cooling rates (10³ °C/h) only a formation of very fine GP (Guiner-Preston) zones and, eventually, a fine θ' (Theta prime) phase can be expected. Lower cooling rates are undesirable because of the formation of other larger intermetallic phases such as S' or θ phases.^{7,8}

The experimental cooling DSC curve (Figure 4) shows only one large exo peak with its beginning at 637.9 (637.2) °C, which is the result of the sample solidification during cooling. The solidification is finished between approximately 580 °C and 590 °C. Later, only one, almost invisible exo peak appears at approximately 570.1 (563.5) °C. This could be associated with the precipitation of intermetallic phases. The precipitation of phases Al₂Cu and Mg₂Si is possible during a relatively slow cooling (5 °C/min). This could only be confirmed

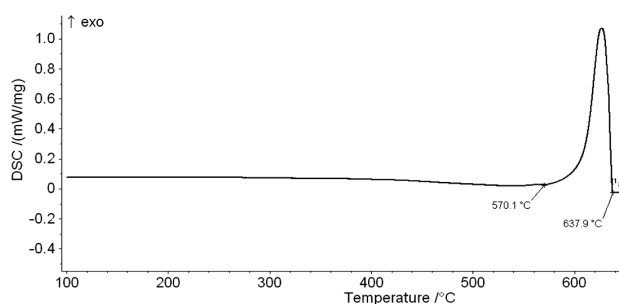


Figure 4: Cooling DSC curve of alloy A, protective atmosphere of N₂ 5,9, flow of 10 mL/h, 1 × vacuum, T_{max} = 650 °C, 5 °C/min

Slika 4: Ohlajevalna DSC-krivulja zlitine A, zaščitna atmosfera N₂ 5,9, pretok 10 mL/h, 1 × vakuum, T_{maks} = 650 °C, 5 °C/min

Table 3: Comparison of the results of DSC analyses in the flow of N₂ for the selected powders

Tabela 3: Primerjava rezultatov izvedenih DSC-analiz v toku N₂ za izbrane prahove

Alloy	Dewaxing*			Alloy formation*			Melting*		Solidification**	
	(temperature, °C)			(temperature, °C)			(temperature, °C)		(temperature, °C)	
	Start	Intermediate	Finish	Start	Intermediate	Finish	Start	Finish	Start	Finish
A	138	348	447	440	506.2	534.2	567.8	650	637.9	570.1
B	138	344	426	498	509.0	-	526.0	600	520.0	615.0
C	139	332	406	466	-	-	542.0	655	542.0	638.0

* endo peaks, ** exo peaks

Table 4: Theoretical temperature thermodynamic phase stability of the selected alloying systems, calculated with ThermoCalc³**Tabela 4:** Teoretična temperaturna termodinamska stabilnost faz v izbranih zlitinskih sistemih, izračunana z orodjem ThermoCalc³

Designation temperature, °C	α -Al	Al ₂ Cu	Al ₅ Cu ₂ Mg ₈ Si ₆	Al ₇ Cu ₂ M	Si	AlFeSi_Beta	Mg ₂ X_Cl	S_Al ₂ CuMg	MgZn ₂	T_AlCuMgZn	α -Al + L	L
Alloy A	< 637.8	< 501.0	< 500	223.2–565.0	< 395.8	< 223	–	–	–	–	525.0–637.8	> 525.0
Alloy B	< 562.6	< 447.8	< 526	–	< 619.7	–	–	–	–	–	532.6–562.6	> 532.6
Alloy C	< 630.0	–	–	–	–	–	< 511.1	< 442.7	< 409.7	> 250.1	516.5–630.0	> 516.5

with XRDS (X-ray diffraction spectroscopy) of the metallographic samples (not performed yet).

The results of the DSC experiments for alloys B and C are compared with the ones for alloy A in **Table 3**. The theoretical calculations of the thermodynamic equilibrium performed with ThermoCalc were also obtained for alloys B and C. The temperatures of the thermodynamic stability of all the phases are given in **Table 4**.

Figure 5 shows a typical measuring protocol and the results of the TG analysis obtained for both experimental conditions during the investigation of alloy A. The heating/cooling program is recorded with a dashed line. One can notice that the resulting TG curve for the analysis performed with stationary Ar is almost the same as the one performed with the flow of nitrogen. The cooling part of the TG curve shows no changes and can, therefore, be omitted. **Figure 6**, therefore, shows only the heating TG curve of alloy A obtained for the flow of nitrogen.

From **Figure 6** one can clearly see that the mass decrease starts at 248 (247) °C because of the lubricant removal (dewaxing). It is completely finished at 447 (446) °C. The total mass loss in this temperature region is 1.42 (1.38) %. This result is in accordance with the powder-producer specification (the wax content $w = 1.5$ %) considering the fluctuation of the wax content inside the volume of the compacted tensile-test specimen. Surprisingly, the mass of the sample again starts to increase

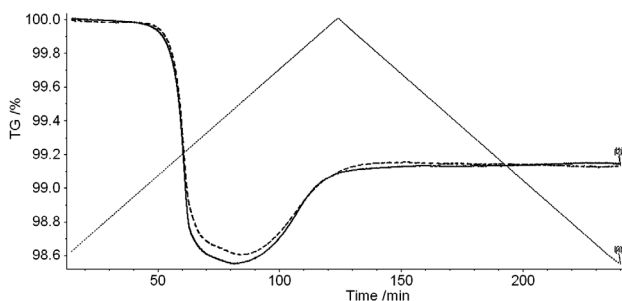


Figure 5: Measuring protocol of the TG analysis of alloy A (heating/cooling is presented as a fine dotted line), comparison of the TG curves obtained during the experiment performed in stationary Ar (dashed line) and the flow of N₂ (full line)

Slika 5: Merilni protokol TG-analize zlitine A (segrevanje/ohlajanje – pikčasta črta), primerjava TG-krivulj, dobljenih med preizkusom v stacionarnem pretoku Ar (črtkana črta) in pretoku N₂ (polna črta)

after dewaxing up to $w = 0.53$ (0.48) %. At the higher temperatures, a reoxidation of the sample is possible and most likely to happen. The first experiments were performed in the pure stationary Ar, and the first assumption was that either the entrapped vapour of the wax caused the sample to reoxidise, or a small leakage of the cell occurred. Therefore, the new DSC/TG experiments were performed in the flow of nitrogen. As one can see, the results of the analyses are very similar (**Figure 6**) and the final conclusion is that the reoxidation is a consequence of the entrapped molecules of air in the green compact because the released vapours of the wax are removed from the cell together with the flow of nitrogen.

The powder producer recommends the following dewaxing procedure during the sintering process: the flow of N₂ in the temperature region between 380 °C and 420 °C for 20 min. However, our TG experiments show that the dewaxing starts much earlier (at approximately 245 °C) and finishes later (at approximately 450 °C). The process of dewaxing must be, therefore, optimized by adequately slowing down the heating procedure in this temperature region. The results of the TG experiments involving alloys B and C are compared with the ones for alloy A in **Table 5**. Dewaxing of the samples made of the green compacts of alloys B and C starts at even lower temperatures (below 200 °C) in the case of the TG performed with stationary Ar. In spite of this, dewaxing of the green compacts made of these materials can be performed in the same way as for alloy A. An interesting result of the TG analyses is that alloy (pow-

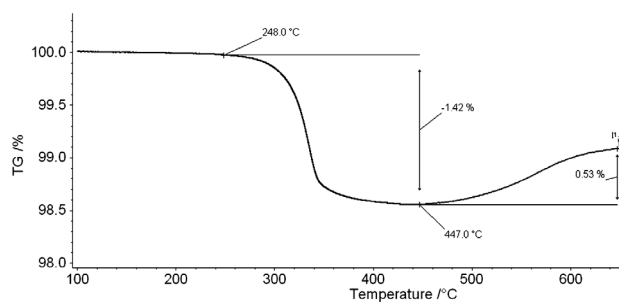


Figure 6: Heating TG curve of alloy A, protective atmosphere of N₂ 5.9, flow of 10 mL/h, 1 × vacuum, T_{max} = 650 °C, 5 °C/min

Slika 6: Segrevalna TG-krivulja zlitine A (sprememba mase vzorca med segrevanjem), zašč. atm. N₂ 5,9, pretok 10 mL/h, 1 × vakuum, T_{maks} = 650 °C, 5 °C/min

Table 5: Comparison of the results of the TG analyses of the selected powders**Tabela 5:** Primerjava rezultatov izvedenih TG-analiz izbranih prahov

Designation	Dewaxing			Reoxidation			Remarks
	Start	Finish	Mass decrease	Start	Finish**	Mass increase	
	°C		w/%	°C		w/%	
Alloy A	248 (247)*	447 (446)	1.40 (1.38)	447 (446)	650	0.53 (0.48)	–
Alloy B	249 (194)	426 (477)	1.53 (1.93)	426 (477)	650	0.25 (0.14)	Early start and late finish of dewaxing in Ar
Alloy C	249 (198)	426 (463)	1.38 (1.73)	426 (463)	650	1.38 (1.92)	

* ... Results of the experiments performed in stationary Ar are given in parenthesis

** ... All experiments finished at 650 °C

der) C with the lowest original oxidation was reoxidised the most during the TG test and that alloy B with the highest original oxidation was reoxidised the least during the TG test. One can speculate that, under the given conditions (time/temperature/atmosphere), each Al-based alloy has a specific oxidation potential if exposed to oxygen.

SEM/EDS analyses¹ showed that powder particles are surface oxidised and that the selected powders are mixtures of different alloys. During ADC some molecules of air are also entrapped. The exact wax composition is not known and it is, therefore, difficult to determine the nature of its melting, evaporation and oxidation. Generally, it is the producer's know-how. But, the waxes appropriate for ADC generally consist of multicomponent systems. The performed DSC/TG analyses can give only the basic but important information about the optimization of dewaxing and sintering processes, respectively.

4 CONCLUSIONS

In the frame of the present work the theoretical thermodynamic analyses and microstructure characterization of the selected Al-alloyed powders are completed with DSC/TG analyses. These provide a more precise insight into the events occurring during the heating and cooling of the green compacts made of the selected Al powders, as well as the optimization of the sintering process. The investigations show that DSC/TG experiments must be performed very carefully and must be, as much as possible, similar to the performed sintering procedure. In the first heating phase, the mass of the samples gradually decreases because of dewaxing. This is associated with the endo (melting and evaporation) and exo (burning) reactions detected on DSC heating curves. Unexpectedly, in all the cases the increase in the sample mass starts above approximately 450 °C. The most probable reason for this is the reoxidation of the samples with the molecules of air entrapped in the green compact. DSC analyses have also shown when exactly, during the heating,

the solution of the alloying elements is formed and the homogeneous solid solution of α -Al, the formation of the first melt, takes place, and when the general melting of the sample starts and finishes. During cooling, DSC analyses have shown the start and finish of the solidification, also indicating when the precipitation of the secondary intermetallic phases occurs at a given cooling rate. These analyses were completed with the theoretical thermodynamic calculations that allow a better understanding of the microstructure evolution, the optimization of heat treatment (precipitation hardening) and an improvement in the mechanical properties.

Acknowledgement

The authors wish to thank the Slovenian Research Agency for the financial support in the frame of project No. L2-4283.

5 REFERENCES

- B. Šuštaršič, I. Paulin, M. Godec, S. Glodež, M. Šori, J. Flašker, A. Korošec, S. Kores, G. Abramovič, Morphological and microstructural features of Al-based alloyed powders for powder-metallurgy applications, *Mater. Tehnol.*, 48 (2014) 3, 439–450
- ECKA Granules, <http://www.ecka-granules.com/en/ecka-granules/products/>
- Thermocalc software, <http://www.thermocalc.com/Software.htm>
- <http://www.netzsch-thermal-analysis.com/en/home.html>
- Netzsch: STA 449 F1: Simultaneous Thermal Analysis, Method, Technique, Applications, <http://private.netzschcdn.com/uploads/>
- International Standard ISO 2740-1986 (E), Sintered metal materials – Tensile test pieces, 1986-10-01, (connected with ISO 6892, Metallic materials- Tensile testing)
- J. F. Chinella, Z. Guo, Computational Thermodynamics Characterization of 7075, 7039, and 7020 Aluminum Alloys Using JMatPro, ARL, MD, USA, 2011
- Z. Guo, N. Saunders, A. P. Miodownik, J. P. Schillé, Prediction of room temperature mechanical properties in aluminium castings, Proceedings of the 7th Pacific Rim International Conference on Modeling of Casting and Solidification Processes, Dalian, China, 2007

MICROSTRUCTURE CHARACTERISTICS OF THE MODEL SPRING STEEL 51CrV4

ZNAČILNOSTI MIKROSTRUKTURE MODELNEGA VZMETNEGA JEKLA 51CrV4

Matjaž Torkar¹, Franc Tehovnik¹, Boštjan Arh¹, Monika Jenko¹, Božidar Šarler²,
Žarko Rajič³

¹Institute of Metals and Technology, Lepi pot 11, 1000 Ljubljana, Slovenia

²Laboratory for Multiphase Processes, University of Nova Gorica, Slovenia

³CIMOS, d. d., Koper, Slovenia

matjaz.torkar@imt.si

Prejem rokopisa – received: 2014-01-28; sprejem za objavo – accepted for publication: 2014-04-03

There are many data on solidification processes in the literature, but there are no relevant comparisons performed for the formation of an as-cast microstructure, the formation of gas porosity, and the influence of different cooling rates on the solidification of the molten, non-killed spring steel 51CrV4. During a relatively rapid solidification the majority of the dissolved gases remain entrapped and due to a solid shell being formed they cannot escape from the steel. The result is the formation of gas porosity and a shrinkage cavity. Here we present the results of an investigation of the appearance and distribution of gas bubbles and a shrinkage cavity as well as the characterization of an as-cast microstructure in ingots of model spring steel, cast and cooled in different ways.

Keywords: spring steel, solidification, gas porosity, shrinkage cavity, SDAS, segregations

V literaturi je mnogo podatkov o procesu strjevanja, vendar pa ni podatkov o primerjavi med nastankom strjevalne strukture in nastankom poroznosti med strjevanjem nepomirjenega vzmetnega jekla 51CrV4. Pri relativno hitrem strjevanju večina raztopljenih plinov ostane ujetih v jeklu in zaradi nastanka skorje ne morejo pobegniti iz njega. Rezultat tega je nastanek plinske poroznosti in lunke. Predstavljeni so rezultati preiskav ter pojava in razporeditve plinskih mehurčkov in lunke, kot tudi karakterizacija mikrostrukture v ingotih vzmetnega jekla, ulitih in ohlajenih na različne načine.

Ključne besede: vzmetno jeklo, strjevanje, plinska poroznost, lunke, SDAS, izceje

1 INTRODUCTION

The typical stages of the solidification process in alloys can be described with the following stages: nucleation of a solid (stable nucleus); growth, which can be cellular or dendritic; solute distribution; and further growth, which proceeds by the movement of the interface and makes up the final as-solidified structure. The accumulation of the solute and the heat ahead of the interface can lead to conditions in which the liquid in front of the solidification front is supercooled. Under specific conditions the solidification becomes dendritic.

A characteristic tree-like structure of crystals growing along an energetically favourable crystallographic direction is called a dendrite in metallurgy. The form and the size of dendrites have a large influence on material properties.¹

The requirement for dendrite formation is that the molten material is undercooled, below the freezing point of the solid. After the nucleation a spherical solid nucleus starts to grow as a sphere, later it becomes unstable and the solid shape depends on the preferred growth directions of the crystal. The anisotropy of the surface energy of the solid-liquid interface influences the growth direction. Besides that, the solidification rate influences

the secondary dendrite arm spacing (SDAS), which can also be calculated using equation (1).²

The SDAS (λ) is a function of the cooling rate and can be written as:

$$\lambda = B \cdot \dot{T}^{-n} \quad (1)$$

where B and n are experimental constant parameters with values of 319.4 and 0.378, respectively,³ and \dot{T} is the cooling rate (°C/s) for this type of steel.

The SDAS (λ) can also be determined from a micrograph.⁴

During their growth dendrites bump into one another, until their growth is restricted by the other dendrites around them. At that point, the dendrite has reached its maximum size and it represents a grain. The space that exists between the grains is referred to as a grain boundary. If molten steel is cooled slowly, the result is the formation of a large grain size. However, when the steel is cooled quickly, the number of dendrites increases and a smaller grain size is the result.⁵ All these parameters influence the microstructure development and the properties of the spring steel.⁶

Solidification proceeds at various rates. For that reason the microstructure is not homogeneous and variations in the composition appear as segregation. Segregation occurs because the diffusion in the solid phase is

too slow to achieve a uniform equilibrium structure, as predicted in the phase diagram. Segregation is classified, according to its scale, as macro-segregation or micro-segregation. This macro-segregation occurs on the scale of the grains or the entire casting and can be observed visually. It arises from a large-scale fluid caused by forced natural and solutal convection. The formation of segregation requires the transport of a solute-poor liquid and solid phases during the solidification over distances much larger than the dendrite arm spacing. The interdendritic flow of the liquid due to solidification shrinkage and changes in the liquid density are an unavoidable cause. These density changes can be caused by temperature changes or by changes in the composition of the liquid.⁷⁻¹⁰

It was revealed that the cooling rate also has an influence on the nucleation temperature and the width of the solidification interval.¹¹

Micro-segregation usually arises between the dendrite arms. Due changes in the chemical composition, the strength and the ductility are lower in the transverse direction compared to the longitudinal axis of the dendrites.¹²

An important piece of data on the solidification structure is the coefficient of segregation k . It is determined as the rate of maximum and minimum concentration among the secondary dendrite arms ($k = C_{\max}/C_{\min}$)¹³ or on the scale of the crystal grains.

Shrinkage cavities and voids are formed during the solidification due the volumetric shrinkage of the metal. This type of defect occurs because most metals contract by 2–6 % in terms of volume when the liquid transforms to a solid.¹² During hot rolling most of the voids are welded without any influence on the mechanical properties. In the case of gas bubbles (hydrogen), especially if they are close to the surface, they can form blisters on the surface during the cold rolling of sheets.¹⁴

Large shrinkage cavities can be minimized by the careful control of the heat transfer during the solidification process. For example, attaching a liquid metal reservoir, or riser, to a sand casting or to an ingot head, encourages shrinkage to occur in the riser, which feeds metal into the casting.

The molten metal dissolves and contains gases. The gases originate from the material, from the atmosphere or from reactions between the molten metal and the mould material. Since a liquid metal has a much higher solubility for gases than a solid metal, the gases are expelled during the solidification of steel. If they cannot escape they may form various defects in the material, e.g., porosity in the metal casting¹⁵.

The maximum solubility of nitrogen in liquid iron is approximately $450 \cdot 10^{-6}$, and less than $10 \cdot 10^{-6}$ at ambient temperature (Figure 1).¹⁶ The presence of the alloying elements in the liquid iron or steel affects the solubility of nitrogen. An important feature is that the presence of dissolved sulfur and oxygen limit the absorp-

tion of nitrogen because they are surface-active elements. This is exploited during steelmaking to avoid excessive nitrogen pickup, particularly during tapping.¹⁶

Shrinkage porosity is represented by small voids in a casting due to solidification shrinkage. Gas porosity is caused by gas bubbles that are evolved during the solidification and become trapped to form small, smooth, round voids or pinholes inside the casting.¹⁷

The bubbles can also be formed by a chemical reaction between the dissolved oxygen and the carbon in steel, to create carbon-monoxide bubbles. The carbon-oxygen reaction in Al-free steel can lead to blowholes, but also to pinholes in the cast material. Carbon and oxygen become enriched during the solidification in the interdendritic melt (as all elements), and the pressures of the carbon monoxide and carbon dioxide increase according to the reactions: $[C] + [O] = \{CO\}$ and $[C] + 2[O] = \{CO_2\}$.

After the CO and CO₂ bubbles are initiated they start to grow with the advancing solid shell and form elongated blowholes.

During rapid solidification a majority of the dissolved gas remains entrapped, as due to the solid shell they cannot escape from the steel and this causes gas bubbles below the solidified shell during the solidification process. In the literature no comparisons are made from among the formation of gas porosity and the properties of the as-cast microstructure during the solidification of the molten spring steel 51CrV4 (1.8159) at different cooling rates. The standardized chemical composition of this type of steel is in mass fractions $w(C) = 0.47-0.55$ %, $w(Si, \max) = 0.4$ %, $w(Mn) = 0.7-1.1$ %, $w(P, \max) = 0.025$ %, $w(S, \max) = 0.025$ %, $w(Cr) = 0.9-1.2$ %, $w(V) = 0.1-0.25$ %.

The aim of the present investigation was to study the influence of the cooling rate of the not killed model spring steel on the appearance and distribution of the gas bubbles and the shrinkage cavity as well as the characterization of the as-cast microstructure.

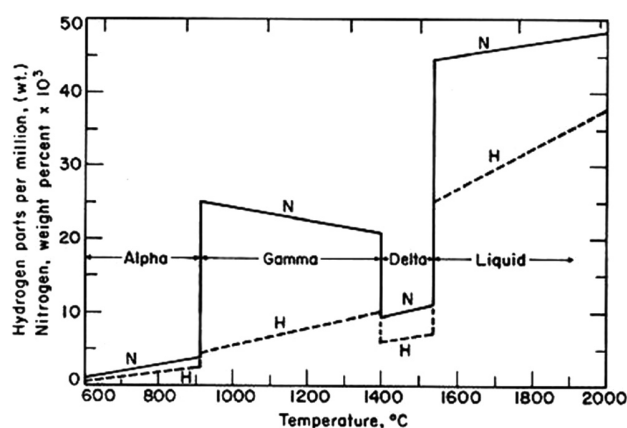


Figure 1: Solubility of nitrogen in iron for the temperatures 600–2000 °C¹⁶

Slika 1: Topnost dušika v železu pri temperaturah 600–2000 °C¹⁶

2 EXPERIMENTAL

The base material was prepared by the remelting of C, Si, Mn, Cr, V spring steel 51CrV4 in a Heraeus induction melting furnace. The final chemical composition of the experimental ingots was: $w(\text{C}) = 0.53 \%$, $w(\text{Si}) = 0.31 \%$, $w(\text{Mn}) = 0.96 \%$, $w(\text{Cr}) = 1.11 \%$, $w(\text{Mo}) = 0.06 \%$, $w(\text{Ni}) = 0.17 \%$ and $w(\text{V}) = 0.16 \%$. The melt was not deoxidized with Al prior to casting. The temperature of the melt in the melting furnace was $1580 \text{ }^\circ\text{C}$. The melt was poured from the furnace into the preheated ceramic pot and then the melt with a temperature of $1530 \text{ }^\circ\text{C}$ was cast into an iron mould and sand form, to obtain different solidification cooling rates. The cross-section of the moulds and the sand cavity was $60 \text{ mm} \times 60 \text{ mm}$.

Special iron moulds were taken for the casting. The moulds consisted of two parts, separated by the diagonal cross-section, enabling the rapid opening and release of the ingot with a solidified shell. The thickness of the mould wall was 25 mm. The moulds were protected with a zirconium-oxide-based coating and heated prior to casting at $150 \text{ }^\circ\text{C}$. The first sample, cast into an iron mould, was taken immediately after casting from the mould and cooled down in water. The second sample was cast into iron mould and cooled down in the mould. The third sample was cast and cooled down in a sand form. Three ingots were produced from the same melt, using three different cooling rates.

To characterize the soundness and the microstructure of the as-cast ingots, a 1-cm-thick plate was cut with a water-jet cutter, in a longitudinal direction, from all three ingots. Samples for metallography were cut from the plate in the middle of the ingots. The samples were prepared by a standard metallographic method and etched in Nital for observation in a light microscope.

Also, the individual micrographs were taken in 5 mm steps from the surface to the center of the ingots. The microstructure was observed using a Nikon Microphot FXA light microscope. The secondary dendrite arm



Figure 2: Longitudinal section of ingot cooled in water and cut with a high-pressure water jet cutter. The presence of gas bubbles disturbed the cutting process. The other two ingots were cut in the same way.

Slika 2: Vzdolžni prerez ingota, ohlajenega v vodi in razrezanega na rezalniku z visokotlačnim vodnim curkom. Tudi druga dva ingota sta bila razrezana na enak način.

spacing was determined from the etched samples. The microstructure was also observed with a JSM-6500F scanning electron microscope (SEM) equipped with a field-emission source of electrons and analysed with an INCA ENERGY Oxford Instruments Energy-Dispersive Spectroscopy (EDS).

3 RESULTS WITH DISCUSSION

The ingots solidified with three cooling rates were manufactured using the casting protocols as follows: a) cast in an iron mould and cooled in water, b) cast and cooled in an iron mould, c) cast and cooled in a sand form.

The ingot cooled in water was cut in a longitudinal direction, as presented in **Figure 2**. The cut was not very clear as the internal gas bubbles and shrinkage cavity (**Figure 3**) disturbed the high-pressure water-jet cutting process. A similar effect was also observed for the other two ingots, as presented in **Figures 4** and **5**.

The dendrites in the microstructure were observed only in the ingot cooled in water. The microstructure was martensitic. Normal crystal grains and no dendritic microstructure were observed in the other two ingots, where the microstructure was pearlite with a different inter lamellar spacing, dependent on the cooling rate. In the samples cooled in the mould or in sand some ferrite on the grain boundaries was observed near the surface of the ingot.

From the comparison of the longitudinal cross-sections of the ingots it is evident that there is a different formation and position of the gas bubbles and shrinkage porosity, both dependent on the cooling rate and the movement of the solidification front. In the ingot cooled

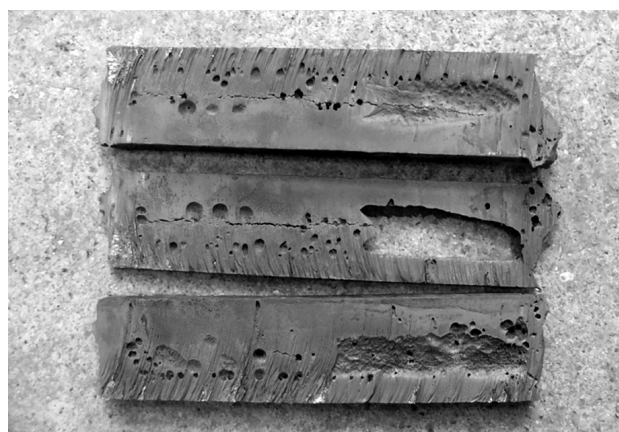


Figure 3: Longitudinal section of ingot, cooled in water. Observed are the gas bubbles and the closed shrinkage cavity in the head and the longitudinal central crack due to rapid cooling after solidification. Evident is the thickness of the solidified shell prior to cooling in the water. All the gas bubbles are below this shell.

Slika 3: Vzdolžni prerez ingota, ohlajenega v vodi, s plinskimi mehurčki in zaprto poroznostjo v glavi ter vzdolžna razpoka v sredini zaradi hitrega ohlajanja po strjevanju. Vidna je debelina strjene skorje pred ohlajanjem v vodi. Vsi plinski mehurčki so pod to skorjo.

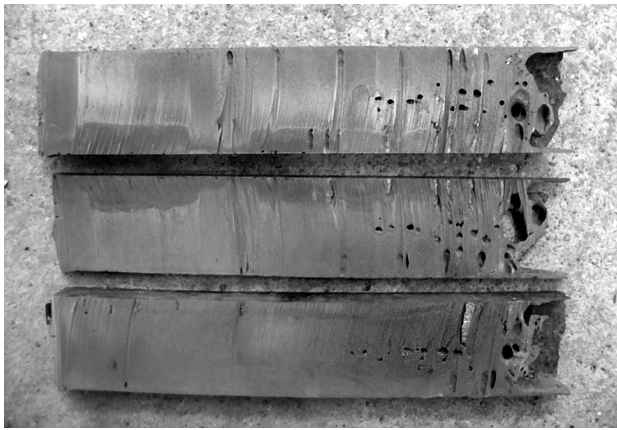


Figure 4: Longitudinal section of ingot cooled in iron mould. Gas bubbles and small closed shrinkage cavity moved toward the head. The solidification front moves toward the head, so the gas bubbles are concentrated below the head, where the last melt solidified.

Slika 4: Vzdolžni prerez ingota, ohlajenega v železni kokili. Plinski mehurčki in majhna zaprta poroznost so pomaknjeni bliže h glavi. Fronta strjevanja se je pomikala proti glavi, zato so plinski mehurčki koncentrirani pod glavo ingota, kjer se je strdila zadnja talina.

in water larger gas bubbles and a large shrinkage cavity was observed, as well as a long crack in the middle of the ingot's longitudinal direction. Evident is also the thickness of the rapidly solidified shell that pushed the bubbles away (**Figure 3**)

The relatively sound material, concerning gas bubbles, is in the ingot cooled in the iron mould. Some gas bubbles are in the central part of the ingot, closer to the head. The reason is the solidification front that moved from the sides and from the bottom toward the head of ingot, where the gas bubbles and the shrinkage porosity are collected (**Figure 4**).

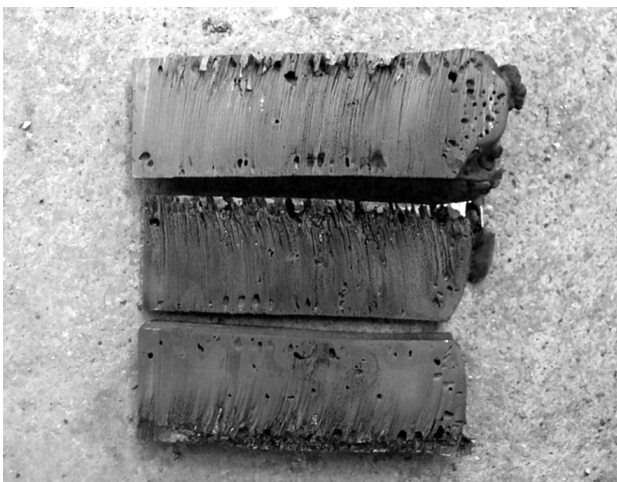


Figure 5: Longitudinal section of ingot, cast and cooled in sand form. Due to the lower solidification rate, the growth of the shell was slower and the bubbles are closer to the surface. No shrinkage cavity is observed.

Slika 5: Vzdolžni prerez ingota, ulitega in ohlajenega v pesku. Zaradi počasnejšega ohlajanja je bila počasnejša tudi rast skorje in iz taline izločeni mehurčki so bližje površini. Lunckerja ni opaziti.

Almost no shrinkage porosity is observed in the ingot cast and cooled in the sand form (**Figure 5**). The gas bubbles (pinholes) are present along the whole ingot and closer to the surface, as the movement of the solidification front was slower. Some individual pinholes are also present in the central part of ingot and more numerous gas bubbles are closer to the head of the ingot.

In general, the gas bubbles and shrinkage porosity for the present steel are more expressed than the steel melt that was not killed with Al or other desoxidant. For that reason the gas content in the melt was higher and as a consequence also the number of bubbles was higher.

It is evident that the dissolved gases (**Figure 1**) did not have enough time to separate completely from the melt, due to the relatively high cooling rate, and the small cross-section at all three ingots. The concentration of gas bubbles depends on the cooling rate. A large closed shrinkage cavity in the head and larger gas bubbles below the surface were observed in the ingot with the fastest solidification rate. In the ingot cooled in the mould the bubbles and the shrinkage cavity moved toward the head of the ingot.

For the ingot cooled in the sand form most of the gas bubbles were observed closer to the surface and no shrinkage cavity was observed in the head of the ingot. This is also evidence that the melt was not killed with aluminium or silicon.

The samples for metallography were prepared from plates cut with a water jet from ingots. Light microscopy revealed that the ingot with the fastest cooling in water has a dendritic microstructure with martensite (**Figure 6**) and visible interdendritic segregations.

The other two ingots, with the slower cooling rate, have a perlitic microstructure with crystal grains of different size and also different interlamellar spacings of cementite lamellas in pearlite (**Figure 7**). The slower cooling rate enables a pearlite transformation in the material.

Due to the relatively slow solidification and cooling in the iron mould and in the sand form, the segregations are clearly visible for the ingot cooled in water. The dendrite arm spacing (**Table 1**) was determined either by measurements of the segregation distance or calculated using equation (1). The cooling rate was also calculated using equation (1).

Table 1: Secondary dendrite arm spacing λ , measured and determined with equation (1), for three cooling rates of the ingots

Tabela 1: Oddaljenost sekundarnih dendritnih vej λ , izmerjena in določena z enačbo (1), za tri hitrosti ohlajanja ingotov

Parameter	Cooling of ingot		
	Water (μm)	Iron mold (μm)	Sand form (μm)
Measured SDAS, $\lambda/\mu\text{m}$	50	150	170
Calculated SDAS, $\lambda/\mu\text{m}$	52	182	210
Calculated $T/(\text{°C/s})$	121.7	4.4	3.0

λ – secondary dendrite arms spacings (SDAS)

T – cooling rate

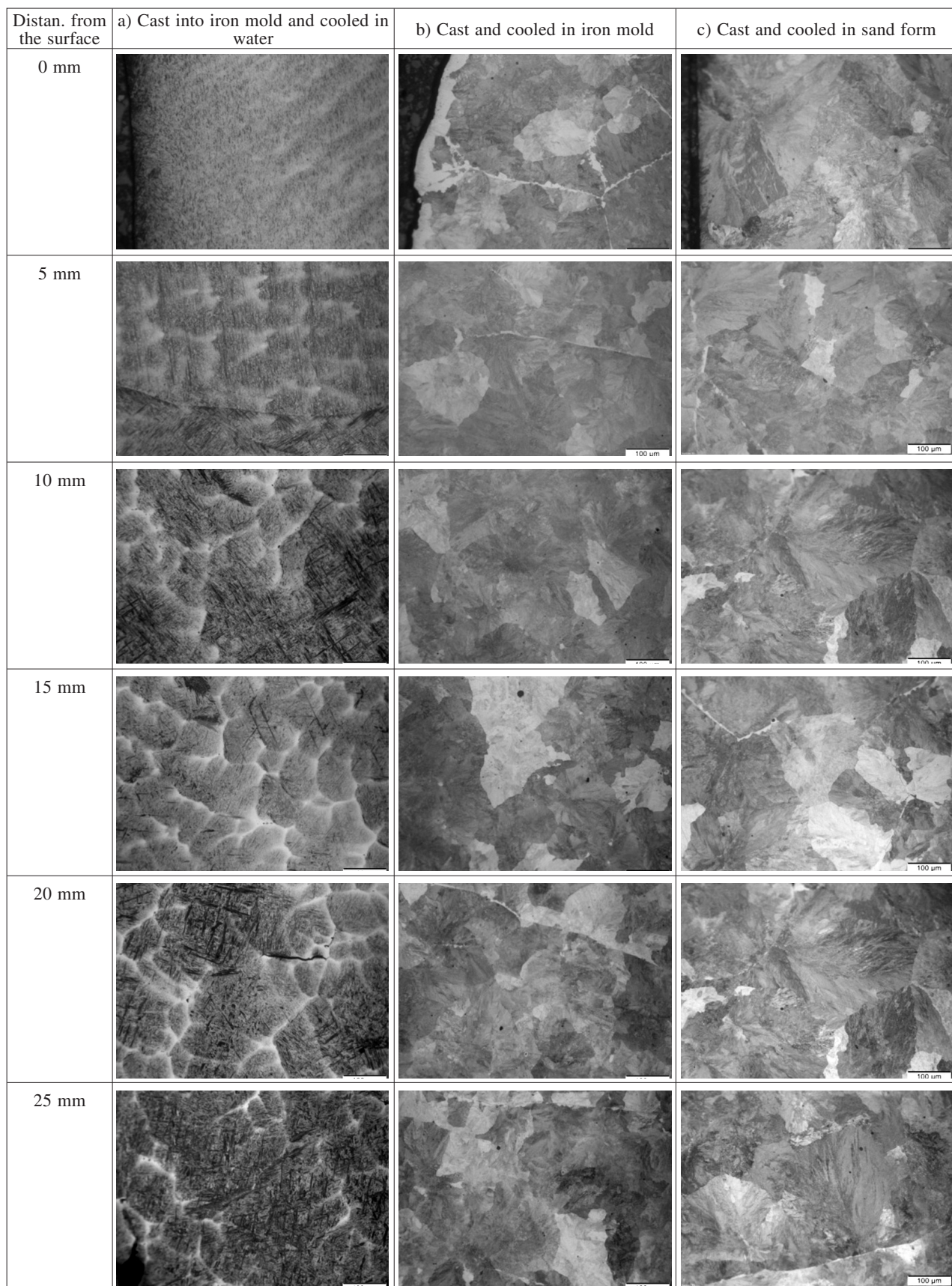


Figure 6: Comparison of as-cast microstructure of ingots at given distances from the surface. Light microscope (magnification 100-times).
Slika 6: Primerjava mikrostrukture ulitih ingotov pri dani razdalji od površine. Svetlobni mikroskop (povečava 100-kratna).

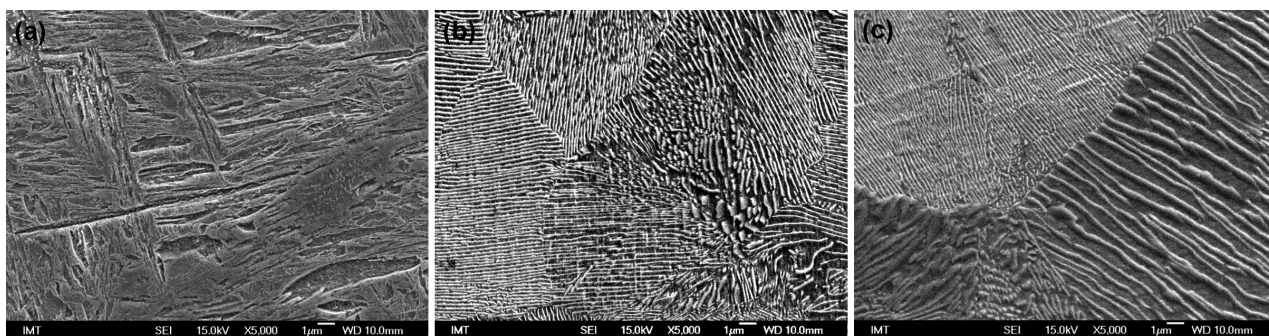


Figure 7: Microstructure of ingots: a) cooled in water, b) cooled in iron mould and c) cooled in sand, (SEM)

Slika 7: Mikrostruktura ingotov: a) ohlajanje v vodi, b) ohlajanje v železni kokili in c) ohlajanje v formi iz peska (SEM)

From the results given in **Table 1** it is clear that the highest cooling rate was in the ingot cooled in water. As can be seen from **Figures 6a** and **7a** the obtained microstructure under the light microscope was martensite for the ingot cooled in water. On the other hand, the cooling rates of other two ingots, solidified in the iron mould and in the sand, are smaller, which is also confirmed by the microstructure (**Figures 6b, 6c, 7b** and **7c**). The microstructures of the ingot solidified in the iron mould and in the sand are pearlite. The reason is in the formation of a gap in the iron mould that prevents faster cooling. The lowest cooling rate is, as expected, in the sand form. The ratio of the cooling rates, compared to the cooling rate in the sand are: 40.56 : 1.46 : 1.00. It means the cooling rate of the ingot in the water was 40.56 times faster compared with the cooling rate of the ingot in the sand form. The cooling rate also influences the SDAS. The secondary dendrite arm spacing, compared to the cooling rates in water, are 1.00 : 3.5 : 4.03. The SDAS is 4.03 times larger in the ingot that was cast and cooled in the sand form, compared to the ingot that was cooled in water.

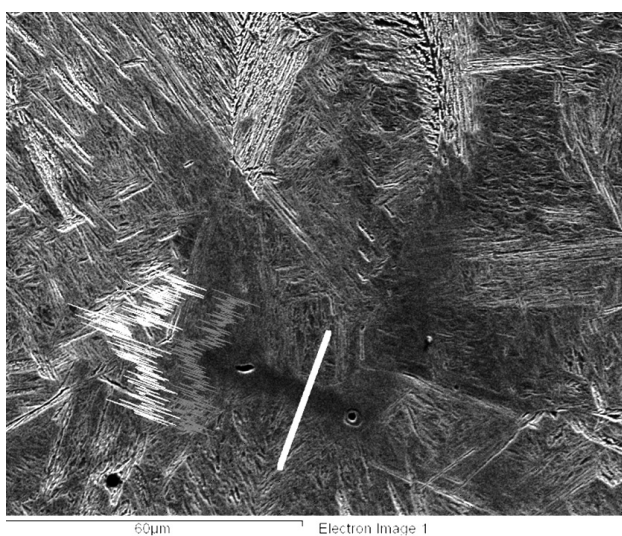


Figure 8: Segregation of chromium and vanadium along the line for ingot cooled in water (SEM)

Slika 8: Izceja kroma in vanadija vzdolž črte v ingotu, ohlajenem v vodi (SEM)

The measurements of the Cr segregations in all three ingots revealed larger differences in the Cr and V concentrations only in the material cooled in water (**Figure 8** and **Table 2**) and less expressed segregations of Cr in ingots cooled in the mould or in the sand (**Tables 3** and **4**), because of the lower cooling rate.

A less expressed segregation of V was observed only in an ingot cooled in water. In the other two ingots the segregation of V was not detected. For that reason only a comparison of the Cr segregations in all three ingots is presented (**Tables 2, 3** and **4**).

Table 2: Segregations of Cr in the ingot cooled in water

Tabela 2: Izceje Cr v ingotu, ohlajenem v vodi

	w(Cr)/%	$k = C_{\max}/C_{\min}$
Centre of Dendrite 1	1.42	
Between dendrite 1/2	1.83	1.28
Centre of Dendrite 2	1.00	
Between dendrite 2/3	1.34	1.34
Centre of dendrite 3	1.42	
Between dendrite 3/4	1.75	1.23

Table 3: Segregations of Cr in the ingot cooled in the mould

Tabela 3: Izceje Cr v ingotu, ohlajenem v kokili

	w(Cr)/%	$k = C_{\max}/C_{\min}$
Centre of Dendrite 1	1.13	
Between dendrite 1/2	1.20	1.06
Centre of Dendrite 2	1.20	
Between dendrite 2/3	1.51	1.25
Centre of dendrite 3	1.27	
Between dendrite 3/4	1.33	1.04

Table 4: Segregations of Cr in the ingot cooled in sand

Tabela 4: Izceje kroma v ingotu, ohlajenem v pesku

	w(Cr)/%	$k = C_{\max}/C_{\min}$
Centre of Dendrite 1	1.20	
Between dendrite 1/2	1.22	1.01
Centre of Dendrite 2	1.20	
Between dendrite 2/3	1.28	1.06
Centre of dendrite 3	1.22	
Between dendrite 3/4	1.26	1.03

The experiments revealed that the increased cooling rate decreases the secondary dendrite arm spacing,

increases the intensity of the segregation of Cr and influences the formation and distribution of gas bubbles and the shrinkage cavity in as-cast material.

For the further processing of the steel the gas bubbles may not be so detrimental because they can be welded during a hot deformation.

To decrease the quantity of gas bubbles, the steel melt needs to be killed more intensively, prior to casting.

4 CONCLUSIONS

Based on the investigations on as-cast 60 mm × 60 mm not-killed spring steel 51CrV4 ingots, the following conclusions can be drawn.

- A comparison of the as-cast microstructures of experimental cast ingots revealed the dendritic structure only in an ingot cooled in water.
- The ingot cooled in water had a martensitic microstructure.
- The ingots cooled in an iron mould or in a sand form have a similar microstructure with pearlite grains, which were coarser for the cooling in the sand form. No dendrites were observed. The slower cooling rate enabled the formation of pearlite with ferrite on some grain boundaries.
- The increased cooling rate decreases the secondary dendrite arm spacing and also influences the formation, as well as the layout, of the gas bubbles and the shrinkage cavity in as-cast spring steel.
- A slower cooling rate caused the formation of gas bubbles closer to the surface of the as-cast ingot.
- In the ingot cooled in water larger gas bubbles were observed, distributed across the whole ingot. A large shrinkage cavity was present, as well as longitudinal cracks in the middle of the ingot.
- The increased cooling rate also increases the segregation of chromium.
- To decrease the quantity of gas bubbles, the steel needs to be aluminium or silicon killed more intensively, prior to the casting.

Acknowledgement

Authors wish to thank to Slovenian Research Agency for the financial support in the frame of projects No. L2-3651 and P2-0132.

5 REFERENCES

- ¹ W. Kurz, D. J. Fisher, *Fundamentals of Solidification*, 4th ed., Trans Tech Publ. Ltd, Switzerland 1998
- ² T. W. Clyne, W. Kurz: *Metall. Trans. A*, 12 (1981), 965–71
- ³ <http://steeluniversity.org>
- ⁴ J. Campbell, *Castings*, Butterworth-Heinemann, 2003, 270
- ⁵ H. Fredriksson Hasse, U. Akerlind, *Solidification and crystallization processing in metals and alloys*, John Willey and sons, 2012
- ⁶ B. Podgornik, V. Leskovšek, M. Godec, B. Senčič, *Microstructure refinement and its effect on properties of spring steel*, *Materials Science and Engineering A*, 599 (2014), 81–86
- ⁷ M. C. Flemings, G. E. Nereo, *Trans. TMS-AIME*, 239 (1967), 1449–61
- ⁸ R. Mehrabian, M. Keane, M. C. Flemings, *Metall. Trans.*, 1 (1970), 1209–20
- ⁹ T. Fuji, D. R. Poirier, M. C. Flemings, *Metall. Trans. B*, 10 (1979), 331–39
- ¹⁰ Y. M. Won, B. G. Thomas, *Simple Model of Microsegregation during Solidification of Steels*, *Metallurgical and Materials Transactions A*, 32 (2001), 1755
- ¹¹ D. Steiner Petrovič, M. Pirnat, G. Klančnik, P. Mrvar, J. Medved, *The effect of cooling rate on the solidification and microstructure evolution in duplex stainless steel*, *J. Therm. Anal. Calorim.*, 109 (2012) 3, 1185–1191
- ¹² K. O. Yu (ed.), *Modeling for Casting and Solidification Processing*, 1st ed., CRC Press, 2001, 12
- ¹³ M. Torkar, B. Šuštaršič, *Preiskava vodno atomiziranega prahu iz zlitine Nimonic 80 A, Kovine zlitine tehnologije*, 26 (1992) 1–2, 100–103
- ¹⁴ H. J. Grabke, *Supersaturation of iron with nitrogen, hydrogen or carbon and the consequences*, *Mater. Tehnol.*, 38 (2004) 5, 211–222
- ¹⁵ P. S. Wei, C. C. Huang, Z. P. Wang, K. Y. Chen, C. H. Lin, *Growths of bubble/pore sizes in solid during solidification – an in situ measurement and analysis*, *Journal of Crystal Growth*, 270 (2004) 3–4, 662–673
- ¹⁶ <http://www.keytometals.com>
- ¹⁷ R. A. Stoeh, *Modeling the influence of fluid flow on the development of porosity and microstructure in castings*, *Canadian Metallurgical Quarterly*, 37 (1998) 3–4, 179–184

EFFECT OF CREEP STRAIN ON CREEP RATE IN THE TEMPERATURE RANGE 550–640 °C

VPLIV DEFORMACIJE NA HITROST LEZENJA PRI TEMPERATURAH OD 550 °C DO 640 °C

Borut Žužek, Franc Vodopivec, Monika Jenko, Bojan Podgornik

Institute of Metals and Technology, Lepi pot 11, 1000 Ljubljana, Slovenia
borut.zuzek@imt.si, franc.vodopivec@imt.si

Prejem rokopisa – received: 2014-03-06; sprejem za objavo – accepted for publication: 2014-04-03

Experimental and calculated creep rates were examined for a high-chromium, creep-resistant steel samples quenched and tempered for 2 h and 400 h at 800 °C. Creep testing and annealing were carried out at 550 °C to 640 °C. It was found that the difference in the creep rates due to the particle coarsening and dissolution was independent of the temperature, while the ratio of the experimental and calculated creep rates increased with the temperature of the creep tests. The results suggest that an increase in the creep rate is related to the process of vacancy climb in parallel with the increase in the diffusion rate of the iron in the ferrite.

Keywords: creep-resistant steel, $M_{23}C_6$ particle coarsening and dissolution, experimental and calculated creep rates, effect of temperature

Hitrost lezenja je bila eksperimentalno določena in izračunana za jeklo, odporno proti lezenju, z visoko vsebnostjo kroma pri vzorcih, ki so bili kaljeni in popuščani 2 h oz. 400 h pri 800 °C. Stourni preizkusi lezenja in žarjenja so bili izvršeni pri 550 °C do 640 °C. Razlika v hitrosti lezenja zaradi raztapljanja oziroma rasti izločkov je bila neodvisna od temperature, medtem ko je razlika med eksperimentalno in izračunano hitrostjo lezenja večja pri višji temperaturi. Rezultati meritev in izračunov kažejo, da je povečanje hitrosti lezenja povezano z večjo hitrostjo plezanja vrzeli, ki je vzporedno s povečanjem hitrosti difuzije železa v feritu.

Ključne besede: jeklo, odporno proti lezenju, rast in raztapljanje izločkov $M_{23}C_6$, eksperimentalna in izračunana hitrost lezenja, vpliv temperature

1 INTRODUCTION

The microstructure of creep-resistant steels consists of a ferrite matrix with different elements, mostly chromium in solid solution, and particles, mostly carbides and carbonitrides, with sizes in the range from a few nm to about $1 \cdot 10^3$ nm. Those particles are unsharable obstacles to the gliding of the matrix mobile dislocations. For a particle size (d_p) greater than the spacing (mutual distance) of the mobile dislocations, the particles intercept the mobile dislocations with a probability $p \geq 1$, while for smaller particles the intercept probability is $p \leq 1$.¹ So far, it has not been determined whether the unsharability is related to a minimum particle size, i.e., the number of carbide molecules in the particle. For example, the lattice parameter (l_p) of the cubic carbide $Cr_{23}C_6$ is $l_p = 1.016$ nm,² and the number of molecules in the particles is $N_{pm} \approx d_p^3/l_p$. The number increases rapidly with the particle size: it is $N_{pm} = 8$ for particles with $d_p = 2$ nm and $N_m = 125$ for $d_p = 5$ nm. With isothermal tempering, the average particle size increases and their number decreases, as a result of the duality of the particle-coarsening process: the growth of coarser particles, the shrinking of particles with an intermediate size and even the dissolution of smaller particles.¹ This means that by tempering, the average size of the particles increases, and it increases more rapidly during a creep test, as the

iron self-diffusion and the chromium diffusion in ferrite are enhanced by tensile stress.^{3,4}

For creep-resistant steels, the improvement of Hornbogen's creep equation^{5,6} for a uniform distribution of particles was proposed, with the substitution of the particle spacing λ by $(\lambda - d)$ as a measure of the dislocation climb length increase by overcoming of particles inclusion of a constant representing the increase of the stress exponent n from $n = 2$ to $n = 3.65$:

$$\dot{\epsilon} = \frac{k_\sigma \cdot b^2 \cdot \sigma^n \cdot \rho \cdot D \cdot (\lambda - d)}{k_b \cdot T \cdot G} \quad (1)$$

where σ is the acting stress ($\sigma = 170$ MPa), ρ is the density of the mobile dislocations ($\rho = 0.978 \cdot 10^{14} \text{ m}^{-2}$), D is the diffusion coefficient, d is the average particle size, λ_p is the average particle spacing, b is the Burgers vector ($b = 2.5 \cdot 10^{-10}$ m), k_b is the Boltzmann constant ($k_b = 1.38 \cdot 10^{-23} \text{ J K}^{-1}$), T is the temperature, G is the shear modulus⁷ and $k_\sigma = \sigma^{3.65}/\sigma^2 = 4.78 \cdot 10^3$.

By substituting the molar content of carbide $M_{23}C_6$ with the molar content of the chromium in solution in ferrite as a parameter in the LSW (Livshitz-Slyozov-Wagner) equation, a reasonable agreement was obtained for the calculated (Eq. 2) and experimental coarsening rate of the $M_{23}C_6$ particles at 800 °C. Also, Eq. 3 was deduced for the calculation of the coarsening rate at lower temperature:⁸

$$d_t^3 - d_0^3 = \left(\frac{8 \cdot S \cdot \gamma \cdot \Omega \cdot D}{9 \cdot k_b \cdot T} \right) \cdot t \quad (2)$$

$$k_{cT} = k_{c,1073} \left(\frac{D_{Cr,T} \cdot 1073}{D_{Cr,1073} \cdot T} \right) \quad (3)$$

where d_t is the particle size at the tempering time t , d_0 is the initial particles size, D is the chromium diffusion rate, T is the tempering temperature, S is the atomic content of chromium in solid solution in the ferrite, γ is the carbide particle matrix interfacial energy ($\gamma = 0.37$ J m⁻²), Ω is the volume of diffusing atoms, D is the chromium diffusion rate ($D = D_0 \exp(-Q/RT)$) with $D_0 = 3.7 \cdot 10^{-3}$ m² s⁻¹ and Q is the activation energy ($Q = 267$ kJ mol⁻¹),⁹ k_b is the Boltzmann constant and k_{c1073} is the experimental coarsening rate at 800 °C ($k_{c1073} = 2.94 \cdot 10^{-27}$ m³ s⁻¹).

In this work, the effect of the creep strain on the change of particle size and spacing is investigated with a constant creep stress and time.

2 CALCULATIONS

The creep rate and creep fracture of creep-resistant steels depend of a large number of variables,¹⁰ because with the creep temperature, the initial microstructure of the ferrite and the uniform distribution of particles is changed due to particle coarsening. With this coarsening, several processes occur, i.e., the growth of the particles' average size and spacing, the dissolution of small particles, the decrease in the number of particles and of grain-boundary stringers.¹⁰ The change in the particles size and spacing is calculated for 100 h of tempering at 550–640 °C in steps of 30 °C using Eqs. 2 and 3. Assuming the particles to be spheres, the number of particles N_p was calculated by applying the series:¹

$$f = \frac{\pi}{6} \cdot \sum_1^n d_1^3 + d_2^3 + d_3^3 + \dots + d_n^3 = \frac{\pi}{6} N_p d_a^3 \quad (4)$$

and $N_p = \frac{6f}{\pi d_a^3}$

where f is the volume of particles, N_p is the number of particles, $d_1, d_2, d_3, \dots, d_n$ is the decreasing size of the particles and d_a is the average particles size. The volume of particles in the investigated steel was $f = 0.047$ ¹⁰ and it was determined that the particles were carbide M₂₃C₆ (Cr₁₈Fe₃Mo₂C₆).^{11,12}

The particles dissolution velocity was deduced as:¹

$$d_d^3 - d_0^3 = k_{cd} \quad t_d = \frac{d_d^3 - d_0^3}{k_c} \quad v_d = \left(\frac{d_d^3}{t_d} \right)^{1/3} \quad (5)$$

where d_d is the size of the dissolving particles, k_c is the isothermal coarsening rate (the term in parenthesis in Eq. 2), t_d is the dissolution time, $d_0 = 2$ nm and, v_d is the dissolution velocity.

The volume of the particles increases with d_d^3 , and for this reason the parameter $d_0 = 2$ nm was omitted from the calculations of the dissolution velocity.

The initial average particle size d_{ia} was deduced for the tempering of specimens quenched in oil as:¹

$$(d_{ia})^3 = k_{cT} t \quad (6)$$

where k_c is the coarsening rate at 1073 K ($k_{c800 \text{ °C}} = 2.94 \cdot 10^{-27}$ m³ s⁻¹) and t is the tempering time at 1073 K, and $d_{ia} = 148$ nm was deduced.⁸ The volume of carbide particles Cr₁₈Fe₃Mo₂C₆ $f = 0.047$ was deduced from the content of chromium in the investigated steel.¹³ The calculated average particle size agrees well with the average size $d = 140$ nm assessed from micrographs.¹³

The increase of the particle size with a tempering time of 100 h and the creep test temperature is deduced as:

$$\Delta d_{aT} = (k_{cT}/k_{c1073}) \Delta d_{1073} \quad (7)$$

where Δd_{aT} is the increase of the average particle size with 100 h of tempering at temperature $T = (823, 853, 883 \text{ and } 913)$ K, k_{cT} is the coarsening rate deduced from Eq. 3, k_{c1073} is the coarsening rate at 1073 K ($k_{c1073} = 2.94 \cdot 10^{-27}$ m³ s⁻¹) and Δd_{1073} is the increase of particles with an initial size of 148 nm after 100 h tempering at 1073 K. The number of particles $N_{1p} = 2.11 \cdot 10^{19}$ m⁻³ was then deduced from Eq. 4 for $f = 0.047$.¹⁴

Then, the average particle spacing λ for the particles coarsening at the test temperature was calculated as:⁶

$$\lambda = 4 d/\pi f^{1/3} \quad (8)$$

With tempering resp. creep test temperature, a significant number of particles with a size in the lower part of size distribution is dissolved.¹ The size of the dissolved particles d_{dm} was first deduced from Eq. 5, and then the part of particle with size $d_d \leq d_{dm}$ determined for M₂₃C₆ of average size $d_a = 157$ nm.¹ Following that the number of undissolved particles after 100 h of tempering at the creep temperature was deduced to be $N_{pT} = N_{ip} (10^{-2} N_{nd})$.

The changes of the average particle size d_u and spacing λ_u for the undissolved particles with 100 h at the creep test temperature were calculated as:

$$d_u = \left(\frac{6 \cdot 10^{27} \cdot f}{\pi \cdot N_{pT}} \right)^{1/3} \quad \text{and} \quad \lambda_u = k_u \cdot \left(\frac{6 \cdot 10^{27}}{N_{pT}} \right)^{1/3} \quad (9)$$

with $k_u = 1.585$ constant characteristic for the stochastic distribution of cube particle. With an equal average particle size and $f = 0.047$ the difference of in the particle spacing deduced from Eq. 8 and 9 is about 1 %.

With the change of the creep temperature in Eq. 1, the parameters T, D_{Fe}, λ, d and G are changed, and it is possible to calculate the change of creep rate with the known iron self-diffusion rate D_{FeT} and chromium D_{CrT} diffusion rate by tempering, particles size and spacing and shear modulus. In the calculation it should be kept in mind that by creep test iron self-diffusion rate is increased and the chromium diffusion rate, determining the change of particles size and spacing, changes as well. The iron self-diffusion and chromium diffusion rates were calculated from the data in⁸ and the shear modulus deduced from.⁹

3 RESULTS

In^{3,4} it is stated that the number of vacancies in ferrite is increased by tensile stress and the iron and chromium diffusion rate are increased. It is reasonable to presume that with an increased content of vacancies, the climb velocity is also increased. Eq. 1 indicates that with a constant creep stress, the increase of the creep rate is proportional to changes of the iron diffusion rate, of the parameter $(\lambda - d)$ and of the shear modulus G .⁷ Assuming that the effect of temperature and creep is equal for iron and chromium diffusion, the change of particle size and spacing was calculated.

The results of the calculations listed in **Table 1** indicate that the increase of coarsening rate due to the growth of the average particle size is much lower than that due to the dissolution of small particles. The greatest increase of creep rate due to particle growth was $\Delta\dot{\epsilon} = 0.3 \cdot 10^{-8} \text{ s}^{-1}$, about 0.4 %, which was obtained at the highest creep test temperature of 913 K (640 °C). The increase of the creep rate due to the dissolution of small particles was significantly greater and it increased with the creep test temperature. At 913 K (640 °C) it was $\Delta\dot{\epsilon} = 4.3 \cdot 10^{-8} \text{ s}^{-1}$ and by 6.1 %, about 15 times, greater than that due to the growth of the average particle size.

The difference of the experimental creep rate and that due to the particle dissolution increased with the test temperature and was $\Delta\dot{\epsilon} = 0.47 \cdot 10^{-8}$ at 823 K and $\Delta\dot{\epsilon} = 645.4 \cdot 10^{-8}$ at 913 K.

In **Figure 1** the experimental creep rate, as well as the iron diffusion rate by tempering and the apparent iron diffusion rate by creep are depicted as the dependence of creep test temperature. As expected for diffusion-controlled processes, the log value of the ordinate is proportional to the abscissa ($1/T$). However, the dependences

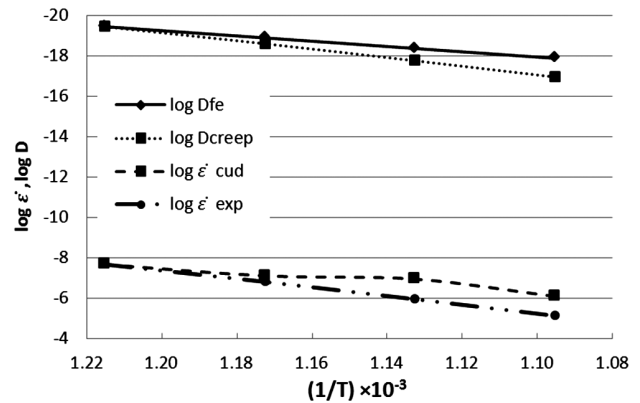


Figure 1: Creep rate calculated for undissolved particles ($\dot{\epsilon}_{\text{cud}}$), experimental creep rate ($\dot{\epsilon}_{\text{creep}}$), iron diffusion rate by tempering (D_{Fetemp}) and apparent iron diffusion rate by creep test (D_{Fecreep}) versus the inverse of the creep test temperature

Slika 1: Hitrost leženja, izračunana za nerastopljene izločke ($\dot{\epsilon}_{\text{cud}}$), eksperimentalna hitrost leženja ($\dot{\epsilon}_{\text{creep}}$), hitrost difuzije železa pri žarjenju (D_{Fetemp}) in navidezna hitrost difuzije železa pri leženju (D_{Fecreep}) v odvisnosti od recipročne vrednosti temperature

are not parallel, as with creep tests the changes of the parameter $(\lambda - d)$ and shear modulus G in Eq. 1 are independent of the iron diffusion rate.

For $T \geq 823 \text{ K}$ and creep stress 170 MPa, the effects of an increase of the temperature on the experimental creep rate and the iron creep diffusion rate are:

$$\begin{aligned} \lg \dot{\epsilon}_{\text{exp}} &= -7.677 + 2.11 \cdot 10^4 / T \text{ and} \\ \lg D_{\text{Fecreep}} &= -19.277 + 2.07 \cdot 10^4 / T \end{aligned} \quad (10)$$

In Eq. 1 the constant $k = 4.78 \cdot 10^3 = \sigma^{3.5}/\sigma^2 = 4.78 \cdot 10^3$. The equation can be written for the similar steel as well as coarsening and dissolution rate of carbide par-

Table 1: Basic parameters and results of the calculations for the temperature 823–913 K (550–640 °C)

Tabela 1: Osnovni parametri in rezultati izračunov za temperature 823–913 K (550–640 °C)

Temperature (K)	823	853	883	913
Temperature (°C)	550	580	610	640
Shear modulus (MPa · 10 ³)	54.7	53.7	52.3	51.7
Coars. part size, d /nm	148	148	148.2	148.7
Average spacing of d_i particles (λ_i)	523	523	524	526
Particles coarsening rate (m ³ s ⁻¹)	$2.52 \cdot 10^{-31}$	$1.28 \cdot 10^{-30}$	$4.42 \cdot 10^{-30}$	$1.40 \cdot 10^{-29}$
$D_{\text{Fetemp}}/(m^2 \text{ s}^{-1})$	$3.68 \cdot 10^{-20}$	$1.33 \cdot 10^{-19}$	$4.41 \cdot 10^{-19}$	$1.35 \cdot 10^{-18}$
$D_{\text{Cttemp}}/(m^2 \text{ s}^{-1})$	$4.72 \cdot 10^{-20}$	$1.85 \cdot 10^{-19}$	$6.64 \cdot 10^{-19}$	$2.18 \cdot 10^{-18}$
$D_{\text{Fecreep}}/(m^2 \text{ s}^{-1})$	$3.74 \cdot 10^{-20}$	$2.61 \cdot 10^{-19}$	$1.80 \cdot 10^{-18}$	$1.14 \cdot 10^{-17}$
$K_{\text{creep}}/(m^3 \text{ s}^{-1})$	$2.52 \cdot 10^{-31}$	$3.29 \cdot 10^{-31}$	$1.80 \cdot 10^{-29}$	$5.65 \cdot 10^{-29}$
Creep rate by d_i and λ_i , $\epsilon_i/(10^{-8} \text{ s}^{-1})$	1.99	7.08	23.80	70.20
Creep rate of growth of d_n , $\epsilon_n/(10^{-8} \text{ s}^{-1})$	1.99	7.09	24.00	70.50
Size of dissolved particles, d_d /nm	6.26	8.36	11.90	17.30
Part of undissolved particles, $d_d/(10^{-2} N_i)$	90.16	88.09	85.12	82.22
Number of undissolved particles, $N_{pr}/(10^{19} \text{ m}^{-3})$	1.28	1.25	1.21	1.17
Average size of undissolved particles (nm)	154.00	155.00	157.00	159.00
Average spacing of undissolved particles, λ_{nd} /nm	569.00	574.00	580.00	587.00
Creep rate due to λ_i increase, $\epsilon_i/(10^{-8} \text{ s}^{-1})$	2.07	7.44	25.30	74.60
Experimental creep rate, $\epsilon_{\text{exp}}/(10^{-8} \text{ s}^{-1})$	2.50	15.50	110.00	720.00
Ratio 19/18	1.21	2.08	4.34	9.65
Ratio 9/7	1.02	2.04	4.27	8.44
Ratio 18/11	1.05	1.05	1.05	1.05

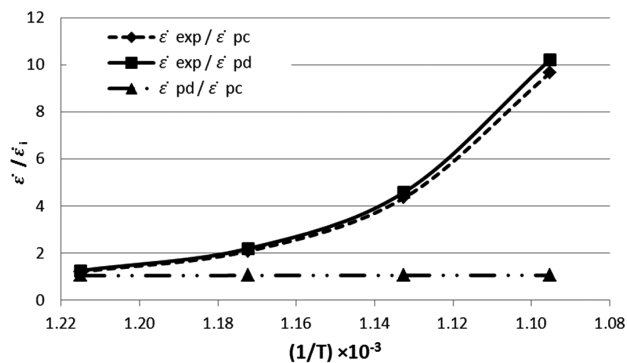


Figure 2: Effect of creep test temperature on the ratio of the experimental creep rate ($\dot{\epsilon}_{\text{exp}}$) versus creep rates calculated considering the particles coarsening ($\dot{\epsilon}_{\text{pc}}$) and dissolution ($\dot{\epsilon}_{\text{pd}}$) by tempering at creep test temperature and ratio of creep rates calculated for dissolution and growth of average particles size ($\dot{\epsilon}_{\text{pd}}/\dot{\epsilon}_{\text{pc}}$)

Slika 2: Vpliv temperature preizkusa lezenja na razmerje eksperimentalna hitrost lezenja ($\dot{\epsilon}_{\text{exp}}$) proti hitrosti lezenja, izračunani za rast ($\dot{\epsilon}_{\text{pc}}$) in raztapljanje ($\dot{\epsilon}_{\text{pd}}$) izločkov pri žarjenju pri temperaturi preizkusa, in razmerje izračunanih hitrosti lezenja za raztapljanje izločkov in rast povprečne velikosti izločkov ($\dot{\epsilon}_{\text{pd}}/\dot{\epsilon}_{\text{pc}}$)

ticles as $\dot{\epsilon} = k_1 \sigma^n D_{\text{Fecreep}}$ with $k_1 = (b^2 \rho / k_b TG)$ and $n = 3.65$ and the effect of change of creep stress on iron diffusion and creep rate deduced.

The ratio of the experimental creep rate resp. creep rate calculated considering the coarsening of particles and the dissolution of particles versus the creep temperature shown in **Figure 2** is independent of the creep temperature. It indicates that the increase of temperature has an equal effect on the dissolution and coarsening of the particles, as both depend on the diffusion rate of iron and chromium.

The growth of iron creep diffusion rate (D_{Fetemp}) with increasing temperature is lower than the change of the creep rate and the difference is much higher than 1.15 due to the creep stress deduced from data in.⁴ In the particle disjunctive matrix the gliding stress is decreased strongly, while the climbing stress is diminished much less. As creep strain consists of the glide and the climb of dislocations, it is reasonable to assume that the climb velocity is greater with the greater diffusion rate of vacancy in matrix. Based on available data, it seems reasonable to assume that D_{Fecreep} in **Table 1** and **Figure 1** represent⁵ the increase of a parallel increase of climb velocity, resp. creep rate related to the content of vacancies.

4 CONCLUSIONS

- The coarsening and dissolution rates for $M_{23}C_6$ particles in a high-chromium, creep-resistant steel was calculated for the temperature interval 550 °C to 640 °C;
- The creep rate was then calculated for the investigated range of temperature using the equation with particle size and spacing as parameters and determined experimentally with static tests 100 h by creep stress 170 MPa for equal temperatures;

- In the considered temperature interval, the creep rate was increased for above one order of magnitude stronger with small particles dissolution than with coarser particles growth;
- The iron apparent diffusion rate increased strongly by increasing creep tests temperature;
- Based on the obtained results, empirical relations are deduced for the increase of the experimental creep rate and the apparent iron diffusion rate in ferrite by creep tests with increased temperature.
- It is suggested that the increase of the experimental creep rate with creep temperature are related to a greater iron diffusion rate and a greater climb velocity due to the greater content of vacancies as well as the climb stress in the particles disjunctive matrix.

Acknowledgement

The authors are indebted to the Slovenian Research Agency (ARRS) for the support of the investigation.

5 REFERENCES

- 1 F. Vodopivec, B. Žužek, F. Kafexhiu, Change of $M_{23}C_6$ particles size and spacing by tempering a high chromium creep resistant steel in range 800 to 550 °C, *Steel Research Int.*, doi: 10.1002/srin.201400013
- 2 A. L. Bowman, G. P. Arnold, E. K. Storman, N. G. Nereson, *Acta Cryst. B*, 28 (1972), 3102–3103
- 3 I. V. Valikova, A. V. Nazarov, Simulation of Characteristics Determining Pressure Effects on Self Diffusion in BBC and FCC Metals, *The Physics of Metals and Metallography*, 109 (2010), 220–226
- 4 J. W. Jang, J. Kwon, B. J. Lee, Effect of stress on self diffusion in bcc Fe, An atomistic simulation study, *Scripta Mat.*, 63 (2010), 39–42
- 5 F. Vodopivec, B. Žužek, M. Jenko, D. A. Skobir-Balantič, M. Godec, *Mat. Sci. Tech.*, 29 (2013), 451–455
- 6 E. Hornbogen, Einfluss von Teilchen einer zweiten Phase auf das Zeitverhalten, In: W. Dahl, W. Pitch, *Festigkeits- und Bruchverhalten bei höheren Temperaturen*, Verl. Stahleisen, Düsseldorf 1980, 31–52
- 7 Y. F. Yin, R. G. Faulkner, Physical and elastic behaviour of creep resistant steels, In: F. Abe, T. U. Kern, R. Viswanathan (eds.), *Creep resistant steels*, Woodhead Publ. LTD., Cambridge, England 2008, 217–240
- 8 F. Vodopivec, D. Steiner - Petrovič, B. Žužek, M. Jenko, Coarsening rate of $M_{23}C_6$ particles in a high chromium creep resistant steel, *Steel Res. Int.*, 84 (2013), 1110–1114
- 9 H. Oikawa, Y. Iijima, Diffusion behaviour of creep-resistant steels, In: F. Abe, T. U. Kern, R. Wiswanathan (eds.), *Creep resistant steels*, Woodhead Publ. Lim., Cambridge, England 2008, 241–264
- 10 H. K. D. H. Bhadeshia, *Mat. Sci. Techn.*, 24 (2008), 128–130
- 11 D. A. Skobir, F. Vodopivec, M. Jenko, S. Spaič, B. Markoli, *Z. Metallkd.*, 95 (2004) 11, 1020–1024
- 12 F. Vodopivec, D. A. Skobir - Balantič, M. Jenko, B. Žužek, M. Godec, *Mater. Tehnol.*, 46 (2012) 6, 633–636
- 13 F. Vodopivec, J. Vojvodič-Tuma, B. Šuštaršič, R. Celin, M. Jenko, *Mat. Sci. Tech.*, 27 (2011), 939–942
- 14 B. Žužek, Influence of the distribution of carbide particles on the activation energy for the creep deformation of steels, Ph. D. Thesis, J. Stefan International Postgraduate school, Ljubljana, 2013

IDENTIFICATION OF THE INITIAL FAILURE AND DAMAGE OF SUBSTITUENTS OF A UNIDIRECTIONAL FIBER-REINFORCED COMPOSITE USING A MICROMODEL

UPORABA MIKROMODELA ZA UGOTAVLJANJE ZAČETNIH NAPAK IN POŠKODB SESTAVIN KOMPOZITA, ENOSMERNO OJAČANEGA Z VLAKNI

Hana Srbová, Tomáš Kroupa, Robert Zemčík

University of West Bohemia in Pilsen, Department of Mechanics, Univerzitní 22, 306 14 Plzeň, Czech Republic
hsrbova@kme.zcu.cz

Prejem rokopisa – received: 2012-08-31; sprejem za objavo – accepted for publication: 2013-10-11

The main goal of this investigation was to test the capabilities of simple failure and damage criteria for the material phases of a unidirectional long-fiber carbon-epoxy composite material. This goal requires the identification of the material parameters in order to simulate simple tensile tests performed on thin coupons with various fiber orientations. Furthermore, a failure criterion for the fibers and a damage criterion for the matrix are proposed and the material parameters are identified in order to capture the moment of the first failure or damage. Finite-element analyses are performed on a unit cell with applied periodical boundary conditions. The identifications were performed using Optislang 3.2.0 and Python 2.4. The finite-element analyses were performed using Abaqus 6.11-1.

Keywords: unidirectional fiber composite, identification, matrix work-hardening function, unit cell, micromodel, non-linear

Glavni namen predstavljenega dela je preizkus sposobnosti enostavnih meril za napake in poškodbe pri sestavinah epoksikompozita, enosmerno ojačanega z dolgimi ogljikovimi vlakni. Ta cilj zahteva poznanje parametrov materiala za simulacijo enostavnega nateznega preizkusa, izvedenega na tankih ploščicah z različno orientacijo vlaken. Predlagana so merila za porušitev vlaken, za poškodbe osnove in ugotovljeni so parametri materiala za ugotovitev trenutka prve porušitve ali poškodbe. Analiza končnih elementov na osnovni celici je bila opravljena z uporabo periodičnih robnih pogojev. Identifikacija je bila izvršena z uporabo Optislang 3.2.0 in Python 2.4. Analize končnih elementov so bile izvršene z Abaqus 6.11-1.

Ključne besede: kompozit, enosmerno ojačan z vlakni, identifikacija, funkcija deformacijskega utrjevanja osnove, osnovna celica, mikromodel, nelinearen

1 INTRODUCTION

Composite materials are widely used due to their advantageous stiffness-to-weight and strength-to-weight ratios. The composites' material properties depend on the volume ratio of the constituents and their properties.

There are several approaches to modeling a composite material's behavior. The material model can be modeled on the micro-, meso- and macro-scale levels. The macromechanical approach requires, compared to the micromechanical, less detailed and time-consuming modeling. In¹ the non-linear behavior of composites was modeled using a macroscopic approach. Nevertheless, the micromechanical approach gives more detailed information about the constituents,² for example, the damage and failure of the matrix and fiber. It is also possible to capture the nonlinear behavior of a composite by assuming the constituents to be nonlinear materials. A composite material may vary its properties due to matrix cracking and fiber breaking during loading.

A knowledge of damage mechanisms on the micro level of the material is important during the design processes of structures. This fact is more important when it

comes to a structure made of heterogeneous materials, such as composites or when the task is to avoid the damage or failure of the structure.

2 EXPERIMENT

Tensile tests of thin coupons made of unidirectional longfiber carbon-epoxy composite SE84LV-HSC-450-400-35 were performed on a ZWICK/ROELL Z050 test machine. The coupons were cut from one large plate using a water jet.³

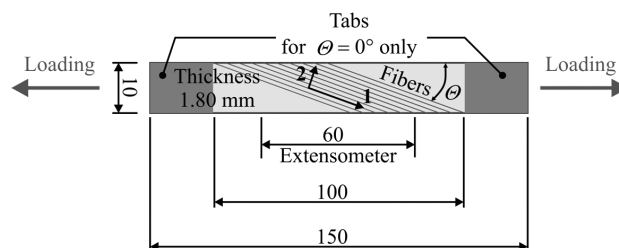


Figure 1: Geometry of composite coupons (mm)²

Slika 1: Geometrija ploščice kompozita (mm)²

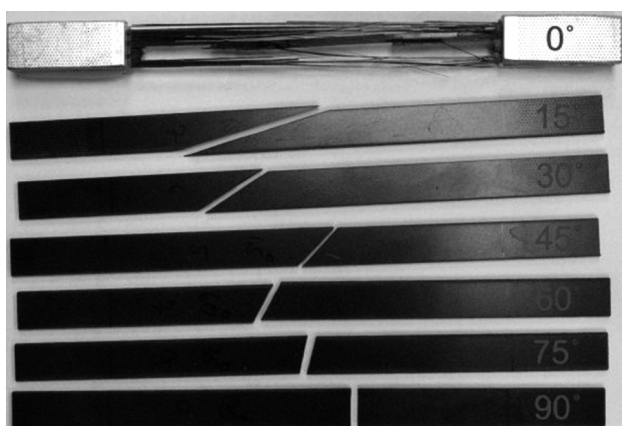


Figure 2: Cracked specimens with aluminum tabs on a specimen with a 0° orientation²

Slika 2: Razpokani vzorci z aluminijevimi zavihki na vzorcu z orientacijo 0°²

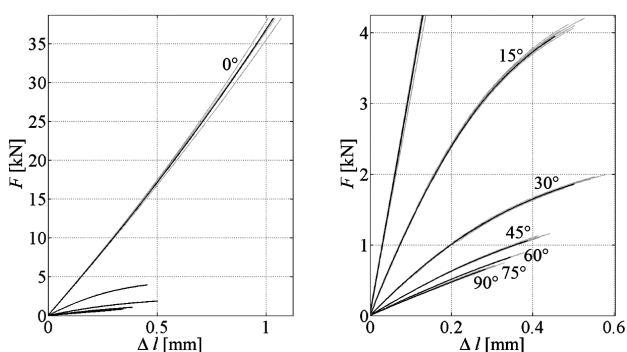


Figure 3: Measured force-displacement diagrams (grey) and averaged values (black)²

Slika 3: Diagrami sila – raztezek (sivo) in povprečne vrednosti (črno)²

The fiber direction forms angles of 0°, 15°, 30°, 45°, 60°, 75° and 90° with the direction of the loading force (Figure 1). There were 10 specimens tested for each angle θ . The cracked specimens are shown in Figure 2. The specimens loaded along the fiber direction were fractured by fiber failure. All the specimens loaded at a different angle are fractured by matrix failure. The resulting force-displacement diagrams are shown in Figure 3.

2.1 Micromodel

The geometry of the finite-element model (micro-model) with a periodically repeated volume (unit cell) of the unidirectional composite material was created in the CAD program Siemens NX. The unit cell is meshed using ten-node tetrahedral elements. A perfect honeycomb distribution of fibers and a fiber volume ratio of 55 % were assumed (Table 1). Furthermore, the finite strain theory was used. The geometry of the unit cell was exported to Abaqus/CAE 6.11-1 for the finite-element analysis.

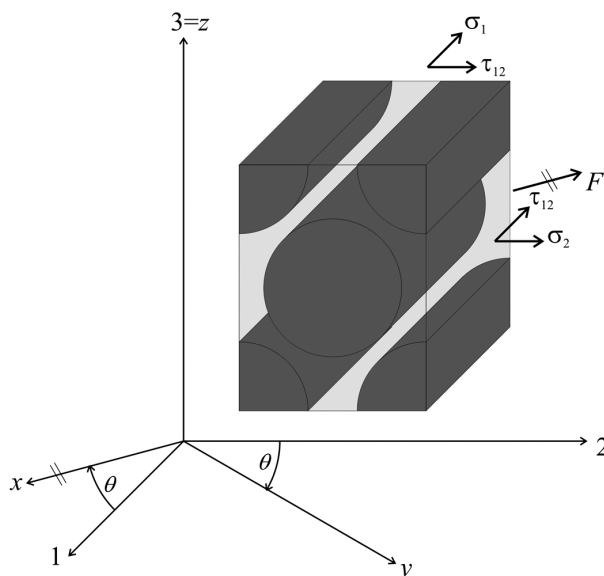


Figure 4: Rotated coordinate systems and loading of the unit cell
Slika 4: Rotirani koordinatni sistemi in obremenitve osnovne celice

Table 1: Geometry ratios of the unit cell

Tabela 1: Geometrijska razmerja osnovne celice

Fiber radius	r
Short side length	1.28 r
Long side length	2.22 r

The global coordinate system (xyz) is given by the force direction (x) and the direction perpendicular to the composite surface (z). The local coordinate system (123) is defined by the unit-cell edges, where the axis directions correspond to the fiber direction (1) and the directions perpendicular to it (Figure 4).

Assuming uniaxial stress across the whole specimen, the behavior of the material can be simulated by loading the unit cell with a normal stress corresponding to an external force F :

$$\sigma_x = \frac{F}{A} \quad (1)$$

where A is the cross-section of the specimen.

The effect of the loading force is transformed to the local coordinate system using the transformation:

$$\begin{bmatrix} \sigma_1 \\ \sigma_2 \\ \tau_{12} \end{bmatrix} = \begin{bmatrix} \cos^2 \theta & \sin^2 \theta & 2 \sin \theta \cos \theta \\ \sin^2 \theta & \cos^2 \theta & -2 \sin \theta \cos \theta \\ -\sin \theta \cos \theta & \sin \theta \cos \theta & \cos^2 \theta - \sin^2 \theta \end{bmatrix} \begin{bmatrix} \sigma_x \\ 0 \\ 0 \end{bmatrix} \quad (2)$$

where θ is the angle of rotation between the local and global coordinate systems.³

The results from the finite-element analysis (strains) are transformed back to the global coordinate system using the transformation:

$$\begin{bmatrix} \epsilon_x \\ \epsilon_y \\ \gamma_{xy} \end{bmatrix} = \begin{bmatrix} \cos^2 \theta & \sin^2 \theta & -\sin \theta \cos \theta \\ \sin^2 \theta & \cos^2 \theta & \sin \theta \cos \theta \\ 2 \sin \theta \cos \theta & -2 \sin \theta \cos \theta & \cos^2 \theta - \sin^2 \theta \end{bmatrix} \begin{bmatrix} \epsilon_1 \\ \epsilon_2 \\ \gamma_{12} \end{bmatrix} \quad (3)$$

The unit cell must also respect the periodical boundary conditions:

$$\begin{aligned} \Delta u &= u_B - u_A \\ \Delta v &= v_B - v_A \\ \Delta w &= w_B - w_A \end{aligned} \quad (4)$$

where Δu , Δv and Δw are the translation differences of a pair of opposing nodes in directions 1, 2 and 3, respectively. These differences must remain constant for all the pairs of corresponding nodes on opposite sides. The periodical boundary conditions were implemented in Abaqus/CAE.

2.2 Material model of fiber

The fibers were modeled as transversely isotropic elastic material respecting the non-linear behavior in the axis direction. The dependence of the longitudinal Young's modulus of the fibers on the strain in the axial direction of the fibers is⁴:

$$E_{11}(\epsilon_{11}) = E_1^0(1 + g\epsilon_{11}) \quad (5)$$

where g is the coefficient describing the measure of non-linearity and E_1^0 is the initial Young's modulus of the fiber in the longitudinal direction.

It is assumed that fiber failure occurs when the failure index in the axial direction, defined as:

$$f_1 = \frac{\sigma_1^f}{X_T^f} \quad (6)$$

where σ_1^f is stress in direction 1 in the fibers and X_T^f is the tensile strength of the fibers, reaches the value of 1.

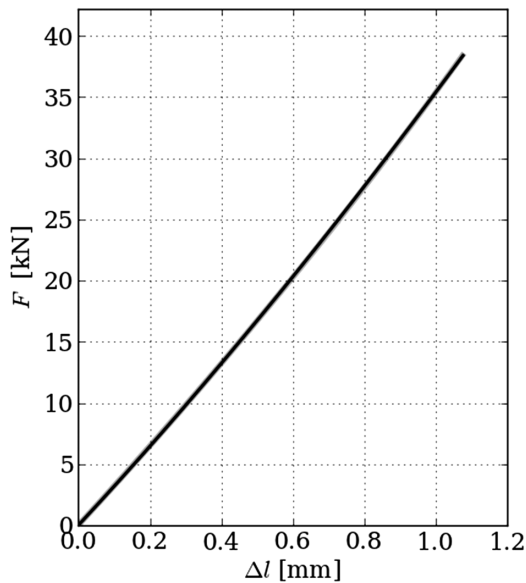


Figure 5: Force-displacement diagram for 0° specimen (black – identified, grey – experiments)

Slika 5: Diagram sila – raztezek za vzorec 0° (črno – identificirano, sivo – eksperimenti)

2.3 Material model of matrix

The matrix was modeled as an isotropic elasto-plastic material. The elastic parameters were the Young's modulus E_m and the Poisson's ratio μ_m . The Von Mises plasticity was used with the isotropic hardening and work-hardening function proposed in the form:

$$\sigma^y = \sigma_0^y + \frac{T_0 \bar{\epsilon}_p}{\left[1 + \left(\frac{T_0 \bar{\epsilon}_p}{\sigma_A^y} \right)^n \right]^{\frac{1}{n}}} \quad (7)$$

where the yield stress σ^y depends on the equivalent plastic strain $\bar{\epsilon}_p$ and on additional material parameters where σ_0^y is the initial yield stress, T_0 is the tangent of the hardening curve for $\bar{\epsilon}^p = 0$, σ_A^y is asymptotic stress and n is a shape parameter.

The damage initiation criterion inspired by the criterion for the ductile damage of metals was used, where the fracture is assumed to be caused by the coalescence of voids in a matrix and the damage initiates when the following condition (damage factor) is fulfilled:

$$\omega_D = \int \frac{d\bar{\epsilon}^p}{\bar{\epsilon}_D^p(\eta)} = 1 \quad (8)$$

where function:

$$\bar{\epsilon}_D^p = \bar{\epsilon}_D^p(\eta) \quad (9)$$

is the equivalent plastic strain at the onset of the damage and it is a function of the stress triaxiality factor:

$$\eta = \frac{\sigma_h}{\sigma_{eqv}} \quad (10)$$

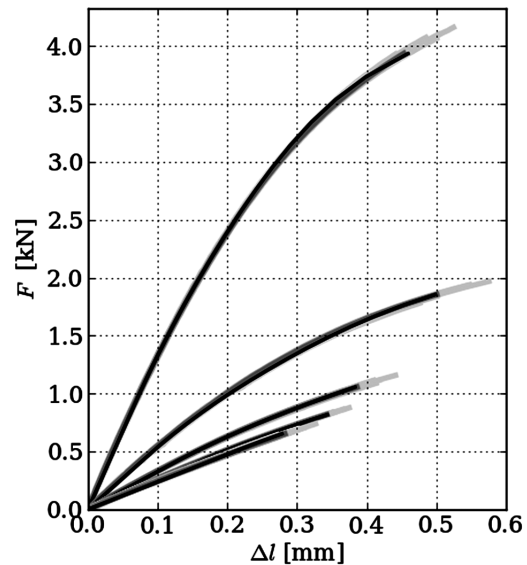


Figure 6: Force-displacement diagrams for 15° to 90° specimens (black – identified, grey – experiments)

Slika 6: Diagrami sila – raztezek za vzorce od 15° do 90° (črno – identificirano, sivo – eksperimenti)

where σ_h is hydrostatic stress and σ_{eqv} is the Von Mises stress.⁵

2.4 Identification process

An optimization process, similar to the one used in², was performed using Python scripts, the optimization software OptiSlang and the finite-element system Abaqus. The identification consisted of two steps. The first step was to find the best combination of all the elastic and plastic material parameters by minimizing the difference between the experimental and numerical force-displacement diagrams. Moreover, the parameter $\Delta\theta$ which represents the inaccuracy when cutting the samples from the plate was identified. The second step was to identify the tensile strength of fibers and the function $\bar{\epsilon}_D^p$ by minimizing the difference between the value of ω_D and 1 at the moment of fracture in the experiment. The dependency of the equivalent plastic strain on the onset of damage $\bar{\epsilon}_D^p$ was proposed as a piecewise linear function with five control vertices.

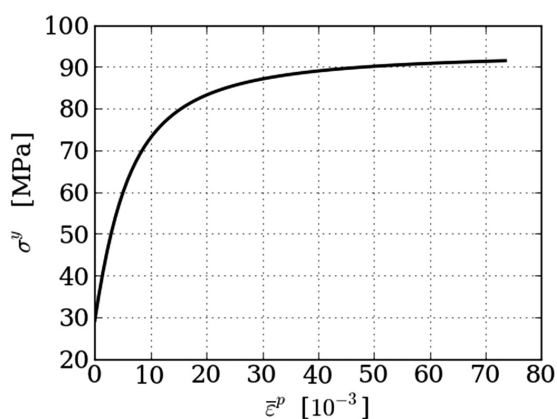


Figure 7: Work-hardening curve
Slika 7: Krivulja deformacijskega utrjevanja

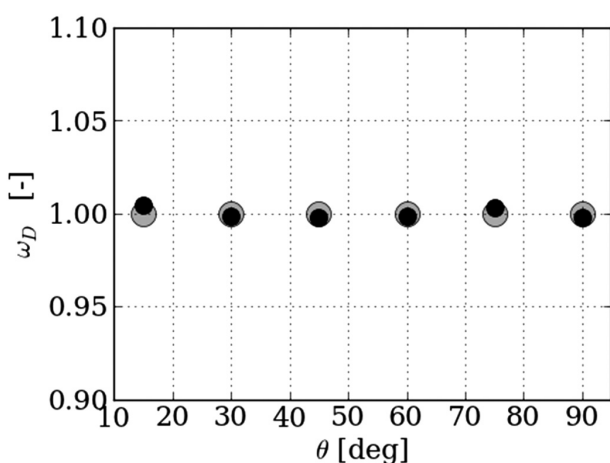


Figure 8: Maximum damage factors for specimens from 15° to 90° (black – identified, grey – experiments)
Slika 8: Faktorji maksimalne poškodbe pri vzorcih od 15° do 90° (črno – identificirano, sivo – eksperimenti)

3 DISCUSSION OF RESULTS

The identified parameters and the parameters given by the manufacturer are summarized in Table 2. The identified parameters correspond well with the ones identified in² where the analysis was performed in MSC.Marc software using eight-node brick elements.

The force-displacement diagram for the specimen 0° shows a convex shape caused by stiffening of the fibers (Figure 5). The force-displacement diagrams of the rest of the specimens have concave shapes caused by the matrix non-linearity (Figure 6). The identified shape of the work-hardening function is shown in Figure 7. The ability of the model to predict the initial damage of the matrix is visualized in Figure 8. The identified dependency of $\bar{\epsilon}_D^p$ on the triaxiality stress factor is shown in Figure 9. The distribution of the damage factor for the matrix in the 45° specimen in the moment when the first damage to the matrix occurs is shown in Figure 10.

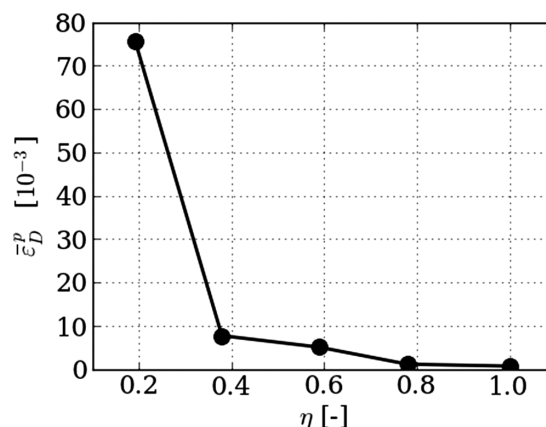


Figure 9: Dependency of the equivalent plastic strain at the onset of damage on the triaxiality stress factor
Slika 9: Odvisnost ekvivalenta plastičnega raztezka na začetku poškodbe od triosnega faktorja napetosti

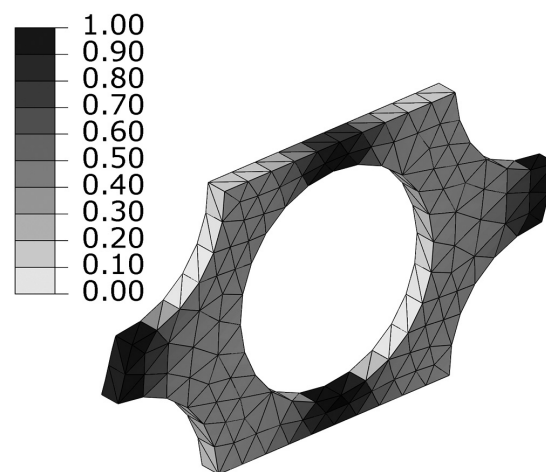


Figure 10: Distribution of damage factor (factor is not calculated for fibers, deformation is magnified 10 times)
Slika 10: Razporeditev faktorja poškodbe (faktor ni izračunan za vlakna, deformacija je povečana za 10-krat)

Table 2: Summarized parameters (i = identified, m = manufacturer)**Tabela 2:** Povzeti parametri (i = ugotovljeni, m = proizvajalec)

Parameter	Units	Value	note
E_1^0	GPa	188.73	i
g	–	18.76	i
$E_2 = E_3$	GPa	15.00	m
$\mu_{12} = \mu_{13}$	–	0.30	m
μ_{23}	–	0.40	m
$G_{12} = G_{13}$	GPa	5.00	m
G_{23}	GPa	4.00	m
X_1^f	GPa	3.88	i
E_m	GPa	3.61	i
μ_m	–	0.40	m
σ_0^y	MPa	29.24	i
T_0	GPa	8.49	i
σ_A^y	MPa	93.54	i
n	–	1.35	i
$\Delta\theta$	°	–0.98	i

4 CONCLUSION

Finite-element analyses of simple tensile tests on unidirectional composite specimens with various fiber orientations were performed. The material parameters of the orthotropic non-linear elastic material of the fibers and of the non-linear elasto-plastic material of the matrix were identified. The simple failure (fiber) and the damage (matrix) criteria were successfully tested and good agreement with the experiments was achieved.

Future work will focus on an approximation of the dependency of the equivalent plastic strain at the onset of

the damage on the triaxiality stress factor using a smooth function and modeling of the subsequent damage process using a cohesive-theory-based approach.

Acknowledgement

The work has been supported by the projects GA P101/11/0288 and European project NTIS – New Technologies for Information Society No. CZ.1.05/1.1.00/02.0090.

5 REFERENCES

- ¹ T. Kroupa, V. Laš, R. Zemčík, Improved Non-Linear Stress–Strain Relation for Carbon–Epoxy Composites and Identification of Material Parameters, *Journal of Composite Materials*, 45 (2011) 9, 1045–1057
- ² H. Srbová, T. Kroupa, R. Zemčík, Identification of the Material Parameters of a Unidirectional Fiber Composite Using a Micromodel, *Mater. Tehnol.*, 46 (2012) 5, 431–434
- ³ D. Roylance, Transformation of Stresses and Strains, Department of Materials Science and Engineering, Massachusetts Institute of Technology, Cambridge, 2001
- ⁴ I. M. Djordjević, D. R. Sekulić, M. M. Stevanović, Non-Linear Elastic Behavior of Carbon Fibers of Different Structural and Mechanical Characteristic, *Journal of the Serbian Chemical Society*, 72 (2007) 5, 513–521
- ⁵ S. S. Bhadauria, M. S. Hora, K. K. Pathak, Effect of Stress Triaxiality on Yielding of Anisotropic Materials under Plane Stress Condition, *Journal of Solid Mechanics*, 1 (2009) 3, 226–232

TRANSFORMATION-INDUCED PLASTICITY IN STEEL FOR HOT STAMPING

VPLIV PRETVORBE NA PLASTIČNOST JEKLA ZA VROČE ŠTANCANJE

Bohuslav Mašek¹, Ctibor Štádler¹, Hana Jirková¹, Peter Feuser², Mike Selig³

¹Research Centre of Forming Technology – FORTECH, University of West Bohemia in Pilsen, Univerzitní 22, 306 14 Pilsen, Czech Republic

²Daimler AG, Bela-Barenyi-Str. 1, 71063 Sindelfingen, Germany

³AutoForm Development GmbH, Technoparkstrasse 1, 8005 Zürich, Switzerland
ctibor@email.cz

Prejem rokopisa – received: 2012-10-01; sprejem za objavo – accepted for publication: 2013-10-07

The hot-stamping process for manufacturing car-body components was patented in 1977. Its main advantages include the precision of the product shape, the reduced spring-back effect and the resulting high strength of steel parts upon hardening. Boron- and manganese-alloyed steels have been specially developed for this process. The 22MnB5 grade is a typical representative of this group with its strength up to 1500 MPa.

For the desired mechanical properties to be achieved, the final microstructure should consist primarily of martensite without any substantial amounts of other phases. Further development of press hardening, therefore, requires all the phenomena associated with the phase transformations during the cooling between dies to be well mapped. Significant parameters, in this respect, include phase-transformation temperatures and the data on a number of additional phenomena, including transformation-induced plasticity. Transformation-induced plasticity is manifested when a part held between dies undergoes a phase transformation, typically, when being under stress. In the course of a lattice rearrangement, this stress causes the atoms to occupy more favourable positions in terms of energy. At the macro-level, this can be detected as a change in the dimensions, which, at the same time, significantly relieves the stress, therefore, eliminating the spring back. Despite a profound importance of this phenomenon for the press-hardening process, it has not been explored in detail up to now.

For these reasons, a 22MnB5 steel grade was employed in this project. The impacts of the tensile and compressive stresses occurring during phase transformations, upon the changes in the expansion of the sheet specimens, were explored using the schedules that simulated real-world hot-stamping and press-hardening processes.

Keywords: press hardening, hot stamping, spring-back effect, 22MnB5, transformation-induced plasticity

Postopek vročega štancanja za izdelavo komponent karoserije avtomobilov je bil patentiran leta 1977. Njegove glavne prednosti so natančnost oblike izdelka, zmanjšan vzmetni učinek in visoka trdnost jeklenih delov po toplotni obdelavi. Posebno za ta postopek so bila razvita jekla, legirana z borom in manganom. Značilen predstavnik te skupine je jeklo 22MnB5 s trdnostjo do 1500 MPa.

Za doseganje zelenih mehanskih lastnosti mora biti končna mikrostruktura martenzitna, brez večjih deležev drugih faz. Nadaljnji razvoj utrjevanja pri stiskanju zahteva, da se obvladajo vsi pojavi, ki so povezani s faznimi premenami med ohlajanjem v orodju. S tega vidika so pomembni parametri, ki vključujejo temperature faznih premen in podatki o številnih drugih pojavih, vključno z vplivom fazne premene na plastičnost. Vpliv fazne premene na plastičnost se pokaže, ko se v delu med orodjema zgodi fazna premena, navadno pod tlakom. Med preureditvijo mreže napetosti povzročijo, da atomi zasedejo energijsko bolj ugodne položaje. Na makronivoju se to kaže kot sprememba dimenzij, ki istočasno zmanjšajo napetosti in odpravijo učinek vzmeti. Kljub pomembnosti ta pojav utrjevanja pri stiskanju do sedaj še ni bil podrobno raziskan. Zato je bilo v tej raziskavi uporabljeno jeklo 22MnB5. Raziskani so bili učinki nateznih in tlačnih napetosti, ki se pojavijo med fazno premeno pri spremembi širjenja vzorcev pločevine, s simulacijo realnega vročega štancanja in procesa utrjevanja s stiskanjem.

Ključne besede: utrjevanje s stiskanjem, vroče štancanje, vzmetni učinek, 22MnB5, vpliv pretvorbe na plastičnost

1 INTRODUCTION

Transformation-induced plasticity is an all-too-often overlooked phenomenon in manufacturing today. One of the reasons for this is the fact that its impact on the outcome of the entire manufacturing process is not readily visible. Yet, there are technological problems in the industry that may be caused by transformation-induced plasticity and other issues that could be resolved by making use of the very same transformation-induced plasticity phenomenon.^{1,2} An example of the important role of transformation-induced plasticity is the production of sizable forgings, namely, their heat treatment.³ Only recently have these phenomena received more attention and the findings are reflected in FEM simulations. Their

descriptions have become more detailed, having an effect on the current material models. Transformation-induced plasticity has an important role in the process of hot sheet forming with the subsequent press hardening, known as hot stamping. In the hot-stamping process, transformation-induced plasticity combined with other effects reduces the spring back. Consequently, the final pressed parts achieve greater shape precision than the high-strength deep-cold-drawn sheet products.⁴ Since this phenomenon typically occurs in the production of complex-shape deep-drawn sheet products, it is difficult to assess it accurately. Without an exact description of its effect, no production-relevant and sufficiently accurate material-based model can be constructed.⁵ This was the background of the present experiment.

2 EXPERIMENTAL WORK

Modified tension-test pieces with a 10 mm width, 50 mm length and a thickness of 1.5 mm were used in this study. The schedules were simulations of real-world hot-stamping and press-hardening processes. The material was a standard 22MnB5 steel grade (**Table 1**).

Table 1: Chemical composition of the 22MnB5 grade in mass fractions (w/%)

Tabela 1: Kemijska sestava jekla 22MnB5 v masnih deležih (w/%)

C	Cr	Mn	Si	B	P	S	Al
0.22	0.2	1.25	0.2	0.0029	0.025	0.015	0.006

The main objective of the research was to explore the intensity of the transformation-induced plasticity phenomenon during the cooling process. The hot-stamping process was simulated by heating the specimens to 950 °C. The specimens were kept free from the longitudinal stress during the heating. They were held at the above temperature for 3 min and then cooled down to 770 °C in 10 s. This step was a simulation of cooling the trimmed feedstock during handling. Between 770 °C and 600 °C, the stress within the specimen increased linearly from 0 to the prescribed level, representing the stress formation in a real-world process. This stress level was then maintained during the subsequent constant-rate cooling. The cooling rates were specified on the basis of the CCT diagrams constructed under the conditions identical to real-world processes. The cooling rates of 25 °C/s and 40 °C/s were selected as the characteristic values resulting in various microstructural states. The first cooling rate led to a formation of a mixed microstructure of bainite, martensite and some ferrite. The higher cooling rate led to a transformation into martensite. Consequently, the differences between the final dimensions of the final disparate microstructures could be compared.

The changes in the length of the test specimen were monitored in the course of the experiment, while the longitudinal stress in the part was controlled.

The amount of stress was defined on the basis of the measurements of the stress-strain characteristics at the constant temperature of 600 °C, carried out at the beginning of this research. It was less than one quarter of the stress that caused plastic deformation. In the subsequent tests, this amount was gradually increased to twice and three times its value. Hence, the stress was kept in the elastic region at all times to prevent any substantial contribution to the elongation of the test specimen, caused by the ordinary plastic deformation and creep during the testing. These stress levels were as follows: (31, 62 and 93) MPa. The ratio of the extension caused by the elastic deformation under the highest load to the sum of the overall contraction and the deformation due to transformation-induced plasticity was no more than a mere fraction of one percent (**Figure 1**).

3 RESULTS AND DISCUSSION

In the region of transformation, the experiment revealed a non-linear extension of the material along the applied stress direction (**Figure 1**). This is a definite evidence of the profound effects of transformation-induced plasticity. Transformation-induced plasticity takes effect at the moment of lattice reconfiguration, when the atoms take their new positions. The new positions are consistent with the transition into a lower-energy, more favourable state. This is the main cause of the permanent deformation, manifested as the non-linearity on the specimen elongation curve.

The experiment showed that the length of the test specimen decreased by about 0.5 mm upon the cooling from 600 °C to 70 °C without any longitudinal stress. This corresponds to the 0 % transformation plasticity. When the longitudinal stress of 31 MPa was applied, the contraction was approximately 0.35 mm. The contraction of the test specimen was, in this case, by 0.15 mm lower than in the previous case, due to the transformation plasticity. Once the longitudinal stress doubled, the contrac-

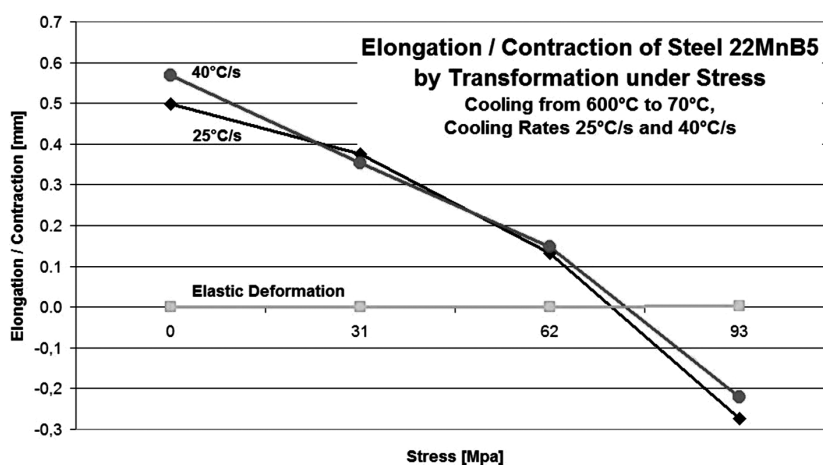


Figure 1: Effect of stress on the length of the test specimen

Slika 1: Vpliv napetosti na dolžino preizkušanca

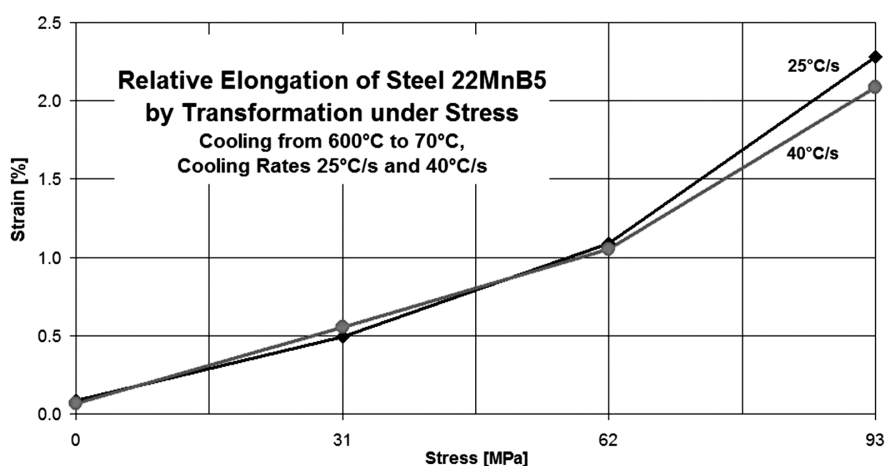


Figure 2: Relative elongation versus longitudinal stress

Slika 2: Relativni raztezki v odvisnosti od vzdolžne napetosti

tion was 0.13 mm. At the triple stress value, the contraction caused by the cooling was outweighed by the transformation-induced plasticity effect, causing the specimen to extend by an amount between 0.22 mm and 0.27 mm.

In this experiment, the effect of diffusion should be taken into account as well, as it contributes to the process even though its extent varies. However, its impact cannot be explored separately from the other effects. The experiment showed that at the lower cooling rates – when the times available for diffusion were longer – the elongation increased, though slightly. The impact of creep increases with the stress level.

At the stresses above 70 MPa, the effect of transformation-induced plasticity can compensate for the contraction, thus eliminating residual stresses (**Figure 1**).

The relative extension between 600 °C and 70 °C rose from 0 %, which was detected during the cooling without any stress applied, to approximately 0.55 % at 31 MPa. It then increased almost linearly with the increasing longitudinal stress to twice as high a value. At 62 MPa, it reached 1 % (**Figure 2**). When the stress was increased further by one third of its value, the relative extension was doubled, reaching more than 2 %.

4 CONCLUSION

The experiment conducted on the sheet specimens made from the 22MnB5 steel involving the cooling rates of 25 °C/s and 40 °C/s and various applied stress levels revealed the intensity of the transformation-induced plasticity effects during hot-stamping and press-hardening processes. At the temperatures between 600 °C and 70 °C, the test specimens contracted. The contraction was compensated for by an expansion due to the longitudinal tensile stress and transformation-induced plasticity. With the longitudinal stress increasing from 0 to 93

MPa, the relative extension of the test specimen becomes non-linear, increasing from 0 % up to 2 %. The results show that at the stresses above 70 MPa, transformation-induced plasticity and additional related phenomena can compensate for the contraction due to cooling, thus reducing the spring back.

The present experiment was not intended to exactly match the real-world contraction behaviour of the press-hardening process. Its purpose was to provide an insight into and the data on the transformation-induced plasticity under the specific cooling conditions of the hot-stamping process.

Acknowledgement

This paper includes the results created within project SGS-2012-040, New Methodology for Description of Transformation Processes in Real Materials. The project is subsidised from the specific resources of the state budget for research and development.

5 REFERENCES

- ¹ B. Norrbottens Jaernverk, Patent GB 1490535, Manufacturing of a hardened steel article, 11 February 1977
- ² H. Karbasian, A. E. Tekkaya, A review on hot stamping, *Journal of Materials Processing Technology*, 210 (2010), 2103–2118
- ³ M. Taschauer, V. Wieser, S. Schramhauser, T. Hatzenbichler, B. Buchmayer, Die Wärmebehandlung der Stähle unter Einbeziehung des Selbstanlassens, Proc. of the XXXI. Verformungskundliches Kolloquium, Plannersalm, 2012, 91–96
- ⁴ A. Turetta, S. Bruschi, A. Ghiotti, Investigation of 22MnB5 formability in hot stamping operations, *Journal of Materials Processing Technology*, 177 (2006), 396–400
- ⁵ S. Ertürk, M. Sester, M. Selig, P. Feuser, K. Roll, A Thermo-Mechanical-Metallurgical FE Approach for Simulation of Tailored Tempering, Proc. of the 3rd International Conference – Hot sheet metal forming of high-performance steel, Kassel, Germany, 2011

INFLUENCE OF TEMPERATURE AND BINDER CONTENT ON THE PROPERTIES OF A SINTERED PRODUCT BASED ON RED MUD

VPLIV TEMPERATURE IN KOLIČINE VEZIVA NA LASTNOSTI PROIZVODA IZ SINTRANEGA RDEČEGA BLATA

Milun Krgović¹, Ivana Bošković¹, Radomir Zejak², Miloš Knežević²

¹University of Montenegro, Faculty of Metallurgy and Technology, Džordža Vašingtona bb, 81000 Podgorica, Montenegro

²University of Montenegro, Faculty of Civil Engineering, Džordža Vašingtona bb, 81000 Podgorica, Montenegro
milun@ac.me

Prejem rokopisa – received: 2013-01-29; sprejem za objavo – accepted for publication: 2013-10-30

In this paper we present an investigation into the properties of a sintered product based on red mud with respect to the sintering temperature and the binder content (illite-kaolinite clay). In the Bayer process for obtaining alumina, red mud is a by-product (solid waste from the leaching of bauxite). Using red mud as a raw material mixture component to obtain sintered products, a cheap raw material for construction and ceramics would be obtained, and the environmental problems resulting from the frequent deposits of red mud in pools would be solved. Based on the overall results of our examinations in this study, it can be concluded that the change of basic parameters, sintering temperature and binder content (illite-kaolinite clay), can provide satisfactory characteristics for the sintered product in terms of mechanical properties, volume shrinkage during sintering and total porosity.

Keywords: red mud, clay, porosity, compressive strength

Članek obravnava preiskavo lastnosti sintranjih proizvodov na osnovi rdečega blata v odvisnosti od temperature sintranja in vsebnosti veziva (glina illit-kaolinit). Rdeče blato (trden odpadki pri izpiranju boksita) je stranski proizvod pri Bayerjevem procesu pridobivanja glinice. Rdeče blato kot surovina v mešanici za sintranje komponent je poceni material za gradnjo in keramiko, rešuje pa tudi okoljske probleme, ki izvirajo iz rednega odlaganja rdečega blata v bazene. Na podlagi rezultatov te študije se lahko sklene, da spreminjanje osnovnih parametrov, temperature sintranja in vsebnosti veziva (glina illit-kaolinit), omogoča zadovoljive lastnosti sintranega proizvoda glede mehanskih lastnosti, krčenja prostornine med sintranjem in celotne poroznosti.

Ključne besede: rdeče blato, glina, poroznost, tlačna trdnost

1 INTRODUCTION

Red mud contains the following basic components: iron in the form of oxides, silicon in the form of sodium-aluminosilicate and titanium as sodium-titanate. Caustic soda, NaOH, is also present in red mud, while with the addition of lime to the process it also contains CaO in either the free or bound forms.

Illite-kaolinite clays, apart from basic clay minerals, illite and kaolinite, mostly contain α -quartz, Fe_2O_3 , CaCO_3 , and are considered as refractory clays (stable up to a temperature of 1350 °C).¹ During the sintering of this two-component mixture (red mud, illite-kaolinite clay), depending on the sintering temperature, different reactions in the solid state occur, as well as the polymorphic transformation of quartz and the formation of a liquid phase.² The relationship between the particular elements of the microstructure during sintering, in addition to the firing regime, is importantly influenced by the mineral content of the raw materials.^{3,4} Liquid-phase formation accelerates the reactions in the solid state due to the diffusion-coefficient increase in such systems by up to one thousand times.⁵ The formation of new crystalline phases in the solid-state reactions during

the sintering process, apart from the above-mentioned factors, is also influenced by the temperature of the sintering.^{6,7}

Investigations have shown that the relations between the elements of the microstructure and the total porosity of the sintered product are importantly influenced by the mass-ratio changes between the red mud and the clay in a two-component mixture.^{8,9}

2 EXPERIMENTAL

The raw material mixture for the production of samples was formed on the basis of red mud (Aluminium Plant Podgorica) and illite-kaolinite clay ("Bijelo Polje") as binders. The content of the red mud in the raw material mixture in mass fractions was (10, 20, 30, 40 and 50) %. The samples were formed by plastic shaping in a mould corresponding to a parallelepiped with dimensions of 7.7 cm × 3.9 cm × 1.6 cm. The raw material mixture components were characterized by a determination of mineral content and the chemical content, while the particle size distribution was determined by granulometric analyses. The density and humidity of the raw material mixture components were also determined.

The sintering of the samples with different red mud contents was performed at temperatures of 1100 °C and 1200 °C.^{5,8} The characterization of the sintered products included the following: a determination of the linear and volume shrinkage during sintering, and a determination of the total porosity and compressive strength. The determination of the mineral content of the sintered products was performed by X-ray analysis.

3 RESULTS AND DISCUSSION

The mineral composition of red mud (**Figure 1**) determined by the X-ray analysis shows the presence of the following minerals: hematite, goethite, boehmite, diaspora, calcite, as well as the presence of soda. The results of the chemical analysis of red mud (**Table 1**) show a high mass content of Fe₂O₃ (40.78 %) and because of its negative influence on the quality of sintered product,¹ the content of red mud in the raw material mixture does not exceed 50 %. The clay used as a binder is an illite-kaolinite type (**Figure 2, Table 2**), with the presence of α-quartz.

Table 1: The chemical content of red mud in mass fractions (w/%)
Tabela 1: Kemijska sestava rdečega blata v masnih deležih (w/%)

Oxides	Fe ₂ O ₃	Al ₂ O ₃	SiO ₂	TiO ₂	Na ₂ O	CaO	lg. loss
	40.78	17.91	11.28	10.20	6.90	1.50	9.36

The results of the granulometric analysis show that the red mud has a larger fraction (average grain size 30 μm) compared to the used clay (average grain size 17 μm). The density of the clay determined by the pycnometer method is 2.34 g cm⁻³, while the density of the red mud is 2.76 g cm⁻³.

The results of the volume shrinkage during sintering (**Figure 3**) show higher values of shrinkage at the sintering temperature of 1200 °C compared to 1100 °C, and the shrinkage decreases with an increase in the

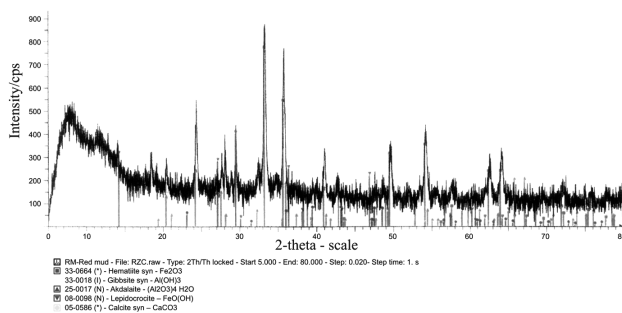


Figure 1: X-ray diffractogram of red mud
Slika 1: Rentgenski difraktogram rdečega blata

Table 2: The chemical content of "Bijelo Polje" clay in mass fractions (w/%)
Tabela 2: Kemijska sestava gline "Bijelo Polje" v masnih deležih (w/%)

Oxides	SiO ₂	Fe ₂ O ₃	Al ₂ O ₃	CaO	MgO	Na ₂ O	K ₂ O	SO ₃	lg. loss
	72.68	5.7	10.98	0.48	0.7	0.31	1.12	–	8.03

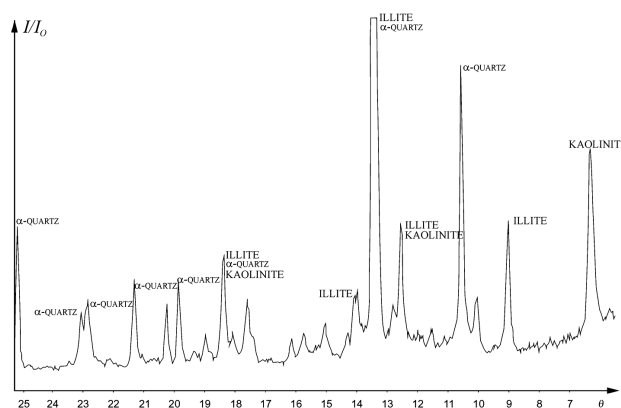


Figure 2: X-ray diffractogram of "Bijelo Polje" clay
Slika 2: Rentgenski difraktogram gline "Bijelo Polje"

content of red mud in the raw material mixture. This is explained by the granulometric analysis of the raw material mixture (red mud has a larger fraction), the relations between the elements of the microstructure, as well as by an increase of the total porosity of the sintered product with an increase of the red mud content.

The total porosity (**Figure 4**) has lower values at the sintering temperature of 1200 °C, compared to the sintering temperature of 1100 °C, and increases with an increase of the red mud content in the raw material mixture. During the sintering process of the ceramic particles all the well-known mass-transport mechanisms can occur, depending on the sintering conditions.¹⁰ Based on the already-existing data and results it can be concluded that diffusion is the dominant mass-transport mechanism under these conditions. Along with the temperature rise, the reactions in the solid state are generated by increased diffusion.

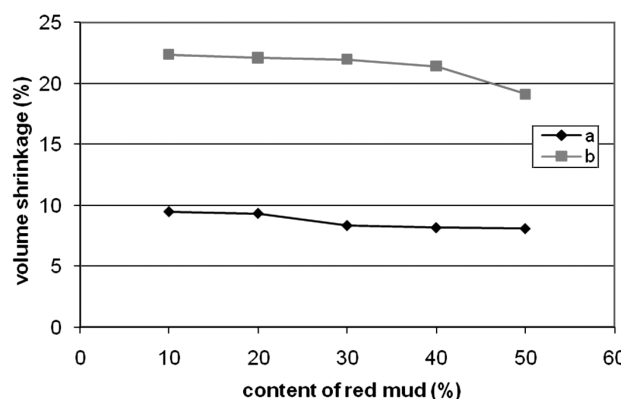


Figure 3: Volume shrinkage of products during sintering: a) T = 1100 °C, b) T = 1200 °C
Slika 3: Krčenje prostornine proizvoda med sintranjem: a) T = 1100 °C, b) T = 1200 °C

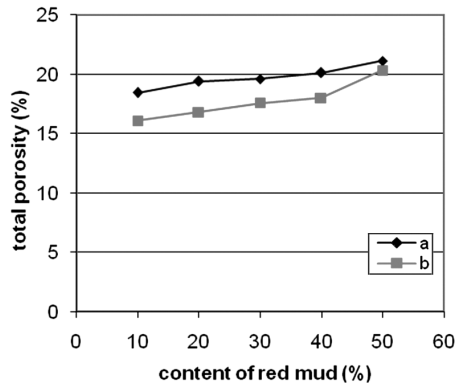


Figure 4: Total porosity of sintered products: a) $T = 1100\text{ }^{\circ}\text{C}$, b) $T = 1200\text{ }^{\circ}\text{C}$

Slika 4: Skupna poroznost sintranih proizvodov: a) $T = 1100\text{ }^{\circ}\text{C}$, b) $T = 1200\text{ }^{\circ}\text{C}$

The highest values of the compressive strength (**Figure 5**) are present for the samples with the lowest content of red mud. The samples sintered at the temperature of $1200\text{ }^{\circ}\text{C}$ have significantly higher values of compressive strength than those sintered at the temperature of $1100\text{ }^{\circ}\text{C}$.

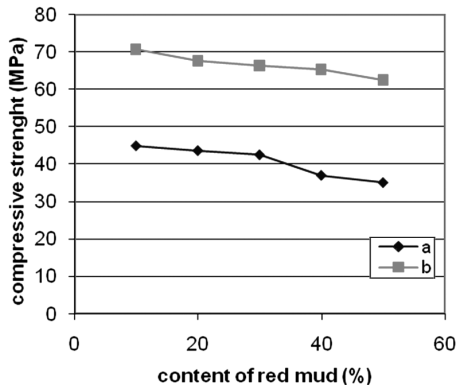


Figure 5: Compression strength of sintered products: a) $T = 1100\text{ }^{\circ}\text{C}$, b) $T = 1200\text{ }^{\circ}\text{C}$

Slika 5: Tlačna trdnost sintranih proizvodov: a) $T = 1100\text{ }^{\circ}\text{C}$, b) $T = 1200\text{ }^{\circ}\text{C}$

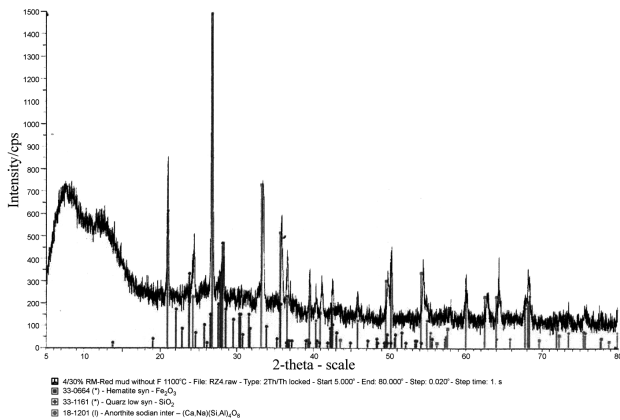


Figure 6: X-ray diffractogram of sintered product ($w = 30\%$ red mud; $T = 1100\text{ }^{\circ}\text{C}$)

Slika 6: Rentgenski difraktogram sintranega proizvoda ($w = 30\%$ rdečega blata; $T = 1100\text{ }^{\circ}\text{C}$)

The X-ray analysis results (**Figures 6, 7, 8 and 9**) show different relations for the crystalline phases at the different sintering temperatures. The Fe_2O_3 remains

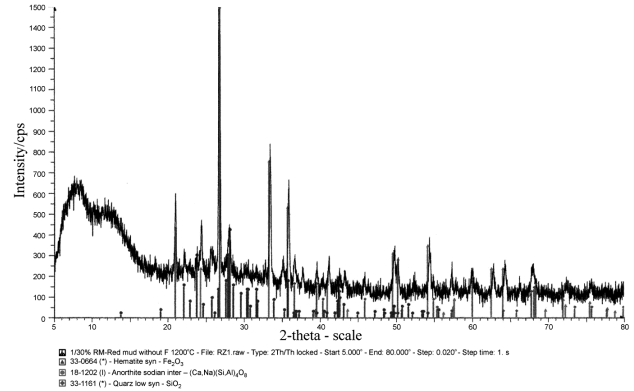


Figure 7: X-ray diffractogram of sintered product ($w = 30\%$ red mud; $T = 1200\text{ }^{\circ}\text{C}$)

Slika 7: Rentgenski difraktogram sintranega proizvoda ($w = 30\%$ rdečega blata; $T = 1200\text{ }^{\circ}\text{C}$)

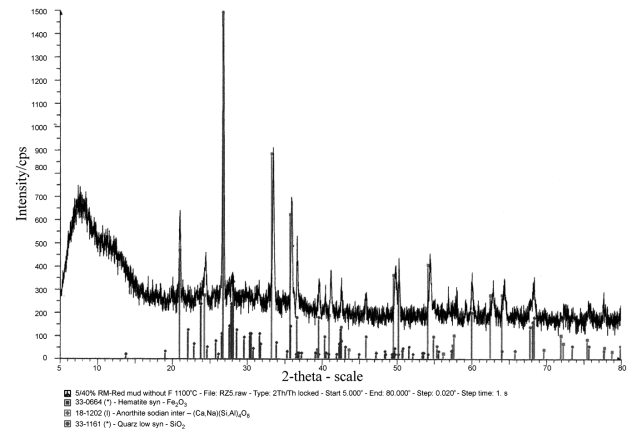


Figure 8: X-ray diffractogram of sintered product ($w = 40\%$ red mud; $T = 1100\text{ }^{\circ}\text{C}$)

Slika 8: Rentgenski difraktogram sintranega proizvoda ($w = 40\%$ rdečega blata; $T = 1100\text{ }^{\circ}\text{C}$)

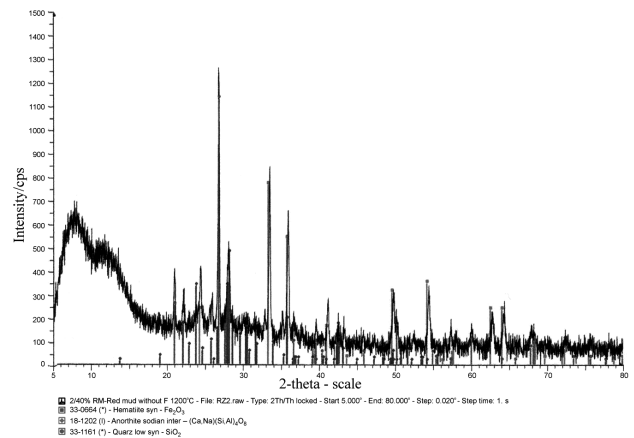


Figure 9: X-ray diffractogram of sintered product ($w = 40\%$ red mud; $T = 1200\text{ }^{\circ}\text{C}$)

Slika 9: Rentgenski difraktogram sintranega proizvoda ($w = 40\%$ rdečega blata; $T = 1200\text{ }^{\circ}\text{C}$)

mostly unbound (which is more evident at the lower sintering temperature). This also influences the different values of the total porosity and the microstructure changes of the sintered product, which has an effect on the values of the compressive strength.

4 CONCLUSION

On the basis of the performed examinations the influence of the sintering temperature and the binder content on the properties of a sintered product containing red mud we can conclude:

- red mud as a component of a raw material mixture can be used in ceramic technology (for bricks, blocks, etc.),
- the most important factors that determine the properties of the sintered products based on red mud are: the amount of red mud in the raw material mixture, the granulometric content of the components of the raw material mixture and the sintering temperature,
- at the higher sintering temperature (1200 °C) more favourable results regarding the total porosity and the compressive strength are obtained,
- the differences in the values of the total porosity, the volume shrinkage during sintering and the compressive strength, with an increase of the red mud in a raw material mixture (up to $w = 50 \%$) are not significantly higher.

5 REFERENCES

- ¹ Lj. Kostić - Gvozdenović, R. Ninković, Inorganic Technology, Faculty of Technology and Metallurgy, University of Belgrade, Belgrade 1997
- ² M. Krgović, Z. Jaćimović, R. Zejak, *Tile & Brick Int.*, 17 (2001) 3, 178–181
- ³ M. Krgović, M. Ivanović, N. Blagojević, Ž. Jaćimović, R. Zejak, M. Knežević, The Influence of the Mineral Content and Chemical Composition of Illite-Kaolinite Clays on the Properties of the Properties of the Sintered Product, *Interceram*, 55 (2006) 2, 104–106
- ⁴ M. Krgović, R. Zejak, M. Ivanović, M. Vukčević, I. Bosković, M. Knežević, B. Zlatičanin, Properties of the Sintered Product based on Electrofilter Ash depending on the Mineral Content of Binder, *Research Journal of Chemistry and Environment*, 15 (2011) 4, 52–56
- ⁵ S. Đurković, The Possibilities of using Electrofilter Ash TE "Pljevlja" as Raw Materials component Mixture for producing sintered product, Master Thesis, University of Montenegro, Podgorica, 2008, 4–5
- ⁶ M. Krgović, N. Marstijepović, M. Ivanović, R. Zejak, M. Knežević, S. Đurković, The Influence of Illite-Kaolinite Clays' Mineral Content on the Products' Shrinkage during drying and firing, *Mater. Tehnol.*, 41 (2007) 4, 189–192
- ⁷ B. Živanović, R. Vasić, O. Janjić, *Ceramic Tiles*, Monography, Institute of Materials in Serbia, Belgrade 1985, 12–17
- ⁸ M. Krgović, M. Knežević, M. Ivanović, I. Bošković, M. Vukčević, R. Zejak, B. Zlatičanin, S. Đurković, Influence of the Temperature on the Properties of the Sintered product on the basis of Electrofilter ash as a component of the Raw Material Mixture, The Eleventh Annual Conference "YUCOMAT 2009", Herceg Novi, 2009, 150–151
- ⁹ M. Krgović, M. Knežević, M. Ivanović, I. Bošković, M. Vukčević, R. Zejak, B. Zlatičanin, S. Đurković, The Properties of a Sintered Product based on Electrofilter Ash, *Mater. Tehnol.*, 43 (2009) 6, 327–331
- ¹⁰ M. Tecilazić-Stevanović, Principles of Ceramic Technology, Faculty of Technology and Metallurgy, University of Belgrade, Belgrade 1990, 141–152

INFLUENCE OF THE PRECIPITATION TEMPERATURE ON THE THRUST FORCE AND TORQUE IN DRILLING AN Al 2219-SiC_p COMPOSITE

VPLIV TEMPERATURE IZLOČEVALNEGA ŽARJENJA NA POTISNO SILO IN NAVOR PRI VRTANJU KOMPOZITA Al 2219-SiC

Radhakrishnan Ganesh¹, Kesavan Chandrasekaran²

¹Department of Mechanical Engineering, Anna University, 600025 Chennai, Tamilnadu, India

²Department of Mechanical Engineering, R.M.K Engineering College, 601206 Kavaraipettai, Tamilnadu, India
ganesh_akmcmc@yahoo.co.in, kesavan.chandrasekaran@gmail.com

Prejem rokopisa – received: 2013-06-10; sprejem za objavo – accepted for publication: 2013-09-13

This paper aims at understanding the influence of the precipitation temperature on the drilling performance of an Al 2219-SiC composite. This type of composite is currently in use in aerospace industries. Drilling is the most frequently employed secondary machining owing to the requirements of the fabrication. This composite was subjected to the precipitation heat treatment, hence calling for a study of the precipitation-temperature effect on the machining performance. The composite was fabricated through the powder-metallurgy route. The drilling trials were conducted with a PCD drill of a 5 mm diameter and 118° point angle. The experiments were conducted with different spindle speeds of (500, 1000 and 1500) r/min and feed rates of (10, 15 and 20) mm/min. The thrust force and torque were the performance indicators. The influences of the mass fraction of reinforcement, the precipitation temperature, the feed rate and the spindle speed on the thrust force and torque during drilling were analyzed. It was observed that the drilling performance was influenced significantly by the feed rate followed by the precipitation temperature, the mass fraction and the particle size of reinforcement. The spindle speed did not influence much the machining performance.

Keywords: powder metallurgy, polycrystalline diamond, precipitation temperature

Namen članka je ugotoviti vpliv temperature izločevalnega žarjenja na zmogljivost vrtnja kompozita Al 2219-SiC. Ta vrsta kompozita se uporablja v letalski industriji. Zaradi potreb pri izdelavi je vrtnje najbolj pogosto uporabljena sekundarna operacija obdelave. Ta kompozit je bil toplotno obdelan z izločevalnim žarjenjem, zato je potrebna študija vpliva temperature izločevalnega žarjenja na zmogljivosti pri obdelavi. Kompozit je bil izdelan po postopkih prašne metalurgije. Preizkusi vrtnja so bili izvršeni s PCD-svedrom premera 5 mm in s konico pod kotom 118°. Preizkusi so bili izvršeni pri različnih hitrostih vrtnja vretena (500, 1000 in 1500) r/min ter hitrostih podajanja (10, 15 in 20) mm/min. Pokazatelja zmogljivosti sta bila potisna sila in navor. Analiziran je bil vpliv masnega deleža delcev za utrjevanje, temperature izločevalnega žarjenja, hitrost podajanja, potisna sila in navor. Opaženo je, da na zmogljivost vrtnja najbolj vpliva hitrost podajanja, nato temperatura izločevalnega žarjenja, masni delež in velikost delcev SiC. Hitrost vrtnja vretena nima bistvenega vpliva na zmogljivost obdelave.

Ključne besede: prašna metalurgija, polikristalni diamant, temperatura izločevalnega žarjenja

1 INTRODUCTION

The ongoing research on materials over the past decades has produced advanced materials with the properties superior to conventional materials such as metal-matrix composites (MMCs). Metal-matrix composites (MMCs) are one of the widely known composite groups due to their superior specific strength, stiffness, wear and corrosion resistances. Silicon-carbide-particulate (SiC_p) reinforced aluminium-based MMCs are among the most common and commercially available MMCs due to their economical production.¹ These low-cost composites show their advantages in the applications requiring the ability to withstand a relatively high temperature besides high specific strength, stiffness and fatigue resistance, the typical features of the composite materials in the applications such as drive shafts, cylinder block liners, pistons and automotives.² However, because of the hard reinforcement particles in the matrix, MMCs cause very serious problems in machining.³ For

this reason efforts have been made to develop the near-net-shape manufacturing of these products. However, for joining and assembling, secondary machining processes such as drilling, milling, etc., are the prime requirements. Machining, especially drilling, of cast MMC parts is done using diamond-coated tools⁴ causing a considerable increase in the tool life. The published literature on the machining of MMCs indicate that only polycrystalline-diamond (PCD) tools allow good tool life as PCD is harder than the reinforcement materials such as SiC or Al₂O₃ and it mostly does not chemically react with the workpiece material. Kilickap et al.⁴ examined the tool wear and the machined-surface characteristics during machining SiC-reinforced aluminium-matrix composites with coated and uncoated tool materials for different feeds and speeds. They concluded that a higher cutting speed and a lower feed rate result in good surface quality. While a higher drilling speed reduces the mechanical, thermal shock affecting the machine, a low feed rate maintains an adequate flank clearance to avoid

rubbing/sliding. Quan and Ye⁵ investigated the hardness and residual stress of the SiC/Al composites in a surface layer affected by the machining and found that cutting at a larger removal rate increases the possibility for the tensile residual stress in the machined surface layers of the composites. A surface integrity study was done by Suresh Kumar Reddy et al.⁶ during the end milling of Al/SiC composites. It was concluded from the study that the reinforcement in the composites enhances the machinability in terms of a lower tendency to clog the cutting tool than in the case of an unreinforced Al alloy. In addition, the tendency of the reinforcement to spall off can enhance the chip forcing tendency and the consequent machining. Ciftci et al.⁷ proved that cBN is unsuitable for machining the MMCs containing the SiC particles of the average size of 110 μm as there was a heavy fracture of the cutting edge and nose. This could be due to the defects caused when the cBN was inserted onto the core substrate.⁸ The tribological properties and mechanical properties of the Al_2O_3 -SiC reinforced Al composites manufactured through the powder metallurgy route were investigated by Unlu,⁹ Ramulu et al.¹⁰ conducted a drilling of Al_2O_3 -aluminium-based metal-matrix composites, using different drills and found that PCD drills outperformed all the other drills in terms of the drilled-hole quality and the drilling forces encountered. Basavarajappa et al.¹¹ studied the drilling of hybrid metal-matrix composites on the basis of Taguchi techniques and it was revealed that the dependent variables are more significantly influenced by the feed rate than by the speed. Brun and Lee¹² investigated the machinability of the volume fraction Al-40 % SiC composite and concluded that only polycrystalline diamond tools exhibit useful tool life. Quigley et al.¹³ studied the factors affecting the machinability of the Al/SiC metal-matrix composite using different tool materials and found that the triple-coated carbide tool, having the top layer made of TiN performed the best in terms of the flank wear compared to the other materials. The literature is mostly concerned with the effect of the reinforcement on machinability; the machine-specific tool/drill/performance is also reported. Only limited data on the significance of the precipitation temperature is available. The present experimental study aims at investigating the

influence of the precipitation temperature, the mass fraction of reinforcement, the size of reinforcement and the machining parameters on the thrust force and torque when drilling the aluminium-matrix composites reinforced with SiC particles; the selected cutting tool for drilling was a fine-grained PCD drill.^{14,15}

2 EXPERIMENTATION

The details of the MMC used and the working conditions are listed in **Table 1**.

The matrix and reinforcement material are blended mechanically in a planetary ball mill in order to ensure a uniform distribution of the reinforcement for all the mass fractions and particle sizes. It is then cold compacted uniaxially to form cylindrical specimens with a diameter of 10 mm and length of 20 mm. The workpieces were precipitated in a muffle furnace at three different temperatures of 500 °C, 550 °C and 600 °C for 4 h, and then, each time, rapidly quenched in normal water and artificially aged for 10 h at 170 °C in the same furnace. This precipitation heat treatment was done to study the effect of the precipitation temperature on the machining performance of MMCs. The experimental set up is shown in **Figure 1**. The PCD drill used for the experiment is shown in **Figure 2**. The performance indicators such as the thrust force and torque were measured using a two-component piezoelectric dynamometer and the experiment was repeated three times for the same sample

Table 1: Experimental detail

Tabela 1: Eksperimentalne podrobnosti

Workpiece	Al 2219-matrix composite reinforced with SiC-cold-compacted-reinforcement particle Size – 37 μm and 67 μm mass fraction – 10 %, 15 % and 20 %
Drilling machine	ARIX VMC 100 CNC drilling machine
Tool	PCD drill – twist drill of $\varphi = 5 \text{ mm}$, 118° point angle
Drilling conditions	Speed – (500, 1000, 1500) r/min Feed rate – (10, 15, 20) mm/min Environment – Dry



Figure 1: Photograph of the experimental set up with the dynamometer attachment

Slika 1: Posnetek sestave za preizkuse z dodanim dinamometrom



Figure 2: Photograph of a 5-mm-diameter PCD drill used for the experimentation

Slika 2: Posnetek PCD-svedra s premerom 5 mm, uporabljenega pri preizkusih

and the average values of the output parameters were noted.

3 RESULTS AND DISCUSSION

3.1 Density and porosity

From **Figure 3**, showing 37 μm SiC, it is clear that the structural density increases with the precipitation temperature and also with the mass fraction of reinforcement. A trend change can be seen around 550 $^{\circ}\text{C}$. In the case of 67 μm SiC, a reduction in the density can mostly be seen above 550 $^{\circ}\text{C}$. The SiC density increases up to 15 %, followed by a drop.

From **Figure 4**, showing 37 μm SiC, it is clear that the porosity reduces with the precipitation temperature; a visible reduction occurs above 550 $^{\circ}\text{C}$. This complements the observation on density. In the case of 67 μm SiC, the porosity tends to drop up to 550 $^{\circ}\text{C}$, followed by a rise (by 10–15 %). Above 550 $^{\circ}\text{C}$ it rises and falls by 20 %. This finding mostly complements the observation on density.

3.2 Hardness and compressive strength

The observed values of the hardness and compressive strength for different mass fractions and precipitation temperatures are illustrated in **Figures 5** and **6**. For 37 μm SiC, the hardness of the MMC tends to rise up to 550

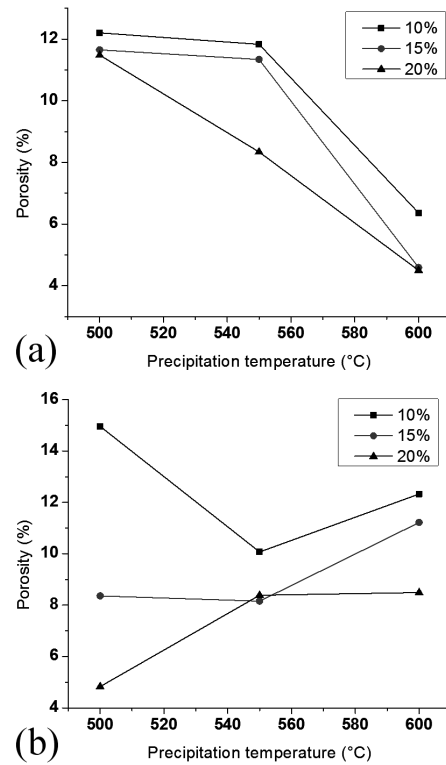


Figure 4: Observed porosity for different precipitation temperatures and mass fractions: a) 37 μm SiC, b) 67 μm SiC

Slika 4: Izmerjena poroznost pri različnih temperaturah izločevalnega žarjenja in masnih deležih: a) 37 μm SiC, b) 67 μm SiC

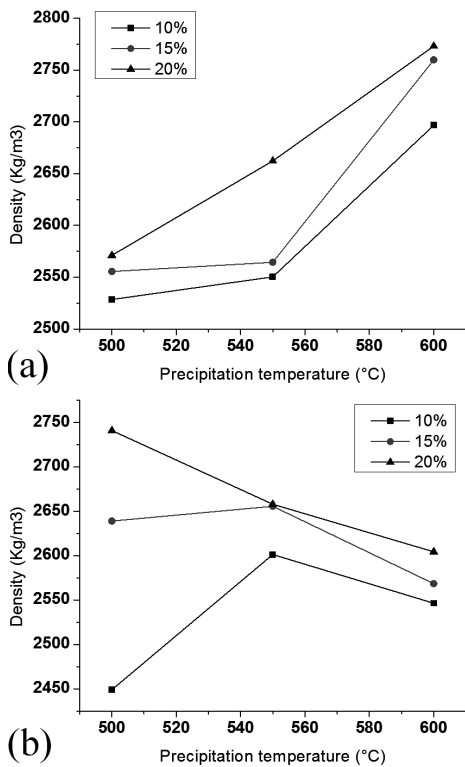


Figure 3: Observed density for different precipitation temperatures and mass fractions: a) 37 μm SiC, b) 67 μm SiC

Slika 3: Izmerjena gostota pri različnih temperaturah izločevalnega žarjenja in masnih deležih: a) 37 μm SiC, b) 67 μm SiC

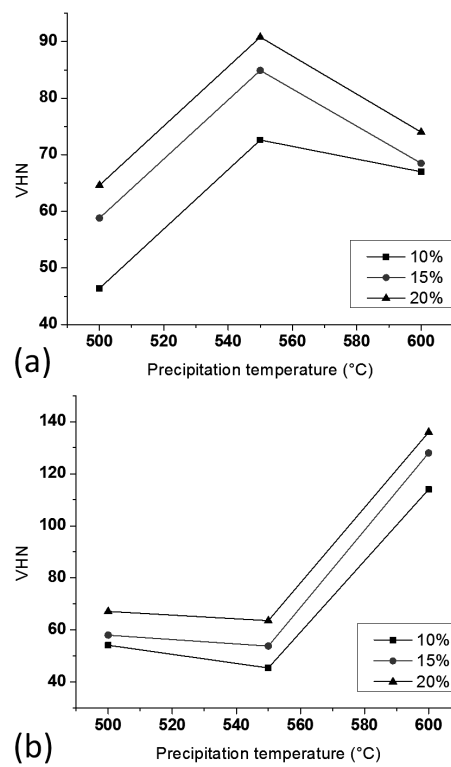


Figure 5: Observed VHN for different precipitation temperatures and mass fractions: a) 37 μm SiC, b) 67 μm SiC

Slika 5: Izmerjena VHN pri različnih temperaturah izločevalnega žarjenja in masnih deležih: a) 37 μm SiC, b) 67 μm SiC

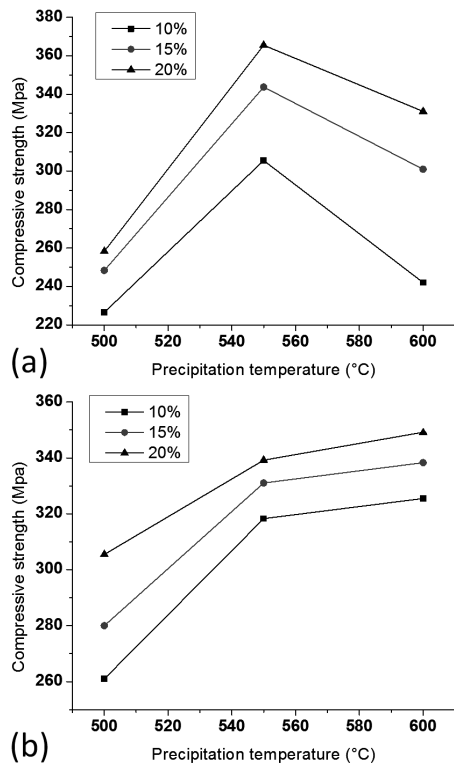


Figure 6: Observed compressive strength for different precipitation temperatures and mass fractions: a) 37 μm SiC, b) 67 μm SiC

Slika 6: Izmerjena tlačna trdnost pri različnih temperaturah izločevalnega žarjenja in masnih deležih: a) 37 μm SiC, b) 67 μm SiC

°C, followed by a reduction. With the increasing mass fraction of reinforcement, the hardness increases. The compressive strength increases up to 550 °C, followed by a drop. It also increases with the mass fraction of reinforcement. Considering the finer-sized SiC-parti-

culate reinforcement and precipitation temperature, the density increases with the reduction in the porosity. With a high temperature (above 550 °C) the rise in the density is associated with the hardness or compressive strength. With the rise in the temperature, the matrix densifies heavily. This is associated with a reduction in the flow strength and the consequent densification but also a reduction in the hardness.

The tendency to agglomerate is also lower. With 37 μm SiC, unlike in the case of 67 μm SiC, the MMC exhibits a reduction in the density, especially at the temperature above 550 °C. A high mass-fraction (15 % and 20 %) reinforcement also exhibits only a marginal difference. The porosity of the MMC tends to drop and rise beyond 550 °C. With the increasing reinforcement percentage, a mixed influence on the porosity (especially with the 15 % and 20 % reinforcements) is seen. With the coarser particulates and the increasing precipitation temperature, a great portion of the heat flux could have been absorbed by SiC resulting in a lower matrix flow and the consequent increase in the porosity. However, the MMC exhibits a rise in the hardness beyond 550 °C due to the agglomeration or pooling of reinforcement, the lower matrix flow and increased hardness, also reflected in the increased compressive strength.

3.3 Thrust force and torque

The drilling performance was evaluated in terms of two indicators: the thrust force and torque. The drill thrust force and torque were monitored for all the trials. The effects of the drilling conditions, the precipitation temperature and reinforcement percentage, on the drilling indicators are illustrated in Figures 7 to 10. It is

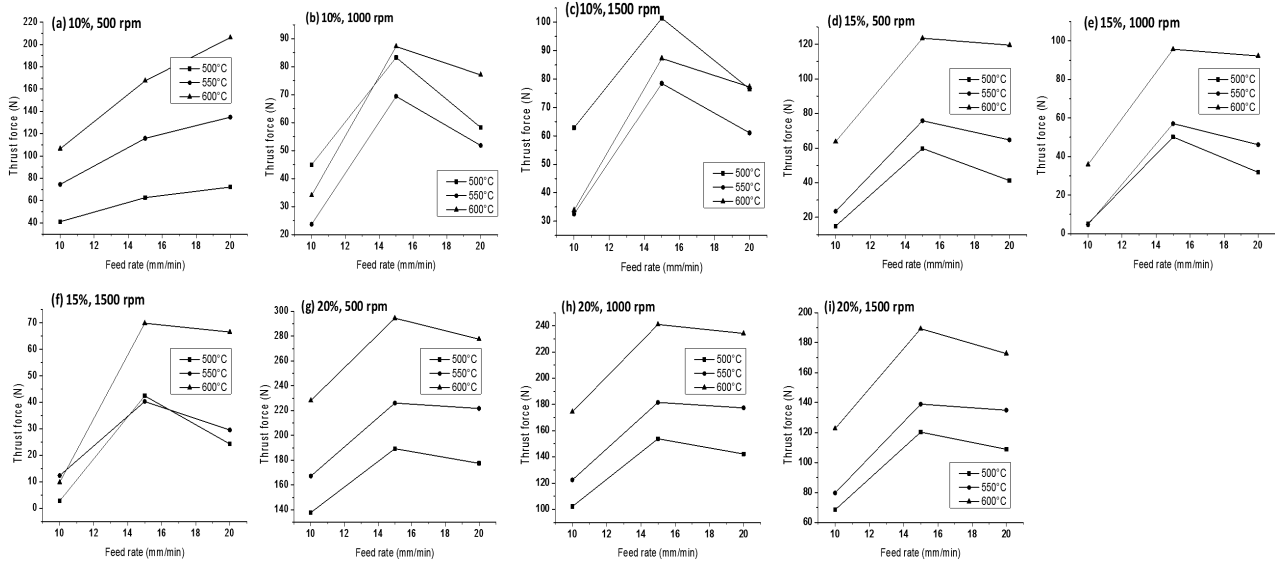


Figure 7: Observed thrust force during the drilling of 37 μm SiC reinforced composites for different mass fractions of reinforcement, precipitation temperatures, cutting speeds and feeds

Slika 7: Izmerjena potisna sila pri vrtnanju kompozita, utrjenega s 37 μm SiC, pri različnih masnih deležih, temperaturah izločevalnega žarjenja, hitrostih rezanja in podajanja

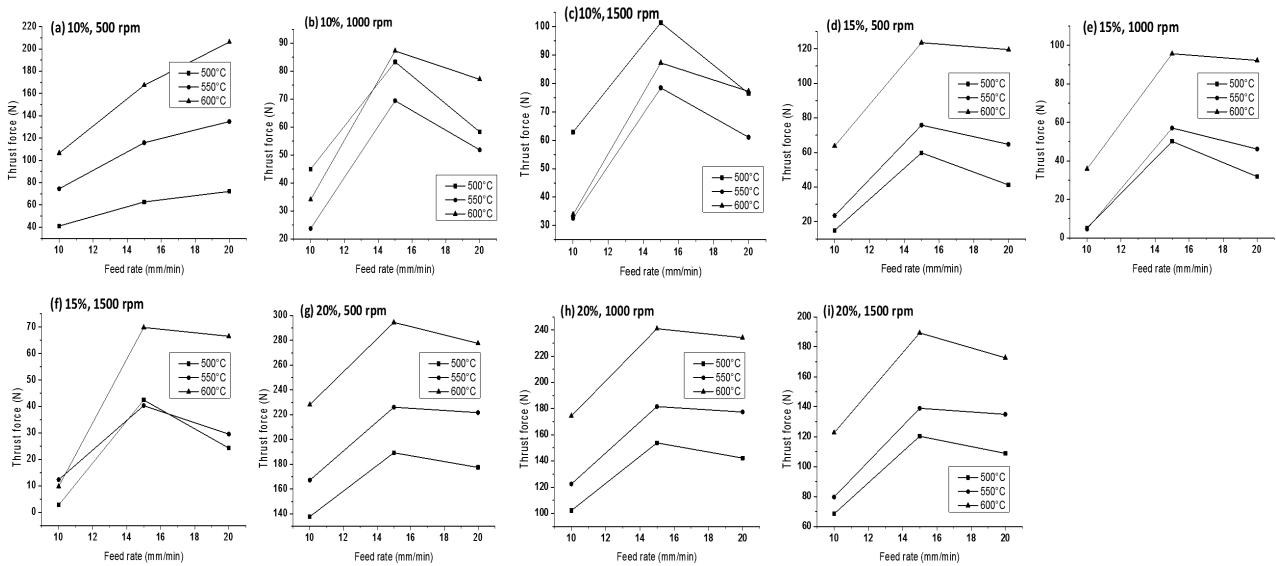


Figure 8: Observed thrust force during the drilling of 67 μm SiC reinforced composites for different mass fractions of reinforcement, precipitation temperatures, cutting speeds and feeds

Slika 8: Izmerjena potisna sila pri vrtnanju kompozita, utrjenega s 67 μm SiC, pri različnih masnih deležih, temperaturah izločevalnega žarjenja, hitrostih rezanja in podajanja

seen that the thrust force increases with the feed rate and speed for all the composites. An increase in the feed rate results in a reduction in the effective clearance on the flank surface (the point region) and the consequent rise in the sliding and thrust force. The observed rise in the thrust force with the increasing drill speed could be attributed to a possible thermal softening of the matrix aluminium with the increasing temperature and the consequent clogging of the drill. With regard to the precipitation temperature, it is seen that with the increasing precipitation temperature, the MMC encounters a

higher-order thrust force. It is also clear that with a small percentage of reinforcement a distinct influence of a higher precipitation temperature (600 °C) on the thrust force can be observed. With the increasing percentage of reinforcement, the influence of the precipitation temperature is more or less evenly spread. With the increasing precipitation temperature, the microstructure becomes more densified, resulting in the observed rise in the thrust force.

Unlike in the case of the MMC with the small-sized SiC particle (37 μm), the MMC reinforced with the

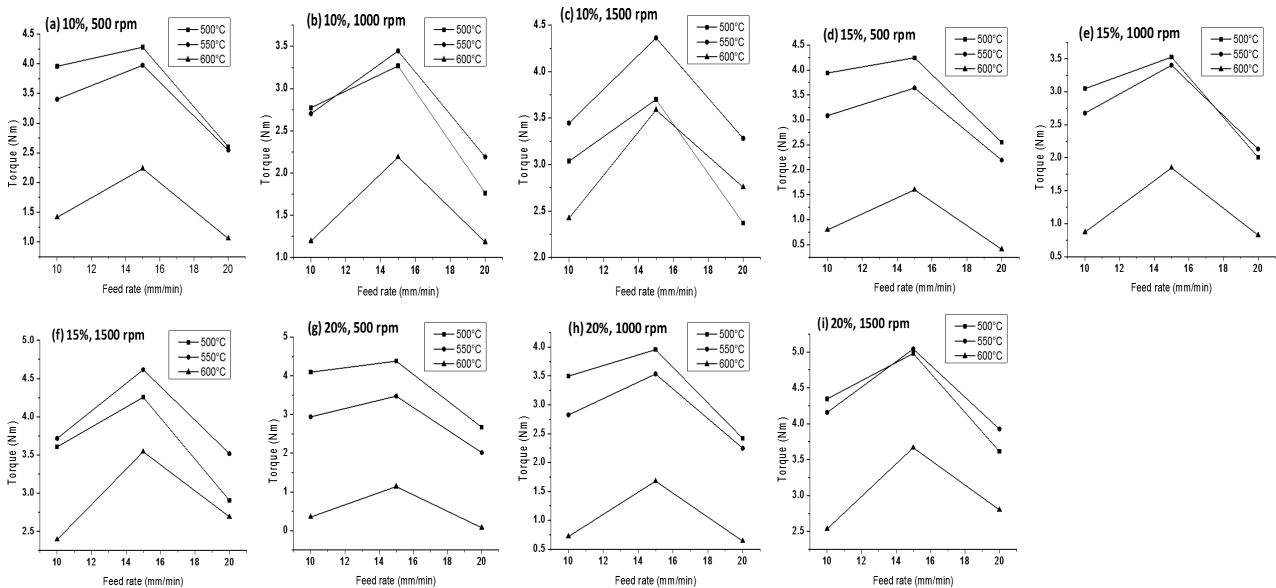


Figure 9: Observed torque during the drilling of 37 μm SiC reinforced composites for different mass fractions of reinforcement, precipitation temperatures, cutting speeds and feeds

Slika 9: Izmerjen navor pri vrtnanju kompozita, utrjenega s 37 μm SiC, pri različnih masnih deležih, temperaturah izločevalnega žarjenja, hitrostih rezanja in podajanja

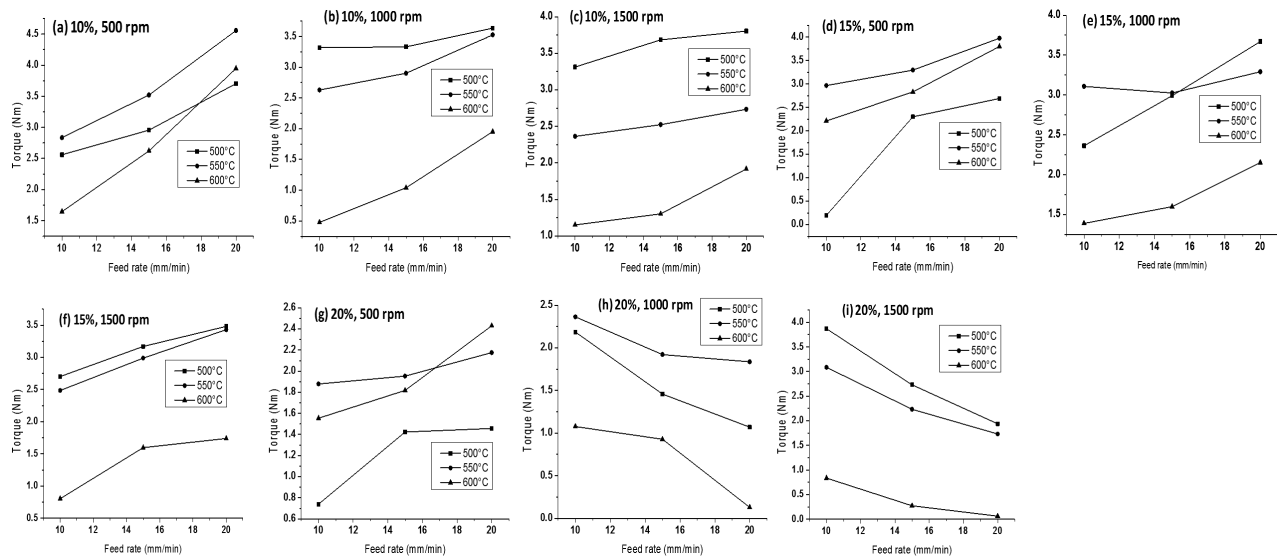


Figure 10: Observed torque during the drilling of 67 μm SiC reinforced composites for different mass fractions of reinforcement, precipitation temperatures, cutting speeds and feeds

Slika 10: Izmerjen navor pri vrtnanju kompozita, utrjenega s 67 μm SiC, pri različnih masnih deležih, temperaturah izločevalnega žarjenja, hitrostih rezanja in podajanja

coarse SiC particle (67 μm) exhibits a distinctly different trend. The MMC with 67 μm SiC mostly encounters a smaller-order thrust force, barring a higher mass fraction. Unlike in the case of the 37 μm SiC reinforcement, the MMC reinforced with the coarser particle, encounters a visible reduction in the thrust force with a high feed rate. Also, with the precipitation temperature, a relatively higher-order thrust force is encountered. Unlike in the case of the 37 μm SiC reinforcement, the MMC with the coarser particulate reinforcement encounters a reduction in the thrust force with the increasing drilling speed. With the coarser reinforcement, the MMC experiences a pooling of reinforcement, resulting in a higher heterogeneity of the structure. With the coarser particulate, the heat partition induces a great heat absorption by the SiC reinforcement, resulting in a more porous and less densified structure. The observed rise in the thrust force for the 20 % reinforcement is attributed to the pooling of reinforcement/higher-order heterogeneity, causing an excessive wear of the drill and the consequent rise in the thrust force.

With regard to the torque, for 37 μm SiC composites, it increases with the feed rate from 10 mm/min to 15 mm/min and decreases by 20 mm/min for all the mass fractions of reinforcement and precipitation temperatures. On the other hand, for 67 μm SiC composites, it shows an increasing trend for the 10 % and 15 % mass fractions at all the cutting speeds and precipitation temperatures, but also a decreasing trend for the higher mass fraction of 20 %. The torque was also observed to have an increasing trend with the feed rate for all the mass fractions and precipitation temperatures when the spindle speed was increased from 500 r/min to 1000 r/min; however, it dropped after 1000 r/min. The feed rate is associated with the chip thickness. A high feed

rate results in a larger cross-sectional area of the undeformed chip, therefore, increasing the value of the thrust force and torque. It was also observed that the thrust force was high for the composites precipitated at 600 $^{\circ}\text{C}$ and low for the ones precipitated at 500 $^{\circ}\text{C}$. This may be attributed to the fact that at the higher precipitation temperature, the matrix material becomes soft and increases the area of contact between the tool and the workpiece. At the higher spindle speeds, there was a slight drop in the torque because of a decrease in the contact area between the tool and the workpiece. With

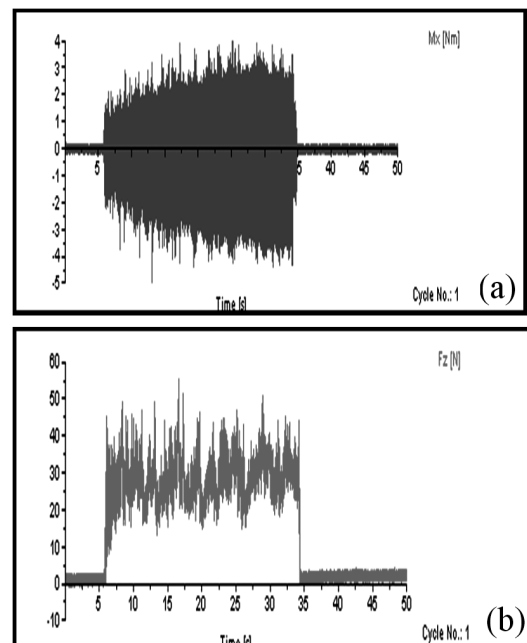


Figure 11: Typical profiles of: a) torque, b) thrust force
Slika 11: Značilen profil: a) navora, b) potisne sile

67 μm SiC composites, the trend for the thrust force and torque was similar to that of 37 μm SiC composites, but the thrust force drops at the higher feed rate of 20 mm/min for all the spindle speeds. This may be due to the larger particle size of reinforcement. The larger particle size results in a poor bonding between the matrix and the reinforcement. At the higher mass fraction and higher spindle speeds, the torque decreases with an increase in the feed rate due to an insufficient bonding between the matrix and reinforcement. In general, for both 37 and 67 SiC reinforced composites, with an increase in the spindle speed, the thrust force and the torque, there is a fall-and-rise trend. This may be initially due to the reduction in the material hardness with the significant increase in the temperature, whereas later the softening of the matrix increases the contact area of the matrix/reinforcement interface, thereby increasing the thrust force and torque. The typical profiles of the thrust force and torque obtained with the data-acquisition system connected to the dynamometer is illustrated in **Figure 11**.

4 CONCLUSION

The thrust force and torque results of the experimental study of the influence of the precipitation temperature during the drilling of the Al 2219-SiC_p composite material using a PCD drill indicated the following conclusions:

The thrust force increases with the feed rate at all the cutting speeds, mass fractions of reinforcement and precipitation temperatures for 37 μm SiC composites, but it shows an increasing and decreasing trend for 67 μm SiC composites. As the mass fraction of reinforcement increased, the thrust force also increased significantly. The thrust force was highly dependent on both the spindle speed and the feed rate, showing an increasing trend in the same way, regardless of the mass fractions of reinforcement and precipitation temperature. The size of the reinforcement particle has an appreciable influence on the thrust force under different experimental condi-

tions. The precipitation temperature also has a significant influence as the lowest thrust force was observed at the higher precipitation temperature of the specimens.

The torque follows the rise-and-fall trend of the feed rate for 37 μm SiC composites, whereas the increasing trend is observed for 67 μm SiC composites. The torque was observed to be the lowest at the lower feed rate and for the higher mass fraction regardless of the sizes of reinforcement. The trend of the torque remains the same for all the precipitation temperatures. The size of the reinforcement particle has an appreciable influence on the torque under different experimental conditions, whereas the precipitation temperature does not have a significant influence on the torque.

5 REFERENCES

- ¹ F. Bedir, B. Ogel, Proceedings of the 11th International Conference on machine design and production, Turkey, 2004
- ² M. Sklad El-Gallab, Journal of Materials Processing Technology, 83 (1998), 151–158
- ³ S. Jahanmir, M. Ramulu, P. Koshy, Machining of Ceramics and Composites, Marcel Dekker, New York 2000
- ⁴ E. Kilickap, O. Cakir, M. Aksoy, A. Inan, Journal of Materials Processing Technology, 164–165 (2005), 862–867
- ⁵ Y. M. Quan, B. Y. Ye, Journal of Materials Processing Technology, 138 (2003), 464–467
- ⁶ N. Suresh Kumar Reddy, S. Kwang-Sup, M. Yang, Journal of Materials Processing Technology, 201 (2008), 574–579
- ⁷ I. Ciftci, M. Turker, U. Seker, Wear, 257 (2004), 1041–46
- ⁸ B. Anand Ronald, L. Vijayaraghavan, R. Krishnamurthy, Materials and Design, 30 (2009), 679–686
- ⁹ B. S. Unlu, Materials and Design, 29 (2008), 2002–2008
- ¹⁰ M. Ramulu, P. N. Rao, H. Kao, Journal of Materials Processing Technology, 124 (2002), 244–254
- ¹¹ S. Basavarajappa, G. Chandramohan, J. Paulo Darim, Journal of Materials Processing Technology, 196 (2008), 332–338
- ¹² M. K. Brun, M. Lee, Wear, 104 (1985), 21–29
- ¹³ O. Quigley, J. Monaghan, P. O. Reilly, Journal of Materials Processing Technology, 43 (1994), 21–36
- ¹⁴ T. S. Mahesh Babu, M. S. Aldrin Sughin, N. Muthukrishnan, Procedia Engineering, 38 (2012), 2617–2624
- ¹⁵ C. Dhavamani, T. Alwarsamy, Procedia Engineering, 38 (2012), 1994–2004

OPTIMIZATION OF THE RECYCLING PROCESSES FOR MAGNESIUM FROM A HIGHLY CONTAMINATED WASTE

OPTIMIRANJE POSTOPKA RECIKLIRANJA MAGNEZIJA IZ MOČNO KONTAMINIRANIH ODPADKOV

Vaso Manojlović¹, Željko Kamberović², Miroslav Sokić¹, Zvonko Gulišija¹,
Vladislav Matković¹

¹Institute for Technology of Nuclear and Other Mineral Raw Materials, Bulevar Franš d'Eperea 86, 11000 Belgrade, Serbia

²Faculty of Technology and Metallurgy, University of Belgrade, Karnegijeva 4, 11000 Belgrade, Serbia
v.manojlovic@itnms.ac.rs

Prejem rokopisa – received: 2013-07-30; sprejem za objavo – accepted for publication: 2013-10-04

With the recently increased use of magnesium alloys, especially in the automotive industry, a large quantity of generated waste, based on magnesium alloys, is expected. Such a waste often contains many impurities such as oil, paint, moisture, non-metallic fractions, oxides, Cu, Fe, etc. In this paper, two different methods for extracting magnesium from a highly contaminated waste are presented: the recycling of magnesium with flux and with the vacuum-distillation process. In addition, we present the process of pre-treating the contaminated magnesium waste that has proved to be a very important step in the recycling process for both economic and environmental reasons. The processing of post-consumer and contaminated magnesium scrap is described with a diagram, providing a sustainable and environmentally friendly procedure for the treatment of such wastes.

Keywords: recycling, magnesium waste, vacuum distillation, flux, contaminated, impurities

Z naraščanjem uporabe magnezijevih zlitin, posebno v avtomobilski industriji, se pričakujejo velike količine odpadkov na osnovi magnezijevih zlitin. Taki odpadki pogosto vsebujejo številne nečistoče, kot so olja, barve, vlaga, nekovinske frakcije, oksidi, Cu, Fe in drugo. V tem članku sta predstavljeni dve različni metodi za ekstrakcijo magnezija iz močno onesnaženih odpadkov: recikliranje magnezija s talilom in z vakuumsko destilacijo. Dodatno je prikazan še postopek predobdelave kontaminiranih magnezijevih odpadkov, ki se je izkazal za pomembnega pri recikliranju, tako iz ekonomskih kot tudi okoljevarstvenih razlogov. Obdelava iztrošenega in kontaminiranega odpadnega magnezija je opisana z diagramom, ki zagotavlja trajnosten in okolju prijazen postopek obdelave takih odpadkov.

Ključne besede: recikliranje, magnezijevi odpadki, vakuumaska destilacija, talilo, kontaminiran, nečistoče

1 INTRODUCTION

Magnesium alloys, being the lightest metals, are used widely for many parts in the automotive industry.¹ Such a trend is mainly a consequence of increased fuel prices, leading to a decrease in the total mass of a vehicle. Furthermore, many environmental regulations require the use of lightmass materials in transport to reduce harmful emissions. The European guideline on car usage has enforced the trend of using parts of lightmass metals.^{2,3}

Due to their poor corrosion resistance, magnesium automotive components exposed to a corrosive atmosphere must be coated (paint and lacquer). Oily and coated magnesium car components, at the end of their life cycle, make the recycling process very difficult because of the contamination of magnesium melts with a lot of impurities. There are several characterizations of magnesium scrap, but the most referenced is the one using eight classes of scrap. Class 1 of magnesium scrap represents high-grade clean scrap without any impurities; Class 2 is clean scrap with aluminium or steel inserts; Class 3 includes clean, dry and uncontaminated turnings and swarfs; Class 4 includes flux-free residues such as dross and sludge; Class 5 refers to painted coated scrap

with/without aluminium or steel inlays and with no copper or brass impurities; Class 6 includes oily and/or wet turnings, swarfs, etc.; Class 7 includes unclean and contaminated metal scrap, e.g., the post-consumer scrap that may contain silicon (Al-alloys, shot blasting), Cu-contaminated alloys, iron inserts, Ni-coatings and non-magnesium sweepings; Class 8 includes the flux-containing residues from Mg recycling, high amounts of oxides, chlorides, fluorides (Mg amount < 30 %) and Fe.⁴⁻⁶

Only the first-class scrap is relatively easy to recycle. The recycling difficulties increase with the increase in the class number of magnesium scrap. At present, only a small amount of magnesium-alloy scrap is recycled (only one third), while the rest is burned or buried in the ground.^{3,7,8} Magnesium-alloy chips represent a big recycling problem, caused by a very large specific surface covered with MgO. Reactions of the chips with humidity lead to a considerable oxidation, resulting in a loss of a lot of metal.^{9,10} On the other hand, the accompanying exothermic reaction can cause fire (the ignition temperature is 450 °C) during which the chips burn at 1000 °C and they are difficult to extinguish. Hydrogen is liberated

during this reaction causing small explosions and entailing another safety problem.^{1,5}

The elements such as Ni, Cu, Fe, and Si have a crucial influence on decreasing the magnesium-alloy corrosion resistance, so the amount of these impurities must be limited to the ppm level. It is very difficult to recycle "old" scrap (especially from a shredder plant), because it always contains a certain amount of these impurities.^{4,9,11-13} A removal of Ni and Cu from a magnesium melt with additives is practically impossible due to strong interactions in the Mg-Ni and Mg-Cu systems.^{6,9} Only the distillation process is an effective way to separate Ni and Cu from magnesium alloys.

The recycling of magnesium must be, above all, economically reasonable. The average price of primary magnesium metal (99.9 %) has been about 3.1 \$/kg in the past five years.¹⁴ Different recycling methods for magnesium scrap have been developed. The most common method for recovering clean scrap (classes 1, 2 and 3) involves flux. The recycling of magnesium scrap classes 4, 5, 6, 7 and 8 is not practical due to the increased impurities (Cu, Ni, Fe, Si) and the dirtiness of the starting material that decrease the economic efficiency of the recycling process. The most efficient process for the treatment of these classes of waste is the vacuum-distillation process.^{5,6,10}

2 EXPERIMENTAL PART

The first part of the experiment covers the most common method of magnesium recovery, the recycling with flux. A pre-treatment was conducted in order to improve both the economy and the technology of the process. The second part of the experiment refers to the most efficient method for recycling contaminated magnesium scrap, the vacuum-distillation process.

In the experiments with the flux treatment of the waste, two types of the samples were used. The first type of the samples mostly included the parts from the automotive industry and the casting process without any oil contaminations, with different thicknesses of the oxide layer on the surface as well as different sizes and shapes. The second type of the samples included oil-contaminated parts with oxides, dust and other inorganic impurities. The dimensions and descriptions of the samples are shown in **Table 1**.

Table 1: Characteristics and dimensions of the samples

Tabela 1: Značilnosti in dimenzije vzorcev

Sample		Characteristics	Dimensions, ($a \cdot h$) mm ²
Without oil (Classes 4 and 7)	1	Compact parts from the auto industry and parts of a gating system. A thin oxide layer is noticeable.	from 15 · 20 to 90 · 200
	2	Spongy, loose parts; mostly casting slag. A 1–3 mm oxide layer is noticeable on the surface.	from 20 · 30 to 30 · 100
Oil contaminated (Class 6)	3	Irregular biconcave parts with oil, oxides, dust and other inorganic impurities.	from 10 · 2 to 60 · 5

The pre-treatment of samples 1 and 2 was conducted in the following four steps:

- mechanical treatment in a rotating drum;
- dust separation;
- chemical treatment in a solution of sulfuric acid;
- washing and drying.

The mechanical treatment was performed in a laboratory rotating drum with a volume of 6 dm³ and rotation of 150 r/min. In this drum, the light fraction containing dust was separated from the massive fraction. The mass of the solid samples in the drum was (2000 ± 10) g. The chemical treatment of the massive fraction was conducted at the temperatures from 45–50 °C with an addition of a solution with mass fractions, $w = 5-10\%$ H₂SO₄. After the chemical treatment, the metal fraction in the lattice basket was washed with water. The drying process was performed in a furnace at the temperature of about 100–200 °C for a period of 6–8 h.

The smelting of prepared Samples 1 and 2 was conducted in an induction 25 kVA furnace with a graphite crucible of 1 dm³ and with additional mechanical stirring. A commercial smelting-salt mixture with the following composition was used: 76 % emgesal, 18 % dekamag and 6 % CaF₂. Since Sample 3 was contaminated with oil, the degree of oil contamination had to be determined. The oil removal was carried out with a prepared water solution of water glass (sodium silicate, 18.3 %), dode-

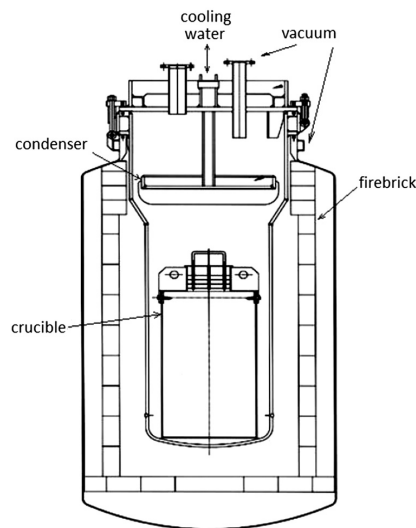


Figure 1: Vacuum-distillation furnace

Slika 1: Vakuumska destilacijska peč

cybenzenesulfonate (DBS, 6.7 %) and sodium hydroxide (NaOH, 5.0 %).

For the processing of the contaminated magnesium scrap with the vacuum-distillation process, highly contaminated magnesium scrap was used, belonging to Classes 5, 6 and 7. The waste was briquetted and its content was determined with a chemical analysis. The vacuum-distillation furnace is shown in **Figure 1**.

A batch of (400 ± 5) kg was melted in the electric-resistance furnace with two chambers under the vacuum of 0.5 bar. In the lower part of the furnace, the temperature was around 840–950 °C and in the upper part it was from 650–680 °C. The temperature of the condenser was about 135 °C. The times of the distillation process for magnesium from the waste were from 24–48 h.

3 RESULTS AND DISCUSSION

The processing of the magnesium waste, of Classes 4, 5, 6 and 7, was conducted with the flux-recycling process and the vacuum-distillation process. In the first part of the experiment, the importance of the waste pre-treatment was shown. The smelting process of Samples 1 and 2 was conducted with different pre-treatment combinations in order to indicate how each step affects the magnesium recovery rate. In addition, smelting salt was added in different amounts. The results are shown in **Table 2**.

Table 2: Magnesium recovery rate of Samples 1 and 2 in dependence of different combinations of the pre-treatment process and smelting salt

Tabela 2: Stopnja pridobitve magnezija v vzorcih 1 in 2 pri različnih kombinacijah predobdelave in talilne soli

Sample	Pre-treatment	Smelting salt, g	Mg recovery rate, %
1	Without pre-treatment, direct smelting	–	71 ± 2.5
	Mechanical treatment, 1 h, dust separation	50	91 ± 0.5
	Chemical treatment with 5% H ₂ SO ₄ , drying at 100 °C	50	81 ± 1.5
	Mechanical treatment, 1 h, dust separation, chemical treatment with 5 % H ₂ SO ₄ , drying at 100 °C	50	94 ± 0.8
2	Mechanical treatment, 1 h, dust separation	–	44 ± 1.5
	Mechanical treatment, 1 h, dust separation	60	47 ± 1.5
	Chemical treatment with 5 % H ₂ SO ₄ , drying at 100 °C	60	46 ± 1.5
	Mechanical treatment, 1 h, dust separation, chemical treatment with 5 % H ₂ SO ₄ , drying at 100 °C	60	49 ± 1.5

By processing Sample 1 (belonging to Class 7), it was shown that it is possible to achieve a utilization of up to 94 % with a pre-treatment. Without the pre-treatment, the utilization is only 71 %, which indicates the importance of the pre-treatment step in the recycling

process of this type of magnesium scrap. The maximum utilization after the processing of Sample 2 (the Class 4 scrap) is about 49 %, which is a consequence of a relatively thick oxide layer of 3 mm and a sponge structure of the waste, i.e., a relatively high surface/volume ratio. The Sample 2 pre-treatment does not significantly increase the recovery of magnesium from the waste due to the thick oxide layer.

The time for removing the oil from Sample 3, with a constant stirring, was 5 min at the temperature of 60 °C, while the sample mass was (1000 ± 10) g. The average degree of oil contamination with powder impurities for Sample 3 was (17 ± 0.5) %. It was shown that the optimum share of the water solution for an efficient removal of oil contamination (about (96 ± 1.5) %) is 10 %. When oil was removed from the surface, the scrap was smelted in an induction furnace. The total metal-recovery rate for Samples 4 was (93 ± 1.8) %. The results for Sample 3 (the Class 6 scrap) showed an effective way to remove oil from the waste, with a high recovery rate.

A pre-treatment of magnesium waste has a significant influence on:

- the utilization of magnesium from the waste,
- the reduction of slag amounts,
- a better economy,
- a better ecology and safety of the process.

It should be noted that same experiments with the flux were done in industrial conditions in the factory Bela stena in Boljevac, Serbia, with the batches of the total mass of 157 t (Samples 1, 2 and 3). The total utilization of magnesium from the waste, in industrial conditions, was (75 ± 0.5) % (118 t of magnesium).

In the second part of the experiment, the vacuum-distillation process was employed for the extraction of magnesium from the contaminated waste (Classes 5, 6 and 7). The share of impurities was about 10 % (7 % moisture and 3 % oil, paint, oxides) and the rest was the magnesium alloy (mostly from the automotive industry). The experiments were conducted in different ranges of temperature and time in order to obtain the optimum parameters of the process. The results are shown in **Table 3**.

Table 3: Parameters for the vacuum-distillation process

Tabela 3: Parametri pri vakuumskem destilacijskem procesu

Sample	Temperatures down/up the furnace, °C	Time of distillation process, h	Metal in crown, kg	Residue, kg	Metal recovery rate, %
v1	840/650	24	200.2	170.5	55.5
v2	840/650	30	201.1	169.7	55.7
v3	840/650	40	203.6	170.3	56.2
v4	840/650	48	206.9	167.9	57.0
v5	900/670	24	207.5	162.4	57.4
v6	950/680	24	212.1	163.7	58.2

The chemical compositions of distilled magnesium crowns are shown in **Table 4**. Since zinc has a lower

vapor pressure than magnesium, the zinc in a crown required higher temperatures and longer times, but, in general, high-purity magnesium was obtained.

Table 4: Chemical composition of the magnesium crown

Tabela 4: Kemijska sestava magnezijeve krone

Sample	Chemical composition of the magnesium distillate						
	Al	Zn	Mn	Fe	Si	Cu	Mg
v1	0.02	0.04	0.005	0.001	0.003	0.001	99.93
v2	0.03	0.05	0.003	0.001	0.003	0.001	99.91
v3	0.03	0.05	0.005	0.001	0.002	0.002	99.91
v4	0.02	0.08	0.002	0.002	0.004	0.001	99.89
v5	0.03	0.14	0.004	0.001	0.003	0.0005	99.82
v6	0.04	0.34	0.005	0.002	0.004	0.001	99.61

The waste in the form of pressed briquettes was contaminated with oil, oxides, paint and dust. The oxides of magnesium and aluminium (MgO and Al_2O_3) contained in a batch cannot be converted to their elementary state; instead, they form a foamed slag along with the impurities and inter-metallic compounds. The distillation residue, besides the foamed slag, consists of a metal fraction that has a chemical composition of 35 % Al, 0.2 % Zn, 1.2 % Mn, 0.03 % Fe, 0.05 % Si, and the rest is magnesium and impurities. During the process, the amount of the magnesium in the metallic fraction of the batch was decreased and the amounts of the slag and aluminium in the batch were increased. Consequently, the utilization of magnesium is at a low level due to the difficulties in the movement of magnesium atoms through the oxides and alloys in the batch at the end of the process.

According to the results from **Tables 3** and **4**, it can be concluded that the duration of the process does not significantly affect the extraction of magnesium from the waste. However, by increasing the temperature, while keeping the same duration of the process, the magnesium recovery was increased by 2–3 %, which is a low rate with respect to the increment of the energy consumption of 7–8 %. In addition, with an increase in the operating temperature, the impurity amount in the distillate increased due to an intense evaporation of the impurities from the batch surface.

The residue from the vacuum-distillation process can be used for a recovery of aluminium, but a large amount of impurities must be taken into consideration. Although the recovery of magnesium from the waste is at a low level (about 58 %), pure magnesium was obtained (up to 99.93 %), justifying the economy of the process. For the industrial use, it is necessary to construct less expensive and more mobile equipment for the vacuum-distillation process. In addition, further research should focus on the combination of pre-treatment and vacuum-distillation process, which should increase the extraction of magnesium from the waste.

To remove an organic coating/paint and oil/moisture the pre-treatment step was used as a very effective

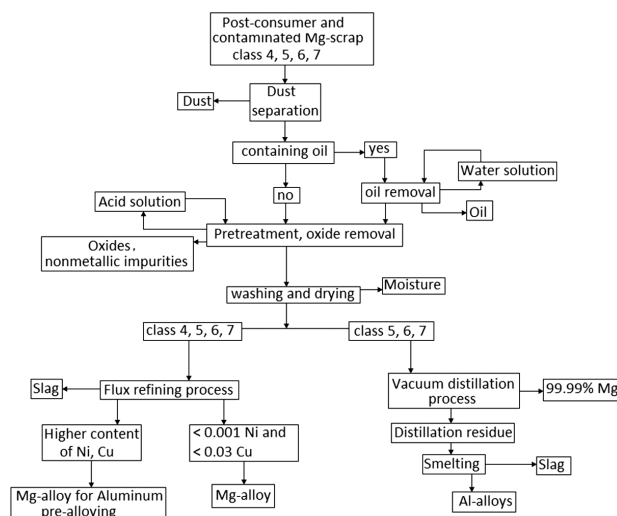


Figure 2: Processing of post-consumer and contaminated magnesium scrap

Slika 2: Obdelava izrabljenih in kontaminiranih odpadkov magnezija

method. The removal of these contaminations is essential for decreasing the dross formation and harmful gas exhaust and, thereby, reducing the loss of magnesium through the dross. Besides, if not removed they can significantly influence the vacuum-equipment lifetime when there is a direct contact. If there is a filter in the vacuum equipment for a disposal of harmful gases it will increase the price of the investment and make it difficult to create a vacuum, so a pre-treatment is a much better solution.

In the post-consumer scrap, the main impurities such as Ni, Cu, Fe and Si are always expected due to the complexity of the waste structure, particularly in the shredder process, where many materials are involved. In the vacuum-distillation process, impurities are easily separated from magnesium due to a different vapor pressure, which is a noticeable advantage of this process. In the process with flux, it is advisable to produce magnesium pre-alloys for the aluminium-alloy production rather than neutralizing it with Zn or Mn, especially at higher levels of Ni and Cu in the alloys (greater than 0.002 % for Ni and 0.03 % for Cu).

A recommended scheme for processing post-consumer and contaminated magnesium scrap is shown in **Figure 2**.

In **Figure 2**, we can see that the by-products such as oil, slag, dust, metallic oxides and non-metallic impurities are obtained. Dust, slug and non-metallic impurities can be used as additions to asphalt and oil can be used as a fuel. The Al-alloy from the vacuum-distillation process can be used for steel desulphurization.

4 CONCLUSION

In this paper two different methods for recycling magnesium waste were investigated: recycling with flux and recycling with the vacuum-distillation process. Mag-

nesium waste with oil, moisture and other non-metallic impurities was used in these processes. On the basis of the presented results, we can conclude that a pre-treatment has a significant role in the recycling process. The main advantages of the pre-treatment step applied to contaminated magnesium waste in the recycling process are the following:

- a significant increase in the recovery of magnesium from the waste (up to 94 %);
- an improvement in the economy of the process;
- a reduced share of the slag in the flux-recycling process;
- a removal of the moisture and oil from the waste enables a proper storage of the waste, without any safety risks;
- elimination of environmental problems (an emission of harmful pollutants into the air is prevented);
- an improved diffusion throughout the batch in the vacuum-distillation process, increasing the intensity of the process;
- prevention of contamination and vacuum-equipment damage.

In addition, a recommended scheme for processing contaminated magnesium waste was given, whereby several semi-products were obtained. In the case of higher proportions of Ni and Cu contained in a magnesium alloy, it is recommended to use these alloys for aluminium pre-alloying. If high-purity magnesium has to be obtained, the vacuum-distillation process is inevitable. By-products such as oil, slag, dust, metallic oxides and non-metallic impurities can be used as a fuel and as building-material components.

Acknowledgement

The authors wish to acknowledge the financial support from the Ministry of Education and Science of the Republic of Serbia within projects TR34002 and TR34033.

5 REFERENCES

- ¹ M. J. Fereiría Gándara, *Mater. Tehnol.*, 45 (2011) 6, 633–637
- ² L. Zhang, T. Dupont, *Materials Science Forum*, TTP USA, 546–549 (2007), 25–36
- ³ Ž. Kamberović, E. Romhanji, M. Filipović, M. Korać, *Metallurgical & Materials Engineering*, 15 (2009), 189–200
- ⁴ H. Antrekowitsch, G. Hanco, *Recycling of Different Types of Magnesium Scrap*, Proc. of the symp. jointly sponsored by the Magnesium Committee of the Light Metals Division of TMS with the Inter-Magnesium Association, Seattle, 2002, 43–48
- ⁵ S. Bell, B. Davis, A. Javaid, E. Essadiqi, *Final Report on Refining Technologies of Magnesium*, The Government of Canada, Enhanced Recycling, Action Plan 2000 on Climate Change, Minerals and Metals Program, 2006, 1–23, available from the World Wide Web: [http://www.nrcan.gc.ca/sites/www.nrcan.gc.ca/minerals-metals/files/pdf/mms-smm/busi-indu/rad-rad/pdf/2003-19\(cf\)cc-eng.pdf](http://www.nrcan.gc.ca/sites/www.nrcan.gc.ca/minerals-metals/files/pdf/mms-smm/busi-indu/rad-rad/pdf/2003-19(cf)cc-eng.pdf)
- ⁶ G. Hanco, G. Macher, *Technologies for Efficient Mg-Scrap Recycling*, Proc. of the TMS Annual Meeting, Magnesium technology, Warrendale, 2003, 29–32
- ⁷ Ch. Scharf, A. Ditzel, *Present State of Recycling of Magnesium and its Alloys*, Proc. of Magnesium Alloys and Their Applications, Wolfsburg, Germany, 1998, 685–690
- ⁸ J. Djokić, D. Minić, Ž. Kamberović, D. Petković, *Ecological Chemistry and Engineering S – Chemia I Inżynieria Ekologiczna S*, 19 (2012), 439–450
- ⁹ G. Hanco, H. Antrekowitsch, P. Ebner, *Journal of Metals*, 54 (2002) 2, 51–54
- ¹⁰ A. Gesing, A. Dubreuil, *Recycling of Post-Consumer Mg Scrap*, Proc. of 65th Annual World Magnesium Conference, Warsaw, 2008, 131–141
- ¹¹ W. Stevens, F. Trembay, *Fundamentals of UBC Decoating / De-lacquering for Efficient Melting*, Proc. of the Technical Sessions Presented by the TMS Aluminum Committee at the 126th Annual Meeting, Orlando, Florida, 1997, 709–713
- ¹² W. Green, J. Hillis, *Process for Producing High Purity Magnesium*, Patent number US4891065, 1990
- ¹³ Kh. Sabirov, G. N. Topalova, *Russian Journal of Non-Ferrous Metals*, 41 (2000), 72–75
- ¹⁴ Infomine [online], *5 Year Magnesium Prices and Price Charts.*, Vancouver, 2003, available from the World Wide Web: <http://www.infomine.com/investment/metal-prices/magnesium/5-year/>

MACHINABILITY OF A Ti-6Al-4V ALLOY WITH CRYOGENICALLY TREATED CEMENTED CARBIDE TOOLS

OBDELOVALNOST ZLITINE Ti-6Al-4V S KRIOGENSKO OBDELANIMI ORODJI IZ KARBIDNE TRDINE

Ahmet Mavi¹, Ihsan Korkut²

¹Gazi University, OSTIM Vocational School, Mechatronics Programs, Ankara, Turkey

²Gazi University, Faculty of Technology, Manufacturing Engineering, Ankara, Turkey
amavi@gazi.edu.tr

Prejem rokopisa – received: 2013-09-09; sprejem za objavo – accepted for publication: 2013-09-20

In this study, the effects of the treatment (applied to cutting parameters and cutting tool) on the cutting forces, surface roughness and tool life were investigated. Part of the cutting tools was subjected to a cryogenically treatment at $-145\text{ }^{\circ}\text{C}$ for 24 h. The effects of the cryogenically treated and untreated cemented carbides (uncoated) on the cutting forces, surface roughness and wear behaviors were investigated. Machinability tests were carried out at four different cutting speeds (30, 45, 60, 75) m/min, three different feed rates (0.20, 0.25 and 0.30) mm/r and the 1 mm cutting depth. Wear tests were made for four different chip volumes (20, 40, 60 and 80) cm^3 , four different cutting speeds (30, 45, 60, 75) m/min, the 0.25 m/r feed rate and the 1 mm cutting depth. At the end of the tests, the cryogenically treated inserts gave better results compared to the untreated tools with respect to the wear behavior, cutting forces and surface roughness.

Keywords: Ti-6Al-4V, tool wear, cryogenic process, cutting forces, surface roughness

V tej študiji je bil preiskovan vpliv obdelave (uporabljene za rezalne parametre in rezalno orodje) na sile pri rezanju, hrapavost površine in zdržljivost orodja. Del orodij iz karbidne trdine je bil kriogeno obdelan 24 h pri $-145\text{ }^{\circ}\text{C}$. Preiskovan je bil vpliv kriogeno obdelanih in neobdelanih orodij iz karbidne trdine (brez prevleke) na sile rezanja, hrapavost površine in vedenje pri obrabi. Preizkusi obdelovalnosti so bili izvršeni pri štirih različnih hitrostih rezanja (30, 45, 60, 75) m/min, pri treh različnih hitrostih podajanja (0,20, 0,25 in 0,30) mm/r in pri globini rezanja 1 mm. Preizkusi obrabe so bili izvršeni pri štirih volumnih odrezkov (20, 40, 60 in 80) cm^3 , pri štirih hitrostih rezanja (30, 45, 60, 75) m/min, pri podajanju 0,25 m/r in pri globini rezanja 1 mm. Preizkusi so pokazali, da dajejo s stališča obrabe, sil pri rezanju in hrapavosti površine, kriogeno obdelani vložki boljše rezultate v primerjavi z neobdelanim orodjem.

Ključne besede: Ti-6Al-4V, obraba orodja, kriogeni postopek, sile rezanja, hrapavost površine

1 INTRODUCTION

Titanium and its alloys have high strength, heat and corrosion resistance. They are used in the medical, electronics and computer, aviation and space industries.^{1,2} These alloys preserve their properties even at high temperatures during machining. Therefore, titanium belongs to the group of hard-to-machine materials. Among these alloys with different properties, Ti-6Al-4V has the lion's share with a 60 % usage in industrial applications.^{3,4} While at the higher temperatures during the treatment, a titanium alloy can preserve its strength, the cutting tool loses its strength due to the high temperature and pressure. The reaction with the cutting-tool material at high temperatures and the build-up edges (BUE) on the cutting-tool tip significantly affect the cost and efficiency of the treatment.⁵⁻⁷ Siekman indicated that the machining of these alloys is always problematic no matter which classical method is used.⁸ From this aspect, an investigation of suitable machining conditions is important for the machining of these alloys.

Cryogenic treatment is a supplementary process for the heat treatment applied to increase the wear resistance of the materials subjected to high wear. It is also known

as the below-zero cryogenic treatment. Contrary to the coatings, it is a cheap, long-lasting process; it is carried out once and it affects the whole piece. With this method, a conversion of the residual austenite into martensite in a conventionally heat-treated material, a formation of thin carbide precipitates and a uniform carbide distribution are obtained. In this way, serious improvements in the mechanical properties of the materials such as the hardness and wear resistance are achieved. Cryogenic treatment used to be applied to molding materials, but nowadays, due to its application to the cutting tools in the machining practice, significant developments have been made with respect to tool wear, tool life and cutting conditions. It was found that by applying cryogenic treatment to certain tool materials, improvements in the tool wear by 91 % to 817 % were achieved.⁹⁻¹²

In this study, during the turning of an Ti-6Al-4V alloy under dry cutting conditions with cryogenically treated and untreated, uncoated cemented carbide tips, the effects of different combinations of the cutting depth, cutting speed and feed rate on the cutting forces, surface roughness and tool wear were examined.

2 EXPERIMENTAL PROCEDURES

2.1 Materials

In the tests, the Ti6Al4V alloy having the AMS 4928 characteristics was used. The chemical constituents and the physical properties of the material are given in **Tables 1** and **2**, respectively.

Table 1: Chemical composition of Ti-6Al-4V (mass fractions, w/%)

Tabela 1: Kemijska sestava Ti-6Al-4V (masni deleži, w/%)

N	C	H	Fe	O	Al	V
0.08	2.00	0.75	0.045	0.03	16.0–18.0	10.0–14.0

Table 2: Mechanical properties of Ti-6Al-4V

Tabela 2: Mehanske lastnosti Ti-6Al-4V

Tensile strength	Yield strength	Hardness, Rockwell C	Elongation
900–1100 MPa	830 MPa	36	10 %

2.2 Machining tests

The tests were made using a JohnfordTC35 CNC turning center with no cooling liquid at four different cutting speeds (30, 45, 60, 75) m/min, three different feed rates (0.20, 0.25, 0.30) mm/r and a constant cutting depth (1 mm). The wear tests were realized for four different chip volumes (20, 40, 60 and 80) cm³, four different cutting speeds (30, 45, 60 and 75) m/min, a 0.25 mm/r feed rate and a 1 mm cutting depth. In the tests, the uncoated cemented carbide tips of the SANDVIK Coromant company were used. Half of these tips were cryogenically treated for the purpose of making a comparison. A graphic presentation of the steps of the cryogenic treatment is given in **Figure 1**.

The surface-roughness measurements on the machined surfaces of the samples were made with a Mahr Perthometer, type M1, surface-roughness-measurement device. The measurements were made parallel to the working-piece axis and on three different surfaces by rotating a workpiece 120° around its axis after each measurement. The average surface-roughness (R_a) values

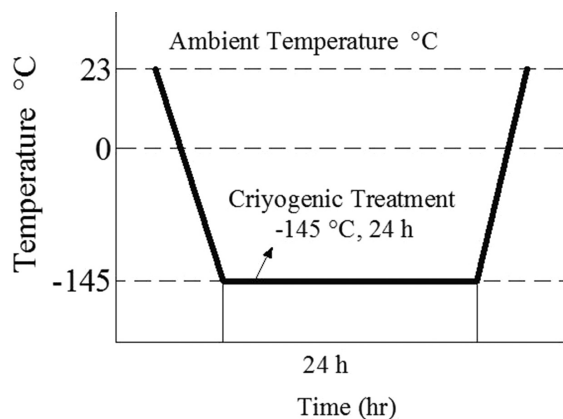


Figure 1: Schematic diagram of the cryogenic treatment

Slika 1: Shematski prikaz kriogenske obdelave

were determined by taking the arithmetical mean of the three values obtained at the end of the tests. The cutting force was measured with a Kistler 9257A three-component piezoelectric dynamometer and the associated 5019 B130 charge amplifiers connected to a PC employing the Kistler Dynaware force-measurement software.

The measurement of the tool flank wear obtained at the end of the turning operations was made with a scanning electron microscope (SEM).

3 RESULTS AND DISCUSSIONS

3.1 Flank wear

Tool wear is the result of the frictions and temperature taking place in the areas where the cutting-tool material and the workpiece material are in contact. Friction is the most important reason for the wear, whereas the temperature decreases the resistance to wear and, for this reason, it is the factor accelerating the wear.¹³ One of the most common types of the wear occurring in machining is flank wear. Flank wear occurs because of the contact between the side surfaces of a cutting tool and the workpiece. In **Figure 2**, the formation of the maximum flank wear at different cutting speeds for normal and cryogenically treated, cemented carbide tools is given. The flank wear increased with the increasing cutting speed (**Figure 2**) because the contact area of the cutting tool increased with an increase in the cutting speed and because the temperature was raised due to the increasing cutting speed leading to flank wear.¹⁴ The flank wear was lower for the cryogenically treated inserts compared to the normal tools. The reason for this was the fact that the cryogenically treated inserts had more uniform and more stable microstructures (**Figure 3**). The effects of more uniform structures on the wear behavior are also known.^{9,15–17} When the wear values of the cutting tools are considered it is seen that the wear of the cryogenically treated inserts is lower by 10–22 %.

The tool wears depending on different cutting speeds are given in **Figures 4** and **5**. From these figures it is

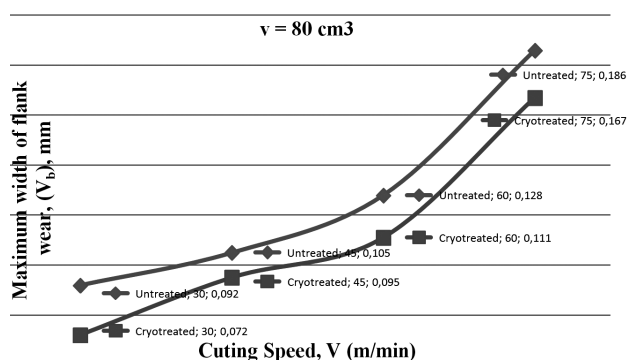


Figure 2: Maximum width of the flank wear at different cutting speeds

Slika 2: Največja širina obrabe boka pri različnih hitrostih rezanja

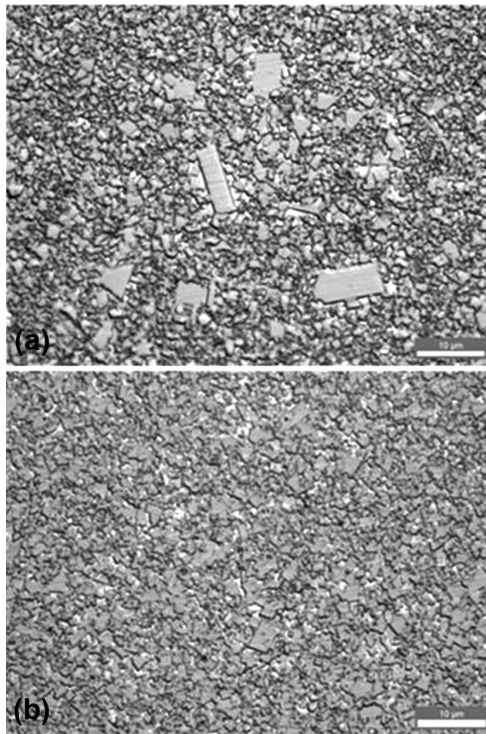


Figure 3: Microstructures of cutting inserts: a) untreated insert, b) cryogenically treated insert

Slika 3: Mikrostruktura vložka za rezanje: a) neobdelan vložek, b) kriogenko obdelan vložek

clear that the wear is higher for the untreated cutting tools compared to the cryogenically treated inserts. In Figures 4 and 5, it is observed that, at all the cutting speeds, the flank wear is lower when the chip volume is 20 cm³ and 40 cm³. However, depending on the increasing chip volume, there is a rapid increase in the flank wear. For both cutting tools (cryogenically treated and untreated) when the chip volume is 80 cm³ and the cutting speed is 75 m/min, the flank wear is maximum. The main reason for this is the fact that the high temperatures at the tool-chip interface depend on the increasing cutting speed and the chip volume.¹⁸

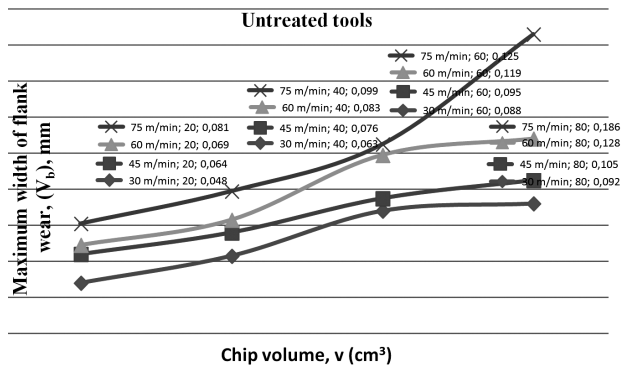


Figure 4: Maximum width of the flank wear at different chip volumes for the untreated insert

Slika 4: Največja širina obrabe bokov pri različnih volumnih ostružkov pri neobdelanem vložku

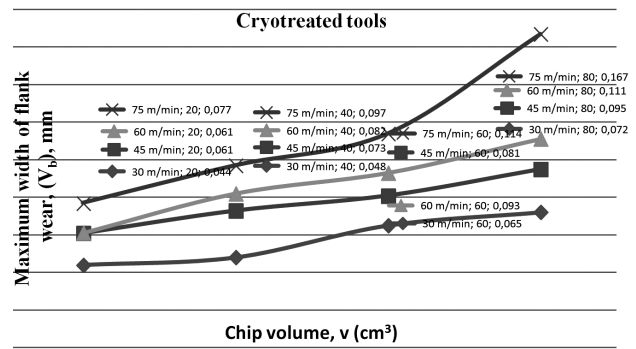


Figure 5: Maximum width of the flank wear at different chip volumes for the cryogenically treated insert

Slika 5: Največja širina obrabe bokov pri različnih volumnih ostružkov pri kriogenko obdelanem vložku

3.2 Cutting forces

In Figure 6 the changes in the main cutting forces of the cryogenically treated and untreated inserts are given. It is clear that a decrease in the main cutting force is due to the increasing cutting speed. It is understood that this tendency is the same for both tools, as the power used in the machining is usually converted into heat on the sliding plane, at the circumference of the cutting tip. Most of the heat created on the sliding plane is removed with the chip, but a certain portion is conducted to the workpiece. This conducted heat decreases the hardness of the workpiece. When the hardness decreases, the ductility increases making the chip removal easier. However, if this conduction of the heat continues to increase, the changes in the cutting forces can occur¹⁸⁻²⁰ due to a start of the BUE tendency. In the cryogenically treated inserts, the main cutting forces are lower compared to the untreated inserts. This situation can be explained with a low heat at the cryogenically treated insert tip and a lower flank wear. The best result with respect to the main cutting forces was 75 m/min for the cryogenically treated inserts.

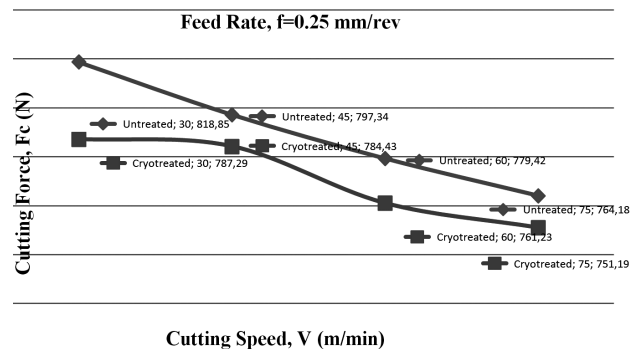


Figure 6: Main cutting force (F_c) at different cutting speeds

Slika 6: Sila rezanja (F_c) pri različnih hitrostih rezanja

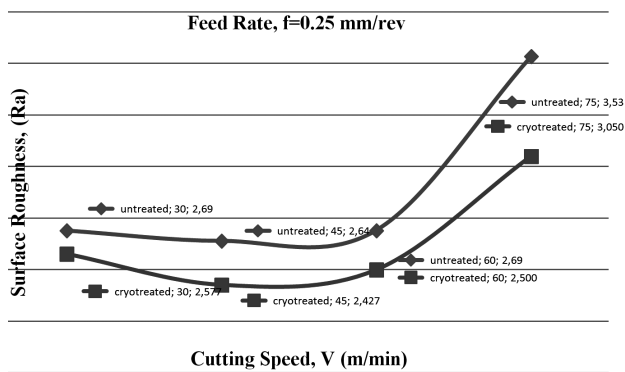


Figure 7: Surface roughness (R_a) at different cutting speeds
Slika 7: Hrapavost površine (R_a) pri različnih hitrostih rezanja

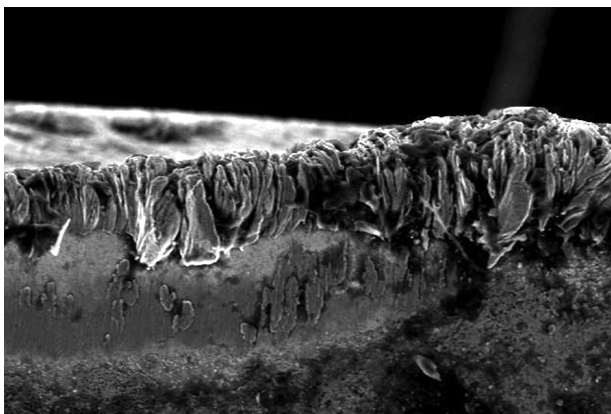


Figure 8: Wear image of cemented carbides
Slika 8: Posnetek obrabe karbidne trdine

3.3 Surface roughness

The surface quality and roughness obtained with each machining method changed. The correct selection of the surface roughness directly affects the product cost. Because of this, the surface roughness is one of the most important machining parameters. As it is seen from **Figure 7**, with the increasing cutting speed the surface-roughness values decrease at first, but when the cutting speed exceeds 60 m/min they are affected adversely, exhibiting a sudden increase. The improvement in the surface roughness with the increasing cutting speed, depending on the increasing temperature at higher speeds, can be explained with an easy deformation of the workpiece material at the cutting edge and the circumference of the tip radius, and the yielding formation at high temperatures.^{19,20} However, as it is observed from the wear graphics in **Figures 4** and **5** and from the SEM image of the cutting tool in **Figure 8**, the reason for the rapid increase in the surface roughness at the 60 m/min cutting speed is caused by the formation of the wear of the cutting tools.

4 CONCLUSION

Cryogenically treated inserts gave better results than the other tools with respect to tool wear.

The wear of the cryogenically treated inserts was lower than the wear of the other inserts by 10–22 %.

At all the cutting speeds, cryogenically treated inserts gave better results with respect to the main cutting forces.

When the cutting speed was 30 m/min and 45 m/min, the surface roughness decreased, but when it increased to higher levels the average surface roughness increased too.

Cryogenically treated inserts gave better results with respect to the main cutting forces and the average surface roughness.

The cryogenic treatment made the microstructure of the cutting tool more uniform and more stable.

Acknowledgements

The authors would like to acknowledge the Gazi University Scientific Research Project (07/2011-58) for the financial support throughout this study.

5 REFERENCES

- F. Nabhani, *Robotics and Computer Integrated Manufacturing*, 17 (2001), 99–106
- E. O. Ezugwu, Z. M. Wang, *Journal of Materials Processing Technology*, 68 (1997), 262–274
- H. A. Kishawy, J. Wilcox, *International Journal of Machine Tools & Manufacture*, 43 (2003), 433–439
- J. K. Schueller, J. Tlustý, S. Smith, E. Leigh, 56th Annual form, Virginia, VA 2000
- C. H. C. Haron, A. Jawaid, *Journal of Materials Processing Technology*, 166 (2005), 188–192
- A. Jawaid, C. H. C. Haron, A. Abdullah, *Journal of Materials Processing Technology*, 92 (1999), 329–334
- T. Kitagawa, A. Kubo, K. Maekawa, *Wear*, 202 (1997), 142–148
- M. V. Riberiro, M. R. V. Moreira, J. R. Ferreira, *Journal of Materials Processing Technology*, 143 (2003), 458–463
- J. Y. Huang, Y. T. Zhu, X. Z. Liao, I. J. Beyerlein, M. A. Bourke, T. E. Mitchell, *Mater. Sci. Eng.*, 339 (2003), 241–244
- D. N. Collins, *Heat Treat. Met.*, 23 (1996), 40–42
- A. Molinari, M. Pellizzari, S. Gialanella, G. Straffelini, K. H. J. Stiasny, *Mater. Process. Tech.*, 5 (2001), 118–130
- F. J. da Silva, D. D. Franco, A. R. Machado, E. O. Ezugwu, A. M. Souza Jr, *Wear*, 261 (2006), 674–685
- Y. Altıntaş, *Manufacturing Automation*, 1st ed., Cambridge University Press, 2000, 53–54
- D. A. Stephenson, J. S. Agapiou, *Metal cutting theory and practice*, Marcel Dekker, New York 1997
- S. Zhirafar, A. Rezaeian, M. J. Pugh, *Mater. Process. Tech.*, 186 (2003), 298–303
- V. Firouzidor, E. Nejati, F. Khomamizadeh, *Journal of Materials Processing Technology*, 206 (2008), 467–472
- I. Uygur, *Industrial Lubrication and Tribology*, 58 (2006) 6, 303–311
- L. N. Lacalle, P. J. de Lopez, J. I. Llorente, J. A. Sanchez, *Journal of Materials Processing Technology*, 100 (2000), 1–11
- I. Çiftçi, *Journal of the Faculty of Engineering and Architecture of Gazi University*, 20 (2005) 2, 205–209
- E. M. Trent, *Metal cutting*, Butterworths Press, London 1989

A COST-EFFECTIVE APPROACH TO THE RAPID FABRICATION OF FUNCTIONAL METAL PROTOTYPES

STROŠKOVNO UČINKOVIT NAČIN ZA HITRO IZDELAVO FUNKCIONALNIH KOVINSKIH PROTOTIPOV

Chil-Chyuan Kuo

Department of Mechanical Engineering, Ming Chi University of Technology, No. 84, Gungjuan Road, Taishan Dist. New Taipei City 24301, Taiwan
jacksonk@mail.mcut.edu.tw

Prejem rokopisa – received: 2013-09-26; sprejem za objavo – accepted for publication: 2013-10-10

A quick response to the market is considered as one of the important factors to ensure a company's competitiveness. New products must be swiftly and cost-effectively developed, manufactured and introduced to the market. This work demonstrates a technology for the rapid manufacturing of the metal prototypes for a laptop hinge using both rapid-prototyping and rapid-tooling techniques. A small-batch production for the laptop hinge of about 20 pieces can be obtained economically via a silicone rubber mold using vacuum casting, without applying any plastic injection molding. The fabricated metal prototypes have excellent physical and mechanical properties, which can be used for functional tests. A cost reduction of 75 % and a time saving of 82 % can be achieved. This technology has considerable economic benefits and prospects for broad market applications.

Keywords: laptop hinge, metal prototype, silicone rubber mold, epoxy resin, surface roughness

Hiter odziv na zahteve trga je eden od ključnih dejavnikov za konkurenčnost podjetja. Novi proizvodi morajo biti hitro in stroškovno učinkovito razviti, izdelani in predstavljeni trgu. To delo predstavlja tehnologijo hitre izdelave kovinskih prototipov tečaja ohišja prenosnega računalnika s tehniko hitre izdelave prototipa in hitre izdelave orodja. Majhna proizvodna serija, okrog 20 kosov tečaja za prenosni računalnik, se lahko izdelata s formo iz silikonske gume in z ulivanjem v vakuumu brez uporabe brizganja plastike. Izdelani prototipi iz kovine imajo odlične fizikalne in mehanske lastnosti ter so uporabni za funkcionalno preizkušanje. Doseže se lahko 75-odstotno zmanjšanje stroškov in 82-odstoten prihranek časa. Ta tehnologija ima velike ekonomske prihranke in možnosti široke uporabe na trgih.

Ključne besede: tečaj ohišja osebnega računalnika, kovinski prototip, forma iz silikonske gume, epoksi smola, hrapavost površine

1 INTRODUCTION

New market realities demand faster product development and a reduced time to market. They also require higher quality, cost reduction and greater efficiencies. To reduce the product development time and reduce the cost of manufacturing, rapid prototyping (RP)¹⁻³ has been developed, which offers the potential to completely revolutionize the process of manufacture. However, the features of the prototype do not usually meet the needs of the end product with the required material. Rapid-tooling (RT) technologies have been developed.⁴⁻⁷ RT is regarded as a natural extension of RP, since it is a technology that uses RP technologies and applies them to the manufacturing of tool inserts. Since the importance of RT goes far beyond component performance testing, RT is regarded as an important method for reducing the cost and time to market in the development of a new product. Several RT technologies are commonly available in industry now. For the purposes of classification, RT is divided into soft and hard tooling as well as indirect and direct tooling. Soft tooling is easier to work with than tooling steels, because these tools are created from materials such as epoxy-based composites with aluminum particles, silicone rubber or low-melting-point alloys. It

is well known that RT is capable of replacing conventional steel tooling, saving both costs and time in the manufacturing process. Indirect soft tooling is used more frequently in the development of new products, rather than direct tooling, because it is fast, simple and cost-effective.

It is a well-known fact that the silicone rubber mold is employed frequently because it has flexible and elastic characteristics, so that parts with a sophisticated geometry can be fabricated.⁸ In addition, epoxy tools are frequently employed for intermediate tooling, because this material has acceptable mechanical properties and a high-temperature resistance.⁹ Although some technologies, such as selective laser melting,¹⁰ direct shell production casting,¹¹ direct metal laser sintering,¹² laser-engineered net shaping,¹³ shape-deposition manufacturing,¹⁴ metal injection molding¹⁵ and high-speed machining¹⁶ can be used to produce metal prototypes, the cost of the hardware is expensive. Thus, developing a low-cost method to manufacture a metal prototype is required. In this work, a cost-effective method for fabricating a functional metal prototype using RP and RT technologies is demonstrated to address this important issue. The surface roughnesses of the metal prototypes were measured using a white-light interferometry (WLI) technique. The

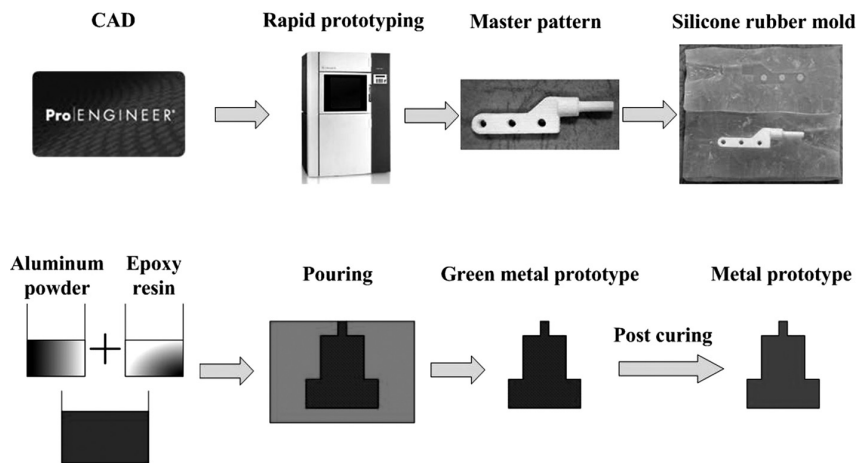


Figure 1: Schematic illustration of the process flow for this work
Slika 1: Shematski prikaz poteka postopka

properties of the fabricated metal prototypes were also discussed, as well as the advantages of this method.

2 EXPERIMENT

Figure 1 shows a schematic illustration of the process flow for this work. The master pattern model for this work is a laptop hinge, which was designed using Pro/ENGINEER software. The master pattern model was fabricated using an RP system (Z Printer 310; Z Corporation, Inc.). A silicone rubber mold was fabricated from the master pattern model. **Figure 2** shows a schematic illustration of the fabrication process for a silicone rubber mold in detail. The base compound (KE-1310ST; ShinEtsu, Inc.) and the hardener (CAT-1310S; ShinEtsu, Inc) were mixed thoroughly to fabricate the silicone rubber mold. The amounts of base compound and hardener were calculated by multiplying the desired volume of the silicon rubber mold to be made by the density of silicone rubber (1.07 g/cm³ at 23 °C). In general, the curing agent and the silicone rubber in a mass ratio of 10 : 1 were mixed thoroughly with a stirrer. The properties of the silicone rubber mold, such as durability and mold life, are significantly affected by the relative amounts of curing agent and silicone rubber, because it will affect the cross-linking of the silicone rubber.^{17,18} Thus, calculating the weight of the base and the curing agent precisely is crucial before mixing. To reduce the level of human error, a user-friendly, man-machine interface was developed using the Visual Basic program. A vacuum machine was used for generating a vacuum atmosphere, which provides the function of the degassing process to remove the air bubbles derived from the mixing process of the silicone rubber and the hardener. Depending on the extent of the air bubbles in the mixture, the degassing process can range from 25 min to 60 min. After this degassing process, the pressure inside the vacuum machine was changed by breaking the vacuum atmosphere. Thus, a silicone rubber mold can be fabricated without

the defects caused by the air bubbles derived from the mixing process.

It is a well-known fact that epoxy-resin composite materials are frequently used for making rapid tooling. Epoxy resin (C1; Devcon, Inc.) was used to fabricate metal prototypes of the laptop hinge. The epoxy resin used is usually aluminum filled to enhance the mechanical or physical properties. The amount of epoxy resin required was calculated by the size of the master pattern. The hardener and base compound (70 % aluminum powder and 30 % liquid epoxy resin) in a weight ratio of 1 : 112 were mixed thoroughly with a stirrer. The mixing process of aluminum powder and epoxy resin is very important because a uniform distribution of the aluminum particles in the epoxy resin has a great effect on the mechanical property of the RT. Depending on the extent of the air bubbles in the mixture, the degas process can range from 30 min to 80 min. A stepwise post-curing cycle for the fabricated metal prototypes was performed in a convection oven (DH400; Deng Yag, Inc.) to ensure the completion of the curing reaction of the composite materials. **Figure 3** shows the temperature profiles used

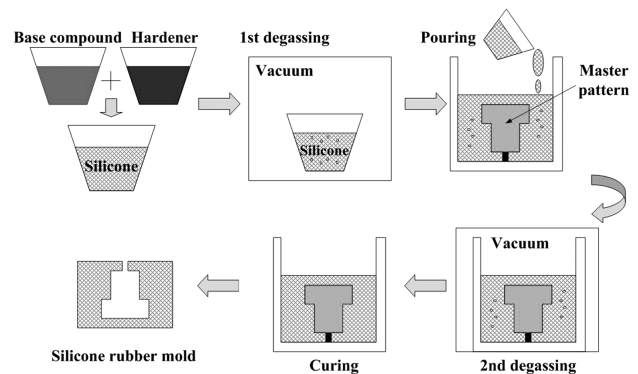


Figure 2: Schematic illustration of the fabrication process for a silicone rubber mold using vacuum casting

Slika 2: Shematski prikaz postopka izdelave forme iz silikonske gume z ulivanjem v vakuumu

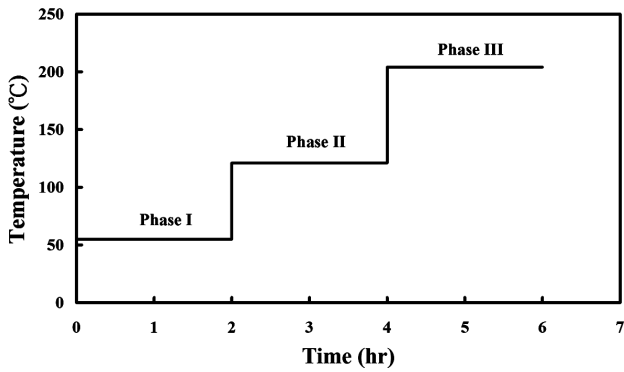


Figure 3: Temperature profiles used for post-curing the metal prototype of a laptop hinge

Slika 3: Temperaturni profil, uporabljen za utrjevanje po strjevanju kovinskega prototipa ležaja ohišja prenosnega računalnika

for post-curing the metal prototype of the laptop hinge. This temperature profile consists of three phases. In the first phase the green part is heated to 55 °C and remains at a constant temperature for 2 h to reach a suitable temperature for the cross-linking of epoxy resins. In the second phase the temperature was increased from 55 °C to 121 °C, and then remains at a constant temperature for 2 h to enhance the mechanical properties of the metal prototypes. In the third phase the temperature was increased from 121 °C to 204 °C and remains constant for 2 h to cure the metal prototypes fully. The surface roughnesses of the metal prototypes were measured using a WLI (vertical resolution 0.1 nm, horizontal resolution 0.5 μm, Chroma 7502). The sampling area was chosen to be 50 μm × 50 μm. The arithmetic average roughness value (R_a) was used to quantify the surface finish. The R_a values represent the average displacement of the peaks and valleys measured with respect to a mean line.

3 RESULTS AND DISCUSSION

Figure 4 shows the master-pattern models of the male and female parts of the laptop hinge. The fabricated

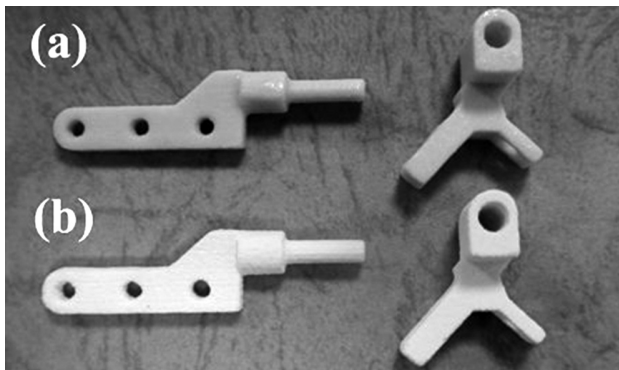


Figure 4: Master-pattern models of: a) male and b) female parts of a laptop hinge

Slika 4: Modeli: a) moškega in b) ženskega dela tečaja za ohišje prenosnega računalnika

master pattern models required further processing, because of their relatively poor surface roughness, which results from the layered structure inherent in the building method.¹⁹ In this work, hand finishing was used to improve the stair-step surface texture inherently in the fabricated master-pattern models.²⁰ **Figure 5** shows the silicone rubber molds for the male and female parts of the laptop hinge. The cured silicone rubber block was cut along the parting line and the master pattern was removed. It is clear that the surfaces of the silicone rubber molds have the desired surface finish. In addition, the silicone rubber mold enables the master-pattern models to release without breakage or damage.^{21,22}

To evaluate the validity of the fabricated silicone rubber mold, some wax patterns were replicated from the elastomeric mold. **Figure 6** shows that the wax patterns of the laptop hinge were replicated from the silicone rubber mold because of the low interfacial free energy and the chemically inert surface.²³ It is clear that the laptop hinges made of wax were successfully transferred from the silicone rubber mold by vacuum casting. The detailed appearance of the laptop hinges was faithfully replicated. This means that the silicone rubber mold fabricated can be used to replicate metal prototypes of the designed laptop hinges. The use of epoxy resin is often the fastest way to complete short runs of functional prototypes manufactured by vacuum casting. **Figure 7** shows the green part of a male laptop hinge fabricated

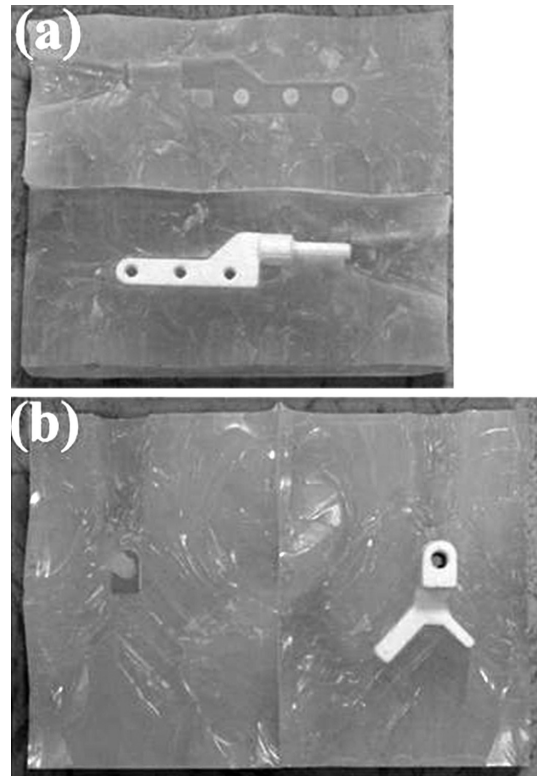


Figure 5: Silicone rubber molds for: a) male part and b) female part of a laptop hinge

Slika 5: Forma iz silikonske gume za: a) moški del in b) ženski del tečaja za ohišje prenosnega računalnika

using a silicone rubber mold. It can be observed that the metal prototype of the male laptop hinge was fabricated faithfully. The life of a silicone rubber mold depends to a large extent on the surface finish of the fabricated laptop hinges. In general, a silicone rubber mold will reproduce up to 20–30 parts with a gradual deterioration of the surface quality under normal operating conditions. After the post-curing process, metal prototypes of the laptop hinge were shown in **Figure 8**. Thus, a small-batch production of the metal prototype can be obtained economically via a silicone rubber mold using vacuum casting without applying any plastic injection molding. According to the specification provided by the epoxy-resin composite supplier, the fabricated metal prototypes have excellent physical and mechanical properties (tensile strength ASTM D 638, compressive strength ASTM D 695, and cured hardness ASTM D 2240). A tensile strength of 35439 kPa (5140 psi) can be achieved, which can be used for a functional test. **Figure 9** shows the WLI image of a metal prototype. The average roughness of the metal prototype is approximately 114 nm. This



Figure 6: Wax patterns of the laptop hinge were replicated from the silicone rubber mold

Slika 6: Voščeni modeli tečaja za ohišje prenosnega računalnika, izdelani z uporabo forme iz silikonske gume

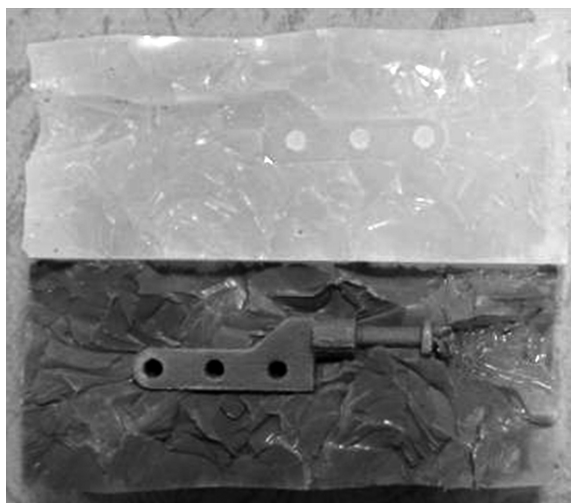


Figure 7: Green part of a male laptop hinge fabricated using a silicone rubber mold

Slika 7: Surovec moškega dela tečaja za ohišje prenosnega računalnika, izdelan v formi iz silikonske gume

result shows that the fabricated metal prototype has the desired surface finish. As described above, this method is a viable alternative for the fabrication of metal prototypes.²⁴ **Table 1** shows the time needed to manufacture metal prototypes of a laptop hinge. **Table 2** shows the cost needed to manufacture metal prototypes of a laptop hinge. The estimated cost and time for manufacturing the metal prototype of a laptop hinge was NT\$ 683 and 19.5 h, which represents a cost reduction of 75 % and a time saving of 82 % compared to the traditional manufacturing method (NT\$ 2730 and 108 h)²⁵ using a metal injection molding process.^{26–28} This method provides a

Table 1: The time needed to manufacture the metal prototype of a laptop hinge

Tabela 1: Čas izdelave kovinskega prototipa tečaja za ohišje prenosnega računalnika

Manufacturing process	Rapid prototyping of a laptop hinge	Silicone rubber mold	Metal prototype of a laptop hinge
Time (h)	0.5	8	11

Table 2: The cost needed to manufacture the metal prototype of a laptop hinge

Tabela 2: Stroški izdelave kovinskega prototipa tečaja za ohišje prenosnega računalnika

Manufacturing process	Rapid prototyping of a laptop hinge	Silicone rubber mold	Metal prototype of a laptop hinge
NT\$	141	444	98



Figure 8: Metal prototypes of the laptop hinge after the post-curing process

Slika 8: Kovinski prototipi tečaja za ohišje prenosnega računalnika po postoku utrjevanja

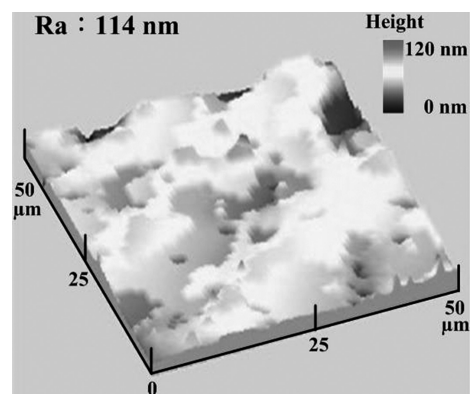


Figure 9: WLI image of a metal prototype

Slika 9: WLI-posnetek kovinskega prototipa

low-cost method to fabricate the functional metal prototype with the desired mechanical properties for the functional test. A major contribution of this work is that this method is a simple and cost-effective method for fabricating metal prototypes of a laptop hinge with high yield.

4 CONCLUSIONS

Manufacturing industry is currently under increasing pressure due to international competition. New products must be developed more quickly and cheaply, and then manufactured and introduced to the market. A procedure for fabricating metal prototypes with the desired surface finish and accuracy has been demonstrated in this work. The research results reported in this study have industrial application values because this is a simple and effective method in terms of cost and time reductions. This process has considerable economic benefits, which can be employed to fabricate metal prototypes for a functional test in the first development phase of a new product. In addition, this process has the potential to be extended to other fields of applications with the development of casting materials, such as ceramics, low-melting-point alloys, or some functional polymers.

Acknowledgement

The authors gratefully acknowledge the financial support of the National Science Council of Taiwan under contracts nos. NSC 102-2221-E-131-012 and NSC 101-2221-E-131-007. The skillful technical assistance of Mr. Zhen-Jia Xu of Ming Chi University of Technology is highly appreciated.

5 REFERENCES

- ¹ B. Valentan, D. Pogacar, T. Brajljeh, T. Z. Hartner, A. Pilipovic, I. Drstvenek, Development of a 3D Printer For Thermoplastic Modeling, *Mater. Tehnol.*, 46 (2012) 6, 589–594
- ² B. Leukers, H. Gülkan, S. H. Irsen, S. Milz, C. Tille, H. Seitz, M. Schieker, Biocompatibility of ceramic scaffolds for bone replacement made by 3D printing, *Materialwissenschaft und Werkstofftechnik*, 36 (2005) 12, 781–787
- ³ C. C. Kuo, Y. C. Tsou, B. C. Chen, Enhancing the efficiency of removing support material from rapid prototype part, *Materialwissenschaft und Werkstofftechnik*, 43 (2012) 3, 234–240
- ⁴ A. Schulz, E. Matthaei-Schulz, S. Spangel, H. Vettters, P. Mayr, Analysis of spray formed tool steels, *Materialwissenschaft und Werkstofftechnik*, 34 (2003) 5, 478–483
- ⁵ H. Meier, Ch. Haberland, Experimental studies on selective laser melting of metallic parts, *Materialwissenschaft und Werkstofftechnik*, 39 (2008) 9, 665–670
- ⁶ G. Ramdeen Link, J. Fessler, A. Nickel, F. Prinz, Rapid Tooling Die Cast Inserts Using Shape Deposition Manufacturing, *Materials and Manufacturing Processes*, 13 (1998) 2, 263–274
- ⁷ C. C. Kuo, M. Y. Lai, Development of an automatic vacuum degassing system and parameters optimization for degassing process, *Indian Journal of Engineering and Materials Sciences*, 18 (2011) 6, 405–410
- ⁸ C. C. Kuo, Z. Y. Lin, Development of bridge tooling for fabricating mold inserts of aspheric optical lens, *Materialwissenschaft und Werkstofftechnik*, 42 (2011) 11, 1019–1024
- ⁹ C. C. Kuo, A simple and cost-effective method for fabricating epoxy-based composites mold inserts, *Materials and Manufacturing Processes*, 27 (2012) 4, 383–388
- ¹⁰ H. Meier, Ch. Haberland, Experimental studies on selective laser melting of metallic parts, *Materialwissenschaft und Werkstofftechnik*, 39 (2008) 9, 665–670
- ¹¹ A. Rosochowski, A. Matuszak, Rapid tooling: the state of the art, *Journal of Materials Processing Technology*, 106 (2000), 191–198
- ¹² M. V. Kuznetsov, I. V. Shishkovsky, Yu. G. Morozov, I. P. Parkin, Design of Three-Dimensional Functional Articles via Layer-by-Layer Laser Sintering of Exothermic Powder Mixtures, *Materials and Manufacturing Processes*, 23 (2008) 6, 571–578
- ¹³ B. Sustarsic, S. Dolinsek, M. Jenko, V. Leskovsek, Microstructure and Mechanical Characteristics of DMLS Tool-Inserts, *Materials and Manufacturing Processes*, 24 (2009) 7–8, 837–841
- ¹⁴ G. R. Link, J. Fessler, A. Nickel, F. Prinz, Rapid Tooling Die Cast Inserts Using Shape Deposition Manufacturing, *Materials and Manufacturing Processes*, 13 (1998) 2, 263–274
- ¹⁵ D. Chong, Metal Injection Molding of PH 13-8 Mo Stainless Steel, *Materials and Manufacturing Processes*, 10 (1995) 3, 415–423
- ¹⁶ R. Blümke, C. Muller, Microstructure of Dominating Parameter for Chip Forming During High Speed Milling, *Materialwissenschaft und Werkstofftechnik*, 33 (2002), 194–199
- ¹⁷ K. R. Marcroft, R. L. Tencate, E. W. Skinner, The effects of heat, aging, and mold separation on the dimensional stability of silicone rubber, *The Journal of Prosthetic Dentistry*, 14 (1964) 6, 1091–1098
- ¹⁸ C. C. Kuo, Y. R. Chen, Rapid optical inspection of bubbles in the silicone rubber, *Optik – International Journal for Light and Electron Optics*, 124 (2013) 13, 1480–1485
- ¹⁹ D. Ahn, J. H. Kweon, J. Choi, S. Lee, Quantification of surface roughness of parts processed by laminated object manufacturing, *Journal of Material Processing Technology*, 212 (2012) 2, 339–346
- ²⁰ P. M. Pandey, N. V. Reddy, S. G. Dhande, Improvement of surface finish by staircase machining in fused deposition modeling, *Journal of Material Processing Technology*, 132 (2003) 1–3, 323–331
- ²¹ C. C. Kuo, Z. S. Shi, Fabrication of a high precision silicone rubber mold for replicating wax patterns of cylinder heads, *Indian Journal of Engineering and Materials Sciences (IJEMS)*, 19 (2012) 3, 157–162
- ²² C. C. Kuo, Z. Y. Lin, Rapid manufacturing of plastic aspheric optical lens, *Materialwissenschaft und Werkstofftechnik*, 43 (2012) 6, 495–502
- ²³ S. Chung, Y. Im, H. Kim, H. Jeong, D. A. Dornfeld, Evaluation of micro-replication technology using silicone rubber molds and its applications, *International Journal of Machine Tools and Manufacture*, 43 (2003), 1337–1345
- ²⁴ Z. L. Lu, J. H. Liu, Y. S. Shi, D. C. Li, Investigation into the densification of AISI304 parts fabricated by hybrid powder metallurgy techniques, *Indian Journal of Engineering and Materials Sciences*, 17 (2010) 1, 49–55
- ²⁵ <http://www.uneec.com>.
- ²⁶ B. Berginc, M. Brezocnik, Z. Kampus, B. Sustarsic, A numerical simulation of metal injection molding, *Mater. Tehnol.*, 43 (2009) 1, 43–48
- ²⁷ S. Butkovic, M. Oruc, E. Saric, M. Mehmedovic, Effect of sintering parameters on the density, microstructure and mechanical properties of the niobium-modified heat-resistant stainless steel 6x40CrNiSi25-20 produced by MIM technology, *Mater. Tehnol.*, 46 (2012) 2, 185–190
- ²⁸ B. Berginc, Z. Kampus, B. Sustarsic, The influence of MIM and sintering-process parameters on the mechanical properties of 316L SS, *Mater. Tehnol.*, 40 (2006) 5, 193–198

THERMOMECHANICAL TREATMENT OF Ti-Nb-V-B MICRO-ALLOYED STEEL FORGINGS

TERMOMEHANSKA OBDELAVA ODKOVKOV IZ MIKROLEGIRANEGA JEKLA Ti-Nb-V-B

Marek Opiela

Silesian University of Technology, Institute of Engineering Materials and Biomaterials, 18a Konarskiego Street, 44-100 Gliwice, Poland
marek.opiela@polsl.pl

Prejem rokopisa – received: 2013-09-30; sprejem za objavo – accepted for publication: 2013-10-09

The work presents the research results of the influence of thermomechanical treatment through forging on the microstructure and mechanical properties of newly elaborated micro-alloyed steel containing 0.28 % C, 1.41 % Mn, 0.028 % Ti, 0.027 % Nb and 0.019 % V. The applied thermomechanical treatment makes it possible to obtain a fine-grained microstructure of austenite during the hot working and the production of forged parts that acquire an advantageous set of mechanical properties and a guaranteed crack resistance after controlled cooling from the finishing plastic-deformation temperature and the successive tempering. The forgings produced with the method of thermomechanical treatment, consecutively subjected to tempering in the temperature range from 550 °C to 650 °C, have $YS_{0.2}$ from 994 MPa to 939 MPa, UTS from 1084 MPa to 993 MPa and KV^{40} from 77 J to 83 J.

Keywords: micro-alloyed steels, thermomechanical treatment, forged parts, mechanical properties

Delo predstavlja rezultate vpliva termomehanske obdelave s kovanjem na mikrostrukturo in mehanske lastnosti novo izdelanega mikrolegiranega jekla z 0,28 % C, 1,41 % Mn, 0,028 % Ti, 0,027 % Nb in 0,019 % V. Uporabljena termomehanska obdelava omogoča doseganje drobnostne mikrostrukture avstenita med vročo predelavo in izdelavo odkovkov, ki dobijo dobre mehanske lastnosti in zagotovljeno odpornost proti razpokam po kontroliranem ohlajanju iz končne temperature plastične deformacije in po popuščanju. Odkovki, izdelani po metodi termomehanske obdelave in nato popuščani v temperaturnem območju od 550 °C do 650 °C, imajo $YS_{0.2}$ od 994 MPa do 939 MPa, UTS od 1084 MPa do 993 MPa in KV^{40} od 77 J do 83 J.

Ključne besede: mikrolegirana jekla, termomehanska obdelava, odkovki, mehanske lastnosti

1 INTRODUCTION

A lowering of the production cost is the basic reason for implementing economical technologies for the products made of constructional alloy steels with the methods of thermomechanical treatment. These methods consist of plastic working in the conditions adjusted to the steel chemical composition and micro-alloying with the consecutive direct cooling of the parts from the temperature of the plastic-deformation finish or after a particular time specified. This allows a reduction of the expensive heat treatment of products involving the tempering.¹⁻⁴

The HSLA-type (high-strength low-alloy) micro-alloyed steels – containing up to 0.3 % C and 2 % Mn, micro-additions with a high chemical affinity to N and C, i.e., Nb, Ti and V in the amount of about 0.1 %, and sometimes also a slightly increased concentration of N and up to 0.005 % of B, increasing hardenability – are particularly useful for the production of forged parts with a fine-grained microstructure using the method of thermo-mechanical processing. The interaction of micro-additions in solid steel depends on their state influenced by the conditions of the performed plastic working. Micro-additions in the solid solution raise the temperature of the recrystallization of plastically deformed austenite. Moreover, the segregation of micro-additions at the grain boundaries decreases their mobility. Instead,

the micro-additions precipitating on dislocations in the form of dispersive particles of MX interstitial phases, slow down the course of dynamic recovery and possibly also dynamic recrystallization during the plastic deformation and additionally decrease the rate of thermal recovery and static or metadynamic recrystallization, limiting the grain growth of the recrystallized austenite in the intervals between the successive stages of deformation and after its completion. Dispersive particles of MX-type phases hamper the grain-boundary movement of the recrystallized austenite and, hence, it is possible to produce fine-grained-microstructure products additionally strengthened by carbonitrides.⁵⁻¹¹ The contribution of micro-additions to the precipitation strengthening can be calculated using the Ashby-Orowan relationship:

$$\sigma_p = \frac{0.538Gb_f^{1/2}}{\kappa} \ln\left(\frac{\kappa}{2b}\right) \quad (1)$$

where G is the shear modulus, b is the Burgers vector, f is the particle-volume fraction and κ is the mean diameter of particles.

When engineering the calculations, there is also another way of assessing the effect of the strengthening from the micro-alloyed particles:¹²

$$\sigma_p = K_p[M] \quad (2)$$

where $[M]$ is the micro-addition content in the mass fraction and K_p is the constant.

Niobium is often used as a micro-addition in the steels subjected to various processes of thermomechanical treatment. Very dispersive Nb(C,N) precipitates have a very important role in this case. Therefore, the value of σ_p is often calculated with the assumption that the precipitation-strengthening effect depends mainly on this element. It should be noted that the effectiveness of Nb in the precipitation hardening is reduced by a Ti micro-addition forming both its carbides and nitrides as well as complex precipitates of (Ti,Nb)C and (Ti,Nb)(C,N).¹³

The state of niobium (in a solution or as a precipitate), determined by the reheating temperature, can affect the recrystallization, the grain growth and the $\gamma \rightarrow \alpha$ transformation of austenite.^{14,15} For example, the recrystallization and grain growth of austenite are significantly suppressed by the precipitation of NbC prior to the $\gamma \rightarrow \alpha$ transformation. In addition, coarse NbC particles can be the preferred sites for the ferrite nucleation. In particular, the control of the austenite recovery and recrystallization is an important part of the grain-refinement technique in the modern thermo-mechanical controlling process.¹⁶ An addition of Nb to steel is considered to have three primary effects:^{17,18} (i) being an inhibitor of the austenite grain coarsening during reheating, (ii) suppressing the austenite recrystallization prior to the $\gamma \rightarrow \alpha$ transformation through the strain-induced precipitation of NbC and (iii) causing the precipitation hardening from NbC in the low-temperature transformation step of the thermo-mechanical process. The strongest contribution to the strengthening is the refinement of the final microstructure (essentially ferrite grain size), which accounts for 80–90 % of σ_y . The key role of the precipitates is to provide the dispersion strengthening that is often generated in micro-alloyed steels by the NbC, VC, Nb(C,N) or V(C,N) particles, depending on whether N is added or not, with less than 20 nm in size.¹⁹ Special attention also has to be paid to the vanadium micro-alloying addition. This element is easily added to liquid steel and its solubility during reheating is very high. The strengthening effect is enhanced as nitrogen is also added to the solution.

The final microstructure and mechanical properties strongly depend on the chemical composition, the controlled hot-working parameters and the cooling conditions of the steel. High strength, good ductility and good formability are developed in steel products during the manufacturing processes and, to achieve these goals, properly balanced quantities of micro-alloying additions and suitable thermomechanical processing schedules have to be carefully applied.^{20,21}

2 EXPERIMENTAL PROCEDURE

The study was performed on newly elaborated micro-alloyed steel, intended for the production of forged

machine parts with a high strength, using thermomechanical treatment. The investigated steel contains 0.28 % C, 1.41 % Mn, 0.29 % Si, 0.008 % P, 0.004 % S, 0.26 % Cr, 0.11 % Ni, 0.22 % Mo, 0.025 % Al and Nb, Ti, V and B in the amounts of (0.027, 0.028, 0.019 and 0.003) %, respectively.

The investigated steel with the weight of 100 kg, molten in a VSG-100 type laboratory vacuum induction furnace and cast in an atmosphere of argon into quadratic hot-topped ingots with the following dimensions: top – 160 per bottom – 140 mm × 640 mm. The ingots were forged into 32 mm × 160 mm flat bars, with open-die forging in a high-speed hydraulic press, using a force of 300 MN.

The conditions of the hot processing and cooling, leading to the desired mechanical properties of the forgings, were selected with the following procedures:²²

- analyses of the kinetics of the MX-type interstitial-phase precipitation in the solid state;
- an investigation of the process of hot working of steel with the method of continuous compression of the specimens at the rate of (1, 10 and 50) s⁻¹ in a temperature range from 1100 °C to 900 °C;
- an examination of the kinetics of strain hardening (recrystallization) and softening of plastically deformed austenite in the mentioned conditions,
- an investigation of the kinetics of the phase transformations of undercooled austenite.

The obtained results were used to develop two variants of forging with thermomechanical treatment of 160 mm × 32 mm flat bars into 14 mm thick flat bars, in the temperature range of 1100 °C to 900 °C at the strain rate of 3 s⁻¹, applying 50 % of draft. The soaking temperature for forging was 1150 °C and the time was 45 min. In the first variant, segments of flat bars were hardened in water directly from the temperature of the forging finish, while, in the second variant, flat bars were isothermally held at the temperature of 900 °C for (10, 60 and 100) s after the forging finish and prior to hardening in water. Directly after quenching, the obtained flat-bar sections were tempered for 1 h at the temperatures of 550 °C and 650 °C.

For the metallographic investigations of the specimens hardened after plastic deformation in the mentioned conditions and after high-temperature tempering, a Leica MEF 4A light microscope was used. The thin foils were examined with a TITAN80-300 FEI ultra-high resolution transmission electron microscope at the accelerating voltage of 300 kV.

Static tensile tests were performed with an INSTRON 1115 universal testing machine on the samples with a diameter of 8 mm and a gauge length of 40 mm. The impact testing at room temperature and at –40 °C was carried out on a Charpy pendulum machine with the initial energy of 300 J, using V-notch specimens with a cross-section of 8 mm × 10 mm. Brinell hardness was also determined for all the specimens.

3 RESULTS

Metallographic examinations of the samples of Variant I of thermomechanical treatment, i.e., the ones quenched in water immediately after plastic deformation, revealed the microstructure of fine-lath martensite (**Figure 1**). The segments produced according to Variant I of thermomechanical treatment, subjected successively to tempering at the temperature of 650 °C, have the microstructure of the tempered martensite with the precipitates of carbide particles (**Figure 2**).

The analyses of the microstructure of thin foils revealed that the microstructure of steel, hardened directly from the forging temperature, consists of lath martensite and an uneven distribution of dislocation density in strongly plastically deformed austenite. Fine (Ti,Nb)C particles, located mainly at the boundaries of martensite laths (**Figure 3**) were observed in the martensite with a diversified spatial orientation of individual laths. Particles of similar chemical composition, morphology and size were also identified in the C-Mn-0.16Nb

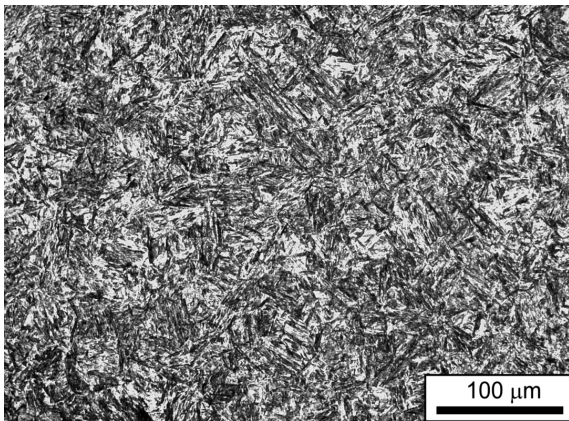


Figure 1: Martensitic microstructure; Variant I of thermomechanical treatment: 900 °C, water

Slika 1: Martenzitna mikrostruktura; Varianta I termomehanske obdelave: 900 °C, voda

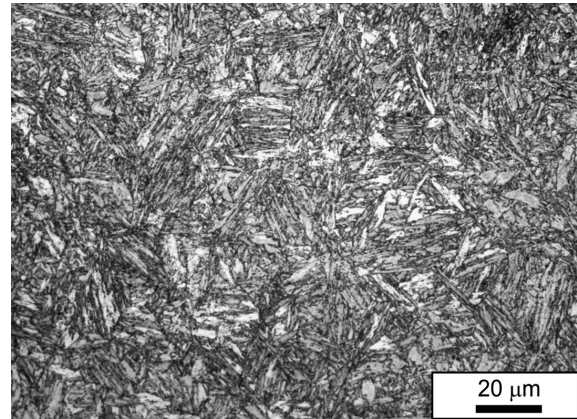


Figure 2: High-tempered martensite; Variant I of thermomechanical treatment: 900 °C, water; tempering temperature: 650 °C

Slika 2: Visoko popuščeni martenziti; Varianta I termomehanske obdelave: 900 °C, voda; temperatura popuščanja: 650 °C

steel.²³ Austenite in the form of thin films between the laths of martensite was observed. The Kurdjumov-Sachs crystallographic relationship between the retained austenite and martensite was confirmed.

A similar morphology of lath martensite was found for the steel coming from the flat bar section obtained with Variant II of thermomechanical forging. Laths of different widths occur in the martensite packets. Some of the martensite laths show a fragmentation caused by high-angle subgrain boundaries formed into the statically recovered austenite that hampers their growth. As in the previous case, the (Ti,Nb)C and (Ti,Nb,V)C (**Figure 4**) particles with the size from 40 nm to 80 nm were found in the martensite.

The forgings produced in both variants of thermomechanical processing and the forgings quenched conventionally from the temperature of 900 °C have quite different microstructures after the tempering in the temperature range from 550 °C to 650 °C. The microstructure of the specimens taken from flat bar sections,

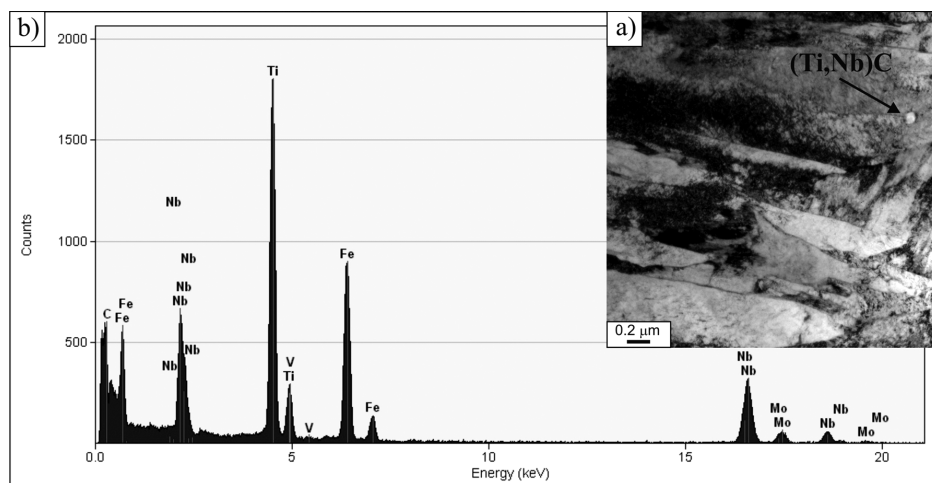


Figure 3: a) Carbide (Ti,Nb)C in the martensite, b) EDS spectrum; Variant I of thermomechanical treatment: 900 °C, water

Slika 3: a) Karbid (Ti,Nb)C v martenzitu, b) EDS-spekter; Varianta I termomehanske obdelave: 900 °C, voda

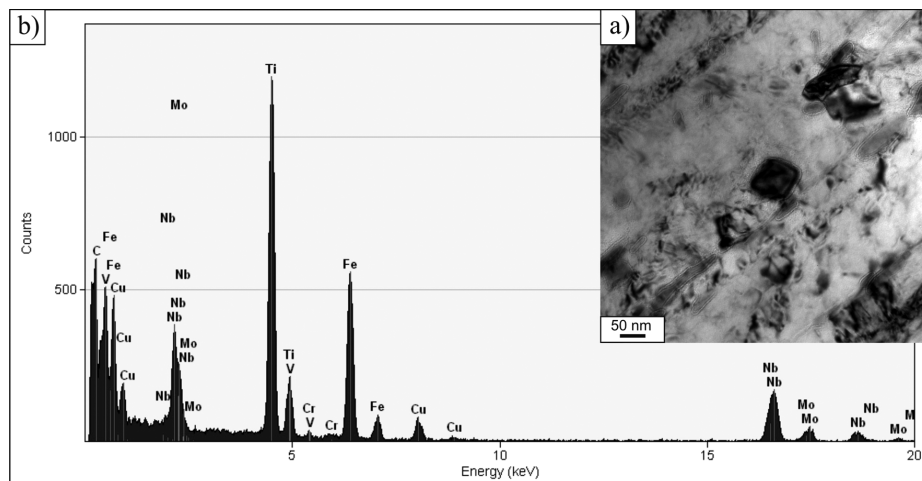


Figure 4: a) Carbide (Ti,Nb,V)C in the martensite, b) EDS spectrum; Variant II of thermomechanical treatment: 900 °C, 60 s, water
Slika 4: a) Karbid (Ti,Nb,V)C v martenzitu, b) EDS-spekter; Varianta II termomehanske obdelave: 900 °C, 60 s, voda

Table 1: Results for the mechanical properties and impact-fracture energy of Charpy-V samples after thermomechanical forging and successive tempering

Tabela 1: Mehanske lastnosti in udarna žilavost Charpy-V vzorcev po termomehanskem kovanju in toplotni obdelavi

Variant	Treatment conditions			Tempering temperature °C	Mechanical properties				Impact energy	
	Charge heating/finish forging temperature, °C	Isothermal holding time, s	Cooling medium		$YS_{0.2}$ MPa	UTS MPa	TEI %	RA %	KV J	KV^{-40} J
I	1150/900	–	water	550	973	1057	13.5	51.5	69.3	55.0
		–	water	650	909	976	14.0	52.0	81.7	68.6
II	1150/900	10	water	550	967	1063	13.6	49.6	91.6	71.3
		10	water	650	892	958	14.5	52.7	99.0	79.7
		60	water	550	994	1084	14.3	50.9	95.0	77.3
		60	water	650	911	974	15.1	50.2	108.7	82.6
		100	water	550	988	1077	13.0	49.6	95.7	75.7
		100	water	650	939	993	14.8	51.3	101.3	80.0

quenched directly after forging, after the tempering at the temperature of 550 °C, consists of the tempered martensite with a precipitation of granular and lamellar Fe_3C particles, distributed inside the grains and at the lath boundaries. The lamellar and granular precipitates, formed in such conditions, fulfill the matrix spatial dependences established by Bagariacki. An increase in the tempering temperature leads to a coagulation of cementite. The M_3C lamellar precipitates retain the privileged spatial orientation with ferrite, while the coagulated granular particles of this phase reveal random crystallographic orientation with respect to the matrix.

The samples obtained with the Variant-II forging of thermomechanical treatment have a similar microstructure in the tempered state. In this case, in the microstructure of the steel tempered at 550 °C there are thin lamellar precipitations of Fe_3C at the lath boundaries, while inside the laths of the recovered ferrite, dispersive lamellar particles of the phase with the privileged spatial orientation with the matrix are observed. Lamellar precipitates transform into granular Fe_3C particles at the lath boundaries and subgrain boundaries of the recovered

ferrite with an increase in the tempering temperature. Moreover, the precipitates of (Ti,Nb)C with a morphology similar to that after thermomechanical processing were found after tempering.

The steel microstructure in both hardened and tempered state significantly affects the mechanical properties of the flat bar sections obtained with both thermomechanical treatments. The results of the investigation of the mechanical properties and the impact energy of the Charpy-V samples, taken from the forgings are listed in **Table 1**. The data presented in this table show that the flat bar sections quenched in water directly from the temperature of the forging finish (Variant I of thermomechanical treatment), have the following properties after the tempering at 550 °C: $YS_{0.2}$ of about 973 MPa, UTS of about 1057 MPa, TEI of about 13.5 % and RA of about 51.5 %. The flat bar sections obtained from Variant II of thermomechanical processing have higher mechanical properties and a distinctly higher crack resistance in the tempered state. However, the best set of mechanical properties and crack resistance was found for the forging isothermally held at the temperature of

900 °C for 60 s prior to hardening in water when, after the tempering in the temperature range from 550 °C to 650 °C, the following properties were obtained: $YS_{0.2}$ from 994 MPa to 911 MPa, UTS from 1084 MPa to 974 MPa, KV from 95 J to 109 J and KV^{-40} from 77 J to 83 J.

The examination of the influence of the applied processing variant and the tempering temperature on the hardness show that the highest hardness – of approximately 330 HBW – is obtained for the forgings of the Variant-II thermomechanical treatment, including isothermal holding at the forging-finish temperature for 60 s prior to water quenching, and tempering at 550 °C. An increase in the tempering temperature for a forging up to 650 °C results in a mild decrease in the hardness, to about 300 HBW.

4 CONCLUSIONS

The implemented thermomechanical processing allows a production of forged products with the following properties achieved after controlled cooling from the temperature of the plastic deformation finish and a subsequent tempering in the temperature range from 550 °C to 650 °C: $YS_{0.2}$ from 994 MPa to 939 MPa, UTS from 1084 MPa to 993 MPa, TEI from 14.3 % to 15.1 %, RA from 51.5 % to 52.7 %, KV from 96 J to 109 J and KV^{-40} from 77 J to 83 J. The high strength in such a state at a high crack resistance, also at a decreased temperature, is noteworthy.

The best set of mechanical properties and crack resistance was obtained for the forging isothermally held at 900 °C for 60 s prior to quenching in water, and subsequently subjected to a tempering at 650 °C.

The relatively low hardness of the steel after a high-temperature tempering should not cause difficulties during the machining of forgings.

Microstructural observations of thin foils using transmission electron microscopy revealed that the microstructure of the steel in the quenched state consisted of lath martensite with a high density of dislocations and a considerable amount of precipitates. In the examined steel, the particles of (Ti,Nb)C and (Ti,Nb,V)C revealed precipitation on dislocations during plastic deformation, decreasing the rate of dynamic recovery, possibly dynamic recrystallization and, after hot working, also decreasing the rate of recovery and static or metadynamic recrystallization. The identified particles with the

sizes between 40 nm and 80 nm significantly increase the precipitation strengthening; however, they limit the grain growth of the recrystallized austenite and stimulate a formation of fine-grained microstructures.

The investigation makes it possible to develop an industrial technology for the forgings with high mechanical properties and a guaranteed crack resistance, also at a decreased temperature, using thermomechanical treatment.

5 REFERENCES

- ¹ A. Ghosh, S. Das, S. Chatterjee, B. Mishra, P. Ramachandra Rao, *Mater. Sci. Eng. A*, 348 (2003), 299–308
- ² J. Adamczyk, E. Kalinowska-Ozgowicz, W. Ozgowicz, R. Wusatowski, *J. Mater. Proc. Tech.*, 54 (1995), 23–32
- ³ M. Cabibbo, A. Fabrizi, M. Merlin, *J. Mater. Sci. Tech.*, 43 (2008), 6857–6865
- ⁴ P. Skubisz, H. Adrian, J. Sińczak, *Arch. Metall. Mater.*, 56 (2011), 93–107
- ⁵ T. Gladman, *The physical metallurgy of microalloyed steels*, 1st ed., The University Press, Cambridge 1997
- ⁶ A. Grajcar, W. Borek, *Arch. Civ. Mech. Eng.*, 8 (2008), 29–38
- ⁷ B. Eghbali, A. Abdullah - Zadeh, *J. Mater. Proc. Tech.*, 180 (2006), 44–48
- ⁸ P. S. Bandyopadhyay, S. K. Ghosh, S. Kundu, S. Chatterjee, *Metall. Mater. Trans. A*, 42 (2011), 2742–2752
- ⁹ D. A. Skobir, M. Godec, M. Balcar, M. Jenko, *Mater. Tehnol.*, 44 (2010) 6, 343–347
- ¹⁰ D. K. Matlock, G. Krauss, J. G. Speer, *J. Mater. Proc. Tech.*, 117 (2001), 324–328
- ¹¹ A. Grajcar, S. Lesz, *Mater. Sci. Forum*, 706–709 (2012), 2124–2129
- ¹² P. D. Hodgson, M. R. Barnett, *ISIJ Int.*, 32 (1992), 1329–1336
- ¹³ H. Kejian, T. N. Baker, *Mater. Sci. Eng. A*, 169 (1993), 53–58
- ¹⁴ S. C. Hong, S. H. Lim, K. J. Lee, D. H. Shin, *Mater. Sci. Eng. A*, 355 (2003), 241–248
- ¹⁵ O. Kwon, A. J. DeArdo, *Acta Metall. Mater.*, 39 (1991), 529–538
- ¹⁶ M. Maruyama, R. Uemori, M. Sugiyama, *Mater. Sci. Eng. A*, 250 (1998), 2–7
- ¹⁷ S. Takaki, K. Kawasaki, Y. Kimura, *J. Mater. Proc. Tech.*, 117 (2001), 359–363
- ¹⁸ W. M. Rainforth, M. P. Black, R. L. Higginson, E. J. Palmiere, C. M. Sellars, *Acta Mater.*, 50 (2002), 735–747
- ¹⁹ M. MacKenzie, A. J. Craven, C. J. Collins, *Scri. Mater.*, 54 (2006), 1–5
- ²⁰ R. Kuziak, T. Bołd, Y. Cheng, *J. Mater. Proc. Tech.*, 53 (1995), 255–262
- ²¹ J. Adamczyk, *Journal of Achievements in Materials and Manufacturing Engineering*, 14 (2006), 9–20
- ²² M. Opiela, A. Grajcar, *Arch. Civ. Mech. Eng.*, 12 (2012), 327–333
- ²³ S. Vervynckt, K. Verbeken, P. Thibaux, *Mater. Sci. Eng. A*, 528 (2011), 5519–5528

PROGRESSIVE FAILURE ANALYSIS OF COMPOSITE SANDWICH BEAM IN CASE OF QUASISTATIC LOADING

NAPREDNA ANALIZA POŠKODB SESTAVLJENEGA KOMPOZITNEGA NOSILCA PRI KVAZISTATIČNEM OBREMENJEVANJU

Tomáš Mandys, Tomáš Kroupa, Vladislav Laš

University of West Bohemia in Pilsen, NTIS - New Technologies for Information Society, Univerzitní 22, 306 14 Plzeň, Czech Republic
tmandys@kme.zcu.cz, kroupa@kme.zcu.cz, las@kme.zcu.cz

Prejem rokopisa – received: 2013-10-02; sprejem za objavo – accepted for publication: 2013-10-28

This paper is focused on a progressive failure analysis of a sandwich composite panel considering a non-linear model of core and skins using explicit analysis. The material properties were determined from tensile and compressive tests of the outer composite skin and the foam core. A user-defined material model was used to describe the non-linear orthotropic elastic behaviour of the composite skin. The material parameters of the outer composite skin were determined using the identification process performed using a combination of optimization method and finite-element simulation. The Low-Density Foam material model was used for the foam core. The obtained material data were validated using a three-point bending test of a sandwich beam.

Keywords: sandwich panel, fiber-glass fabric, foam core, three point bending test, damage, optimization

Članek obravnava napredno analizo poškodb z uporabo eksplicitne analize sestavljene kompozitne plošče z upoštevanjem nelinearnega modela jedra in skorje. Lastnosti materiala so bile določene iz nateznih in tlačnih preizkusov zunanje kompozitne skorje in penaste sredice. Uporabniško določen model materiala je bil uporabljen za opis nelinearnega ortotropnega elastičnega vedenja kompozitne skorje. Materialni parametri zunanje kompozitne skorje so bili določeni z identifikacijskim procesom, izvršenim z uporabo kombinacije metod optimiranja in simulacije s končnimi elementi. Materialni model pene z nizko gostoto je bil uporabljen za jedro iz pene. Dobljeni podatki za material so bili ocenjeni z uporabo tritočkovnega upogibnega preizkusa sestavljenega nosilca.

Ključne besede: sestavljena plošča, tkanina iz steklenih vlaken, jedro iz pene, tritočkovni upogibni preizkus, poškodba, optimizacija

1 INTRODUCTION

The principle of sandwich structures is based on a low-density material (core) placed between two stiffer outer skins. The main purpose of the core is to maintain the distance between the outer skins and to transfer the shear load while the outer skins carry the compressive and tensile load. The outer skins are obviously thinner than the core. This type of structural arrangement has a much larger bending stiffness than a single solid plate made of the same total weight from the same material as a outer skin only. This fact together with other advantages, such as corrosion resistance, product variability and thermal or acoustic insulation, make sandwich structures the preferred alternative to conventional materials in all types of structural applications where the weight must be kept to a minimum value.

2 EXPERIMENTAL SET-UPS AND SPECIMENS

The used sandwich composite panel was manufactured using a vacuum infusion process and its overall thickness was 12.5 mm. The outer composite skins were made from three layers of fibre-glass fabric with the pro-

duct name Aeroglass (material density $\rho = 390 \text{ g/m}^2$) and epoxy resin designated as Epicote HGS LR 285. The thicknesses of the outer composite skins were 1.2 mm. The core of the sandwich panel was a closed-cell, cross-linked polymer foam Airex C70.55. This foam core is characterized by a low resin absorption. The resultant sandwich panel was cured for 6 h at 50 °C.

Tensile and compressive experimental tests were performed using a Zwick/Roell Z050 testing machine on the separated specimens of the laminated composite skin and foam core of the resultant sandwich structure. The foam core was additionally subjected to a three-point bending test too.

Three types of specimens of laminated composite skin were used, the chosen material principal direction (weft) form angle 0° (Type A), 45° (Type C) and 90° (Type B) with the direction of the loading force. The specimens of the laminated outer skin had the dimensions 135 mm × 15 mm and a thickness 1.2 mm. The dimensions of the specimens of the isotropic foam core were 150 mm × 15 mm with a thickness 10 mm. The loading velocity during the tensile tests was 2.0 mm/min in the case of the composite skin and 1.0 mm/min in the

case of the foam core. Four specimens for each angle of composite skin and for the foam core were tested.

The three-point bending tests of the foam core were performed on specimens with the same dimensions that were used for the tensile tests. The distance of the supports of the testing device was 100 mm and the diameters of all three supports were 10 mm.

The resulting sandwich beam with the dimensions 330 mm × 50 mm and a total thickness 12.5 mm was subjected to a three-point bending test in order to validate the material data obtained independently for the composite skin and the foam core. The thicknesses of the composite skins were 1.2 mm. The distance of the supports of the testing device was 250 mm and the supports consisted of rotationally joined cylinders with diameters of 30 mm. The loading velocity of the sandwich beam was 20 mm/min. Three specimens were tested in total.

2.1 Material model of the skin

A user-defined material model of the composite skin was implemented in Abaqus software using the VUMAT subroutine written in the Fortran code. The non-linear function describing the stress-strain relationship starting from the deformation ϵ_{0i} ($i = 1, 2$) was assumed in the case of the principal material directions 1 and 2 (equations (2) and (4)). The non-linear function with a constant asymptote was considered in the case of the shear in plane 12 (equation (8)). The following equations describe the stress-strain relationship of the laminated outer skin:

$$\sigma_1 = C_{11} \cdot \epsilon_1 + C_{12} \cdot \epsilon_2 + C_{13} \cdot \epsilon_3 \quad \text{for } \epsilon_1 < \epsilon_{01} \quad (1)$$

$$\sigma_1 = (C_{11} \cdot (\epsilon_1 + \frac{A_1}{2} \cdot (\epsilon_{01}^2 - \epsilon_1^2)) - A_1 \cdot \epsilon_{01} \cdot (\epsilon_{01} - \epsilon_1)) + C_{12} \cdot \epsilon_2 + C_{13} \cdot \epsilon_3 \cdot (1-D) \quad \text{for } \epsilon_1 \geq \epsilon_{01} \quad (2)$$

$$\sigma_2 = C_{12} \cdot \epsilon_1 + C_{22} \cdot \epsilon_2 + C_{23} \cdot \epsilon_3 \quad \text{for } \epsilon_2 < \epsilon_{02} \quad (3)$$

$$\sigma_2 = (C_{12} \cdot \epsilon_1 + C_{22} \cdot (\epsilon_2 + \frac{A_1}{2} \cdot (\epsilon_{02}^2 - \epsilon_2^2)) - A_2 \cdot \epsilon_{02} \cdot (\epsilon_{02} - \epsilon_2)) + C_{23} \cdot \epsilon_3 \cdot (1-D) \quad \text{for } \epsilon_2 \geq \epsilon_{02} \quad (4)$$

$$\sigma_3 = (C_{13} \cdot \epsilon_1 + C_{23} \cdot \epsilon_2 + C_{33} \cdot \epsilon_3) \cdot (1-D) \quad (5)$$

$$\sigma_{23} = (G_{23} \cdot \gamma_{23}) \cdot (1-D) \quad (6)$$

$$\sigma_{13} = (G_{13} \cdot \gamma_{13}) \cdot (1-D) \quad (7)$$

$$\sigma_{12} = \frac{G_{12}^0 \cdot \gamma_{12}}{\left(1 + \left(\frac{G_{12}^0 \cdot |\gamma_{12}|}{\tau_{12}^0}\right)^{n_{12}}\right)^{\frac{1}{n_{12}}}} \cdot (1-D) \quad (8)$$

The constants occurring in equations (1) to (5) are:

$$\begin{aligned} C_{11} &= \frac{E_1 \cdot (1 - \nu_{23} \cdot \nu_{32})}{\Delta} & C_{12} &= \frac{E_1 \cdot (\nu_{21} + \nu_{23} \cdot \nu_{32})}{\Delta} \\ C_{13} &= \frac{E_1 \cdot (\nu_{31} - \nu_{32} \cdot \nu_{21})}{\Delta} & C_{22} &= \frac{E_2 \cdot (1 - \nu_{31} \cdot \nu_{13})}{\Delta} \\ C_{23} &= \frac{E_2 \cdot (\nu_{32} - \nu_{31} \cdot \nu_{12})}{\Delta} & C_{33} &= \frac{E_3 \cdot (1 - \nu_{12} \cdot \nu_{21})}{\Delta} \end{aligned} \quad (9)$$

$$\Delta = 1 - \nu_{12} \cdot \nu_{21} - \nu_{23} \cdot \nu_{32} - 2 \cdot \nu_{12} \cdot \nu_{23} \cdot \nu_{31}$$

where E_1, E_2 and E_3 are the Young's moduli in the principal directions 1, 2 and 3 and $\nu_{12}, \nu_{23}, \nu_{31}$ are the Poisson's ratios in the planes defined by the principal directions 1, 2 and 3. The shear moduli in planes 23 and 13 are designated as G_{23} and G_{13} , respectively. The non-linear behavior in shear in plane 12 (8) is described using the initial shear modulus G_{12}^0 , the asymptotic value of the shear stress τ_{12}^0 and the shape parameter n_{12} . The parameters A_1 and A_2 in (2) and (4) describe the straightening of the yarns of the fiber-glass fabric and the loss of stiffness in the directions 1 and 2, respectively. The values of the deformations ϵ_{01} and ϵ_{02} indicate the transitions between the linear and non-linear parts of the stress-strain relationship in the given directions 1 and 2 during the loading.

The maximum stress failure criterion was used to predict failure on the composite skin:

$$\begin{aligned} F_{1T} &= \frac{\sigma_1}{X_T} & F_{1C} &= \frac{|\sigma_1|}{X_C} & F_{2T} &= \frac{\sigma_2}{Y_T} \\ F_{2C} &= \frac{|\sigma_2|}{Y_C} & F_{12} &= \frac{\sigma_{12}}{S_L} \end{aligned} \quad (10)$$

where the subscripts T and C denote the tension and compression, X and Y are the strengths in the principal directions 1 and 2, respectively, and S_L denotes the shear strength.

The values of the degradation variable D are dependent on the kind of occurred failure.² The principle of material degradation is shown in **Figure 1** and the degradation parameters are summarized in (11). The degradation parameter after failure initiation was implemented in the case of shear failure ($F_{12} \geq 1.0$ and $\gamma_{12} < \gamma_{12}^F$) from.³ Due to the non-linear behavior of the composite skin the degradation parameters are assumed in the form:

$$\begin{aligned} F_{1T} \geq 1 &\Rightarrow D=1.0 & F_{1C} \geq 1 &\Rightarrow D=0.6 \\ F_{2T} \geq 1 &\Rightarrow D=1.0 & F_{2C} \geq 1 &\Rightarrow D=0.6 \\ F_{12} \geq 1 \text{ and } \gamma_{12} < \gamma_{12}^F &\Rightarrow D=1 - e^{-\left(\frac{1}{m_{12}} (F_{12})^{m_{12}}\right)} \\ F_{12} \geq 1 \text{ and } \gamma_{12} \geq \gamma_{12}^F &\Rightarrow D=1.0 \end{aligned} \quad (11)$$

In the case of shear failure the non-negative material constant m_{12} is represented by the integer and γ_{12}^F is the ultimate deformation when the material is fully damaged.

Mathematical optimization was used to identify the material parameters on data from the performed tensile tests of composite skin. The optimization process was

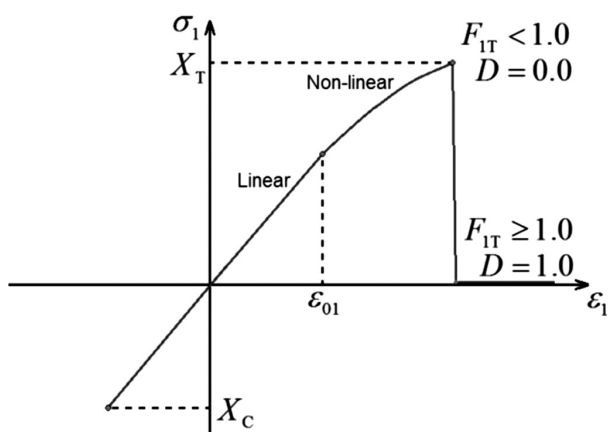


Figure 1: The principle of material degradation in the principal direction 1

Slika 1: Načelo degradacije materiala v glavni smeri 1

handled using Optislang 3.2.0. The material parameters that do not have a significant influence on the results were kept constant during the optimization process. All the material parameters are summarized in Table 1.

The parameters E_3 , G_{13} and G_{23} were taken from the literature.⁴ The strengths of the composite skin were determined directly from the experimental data.

Table 1: Material parameters of the composite skin

Tabela 1: Parametri materiala kompozitne skorje

Optimized values:			Constant values:		
E_1	GPa	16.9	ν_{12}	–	0.337
E_2	GPa	18.5	ν_{23}	–	0.337
G_{12}^0	GPa	4.96	ν_{31}	–	0.28
τ_{12}^0	MPa	39.66	G_{13}	GPa	4.0
n_{12}	–	0.9	G_{23}	GPa	2.75
A_1	–	10.0	E_3	GPa	8.0
A_2	–	14.0	γ_{12}^F	–	0.324
ϵ_{01}	–	0.0008	ρ_C	kg/m ³	1554
ϵ_{02}	–	0.005	X_T	MPa	325
m_{12}	–	5	Y_T	MPa	347
			X_C	MPa	65
			Y_C	MPa	67
			S_L	MPa	35

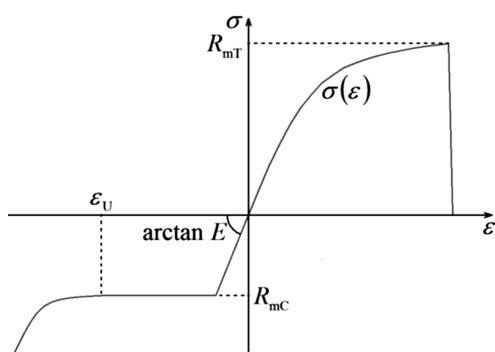


Figure 2: Tensile and compressive uniaxial stress-strain behavior of foam core

Slika 2: Vedenje jedra iz pene pri enoosni natezni in tlačni obremenitvi

2.2 Material model of the foam core

The used material model of the foam core was the Low-Density Foam model from the Abaqus software library.⁵ This material model is intended for highly compressible elastomeric foams. The material behavior was specified directly via uniaxial stress-strain curves for tension and compression (Figure 2). In the case of tension the uniaxial stress-strain behavior was described via a curve added in the form:

$$\sigma(\epsilon) = 435 \cdot 10^9 \cdot \epsilon^3 - 8.76 \cdot 10^8 \cdot \epsilon^2 + 6.09 \cdot 10^7 \cdot \epsilon - 1.44 \cdot 10^4 \quad (12)$$

The material is fully damaged after reaching the tensile strength R_{mT} . The compressive behavior of the foam core was described as an ideally elastoplastic material

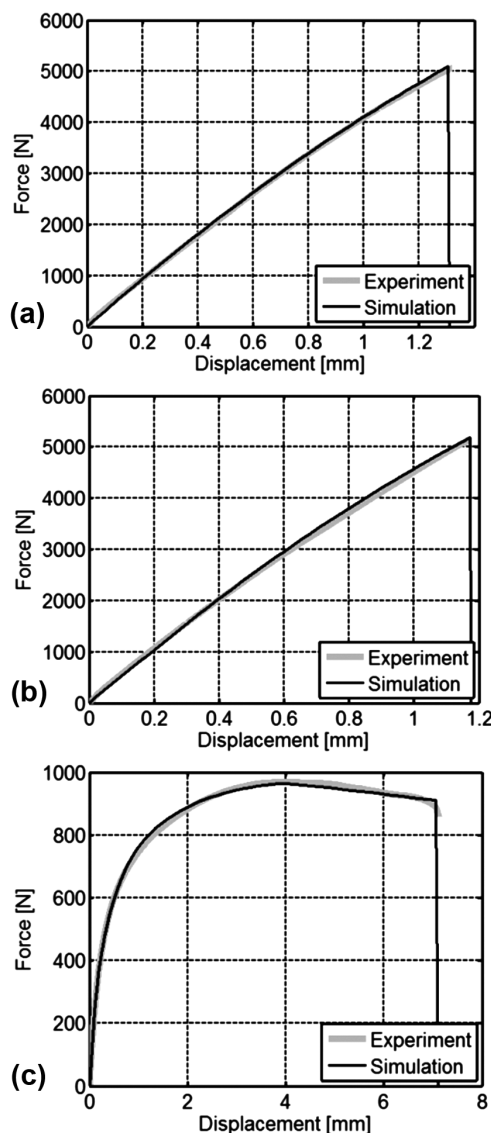


Figure 3: The resultant force-displacement diagrams of the composite skin types A (top), B (center) and C (bottom)

Slika 3: Diagrami sila – raztezek kompozitne skorje A (na vrhu), B (v sredini) in C (spodaj)

with the Young's modulus E and the yield limit R_{mC} . The material parameters are summarized in **Table 2**.

Table 2: Material parameters of foam core
Tabela 2: Parametri materiala pene v jedru

E	R_{mC}	R_{mT}	ρ_f	ν	ϵ_U
MPa	MPa	MPa	kg/m ³	-	-
50	1.2	1.5	60	0.0	0.53

2.3 Numerical simulations and results

The simulations were performed as quasi-static explicit analyses in the FEM software Abaqus 6.11 using finite-strain theory. The numerical models of the outer skin and the foam core were meshed using 8-node solid elements (element type C3D8R).

Figure 3 shows the resulting force-displacement dependencies from averaged experiments and the numerical simulations for specimens of type A, B and C. The resulting force-displacement diagrams of the tensile test and the force-deflection diagram of three-point bending test of the foam core is shown in **Figure 4**.

The numerical model of the sandwich beam was created as a fully contact problem of four bodies – sandwich beam and three supports. The friction between the sandwich beam and supports has been neglected.

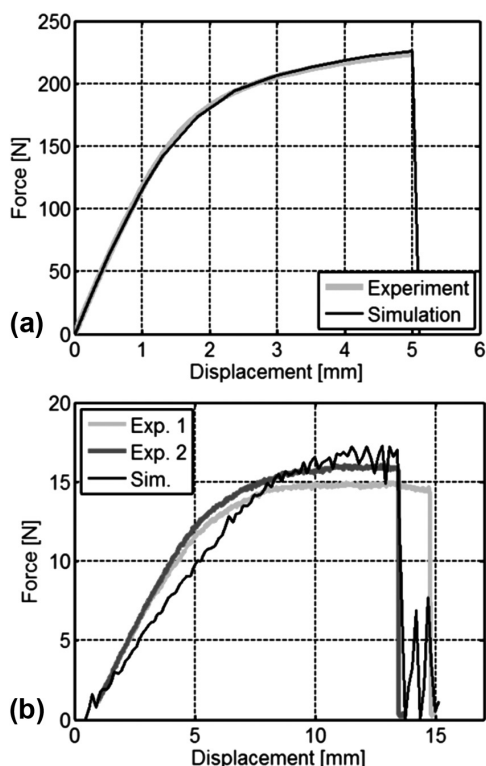


Figure 4: a) The resulting force-displacement diagrams of the tensile test and b) the force-deflection diagram of the three-point bending test of the foam core

Slika 4: a) Diagrami sila – raztezek pri nateznem preizkusu in b) diagram sila – uklon pri tritočkovnem upogibnem preizkusu jedra iz pene

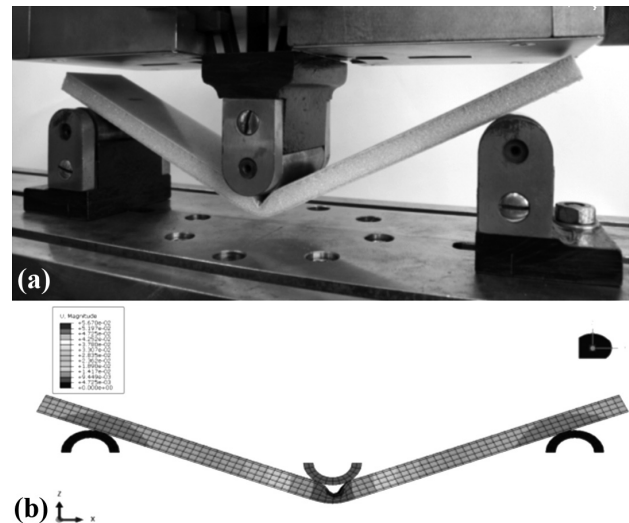


Figure 5: a) The resulting sandwich beam subjected to a three-point bending test and b) the numerical model of loaded sandwich beam
Slika 5: a) Sestavljen nosilec, izpostavljen tritočkovnemu upogibu in b) numerični model obremenjenega sestavljenega nosilca

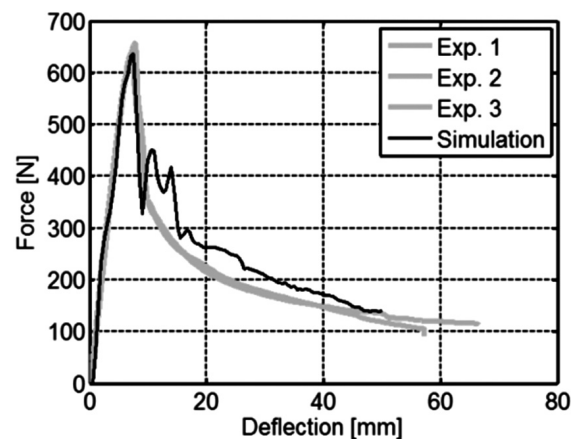


Figure 6: The force-deflection diagram of the three-point bending test of the resulting sandwich beam

Slika 6: Diagram sila – upogib pri tritočkovnem upogibnem preizkusu nosilca

The failure of the upper composite skin occurred in compression in principal direction 2 during loading in place under the center support, both in the case of experiments and the numerical simulation. This situation is shown in **Figure 5**. The comparison of the force-deflection diagrams for the three-point bending tests of the sandwich beam is shown in **Figure 6**.

3 CONCLUSION

The user-defined material model describing the non-linear orthotropic elastic behaviour, considering the progressive failure analysis, was implemented in the FEM system Abaqus. The material parameters of the composite outer skin of the sandwich panel were

identified using the mathematical optimization method. In the case of the foam core the Low-Density Foam material model from FEM software library was used. The obtained material parameters of the composite skin and foam core were verified via a three-point bending test of the resulting sandwich beam. The future work will focus on low-velocity impact events involving sandwich plates.

Acknowledgement

The work has been supported by the European Regional Development Fund (ERDF), project "NTIS – New Technologies for Information Society", European Centre of Excellence, CZ.1.05/1.1.00/02.0090, the student research project of Ministry of Education of Czech Republic No. SGS-2013-036 and the project of Grant Agency of Czech Republic No. GAČR P101/11/0288.

4 REFERENCES

- ¹ T. Kroupa, V. Laš, R. Zemčík, Improved nonlinear stress-strain relation for carbon-epoxy composites and identification of material parameters, *Journal of Composite Materials*, 45 (2011) 9, 1045–1057
- ² V. Laš, R. Zemčík, Progressive damage of unidirectional composite panel, *Journal of Composite Materials*, 42 (2008) 1, 22–44
- ³ C. F. Yen, Ballistic Impact modeling of Composite materials, 7th International LSDyna User's Conference, Dearborn, Michigan, 2006
- ⁴ R. Zemčík, V. Laš, T. Kroupa, H. Purš, Identification of material characteristics of sandwich panels, *Bulletin of Applied Mechanics*, 26 (2011), 26–30
- ⁵ Abaqus 6.11 Documentation, Dassault Systèmes Simulia Corp., 2011

INFLUENCE OF HEAT TREATMENT ON THE MICROSTRUCTURE AND MECHANICAL PROPERTIES OF ALUMINIUM BRONZE

VPLIV TOPLOTNE OBDELAVE NA MIKROSTRUKTURO IN MEHANSKE LASTNOSTI ALUMINIJEVEGA BRONA

Peter Sláma, Jaromír Dlouhý, Michal Kövér

COMTES FHT a.s., Prumyslova 995, 334 41 Dobruška, Czech Republic
peter.slama@comtesfht.cz

Prejem rokopisa – received: 2013-10-03; sprejem za objavo – accepted for publication: 2013-10-24

The paper deals with the influence of heat treatment (annealing, quenching and aging) on the microstructure and mechanical properties of pressed bars made from the CuAl10Ni5Fe4 alloy. The microstructures were observed in light and scanning electron microscopes. The appearance and area fractions of the α and κ phases and their influence on the mechanical properties were examined. Using DSC and EBSD methods, the presence of the γ_2 phase was monitored, as it is a very hard and brittle phase that impairs the material's corrosion resistance. The results were compared with data for the high-alloyed CuAl14Fe5 aluminium bronze, in which high hardness and wear resistance are imparted by the $\beta + \gamma_2$ phases.

Keywords: aluminium bronze, heat treatment, microstructure, mechanical properties, DSC, EBSD, γ_2 -phase

Članek obravnava vpliv toplotne obdelave (žarjenje, kaljenje in staranje) na mikrostrukturo in mehanske lastnosti stiskanih palic iz zlitine CuAl10Ni5Fe4. Mikrostruktura je bila opazovana s svetlobnim in vrstičnim elektronskim mikroskopom. Preučevan je bil pojav in površinski delež faze α in κ ter njun vpliv na mehanske lastnosti. Z metodama DSC in EBSD je bila pregledana prisotnost trde in krhke γ_2 -faze, ki poslabša korozijsko odpornost materiala. Rezultati so bili primerjani s podatki za močno legiran CuAl14Fe5 aluminijev bron, pri katerem ($\beta + \gamma_2$)-faza znižujeta veliko trdoto in odpornost proti obrabi.

Gljučne besede: aluminijev bron, toplotna obdelava, mikrostruktura, mehanske lastnosti, DSC, EBSD, γ_2 -faza

1 INTRODUCTION

CuAl10Ni5Fe4 aluminium bronze is a copper alloy that retains its high strength even at elevated temperatures and which possesses a good corrosion resistance and a high wear resistance.¹⁻³ It has a two-phase microstructure consisting of the poor-formability α phase and the high-temperature β phase, which exhibits excellent hot formability. The addition of nickel increases the alloy's strength without diminishing its excellent ductility, toughness and corrosion resistance. Typical applications of the alloy include valve seats, plunger tips, marine engine shafts, valve guides, aircraft components and pump shafts. The alloy exhibits limited cold formability (due to rapid work hardening), but excellent hot formability in the $\alpha + \beta$ region. The recommended forming temperatures are between 700 °C and 900 °C.^{1,2}

Depending on the cooling rate and the subsequent heat treatment, the β phase may undergo a martensitic transformation into the unstable phase β' , which, being very hard and brittle, enhances the strength and reduces the ductility of the material. In addition, other phases are found in the microstructure, which are termed κ , which consist mostly of Fe and Al or Ni,³⁻⁵ or the γ_2 phase known to occur in Cu-Al binary alloys. The γ_2 phase in alloys containing less than 11.8 % aluminium forms during slow cooling or in the course of annealing at temperatures below 565 °C. These phases increase the

strength and reduce the ductility of the alloy. The microstructure therefore consists of the α phase and the $\alpha + \kappa + \gamma_2$ eutectoid, as shown in the phase diagram in **Figure 1a**.⁶

Several types of the kappa phase have been classified: the sources^{3-5,7,8} list four types, denoted as κ_I , κ_{II} , κ_{III} , κ_{IV} . The κ_I phase forms large dendrite-shape particles that are rich in Fe, which consist of Fe₃Al with Cu and Ni and the cubic structure DO₃. The phase κ_{II} forms smaller, globular particles with identical composition

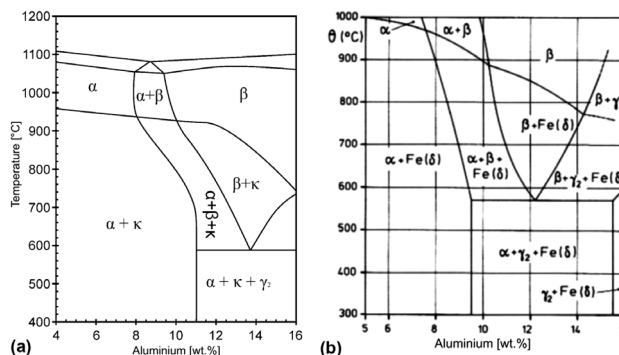


Figure 1: a) Vertical section of the phase diagram of nickel aluminum bronze with 5 % Ni and 5 % Fe, b) vertical section of phase diagram of Cu-Al-Fe at 3 % Fe

Slika 1: a) Navpični prerez faznega diagrama nikelj – aluminijev bron s 5 % Ni in 5 % Fe, b) navpični prerez faznega diagrama Cu-Al-Fe pri 3 % Fe

and structure to κ_1 . The phase (precipitates) κ_{III} are NiAl-based and have the cubic B2 structure and a plate or lamellar shape. The κ_{IV} particles are small precipitates based on Fe_3Al . The composition of the γ_2 phase is Cu_9Al_4 and its structure is the cubic P-43m type.

Where tough requirements for hardness and wear resistance are to be met, high-alloyed Cu-Al-Fe aluminium bronzes are used with an aluminium level above 13 % and an iron content of up to 5 %. The microstructure of these alloys consists of two phases as well, as shown in the phase diagram in **Figure 1b**: α and γ_2 . The high hardness of these alloys is due to the latter, the γ_2 phase, which also exhibits a high hardness and brittleness, but a lower corrosion resistance. Owing to their hardness, excellent compressive strength and wear resistance, and sliding properties, these alloys are used for forming and drawing stainless steels and for worm wheels, valve guides and seats.

2 EXPERIMENTAL

Hot-pressed bars with a diameter of 32 mm from an alloy containing 10 % Al, 5 % Ni and 4 % Fe were used for the experiment. The material is denoted as CuAl10Ni5Fe4 (CW307G) according to EN 12163.

Specimens of bars were used for investigating the influence of annealing between 500 °C 30 min and 850 °C 30 min, quenching from 930 °C and aging of the quenched specimens at 30 °C 30 min to 400 °C 30 min upon the microstructure and mechanical properties. Attention was also paid to the influence of the slow cooling in the furnace and the subsequent rapid cooling after removal from the furnace. The results were com-

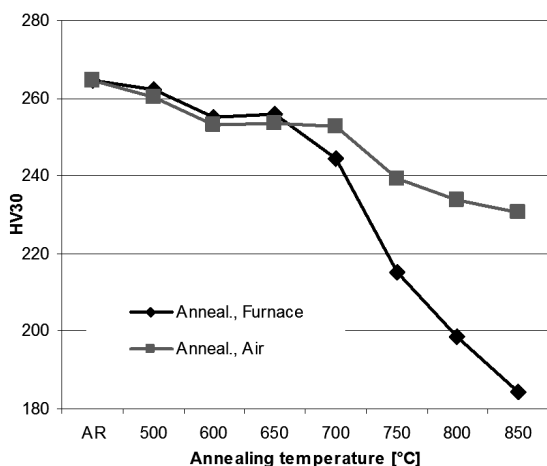


Figure 2: HV30 hardness of annealed specimens
Slika 2: Trdota HV30 vzorcev po žarjenju

Table 1: Chemical composition of alloys in mass fractions (w/%)
Tabela 1: Kemijska sestava zlitin v masnih deležih (w/%)

Alloy	Cu	Al	Ni	Fe	Mn	Sn	Si	Zn	Pb
CuAl10Ni5Fe4	balance	9.9	5.4	4.5	0.77	0.02	0.13	0.02	0.01
CuAl14Fe5	balance	14.5	0.12	4.9	0.97	0.06	0.22	0.006	0.07

pared with data for the high-alloyed CuAl14Fe5 aluminium bronze (sample of a worm wheel).

The chemical compositions of both alloys are given in **Table 1**.

The microstructures were observed on conventional metallographic sections in light (LM) and scanning electron microscopes (SEM). The HV hardness of the materials was measured. The evolution of the microstructure and the formation of the precipitates and phases were monitored using DSC (Differential Scanning Calorimetry) with a LINNSEIS DSC PT 1600 instrument and by means of EBSD (Electron Backscatter Diffraction) in a JEOL JSM 7400F scanning electron microscope equipped with a HKL-NORDLYSS camera and Channel5 software.

3 RESULTS AND DISCUSSION

3.1 CuAl10Ni5Fe4 Alloy

3.1.1 HV Hardness

The HV30 hardness of the as-received specimens (AR) upon annealing was measured. The results are shown in **Figure 2**. The graph shows the hardness levels after annealing of the as-received material and upon annealing (tempering) of the quenched material. The hardness of the as-received material is 265 HV30. Quenching increases this value to 305, and aging, to 400 (**Table 2**).

Table 2: HV30 hardness
Tabela 2: Trdota HV30

Condition cooling	Annealed	
	Furnace	Air
AR	265	
500 °C	262	260
600 °C	255	253
650 °C	256	254
700 °C	245	253
750 °C	215	239
800 °C	198	234
850 °C	184	230
Quenched 930 °C 30 min	305	
Quenched + Aged 400 °C 30 min	400	

The hardness decreases during annealing; first slowly, while the temperature is below 700 °C, but more rapidly when it reaches 750 °C. A greater drop in hardness was seen in the specimens cooled slowly in a furnace than in those cooled in air.

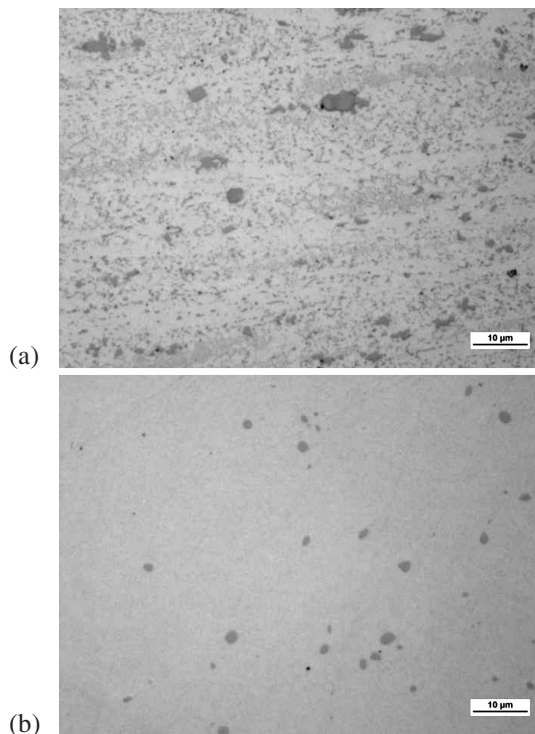


Figure 3: Micrographs of unetched specimens: a) as-received condition (AR), b) 17 – upon quenching

Slika 3: Mikrostruktura nejedkanih vzorcev: a) dobavljeno stanje (AR), b) 17 – po kaljenju

3.1.2 Microstructure

The micrographs of the specimens prior to etching are shown in **Figure 3**. Unetched sections show grey globular particles of the κ_{II} phase (according to EDS analysis, they contain 55 % iron, 11 % aluminium and nickel, copper, manganese and silicon), light grains of

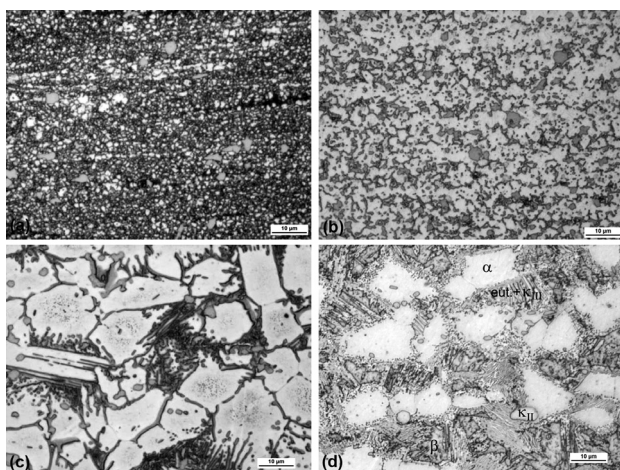


Figure 4: Micrographs of etched specimens: a) as-received condition, b) condition upon annealing at 750 °C, furnace, c) condition upon annealing at 850 °C, furnace, d) condition upon annealing at 850 °C, air

Slika 4: Mikrostruktura jedkanih vzorcev: a) dobavljeno stanje, b) po žarjenju na 750 °C, ohlajanje v peč, c) po žarjenju na 850 °C, ohlajanje v peč, d) po žarjenju na 850 °C, ohlajanje na zraku

the phase α and a eutectoid consisting of $\alpha + \kappa$ or a balance of β . Annealing at the quenching temperature of 930 °C dissolves the κ phase in the eutectoid (except the globular κ_{II}) and the β phase transforms to the non-equilibrium β' phase,¹⁰ as seen in **Figure 3b**.

The microstructures upon etching are shown in **Figures 4** and **5**. Etching reveals light grains of the phase α , grey to light-blue globular particles of the phase κ_{II} and the dark eutectoid $\alpha + \kappa_{III}$.⁷ In the as-received state, the α grain size is very small: 1 µm to 2 µm. With increasing annealing temperature, the size of the α grains grows, as does the size of the eutectoid areas between them. Slow cooling in the furnace leads to coarsening of the κ precipitates and to the formation of larger amounts of lamellar κ_{III} precipitates in the eutectoid. The phase κ also precipitates along the α grain boundaries. With increasing α grain size the strength and hardness decrease. The greatest drop is seen in specimens annealed at 850 °C with slow cooling. However, the elongation decreases as well, which may be attributed to κ precipitating more frequently at the α grain boundaries.

Rapid cooling leads to a higher proportion of the eutectoid at the expense of the α proportion. In addition, a certain fraction of β phase is retained in the microstructure (more dark areas in the eutectoid). This is shown in **Figures 4c** and **4d**, where short etching with $NH_4OH+H_2O_2$ revealed an orange β phase, a bright α phase and the κ phase and eutectoid in light-blue colour.

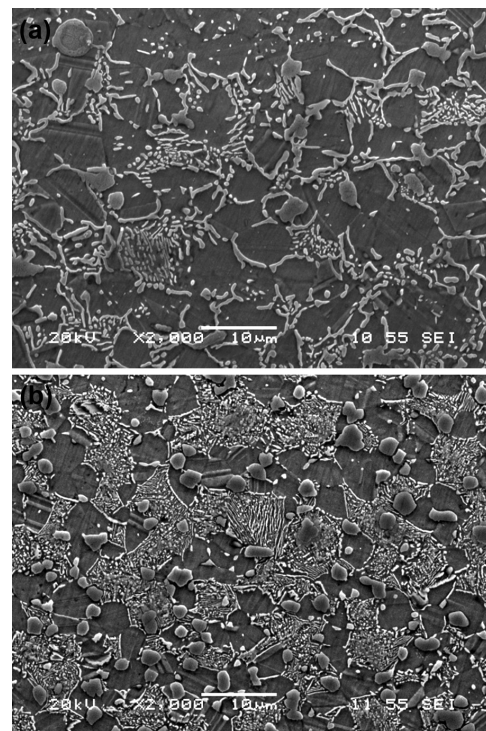


Figure 5: SEM micrographs of etched specimens: a) condition upon annealing at 800 °C, furnace, b) condition upon annealing at 800 °C, air

Slika 5: SEM-posnetka jedkanih vzorcev: a) po žarjenju na 800 °C, ohlajanje v peč, b) po žarjenju na 800 °C, ohlajanje na zraku

In contrast to the products of slow cooling, the κ precipitates are finer. Globular precipitates of κ_{IV} formed as well. The decrease in the strength and hardness is not as great as on slow cooling, which can be explained by a greater proportion of eutectoid and residual β in the microstructure.

The SEM micrographs also confirm that slow cooling leads to coarser κ precipitates than rapid cooling (Figures 5a and 5b).

Upon quenching and aging, fine κ_{IV} precipitates form in the martensitic β' phase, as shown in the light (Figure 6a) and scanning electron (Figure 6b) micrographs. The martensitic β' phase and fine precipitates provide the quenched and aged material with high hardness.

3.2 CuAl14Fe5 Alloy

3.2.1 Hardness and microstructure

The specimen of CuAl14Fe5 alloy was made from a sample taken from a worm-wheel, in which very high hardness was required. The alloy corresponds to the AMPCO® 22 material by AMPCOMETAL.¹¹ According to the company information, it contains β and γ_2 phases and has a nominal hardness of 332 HB30.

The specimen was used for an annealing trial at 950 °C 30 min with subsequent cooling in air. The hardness of the as-received material was 422 HV10. During

annealing, it rose to 462 HV10. Light micrographs are shown in Figures 7a and 7c, and a scanning electron micrograph is shown in Figure 7b. The microstructure consists of light-blue grains of γ_2 embedded in bright β phase matrix, of large dark κ_{II} particles in the γ_2 phase and of minute κ_{IV} precipitates within the β phase. In the as-received specimen, the microhardness of the γ_2 phase is 573 HV0.05 and that of the β phase reaches 341 HV0.05. The presence of the β (β') phase can be deduced from the material's high hardness. Due to annealing, the proportion of the γ_2 phase increased and, as a result of its high hardness, so did the hardness of the

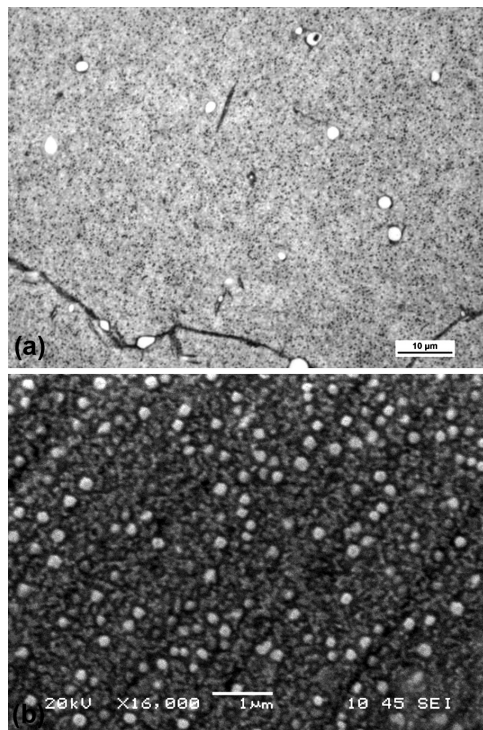


Figure 6: Microstructures of quenched and aged specimen, etched: a) quenched and aged at 400 °C (LM), b) quenched and aged at 400 °C (SEM)

Slika 6: Mikrostruktura hitro ohlajenega in staranega vzorca, jedkano: a) hitro ohlajeno in starano pri 400 °C (SM), b) hitro ohlajeno in starano pri 400 °C (SEM)

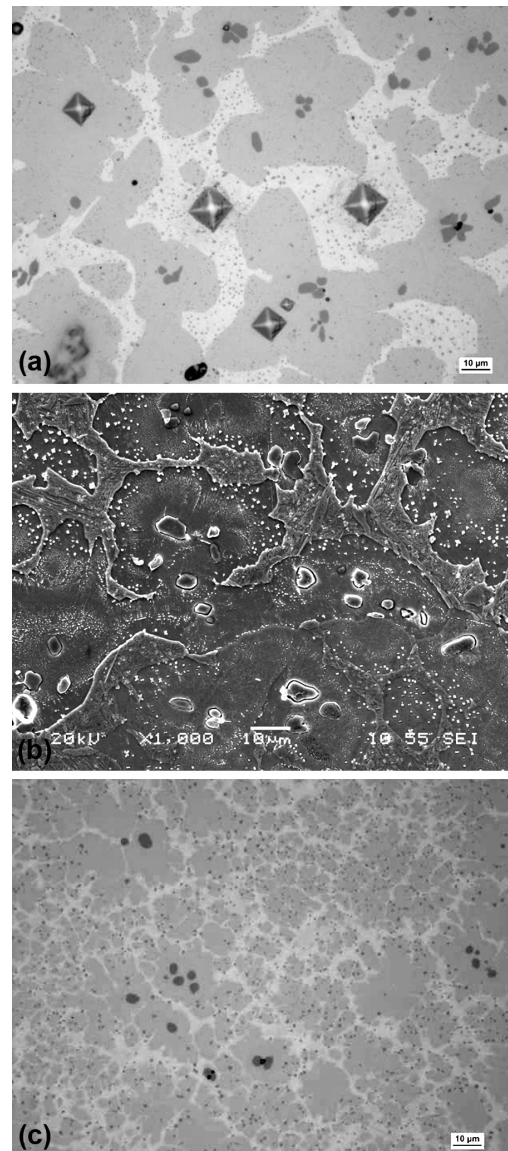


Figure 7: LM and SEM micrographs of CuAl14Fe5: a) as-received condition, unetched, HV0.05 hardness testing indentations (LM), b) as-received condition, etched (SEM), c) annealed at 950 °C 30 min, unetched (LM)

Slika 7: Svetlobni in SEM-posnetek CuAl14Fe5: a) dobavljeno stanje, nejedkano, odtiski trdote HV0,05 (SM), b) dobavljeno stanje, jedkano (SEM), c) žarjeno pri 950 °C 30 min, nejedkano (SM)

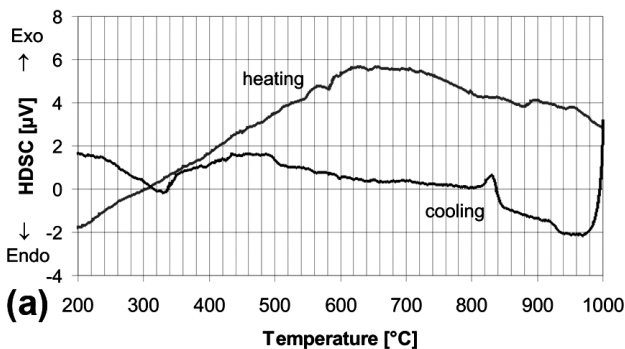
entire specimen. The SEM observation reveals needles of non-equilibrium β' phase in the β phase (**Figure 7b**).

3.3 DSC Analysis

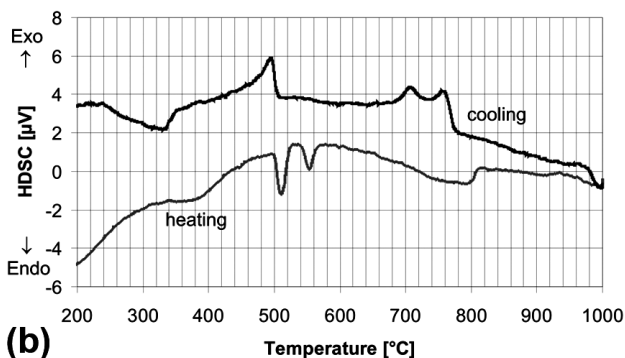
Using DSC, the precipitation of the κ phases and the $\beta \rightarrow \alpha + \gamma_2$ eutectoid transformation were monitored.^{12,13} DSC curves were measured at heating and cooling rates of 10 K/min. **Figure 8** shows the DSC curves for run 2 (after one cycle heating–cooling). The focus was the changes taking place at temperatures around 500 °C, in the vicinity of the eutectoid transformation $\beta \rightarrow \alpha + \gamma_2$ at 565 °C. Small peaks were recorded for the CuAl10Ni5Fe4 alloy. Temperature peaks between 930 °C and 830 °C on the cooling curve correspond to the formation of κ phases. ($\alpha + \beta \rightarrow \alpha + \beta + \kappa$) The peak at approx. 500 °C corresponding to the eutectoid transformation is very indistinct.

According to⁷ at 930 °C the globular κ_{II} phase ($\beta \rightarrow \beta + \kappa_{II}$ transformation) precipitates from the β phase and at 800 °C the $\alpha + \kappa_{III}$ lamellar eutectoid forms ($\alpha \rightarrow \alpha + \kappa_{III}$). At 850 °C fine κ_{IV} precipitates form in the α phase.

In the CuAl14Fe5 alloy, the peaks due to the formation of the κ and γ_2 phases are much more pronounced. At temperatures below 800 °C, two peaks can be observed, which could indicate the formation of the κ and γ_2 phases in the β phase. The 500 °C peak may correspond to the $\beta \rightarrow \alpha + \gamma_2$ eutectoid transformation.



(a) 200 300 400 500 600 700 800 900 1000
Temperature [°C]



(b) 200 300 400 500 600 700 800 900 1000
Temperature [°C]

Figure 8: DSC curves for heating and cooling: a) CuAl10Ni5Fe4 alloy, b) CuAl14Fe5 alloy

Slika 8: DCS-krivulje pri ogrevanju in ohlajanju: a) zlitina CuAl10Ni5Fe4, b) zlitina CuAl14Fe5

The transformation (formation of phases) at temperatures below 800 °C can be described according to **Figure 1b** as follows: $\beta \rightarrow \beta + \kappa \rightarrow \beta + \kappa + \gamma_2 \rightarrow \alpha + \kappa + \gamma_2$.

The peaks at temperatures of 300–400 °C correspond to the martensitic transformations of the β phase (formation of β_1, β').^{10,13,14}

3.4 Identification of phases using EBSD

As the phases of the different structures produce different diffraction patterns (EBSP), the EBSD analysis can be used for identifying the various phases.¹⁵ The EBSD analysis was aimed at identifying the κ and γ_2 phases in both aluminium bronzes. The phase maps and band contrast images are shown in **Figure 9**.

With the CuAl10Ni5Fe4 alloy, a higher band contrast was obtained (better quality of EBSP) in phases identified as α (large grey-coloured areas) and κ_{II} – Fe₃Al (small, bright spots). Due to the low band contrast, the phases in the eutectoid were not identified, most probably owing to the lamellar structure of $\alpha + \kappa_{III}$.

In the CuAl14Fe5 alloy, the phases identified included γ_2 (large grey areas) and κ_{II} (small bright spots). No regions with the β phase were identified, probably due to the presence of needles of non-equilibrium martensitic β' phase within the β phase.

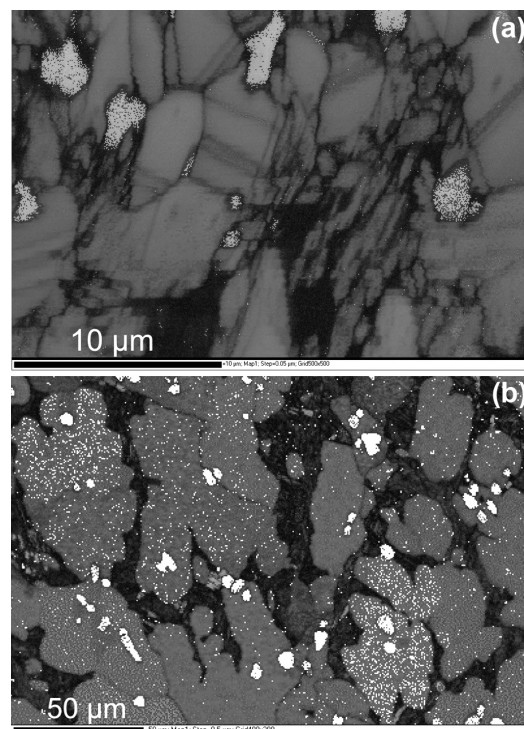


Figure 9: Band contrast and phase maps: a) alloy CuAl10Ni5Fe4, after annealing at 800 °C, air; grey phase – phase α , light phase – phase κ_{II} , b) alloy CuAl14Fe5, grey phase – phase γ_2 , light phase – phase κ_{II}

Slika 9: Trakast kontrast in razporeditev faz: a) zlitina CuAl10Ni5Fe4 po žarjenju na 800 °C, ohlajeno na zraku; siva faza – faza α , svetla faza – faza κ_{II} , b) zlitina CuAl14Fe5, siva faza – faza γ_2 , svetla faza – faza κ_{II}

4 CONCLUSIONS

The outcomes of the investigation of the effect of heat treatment on the microstructure and properties of pressed bars from CuAl10Ni5Fe4 alloy can be summarized as follows:

- Microstructure of the bars upon hot pressing is fine, consisting of α phase grains and the $\alpha + \kappa$ eutectoid. Owing to rapid cooling, the β phase may form as well.
- Annealing causes α grains and the eutectoid regions with κ_{III} -type precipitates to coarsen.
- Maximum hardness was obtained by quenching and aging at 400 °C: 400 HV30. This is due to the fine dispersion of particles κ in the martensitic β' phase.
- The γ_2 phase was not detected in the CuAl10Ni5Fe4 alloy by DSC or EBSD analysis.

CuAl10Ni5Fe4 Alloy

- The hardness of the CuAl14Fe5 is higher. It is determined by the proportion of the very hard γ_2 phase (with a microhardness of more than 550 HV0.05) in the β phase. The as-received specimen had a hardness of 422 HV10. Upon annealing, with subsequent air cooling, the fraction of γ_2 increased. The hardness increased as well: to a level of 462 HV10.
- The microstructure consists of β phases with a greater fraction of γ_2 , particles of κ_{II} within the γ_2 phase and minute κ_{IV} dispersoids in the β phase.
- The presence of κ and γ_2 phases was confirmed by DSC and EBSD analyses.

Acknowledgement

The results presented in this paper were developed under the project "West-Bohemian Centre of Materials and Metallurgy" CZ.1.05/2.1.00/03.0077 co-funded from European Regional Development Fund.

5 REFERENCES

- ¹ ASM Handbook Volume 02: Properties and Selection: Nonferrous Alloys and Special-Purpose Materials, ASM International, 1990
- ² J. R. Davis, ASM Specialty Handbook: Copper and Copper Alloys, ASM International, 2001
- ³ M. Cook, W. P. Fentiman, E. Davis, Observations on the Structure and Properties of Wrought Copper-Aluminum-Nickel-Iron Alloys, *J. Inst. Met.*, 80 (1951-52), 419-429
- ⁴ P. Brezina, Heat treatment of complex aluminum bronzes, *International Metals Reviews*, 27 (1982) 2, 77-120
- ⁵ F. Hasan, A. Jahanafrooz, G. W. Lorimer, N. Rildley, The morphology, crystallography and chemistry of phases in as-cast nickel-aluminum bronze, *Metallurgical Transactions A*, 13 (1982), 1337-1345
- ⁶ H. J. Meigh, Cast and Wrought Aluminum Bronzes – Properties, Processes and Structure, Institute of Materials, London, 2000
- ⁷ E. A. Culpan, G. Rose, Microstructural characterization of cast nickel aluminium bronze, *Journal of Materials Science*, 13 (1978), 1647-1657
- ⁸ A. Jahanafrooz, F. Hasan, G. W. Lorimer, N. Ridley, Microstructural Development in Complex Nickel-Aluminum Bronze, *Met. Trans A.*, 14 (1983), 1951-1956
- ⁹ CDA Publication, No 94, Equilibrium Diagrams, Selected copper alloy diagrams illustrating the major types of phase transformation, 1992
- ¹⁰ R. K. Gupta, B. R. Ghosh, P. P. Sinha, Choice of heat treatment mode for increasing the hardness of Cu – 9% Al – 6% Ni – 5% Fe alloy, *Metal Science and Heat Treatment*, 47 (2005), 526-528
- ¹¹ AMPCO 22 Technical Data Sheet, http://www.ampcometal.com/common/datasheets/en/A22_EX_E.pdf, Accessed on 22 Oct. 2013
- ¹² B. P. Pisarek, Model of Cu-Al-Fe-Ni Bronze Crystallization, *Archives of Foundry Engineering*, 13 (2013) 3, 72-79
- ¹³ M. Kaplan, A. K. Yildiz, The effects of production methods on the microstructures and mechanical properties of aluminum bronze, *Materials Letters*, 57 (2003), 4402-4411
- ¹⁴ A. A. Hussein, Structure-Property Relationships in Dual-Phase Cu-Al Alloys: Part I. Individual Phases, *Metall. Trans. A*, 13 (1982), 837-846
- ¹⁵ J. A. Schwartz, *Electron Backscatter Diffraction in Materials Science*, Kluwer Academic / Plenum Publishers, 2000

ŠOLSKI CENTER
ŠKOFJA LOKA

ŠOLSKI CENTER ŠKOFJA LOKA SE JE PREDSTAVIL TUDI PREDSEDNIKU RS BORUTU PAHORJU

Po uspešni vzpostavitvi Medpodjetniškega izobraževalnega centra (MIC) in energetske sanacije je Šolski center Škofja Loka 18. 4. 2014 obiskal predsednik RS Borut Pahor. Predsednik se je srečal z direktorjem Šolskega centra (ŠC) g. Martinom Pivkom, z vodjo MIC-a g. Alojzom Kokaljem in z ravnateljki šolskega centra. »Kot predsednik ob različnih težavah, s katerimi se srečujem, potrebujem eno krepko dozo optimizma. To je moje današnje srečanje z mladimi,« je obisk komentiral Borut Pahor.

Na Šolskem centru Škofja Loka so predsedniku Pahorju predstavili usposabljanja za tehniške poklice, predvsem iz strojništva in lesarstva: nagrajene projekte iz lesarstva (modularno pisarno, kopalniško opremo, klubsko mizico in leseno kolo), delo z robotom IRB 120 in avtomatizacijo procesov. Vodja projekta energetske sanacije Primož Praper s podjetja EUTRIP je predsedniku Pahorju predstavil sistem digitalnega energetskega monitoringa in spremljanje doseganja energetske učinkovitosti. Predsednik se je sprehodil tudi med dijaki, ki so izvajali postopke CAD-načrtovanja in 3D-modeliranja (3D-tiskalnik in 3D-skener), v laboratoriju modernih CNC-tehnologij pa so mu predstavili inovativni pripomoček za slepe, ki je nastal v šolskem centru. Predsednik se je ustavil tudi ob predstavitvi snežnega topa in podjetniškega projekta e-skiro, zapeljal pa se je tudi z električnim vozilom Smart, ki je nastal v delavnici šolskega centra.

»Prav bi bilo, da bi med našimi ljudmi bolj odmevalo, kako inteligentno, ambiciozno, inovativno mlado generacijo imamo. Tukaj so vsi bodoči inženirji, tudi tisti, ki bodo šli v proizvodnjo, imajo tehniški poklic in jih ne skrbi za prihodnost zaposlitve. Dobro bi bilo, da se vidi te žarke upanja. To so mladi samozavestni ljudje, ki delajo stvari, ki se zdijo nemogoče. Zdaj odhajam spet z žarom do življenja,« je ob slovesu povedal **Borut Pahor**, ki je tudi poudaril, da danes ni več mogoče izobraziti človeka za eno področje, na katerem bo delal vse življenje, ampak da je potrebna iznajdljivost, inovativnost, prilagodljivost. »Najprej izobražujemo osebnosti. Mi še vedno mislimo, da je glavni proces šolskega procesa podajanje znanja. Ni tako. Informacijo lahko danes dobiš kjer koli. Problem je, kako to informacijo razumeti in kako jo vpeti v načrte za prihodnje. To jim lahko dajo profesorji. Ne le s tehničnimi znanji, ampak da nastanejo to kreativne osebnosti, da mislijo s svojo glavo, da profesorji spodbujajo mlade k razmišljanju, da učenci lahko rečejo: 'Jaz sem boljši od tebe', in da so tudi učitelji zadovoljni, ko vidijo, da so učenci boljši od njih. Strokovne šole lahko veliko ponudijo.«

Direktor **Martin Pivk**, ki je gostil predsednika države, je povedal: »Za obisk predsednika nismo pripravili nič posebnega. Pokazali smo samo tisto, kar se vsak dan dogaja v šolskem centru. Tako da lahko rečemo, da ti prikazi niso odsev enodnevnega obiska, ampak odsev sodelovanja dijakov ter pomoči mentorjev, učiteljev pri njihovem vsakdanjem delu.« Direktor je še izrazil



Slika 1: Dijaki predsedniku Borutu Pahorju predstavljajo delo z robotom



Slika 2: Predsednik Borut Pahor in direktor ŠC Martin Pivk med predstavitvijo električnega vozila Smart

veselje, »da imamo tako uspešne in prisrčne dijake, ki imajo znanje. To je dokaz, da ima strokovno in poklicno izobraževanje v Škofji Loki še velike možnosti.«

Vodja MIC-a **Alojzij Kokalj** je ob tem dogodku povedal: »Veseli me, da so vedno bolj prepoznavni projekti, ki v sebi skrivajo veliko realnega znanja, ki so povezani s podjetji in tehnologijami, ki se dogajajo na trgu ali v industriji v tem trenutku. Pravi užitek je spremljati mlade na tej ustvarjalni poti, ko opazuješ, kako raste njihova motivacija ob konkretnih rezultatih, kako se mladi razvijajo ob problemih, s katerimi se srečujejo. Ob tem se človek vpraša, ali jim lahko sploh še kaj več damo. To je odlična popotnica za njihovo življenjsko in karierno pot. Veseli me, da je tudi predsednik države ob današnjem obisku prepoznal potrebo po predstavitvah in potrditvah tovrstnih dosežkov mladih.«

Šolski center Škofja Loka nadgrajuje svoje izobraževalno-razvojno poslanstvo in odmevne projekte. V letu 2013 je v sodelovanju z Inštitutom Metron že predelal in v uporabo predal električni avto, v septembru 2013 pa je končal investiciji gradnje Medpodjetniškega izobraževalnega centra (MIC) in energetske sanacije šolskih objektov. V okviru projekta vzpostavitve MIC-a Škofja Loka, ki se je začel marca 2009, je bil na površini 2200 m² zgrajen izredno napredno opremljen objekt, ki omogoča izvajanje kakovostnega poklicnega in strokovnega izobraževanja, usposabljanja ter povezovanja z gospodarstvom. Vzpostavitev MIC-a je bila sofinancirana iz Evropskega sklada za regionalni razvoj, projekt energetske sanacije pa iz Kohezijskega sklada. Skupna vrednost obeh projektov je bila približno 5,5 milijona evrov.

Avtor fotografij: **Lado Bukovec, Šolski center Škofja Loka**